6. SITE 948[1]

Shipboard Scientific Party[2]

HOLE 948A

Date occupied: 20 May 1994

Date departed: 1 June 1994

Time on hole: 1 day, 23 hr, 45 min

Position: 15°31.559′N, 58°43.936′W

Bottom felt (drill-pipe measurement from rig floor, m): 4940.0

Distance between rig floor and sea level (m): 10.7

Water depth (drill-pipe measurement from sea level, m): 4929.3

Total depth (from rig floor, m): 5523.7

Penetration (m): 583.7

Total core recovered (m): 0

Logged (mbsf): 0–583.7 (LWD)

Comments: Dedicated LWD hole. No coring done.

HOLE 948B

Date occupied: 3 June 1994

Date departed: 4 June 1994

Time on hole: 15 hr

Position: 15°31.464′N, 58°43.935′W, 200 m south of Holes 948A and 948C

Bottom felt (drill-pipe measurement from rig floor, m): 4949.0

Distance between rig floor and sea level (m): 11.0

Water depth (drill-pipe measurement from sea level, m): 4938.0

Total depth (from rig floor, m): 4998.0

Penetration (m): 49.0

Number of cores (including cores having no recovery): 1

Total length of cored section (m): 4.0

Total core recovered (m): 3.71

Core recovery (%): 92.7

Oldest sediment cored:
Depth (mbsf): 3.71
Nature: clay with foraminifers
Age: late Pleistocene

Drill below core (m): 45.0

Comments: Core to establish the mud line for Hole 948D. Jetting test from 4.0 to 49 mbsf.

HOLE 948C

Date occupied: 4 June 1994

Date departed: 9 June 1994

Time on hole: 5 days, 7 hr

Position: 15°31.568′N, 58°43.935′W, same beacon offset as Hole 948A

Bottom felt (drill-pipe measurement from rig floor, m): 4942.5

Distance between rig floor and sea level (m): 11.0

Water depth (drill-pipe measurement from sea level, m): 4931.5

Total depth (from rig floor, m): 5534.5

Penetration (m): 592.0

Number of cores (including cores having no recovery): 19

Cored (mbsf): 0–9.5 (first interval) and 420.8–592.0 (second interval)

Length of cored section (m): 9.5 (first interval) and 171.2 (second interval)

Recovered (m): 10.1 (first interval) and 161.38 (second interval)

Core recovery (%): 106.1 (first interval) and 94.3 (second interval)

Drilled (mbsf): 9.5–420.8

Total length of cored section (m): 180.7

Total core recovered (m): 171.46

Average core recovery (%): 94.9

Oldest sediment cored:
Depth (mbsf): 180.7
Nature: siltstone and claystone with nannofossils
Age: late Oligocene
Measured velocity (km/s): 1.655

Logged (mbsf): 80.0–568.0 (wireline logs)

Comments: Drilled from 9.5 to 420.8 mbsf.

HOLE 948D

Date occupied: 9 June 1994

Date departed: 29 June 1994

Time on hole: 20 days, 12 hr

Position: 15°31.464′N, 58°43.907′W, 200 m south of Holes 948A and 948C

Bottom felt (drill-pipe measurement from rig floor, m): 4949.0

Distance between rig floor and sea level (m): 11.0

Water depth (drill-pipe measurement from sea level, m): 4938.0 (from mud-line core at Hole 948B)

Total depth (from rig floor, m): 5487.0

Penetration (m): 538.0

Total core recovered (m): 0

Casing:
16-in.: 0–43.4 mbsf
13⅜-in.: 0–475.9 mbsf
10¾-in.: 0–535.3 mbsf
Perforated and screened section: 480.7–522.6 mbsf

Comments: Hole was cased and dedicated for VSP, packer, and CORK experiments.

[1] Shipley, T.H., Ogawa, Y., Blum, P., et al., 1995. *Proc. ODP, Init. Repts.*, 156: College Station, TX (Ocean Drilling Program).
[2] Shipboard Scientific Party is as given in list of participants preceding the contents.

Principal results: The northern Barbados Ridge program was designed to investigate the relationship between fluids and tectonic features, particularly the basal décollement of the accretionary prism. Site 948 calibrates the positive-polarity seismic signature of the décollement. It is also as close as we could navigate to Hole 671B, which penetrated the 40-m-thick décollement and 151 m into the underthrust section during Leg 110. Hole 948A was dedicated to logging. Hole 948B was a jet-in test site for the Hole 948D casing program. Hole 948C was dedicated to interval coring and logging. Hole 948D, 200 m south of Holes 948A and 948C, was cased to 535.3 mbsf for special experiments.

At Hole 948A, we collected logs using logging-while-drilling (LWD) technology, which is a more effective technique than wireline logging in unstable formations such as accretionary prisms. The logging provided compensated dual resistivity, natural gamma-ray (CDR tool), compensated density neutron, neutron-porosity, and gamma-ray (CDN tool) measurements from 0 to 582 mbsf. Drilling conditions remained very good to about 515 mbsf, where circulation pressures increased. The section logged included the décollement zone, which was observed in Hole 671B at about 500 to 540 mbsf and in Hole 948C at 498 to 529 mbsf.

The resistivity, gamma-ray, and bulk-density logs correlate with the physical properties measured on Site 671 cores. An abrupt decrease in density below a fault at 132 mbsf marks the overthrusting of tectonic packages recorded at Site 671. This same trend can be observed in the resistivity log. An increase in total gamma-ray count from 315 to 380 mbsf is related to a distinct break in the relative abundances of carbonate and clay minerals, where carbonate is absent and the amount of clay minerals (which contain a larger portion of radioactive elements) increases.

The LWD logs show pronounced changes across the décollement. Resistivity decreases and bulk density increases. Gamma-ray and resistivity changes occur over a 10-m interval corresponding to the middle of the structurally defined décollement. These differences primarily reflect the change in lithology and clay mineralogy at about 514 mbsf. The increase in gamma-ray count in the underthrust section must in part result from an increase in illite (potassium-rich) observed at Sites 671 and 948.

Within the structurally defined décollement, two low-density spikes occur at 505 and 514 mbsf. Assuming these are not related to grain-density changes, they reflect porosities of 68% and 61%, in contrast to surrounding sections, which have porosities of 47% to 53%. The second spike is coincident with the lithologic boundary and spans a 3-m interval. Overall, such changes could reflect dilation of a fault zone across thin zones that are below the resolution of the three-dimensional seismic data.

A substantial decrease in density from about 2.0 Mg/m^3 at 395 mbsf to 1.8 Mg/m^3 at 500 mbsf, just above the décollement, is similar to density trends in the interval from 100 to 200 mbsf. Given the fairly uniform lithologies, this zone must be related to significant undercompaction and high fluid pressures. This zone coincides with the lowest pore-water chlorinity.

LWD is unique in logging the upper 100 m of the hole; this section cannot be studied by wireline logs because of the necessity for leaving some pipe in the hole. The shallow LWD logs will specify the physical property evolution related to both compaction and the unique tectonohydrologic conditions of this environment.

Hole 948C began with a mud-line core from which was recovered 10.1 m of Pleistocene brown clay with nannofossils. The section includes abundant ash layers. The hole was drilled without coring from 9.5 to 420.8 mbsf. Temperature measurements at 65, 103, 200, 248, 327, and 422 mbsf, when added to Site 671 data, yielded gradients from 92° to 97°C/km in the upper part of the hole, to about 66°C/km in the lower part. Coring at Hole 948C resumed with Cores 156-948C-2X to -19X (420.8–592.0 mbsf), with 95% recovery. Note that, based on the seismic reflection geometry and seafloor depths, the depth to the décollement from the seafloor is 6.5 m greater in Holes 948A and 948C than in Hole 948D.

A major lithologic boundary occurs at 513.9 mbsf. The lower unit (Unit III) is early Miocene and late Oligocene in age and consists of greenish-gray claystone as a background lithology, with rhythmic graded interbeds of gray turbidite claystone and nannofossil chalk. The uppermost part of this unit, from 513.9 to 523.8 mbsf, comprises gray to brown banded variegated claystones. The base of the overlying unit starts as a grayish-brown claystone from 507.7 to 513.9 mbsf; this subunit is overlain by distinctive pinkish-gray/brownish-gray radiolarian claystone of early to middle Miocene age from 498.1 to 507.7 m. Above are subunits from undetermined to late Miocene age, including gray claystone with nannofossils, variegated claystone with thin interbeds of tuff and altered volcanic ash, and gray to olive claystone. The bulk mineral content is highly variable in the section below the décollement, largely in response to fluctuations in the carbonate content, which is mostly partitioned into the nannofossil-rich turbidites. Plagioclase decreases to trace abundances below the décollement. Above the décollement, the relative weight percentage of clay minerals is consistently about 60%, with a significant increase in the décollement between 498 and 514 mbsf. The quartz content is uniform throughout.

From 498 to 529 mbsf, low-dip zones of semi-penetrative scaly fabric, interleaved with zones of fracture networks or stratal disruption, and structurally intact sediments define the décollement zone. The fault zone boundary is gradational over several meters at the bottom, but is sharp at the top. The major lithologic change near the middle of the fault zone at 513.9 mbsf marks a boundary between more brittle deformation above and more ductile deformation below. Mineral veins occur in the upper half and higher in the section, not in the lower half of the fault zone. Discrete zones of shear fabric are well developed in both the upper and lower lithologies. Bedding dips define two domains through the cored interval, with moderate to steep dips above the décollement and shallow to subhorizontal dips below. Several smaller shear zones occur both above and below the décollement; some, such as one at 423 mbsf, exhibit fabric-parallel rhodochrosite veins and tight folding on a centimeter scale. Mineral-preferred orientation fabrics were determined by shipboard study of anisotropy of magnetic susceptibility (AMS). Above the décollement, the AMS results indicate horizontal, east-west shortening in the prism. Just above the décollement, the AMS orientation gradually changes to a geometry consistent with a vertical compaction fabric. Below the décollement, the amount of vertical compaction indicated by AMS is more pronounced.

Organic carbon in the accretionary prism and décollement is less than 0.05% and varies between 0% and 1.83% in the underthrust section. Methane concentrations were low, with the highest being 44 ppm just above the décollement. Low concentrations of ethane and propane were found with methane/ethane ratios of 20 to 60, suggesting thermogenic origin of some of the gas. However, shore-based isotopic analyses will be necessary to confirm any thermogenic origins. Interstitial-water samples indicate dilution by fresh water. The chemical concentration depth profiles exhibit both diffusive and advective characteristics. Focused chloride dilution (about 18% seawater dilution) is observed at the top of the décollement. It coincides with the methane concentration maximum of 44 ppm of methane. While the shapes of the curves of chloride and methane are similar to those observed at Site 671, their magnitudes are distinctly different. The concentration-depth profiles of the analyzed major and minor elements are consistent with mostly lateral fluid flow.

Physical-property data provide correlation and calibration of the LWD data and a comprehensive downhole profile through the fault zone. An offset in most downhole profiles occurs within the décollement zone. This is the result of a major lithologic change. Below 508 mbsf, a sharp offset to higher densities is observed. Compressional-wave velocities decrease somewhat, but the overall impedance change is a positive contrast, similar to the seismic data. Shear-wave velocities measured in core samples are low, probably indicative of the low strength of these sediments.

With the use of the (conical) side-entry subsystem, wireline logs of sonic, spectral gamma ray, and density were recorded in Hole 948C to a total depth of 575 mbsf, well below the décollement. Unstable hole conditions prior to logging required frequent pumping to remove obstacles, especially in the vicinity of the décollement. High wireline tensions during logging of the bottom 60 m reflect hole constrictions and generally unstable hole conditions. Sonic logs show a small downhole increase in velocity at the décollement. The caliper log indicates widely variable hole diameters that degrade the logging data. The poor hole conditions prohibited multiple logging runs.

Hole 948D was drilled for the long-term borehole observatory (CORK) and other downhole experiments. A triple-string casing program was

designed to ensure hole stability for the experiments and placement of a screened section across the fault. Cement was pumped down to the bottom of the second casing shoe at 476 mbsf to assure hydrologic isolation of the formations above the décollement for subsequent packer and CORK monitoring. After the second casing placement, the cement-bond and vertical-seismic-profile (VSP) logs were run. Good bonding occurred in the lowermost 25 to 30 m of the logged hole, plus another 10 m estimated below the lowest log depth, hydrologically isolating the lower part of the hole from the upper part. The VSP extends from about 470 mbsf up to about 96 mbsf within the cased hole; magnetically clamped geophones were used. Results confirm the cement-bond log, with the best records near the base of the hole, which is less than 50 m above the décollement. Uphole, the records are more noisy, but basic onboard processing showed that the data were of good quality throughout the logged interval. The velocity estimated from the VSP is generally higher than the laboratory measurements or the sonic logging data.

Screened casing was set through the fault zone from 480.7 to 522.6 mbsf. A series of packer shut-in and flow tests were run with a drill-string packer set in the casing above the screened interval. The packer work consisted of several different experiments. First was a series of "negative" pulse and flow tests that exposed the isolated formation to hydrostatic pressure and monitored its recovery. A positive slug test showed a rapid pressure rise, then a small initial decay; the pressure then remained elevated and constant for the next 55 min. Three more positive pulse tests were run and then three injection tests at three different pumping rates, each followed by shut-in and recovery. The packer recorded pressure increases to near lithostatic values during the time the well was shut in. However, these data require substantial analysis and evaluation, given the significant formation disturbance during casing.

Last, we deployed the CORK with associated temperature and pressure sensors. Our efforts were hampered by sediment infilling from below, into the casing and out the reentry cone at the seafloor. Cleaning attempts could not keep up with the inflow of sediment filling the casing. We stopped this sediment inflow by filling the hole with a column of 1.66 Mg/m^3 mixed barite and bentonite mud from 538 to about 65 mbsf. We do not know if the screen was damaged (allowing for inflow through the perforations in the casing) or if sediment was flowing up from the bottom of the open casing. We then deployed the French data logger, which has 20 temperature sensors and three pressure sensors. Pressure sensors were at 8, 479, and 509 mbsf.

The CORK was then seated, but it would not latch, leaving the weight of the CORK (and its associated pipe) to hold the seal in place. This weight is equivalent to the piston force that will be acting on the CORK if the fluid pressure below it reaches about 1 MPa (142 psi). The radical use of heavy mud to prevent the formation from flowing into the casing will undoubtedly modify the hydrologic system further. The failure of the CORK to latch will also be a potential problem, which may at least in part be accommodated by the heavy mud and multiple pressure sensors. The deepest pressure sensor, within the screened zone, should have come to equilibrium with the formation fluid pressure, provided that it did not become hydraulically isolated from the surrounding formation.

Using the preliminary estimates of fluid density and of the mud volume, the column of mud should exert a force of probably not more than 2.8 MPa (400 psi) at the depth of the center of the screen. Combined with the CORK weight, the total CORK and mud system might balance 3.8 MPa. The calculated lithostatic load, which should be the maximum possible overpressure, was estimated from the LWD density log to be 4.0 MPa (575 psi) at the screen. Should the CORK vent during the next year, we may be able to latch it during any planned submersible work.

BACKGROUND AND SCIENTIFIC OBJECTIVES

The goals of Leg 156 were to investigate the interaction of fluids, structures, and physical properties and the episodicity of related processes in the vicinity of the Barbados accretionary complex décollement. The Leg 156 operational and scientific program was designed to benefit from the information gathered in the region during earlier surveys and drilling expeditions. In addition, the program was to employ several technological advantages not available 8 yr earlier for Leg 110 (Mascle, Moore, et al., 1988; Moore, Mascle, et al., 1990) or 13 yr earlier for DSDP Leg 78A (Biju-Duval, Moore, et al., 1984).

Site 948 (proposed site NBR-2) was placed as close to Hole 671B (Leg 110) as dithered global positioning system (GPS) navigation would allow, within about 200 m of Site 671, which was located with more accurate, undithered GPS (Figs. 1 and 2). Site 671 was positioned 4.5 km west of the frontal thrust, where the accretionary prism above the décollement is 500 m thick and the underthrust section, 400 m thick. During Leg 110, drilling and coring were completed successfully through this active plate boundary, including the 40-m-thick fault zone, and then continuing through 151 m of the underthrust sequence to a total depth of 691 mbsf. At this depth, sand stuck the core barrel and ended coring operations. Recovery was about 80% overall, but much of the recovered core was disturbed heavily by drilling. In addition, recovery was relatively low within several faults and the décollement itself. Significant thrust faults were identified at 128 and 447 mbsf, where they bound large imbricate slices. Smaller scale deformation was evident in the prism from steep dips of folds and faults. At Site 671 the prism comprises lower Miocene to lower Pleistocene, offscraped hemipelagic mud-mudstone, calcareous mud-mudstone, and marl-marlstone.

The main mesoscopic features of the décollement were pervasive scaly fabric and stratal disruptions. The less deformed lower section had few of the steep dips observed within the overlying prism. The section below the prism and décollement comprises Oligocene claystone, mudstone, and sandy layers. Anomalous pore-water chemistry within the prism and underthrust sequence was a primary indication of recent fluid flow.

Site 948 also was positioned to investigate the geologic significance of regional variations in the seismic waveform associated with the décollement. This plate boundary had been characterized previously based on a three dimensional seismic survey (Shipley et al., 1994) (Figs. 3 and 4). Throughout much of the Leg 156 operations area, the décollement appears as a compound-negative-polarity reflection. This seismic character has been modeled as a discrete, thick fault zone of low impedance (Shipley et al., 1994). In several areas where the décollement waveform is of normal polarity, impedance may increase with depth, perhaps associated with drained or nondilated sections of the fault zone. One of the normal-polarity zones is at Site 671, which perhaps explains in part the relative ease with which drilling and coring at this site penetrated the décollement during Leg 110.

During Leg 156, we planned to core the sediment interval within and around the décollement to allow for additional descriptions, measurements, and sampling, particularly of geochemistry, structural geology, and physical properties. Operations at this site were to emphasize downhole measurements of various kinds, including logging and in situ permeability and temperature measurements. An LWD system was made available for the first days of Leg 156, as wireline logging operations were hampered by poor hole conditions during previous drilling expeditions. We also were equipped with a side-entry sub for use with the wireline-logging attempts in unstable boreholes. Neither of these systems was available during earlier drilling programs in this area.

An ambitious triple-hanger casing system also was to be employed during Leg 156 for the first time in ODP history. The lowermost part of the third casing string was to include a screened section to allow for in situ permeability testing. In addition, the casing system was intended to allow vertical seismic profiling, both above and below the décollement. As with conventional wireline logging, VSP experiments had been hindered during previous active-margin drilling programs by poor hole conditions. Finally, the deep casing system was to allow for emplacement of a long-term borehole observatory (CORK) for measuring pressures and temperatures over several years. We hoped that these measurements would record transient dewatering events thought to be associated with the décollement.

The specific operational objectives at Site 948 were as follows:

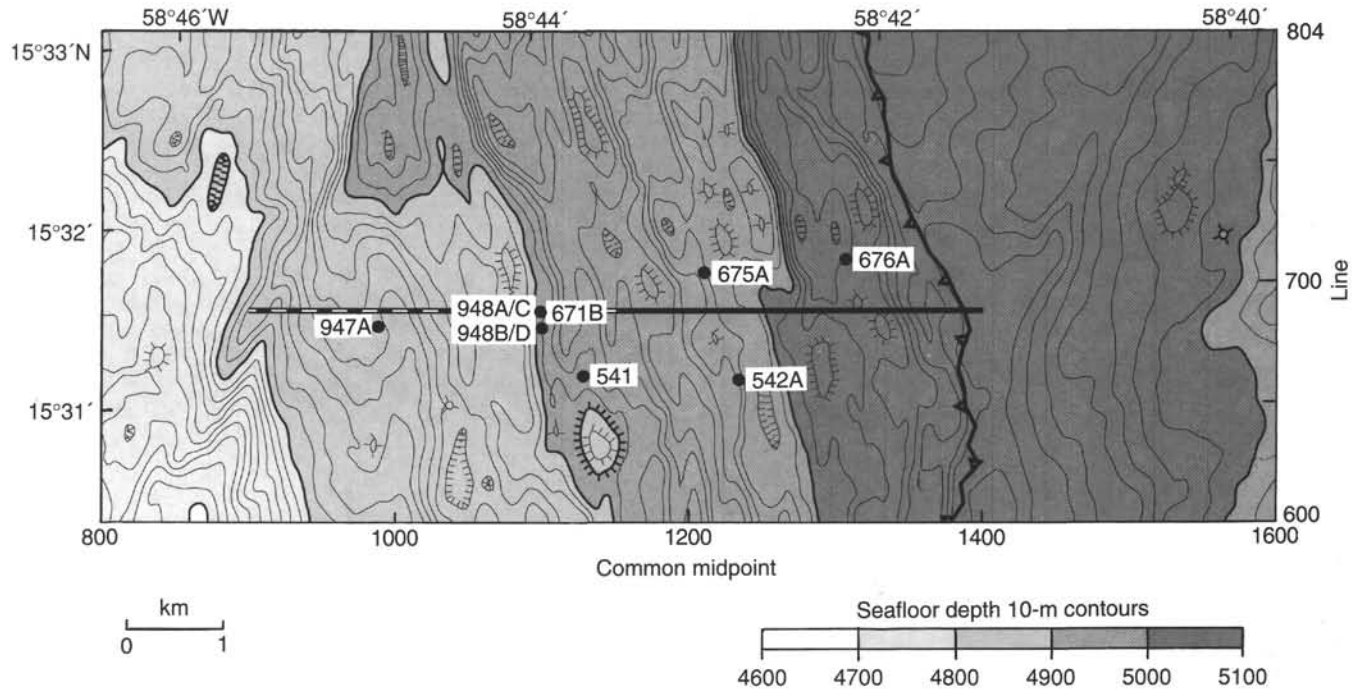

Figure 1. Location map showing the area around Site 948. Bathymetry based on digitizing of three-dimensional seismic data and by assuming a water velocity of 1500 m/s. The frontal thrust (barbed line) is shown for reference, as are Holes 671B, 948A/948C, and 948B/948D. The black line is the location of the seismic profile shown in Figure 2; the dashed line is the location of the seismic section shown in Figure 4.

1. To obtain deep sediment temperature measurements to constrain local dewatering and to establish a baseline for the long-term monitoring experiment;
2. To core the section within and around the décollement (420–590 mbsf) for sedimentological, structural, geochemical, and physical properties analyses;
3. To log completely through the accretionary complex, across the décollement, and into the underthrust section with a variety of geophysical tools;
4. To emplace reentry cone and triple-hanger casing systems, with a screened interval across the décollement;
5. To conduct in situ permeability and seismic experiments (packer and VSP, respectively) within this cased borehole; and
6. To emplace within the casing a sealed borehole observatory, including a data logger capable of recording for several years and a string of temperature and pressure sensors placed across the décollement.

OPERATIONS

Depth Discrepancies at Site 948

Determining true seafloor depths relative to the drill floor proved to be challenging at Site 948 because of a variety of problems. The most serious problem was an early miscount in the pipe tally that led us to overestimate pipe length. Identification of inconsistency and determination of how best to rectify it were complicated because of actual differences in water depth from hole to hole at the site, variations in wireline and pipe stretch, installation of a new (and therefore partly "uncalibrated") coring line, and a later additional error in "stinger" (pipe) length. Pipe depths reported throughout this section in meters below rig floor (mbrf) have been corrected for the error, with uncorrected depths shown for reference in parentheses. Depths in meters below seafloor (mbsf) have not been changed because these were correct all along, having been referenced to the mud line via the mud-line core (for coring depths) or log response (for wireline and LWD data). All other depths shown in other sections in this chapter have been corrected.

Logging-While-Drilling Operations in Hole 948A

Following completion of LWD operations in Hole 947A, the bottom-hole assembly (BHA) and LWD tools were returned to the surface to check data quality and battery power. The LWD tools were re-initialized, and the source was reloaded. The same drilling assembly was run back to the seafloor, while the Site 947 beacon was switched to standby mode and the vessel was offset 1800 m in dynamic positioning (DP) mode to Hole 948A (NBR-2), sited close to Site 671 (Leg 110).

The drillers attempted to determine seafloor depth by tagging the seafloor with the bit. They made a tenuous call when the motion compensator appeared to close slightly with the bit at 4945 (4955) mbrf. The LWD depth of 4940 (4950) mbrf, based on tool response, was adopted as the official seafloor depth of Hole 948A.

Difficulty was experienced in controlling rate of penetration (ROP) during LWD operations in the uppermost 100 m of the section, but experience gained in Hole 947A helped the drillers to maintain a slower and more uniform ROP for better log quality for the rest of the hole. Again, hole conditions were good, and widely spaced sepiolite pills were used only to flush possible large cuttings/cavings from the annulus.

As in Hole 947A, increased circulating pressure was the precursor of drilling problems, which began near 515 mbsf and increased as drilling continued. Mud sweeps did not help. Torque remained normal until the pump was shut down for a connection at 584 mbsf, then it was difficult to regain rotation. A wiper trip was begun, and the pipe stuck briefly at 525 mbsf. The system held 3.4 MPa (500 psi) standpipe pressure with the pump off until the bit had been raised above about 470 mbsf, indicating a packed-off condition. Tight hole was encountered on the downgoing trip at about 502 mbsf (identified from logs and Hole 671B cores as the top of the décollement). Attempts to ream back to total depth were unsuccessful in advancing the bit beyond 535 mbsf because of high torque and sticking.

The interval from 535 to 448 mbsf was back-reamed for a repeated logging section before the bit was run back to 467 mbsf. Because the décollement had been penetrated, the hole was back-filled with 1.4

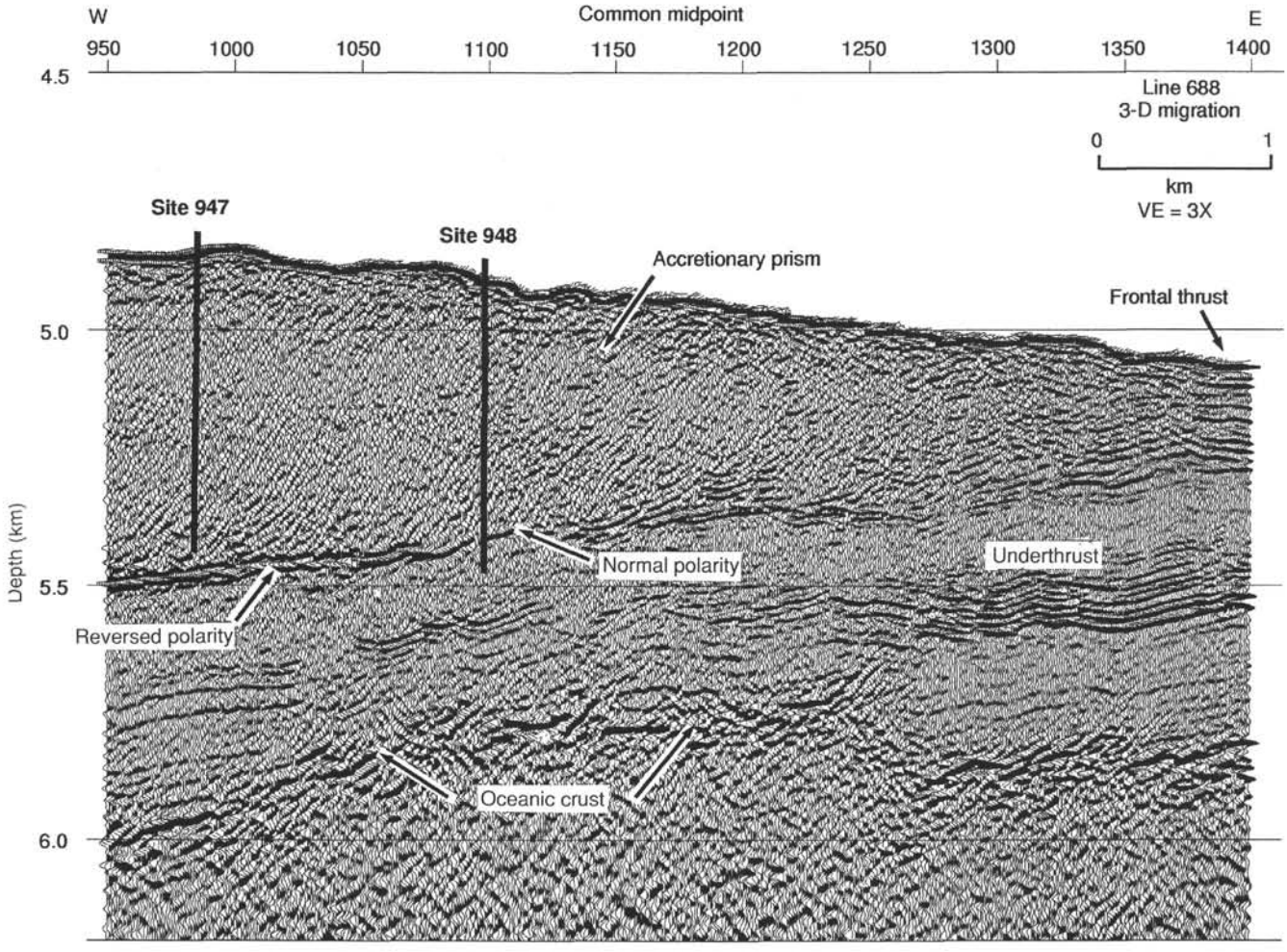

Figure 2. Seismic section illustrating reflection characteristics of the décollement at Site 948. The section was converted to depth using a velocity function derived from Hole 671B (Shipley et al., 1994). Site 948 prism velocity = 1740 m/s; underthrust section velocity = 1779 m/s; Site 947 prism velocity = 1777 m/s; underthrust section velocity = 1811 m/s. Section gain has been equalized with a 500-ms symmetric moving window.

kg/L (12 lb/gal) bentonite/barite mud in an attempt to isolate it hydrologically from holes that were to be drilled nearby.

When the drill string had been tripped and the LWD tools stripped of data and laid down, the positioning beacon was switched to standby mode. *JOIDES Resolution* departed Hole 948A at 1630 EST (local time) on 1 June.

Barbados Port Stop

A brief port call was scheduled primarily to offload the LWD tools, which had been leased at a day-rate, but also this call allowed for onloading of freight that arrived too late to make the primary port call. Prior to departure for Barbados, the ship detoured 7 km east to stop briefly over proposed site NBR-1 and to acoustically switch that beacon to standby mode. We arrived in Bridgetown Harbor at 0915 EST on 2 June.

After the LWD tool shipment was offloaded, several pieces of freight were onloaded, including explosives for the planned shear-wave VSP experiment. Five personnel disembarked and three additional personnel embarked. The 4.5-hr port call ended with the final line aboard at 1445 EST.

Strong trade winds from forward of the beam held the outward average speed to about 10.5 kt. The vessel proceeded to a way point 4.6 km west of Site 948, turned, and made her final approach into the wind. At 0500 EST on 3 June, acoustic commands restarted the positioning beacon, and the vessel shifted to DP mode at 0530 EST once thrusters and hydrophones were lowered.

Jet-in Testing and Mud-line Coring in Hole 948B

An abbreviated, lightweight BHA was assembled with a 29.1-cm ($11\frac{7}{16}$-in.) roller-cone bit because successful coring during Leg 110 through the décollement had been attributed in part to larger bit size and greater annular clearance. The drill string was run at the positioning coordinates of the planned reentry hole to determine seafloor depth and the thickness of soft sediments.

When the top drive was deployed, the bit was lowered until resistance was noted on the weight indicator at 4950 (4960) mbrf. Pump circulation was started, and a jet-in test was performed to determine the depth to which 40.6-cm (16-in.) conductor casing could be advanced without rotation. Satisfactory jetting in was achieved to 4998 (5008) mbrf.

The bit was pulled clear of the seafloor for a mud-line advanced piston core (APC). To avoid the area of greatest disturbance, a minimal (4.5-m) offset was entered into the automatic station-keeping system. The APC was lowered on the coring line and "fired" with the bit at 4943.5 (4953.5) mbrf. The 9.5-m core barrel recovered 3.71 m of sediment (Table 1), and seafloor depth was fixed at 4949 (4959) mbrf. This set the total jet-in depth at 49.0 mbsf. One joint of drill pipe then was laid out, and the vessel was moved to the positioning coordinates of Hole 948A.

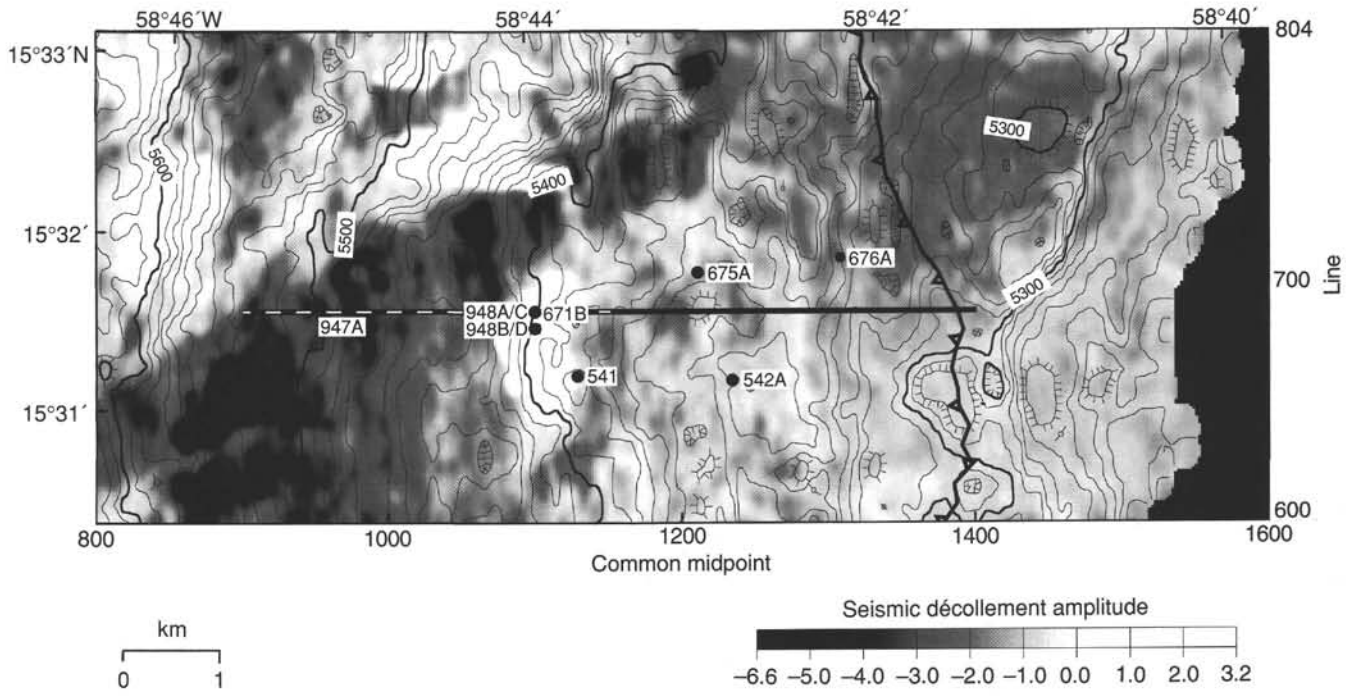

Figure 3. Map of area around the drill site showing the structure of the décollement and the peak amplitude of the reflection. Site 948 is located on the normal polarity seismic décollement (white). Section is equivalent to a three-dimensional horizon crop map of the décollement. Structural contours are at a 10-m interval.

Table 1. Coring summary, Site 948.

Core	Date (June 1994)	Time (UTC)	Depth (mbsf)	Length cored (m)	Length recovered (m)	Recovery (%)
156-948B-						
1H	4	0005	0.0–4.0	4.0	3.71	92.7
Coring totals				4.0	3.71	92.7
156-948C-						
1H	4	0210	0.0–9.5	9.5	10.08	106.1
			******Drilled from 9.5 to 420.8 mbsf******			
2X	5	2200	420.8–430.5	9.7	8.42	86.8
3X	5	2320	430.5–440.1	9.6	9.09	94.7
4X	6	0055	440.1–449.8	9.7	8.61	88.7
5X	6	0230	449.8–459.4	9.6	9.95	103.0
6X	6	0355	459.4–469.0	9.6	6.57	68.4
7X	6	0550	469.0–478.7	9.7	9.80	101.0
8X	6	0745	478.7–488.4	9.7	9.80	101.0
9X	6	0925	488.4–498.1	9.7	8.49	87.5
10X	6	1130	498.1–507.7	9.6	7.29	75.9
11X	6	1400	507.7–517.4	9.7	7.52	77.5
12X	6	1600	517.4–526.8	9.4	8.74	93.0
13X	6	1830	526.8–536.1	9.3	9.89	106.0
14X	6	2100	536.1–545.4	9.3	9.39	101.0
15X	7	0105	545.4–554.8	9.4	9.86	105.0
16X	7	0315	554.8–564.1	9.3	9.48	102.0
17X	7	0510	564.1–573.3	9.2	9.79	106.0
18X	7	0725	573.3–582.8	9.5	8.77	92.3
19X	7	0915	582.8–592.0	9.2	9.92	108.0
Coring totals				180.7	171.46	94.9
Drilled				411.3		
Total				592.0		

Coring and Logging in Hole 948C

To locate Hole 948C as closely as possible to LWD-logged Hole 948A (and Leg 110 Hole 671B), the same beacon and positioning offset coordinates were used. The APC was deployed during the offset, and we attempted to core the sediment/water interface, with the corer actuated from 4933 (4943) mbrf. The APC barrel failed to reach the seafloor and recovered only a "water core." The bit was then lowered 9.5 m, the full length of the APC stroke, and the process was repeated. On the second attempt, the core chamber was completely filled with 10.1 m of sediment. On the assumption that the APC had been fired from the seafloor, seafloor depth was set at 4942.5 (4952.5) mbrf.

A "blind" inner core barrel of the extended core barrel (XCB) configuration was pumped to the bit, and the upper sediment section was drilled without coring to 421 mbsf. With the bit at 64 and 102 mbsf, the core barrel was retrieved and temperatures were measured with the water sampler temperature probe (WSTP) deployed in temperature-only mode with an XCB barrel. WSTP depths reported in the "Heat Flow" section (this chapter) are greater than bit depths because the probe tip extends 1.1 m beyond the bit.

When the WSTP from 102 mbsf was being recovered at about 2900 m below the rig floor, the coring line parted high in the derrick. The lower end of the break became fouled in the line wiper assembly on the traveling block, so the instrument did not fall back down the drill string. The upper end of the break traveled over the crown sheaves and fell to the coring-winch platform. A delay of about 3 hr occurred while the line was clamped off, restrung, and reattached to the coring winch drum. The WSTP was then recovered without incident.

Drilling continued, with additional WSTP runs at 199, 247, 326, and 421 mbsf. All the temperature measurements produced data. No hole problems were encountered in the drilled interval, but the ROP was considerably lower than that in the LWD holes. Continuous XCB coring began at 421 mbsf (Table 1). Core recovery was very good from the beginning, but the cores exhibited moderate-to-severe "biscuiting." No indications of hole problems were encountered as the décollement zone was penetrated around 500 mbsf, except that a circulating pressure increase of about 200 psi was noted beginning at about 507 mbsf. Mud sweeps each second core were initiated at that time, but had no effect on the pressure. "Knobby" drilling joints were used beginning at 517 mbsf in anticipation of sticking of the drill string. At 534 mbsf, the drill string began torquing severely during a wireline trip to retrieve core.

A short trip then was made in an attempt to stabilize the hole and to ream the constricted interval. The string stuck rotationally and vertically each time the pump was stopped, and overpulls of up to 41,000 kg (90,000 lb) were required to free the string. As in the earlier

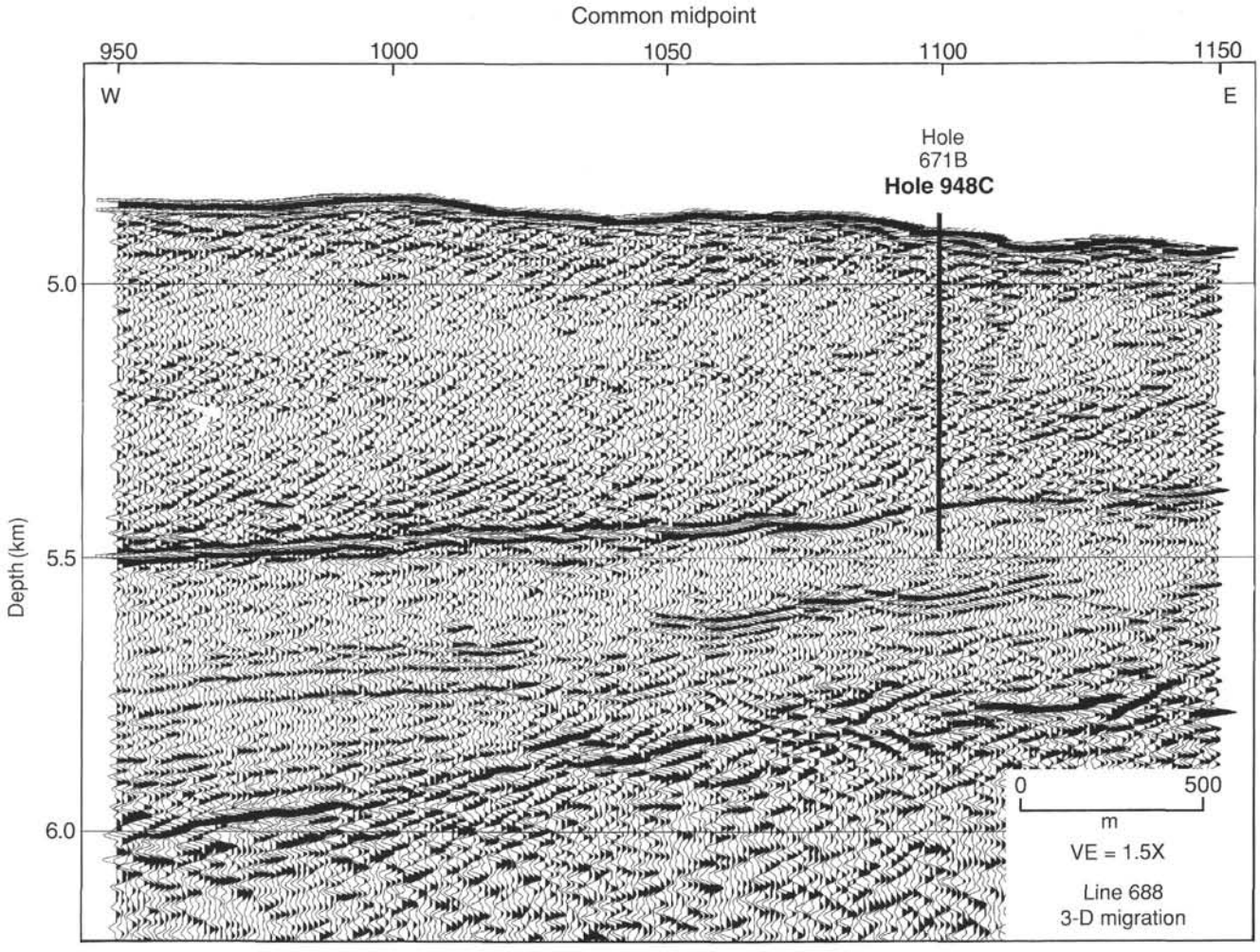

Figure 4. Close-up of seismic section illustrating the location of Hole 948C relative to the décollement and overlying structure. Amplitudes are normalized as in Figure 2.

holes, there was indication that the annulus had been packed off and that circulation had entered the formation. Standpipe pressure remained at 2.6 to 3.4 MPa (400–500 psi) with the pump stopped. Pressure and torque indications returned to normal after the bit had been pulled above 507 mbsf. When the hole had been reamed back to total depth and swept with mud, torque and pressure were close to normal and coring resumed.

Drilling parameters continued to improve with depth, apparently because the formation below the décollement zone was stable and possibly because the 21.0-cm (8¼-in.) drill collars had passed through the constricted zone. With Core 156-948C-19X drilled to 592 mbsf, the depth target of the hole had been reached and coring was terminated. Core recovery for the XCB-cored interval was about 94%, vs. about 79% for the equivalent interval in Hole 671B.

After a mud sweep, a wiper trip was done to prepare the hole for wireline logging. Overpulls of 27,000 to 32,000 kg (60,000–70,000 lb) were required to pull the bit through the décollement zone. Only light drag was experienced above 517 mbsf, but the pipe was "wet" (full of water) for more than 100 m above that point. The upper part of the hole (to 103 mbsf) was in good condition. During the downgoing trip, the top drive was picked up when resistance was met at about 430 mbsf. The bit was washed ahead without rotation to test the feasibility of side-entry-sub (SES) logging operations, while a second pass with rotation was conducted to ream the hole before each connection. A tight hole persisted from 430 to about 535 mbsf, with a weight of 7000 to 9000 kg (15,000–20,000 lb) required to wash through the interval from 511 to 516 mbsf. The lowermost section of hole from 535 to 592 mbsf was open, and no fill was noted at total depth. A sweep of 6500 L (40 bbl) of sepiolite mud was circulated through the hole, and the bit was pulled to logging depth at 64 mbsf. A drag of about 14,000 to 18,000 kg (30,000–40,000 lb) was noted as the "trouble zone" was passed.

The SES then was made up into the drill string, and the logging sheaves were rigged. A combination sonic-density-gamma-ray logging tool string was assembled and run down the pipe. An attempt was made to log the open hole conventionally without lowering the drill string, but bridging in the hole just below the bit foiled the first attempt. Two stands of drill pipe were added, with the same result. The drill string then was run in to 477 mbsf, where resistance was met. After the top drive was deployed, pump circulation was successful in washing through the décollement zone, with a maximum of 14,000 kg (30,000 lb) weight applied. Below 535 mbsf, no more resistance was encountered, and the bit was advanced to 563 mbsf. The logging tool was lowered out of the pipe at that depth and came to rest on an obstruction at 568 mbsf. No further time was spent in attempting to reach total depth, and the pipe was withdrawn while an upgoing log was recorded. The open hole was logged to the end of the drill string at 80 mbsf, and the gamma-ray curve continued inside the pipe to record the sediment/water interface. Restrictions in the hole caused high overpull on the logging tool, even though the bit had passed just

ahead of it. The caliper log curve confirmed that most of the hole was either badly over- or under-gauge and that hole conditions were too poor to warrant additional logs. When the logging tools and SES had been rigged down, the top drive was picked up at 459 mbsf, the first resistance in the hole, and the hole was reamed to 498 mbsf. Since the logging run, the hole had become much tighter and drilling parameters were as though a new hole was being made. Reaming was stopped and the hole was displaced with 74,100 L (455 bbl) of 1.6-kg/L (14-lb/gal) barite/bentonite mud. Freshwater-based mud was used in the hope that it would increase the swelling of hydrophilic clays and hasten closure of the hole. The drill string then was recovered, with all components on deck at 0300 EST on 9 June.

Hole 948D Drilling, Casing, and Downhole Experiments

A new coring line was installed while the ship was offset to the coordinates of Hole 948B, where the reentry/borehole observatory installation was to be located. A 43-m string of 40.6-cm (16-in.) casing was assembled below a preassembled reentry cone that was composed of three joints of range-three 40.6-cm (16-in.) casing, an adapter sub for a 34.0-cm (13⅜-in.) casing hanger, and the 40.6-cm (16-in.) casing hanger. A 37.5-cm (14¾-in.) drill bit and 44.5-cm (17½-in.) underreamer assembly were made up to a BHA of drill collars, with the casing-running tool inserted at a point in the BHA that placed the bit opposite the casing shoe. The BHA was lowered until the casing hanger in the lower section of the reentry cone could be engaged by the running tool. When the entire casing/cone/BHA system was a unit, the moonpool doors were opened and a pipe trip began.

Just above the seafloor, the top drive was deployed and jet-in testing of the casing began at 1145 EST on 10 June. Jet-in was slowed because some of the water that normally would flow through the bit jets was diverted through the underreamer. Penetration came to a halt when the skirt of the reentry cone was calculated to be about 1.5 m above the seafloor. That was within the normal range of error for determining seafloor depth, and circulation was stopped with the casing shoe at 4990.5 (5000.5) mbrf. The drill string was lowered to transfer the weight of the casing/cone to the seafloor and turned to the right to release the assembly. The number of turns and torque indications signaled a normal release, and the string was advanced about 1.5 m with little resistance.

Circulation was started at 45.2 L/s (700 gpm) to open the underreamer arms. The 37.5-cm (14¾-in.) hole below the casing shoe was left for later opening to provide support for the 40.6-cm (16-in.) casing while the sediment reconstituted. Drilling and underreaming then continued at a rapid rate to the planned depth of 5428 (5438) mbrf (479 mbsf) for the casing rathole.

As the string was pulled back with the underreamer arms closed, minor drag was noted about 10 m off total depth. The lowermost 24 m of the hole was re-reamed before the top drive was set back for the trip out. Just below the 40.6-cm (16-in.) casing shoe, the top drive was redeployed and the interval of the 37.5-cm (14¾-in.) hole just below the casing was reamed to 44.5 cm (17½ in.). When the BHA passed through the reentry cone, the running tool reengaged its bushing, which was held in place at the casing hanger with shear pins. An upward pull of about 9000 kg (20,000 lb) was required to shear the pins and free the drill string for retrieval. The drill string then was pulled and the BHA dismantled, with all components on deck at 2000 EST on 11 June.

Thirty-seven joints of 34.0-cm (13⅜-in.) casing were run and attached to the drill string. The drill pipe was tripped to reentry depth, with five stops to fill the string with water (because the casing float shoe had no automatic-fill device). During the fourth stop, the vibration-isolated TV (VIT) frame was deployed and latched around the drill pipe for lowering simultaneously with the drill string. Reentry was achieved at 1745 EST on 12 June.

No significant resistance was met as the casing was lowered into the hole until it reached 219 mbsf, where drag began. At 239 mbsf, all the casing weight below the seafloor was insufficient to advance the casing farther. The top drive was deployed at that point so that the casing could be "washed" to the bottom of the hole. Circulation seemed to help little, and slow progress was made by alternately raising the casing and applying all available weight while pumping at rates of up to 32.3 L/s (500 gpm). Good progress was made with the casing at 276 to 326 mbsf. Firm resistance again was encountered at 326 mbsf, and no amount of "working" and circulation could advance the casing shoe past 336 mbsf. After 1.5 hr with no progress, the effort was abandoned and the pipe trip was begun to recover the casing string back to the ship. The casing hanger and uppermost casing joint were laid out as a unit. When the casing was raised farther, the second joint was found to be visibly deformed near the bottom and the third joint had completely collapsed. The upper end of the fourth joint also had been deformed by the collapse. The collapse apparently occurred because the drill string had not been filled with water frequently enough during the pipe trip and the hydrostatic pressure differential exceeded the collapse pressure of the casing. To determine the extent of damage, the VIT was deployed and run to the end of the casing string. The float shoe was sighted at the proper depth, confirming that no casing had been left in the hole, but lighting, viewing angle, and video quality made any assessment of damage inconclusive.

The damaged second, third, and fourth joints of casing were removed from the string. With full open casing again accessible, a 31.1-cm (12¼-in.) drill bit was lowered to the guide shoe to confirm that the remainder of the string was free of restrictions. Three new casing joints of equivalent length then were added to replace the failed joints and the uppermost joint, with casing hanger, was reinstalled.

Because the hole was known to be obstructed to some degree and because the elapsed time since drilling already had exceeded two days, there was considerable concern about the chances of successfully emplacing the casing string without additional hole conditioning. Thus, plans were made to reenter the hole with the bit/underreamer assembly used for the original drilling. For that operation to be conducted, the casing string had to be disassembled or stored off-centerline below the rig. It would have been relatively straightforward to hang off the string on the moonpool doors just forward of centerline, but two reentries were required and it would have been necessary to open the moonpool doors to deploy and recover the VIT. Rig personnel devised an alternative solution of suspending the casing from a pair of pad eyes on the rig floor support beams about 2 m forward of the centerline. The load was transferred and suspended by means of two sets of slings and shackles attached to a "spider clamp," which in turn supported the casing elevators (which were latched under the uppermost casing collar).

The 37.5-cm (14¾-in.) bit and 44.5-cm (17½-in.) underreamer then were made up to a drilling BHA. After a routine trip and reentry, the bit was run to 183 mbsf before the top drive was deployed. No resistance was "felt" until the bit reached 389 mbsf. Only minor torque and weight indications were noted as the hole was reamed to total depth. Two meters of new "rathole" then were made to 5430 (5440) mbrf (481 mbsf), and the hole was flushed with sepiolite mud. At 0030 EST on 15 June, the BHA had been recovered and the bit and underreamer were on deck.

Slings again were used to transfer the weight of the casing string to the hoisting system and to return it to the rig floor, where it was made up to the DrilQuip casing-running tool. Reentry was done after the pipe trip to the seafloor, and the casing was lowered into open hole. Resistance was first encountered at 383 mbsf, and the top drive was picked up to provide circulating capability. Slow progress was made over the next 148 m, with circulating rates of 12.9 to 22.6 L/s (200–350 gpm) and up to 23,000 kg (50,000 lb) of casing weight required for much of the interval. During the washing-in operation, the drillers noted that all circulation returns to the seafloor were outside the 40.6-cm (16-in.) casing string, causing the sediment to boil around the reentry cone. At the final drill-string connection (471 mbsf) before the casing hanger landed, the cementing swivel and

safety valve (containing the plug-release dart) were attached to the final drilling joint and incorporated into the string below the top drive. The casing then was washed down the final 5 m until progress stopped, and the 34.0-cm (13⅜-in.) casing hanger latched into the 16-in. casing string. This latching in was checked by taking a 14,000-kg (30,000-lb) overpull on the drill string.

With the casing in place, a cement slurry was mixed to 1.8 kg/L (15 lb/gal) with seawater and pumped through the cement swivel. When 32,900 L (202 bbl) had been mixed, the release dart was launched and an additional 1100 L (7 bbl) was pumped to fill the lowermost joint of casing. The cement slurry was followed by 3300 L (20 bbl) of fresh water to flush the lines, then displaced with seawater. The dart landed in the top plug and required 13.8 MPa (2000 psi) to shear pins and release the top plug, which subsequently "bumped" at the casing shoe when the cement had been displaced completely. During the displacement, the circulating pressure increased steadily, indicating the buildup of hydrostatic pressure in the annular cement column, only to drop by about 1.4 MPa (200 psi), approximately 1900 L (500 gal) short of complete displacement. The pressure indication was interpreted to mean that the formation had broken down and that the slurry had fallen some distance back down the annulus. A further disappointment was a strong backflow of water when the cementing hose connection was broken, indicating that the float valve in the casing shoe had not held and that the slurry was "U-tubing" farther down the annulus and into the casing.

As soon as the cementing hose had been disconnected, the weight of the casing string was set down on the cone and the drill string was turned to the right to actuate the DrilQuip running tool. The operation was viewed with underwater television, and the string was observed to turn the required four revolutions—but only after abnormally high torque had been applied. When the drill string was raised to separate the running tool from the hanger, separation was not achieved and the casing string remained attached.

Failure of the running tool to release left the drillers with few options. Circulation was not possible because the casing was sealed by the plug at the bottom and the running tool at the top. It was possible only to apply torque and to place varying amounts of upward tension on the tool. The drillers spent 5 hr "working" the pipe with torque and tension, with up to 2500 N·m (18,000 ft-lb) of torque applied. In addition, circulating pressure was applied to break a possible hydraulic lock imposed by slurry in the annulus. That was effective in returning the cement top plug to the shoe after about 2900 L (750 gal) had been pumped. Tension was kept below 27,000 kg (60,000 lb) above casing weight for most of the time to avoid shearing the retaining lugs and unseating the 34.0-cm (13⅜-in.) casing string. The ship was offset 40 m in each quadrant in case positioning error was imparting lateral stress to the tool. When it appeared that normal release could not be done, the cementing equipment was removed from the string in preparation for a heavy overpull. This overpull was applied in increments with the aim of shearing out and recovering the surface casing string before the cement could set. Between pulls, weight was slacked to the "neutral" point and torque was applied. After a pull to 90,900 kg (200,000 lb) over casing weight had been applied and released, the tool released under high torque and the drill string spun free.

A round trip then was done for a drilling BHA equipped with a 31.1-cm (12¼-in.) drill bit and a mechanical bit release (MBR). After another routine reentry, the bit was run into the hole. The trip proceeded with caution because the casing was expected to be about half full of cement. Remarkably, no cement was tagged until 18 m above the shoe. (Apparently the float valve had held after the top plug was pumped into place the second time.) The cement in the casing, the rubber/aluminum plugs, and the casing shoe were drilled out in 2 hr. The 5.5-m rathole then was cleaned/drilled out to 12¼ in. to the previous total depth, and a sweep of extra-high-viscosity bentonite mud was circulated to clean debris from the hole.

After the VIT had been deployed, the bit was pulled back to the seafloor. The string was pulled clear of the reentry cone, and the rig was offset clear of the cone while the rotary shifting tool (RST) was run down the pipe on the coring line. Release of the drill bit and bit disconnect onto the seafloor was recorded on videotape, and the VIT was held in position while the ship was offset back for reentry. Upon reentry, the open-ended BHA was lowered inside the casing, the VIT was recovered, and the logging sheaves were rigged.

The first logging tool to be run was a Schlumberger cement attenuation (bond) log (CBL) of the surface-casing string. To avoid running the tool into open hole, an upgoing log was recorded from about 14 m above the casing shoe to the end of the drill string at 51 mbsf. Logging results showed cement bonding (80% or better) about 52 m up from the casing shoe (assuming inclusion of the lowermost 14 m), partial cement bonding uphole an additional 118 m, and free pipe for the upper 305 m of 34.0-cm (13⅜-in.) casing. A VSP then was run, with 4900- and 1200-cm^3 (300- and 120-$in.^3$) air guns as the sound source and the Schlumberger array seismic imager (ASI) tool as the downhole sensor. The VSP covered the same interval as the CBL.

After recovery of the drill string, preparations were made for running 27.3-cm (10¾-in.) production casing. About 13 hr was required to assemble 39 joints of casing, with hanger and seal subs. Three joints of perforated casing covered with wire-wrap screen were run near the bottom of the string. At 0830 EST on 19 June, the entire casing string was hung off in the moonpool, and assembly of the inner (stinger) assembly began.

A 25.1-cm (97/8-in.) drill bit was made up to the lower end of a 24.1-cm (9½-in.) Servco underreamer equipped with 38.1-cm (15-in.) arms, and the bit/underreamer assembly was attached to a 19.4-cm (7⅝-in.) Drilex positive-displacement mud motor (PDM). Hydraulics of the bit/underreamer/PDM assembly were tested in the moonpool by circulating with the mud pump through the top drive. Above the motor, a circulating sub, stabilizer, drill collars, and 12.7-cm (5-in.) drill pipe completed the stinger to space the bit about 3.3 m outside the casing's guide shoe. The entire casing/stinger assembly was joined using the DrilQuip running tool, then lowered through the moonpool at 1430 EST on 19 June.

The VIT was deployed soon after the pipe trip began. When the casing shoe had been lowered to about 1400 mbrf, it came into view on the TV monitor, but nothing could be seen extending below it. The obviously incorrect spacing indicated that a measuring error had occurred either in the casing string or the stinger. Both tallies were checked, but no error was found, so the entire assembly was brought back to the rig and the casing string again was hung off in the moonpool. The running tool was removed from the stinger so that the drill string could be lowered through the casing. Visual monitoring with the TV indicated that 8.5 m needed to be added to achieve the correct relative spacing between the casing and the stinger. That was accomplished by adding drill pipe and drill-collar pup joints. The coring line sinker bar was lowered inside the stinger to land in the circulating sub, and the depth measurement indicated that the stinger had been too short and that the casing measurement was accurate. The pipe trip resumed at 0000 EST on 20 June.

After its reentry into the hole, the bit/underreamer was lowered to just above the casing shoe. Solid resistance was met at the casing shoe, where the "rathole" had apparently closed in, and it was necessary to drill/underream from the shoe. Some difficulties (torquing up and slow progress) were encountered when opening the hole past the shoe/rathole area, but slow, steady progress then was established while drilling the casing ahead. Drilling/reaming parameters were 32.3 L/s (500 gpm) circulation rate, approximately 145 rpm on the PDM, and 4500 to 11,400 kg (10,000–25,000 lb) weight applied. The first 38 m was completed in 5 hr, and the operation was almost routine until a sub was connected at 513 mbsf. The familiar sticking tendencies returned, and no further progress could be made. It appeared that the formation was squeezing the casing, inhibiting circulation and preventing weight from being applied at the bit/underreamer. It was necessary to make a short trip back above the casing shoe (where more torque and resistance were met going down). Nearly 20 hr was

required to ream and back-ream the hole through that interval before near-normal drilling parameters were regained and the resistance at 513 mbsf was passed. During that period, techniques were refined for the drilling-in operation. The drillers discovered that better progress could be made at somewhat-reduced circulation rates of 22.6 to 25.8 L/s (350–400 gpm) and that getting restarted after connections involved pulling up a few meters before progressing downward successfully. The casing was advanced from 513 to 528 mbsf in about 1.5 hr, but resistance again was met at 528 mbsf. Repeated attempts failed to advance the hole, and hydraulic resistance as well as sticking tendencies were met at that depth. Finally, additional weight was applied, and the pipe became firmly stuck.

Intervening events, including a check of the length of drill string at the reentry cone during reentry and an additional check of the stinger tally, had convinced rig personnel that the original conclusion of a short stinger had been in error and that the casing was too long by 8.5 m. All depths, including bit depth at the time of casing landing, then had been corrected and the target bit depth had been established at 547 mbsf. Because the symptoms were so similar to earlier drilling difficulties, it was only after considerable effort, overpull, and 4 to 6 hr of pumping at high pressures and volumes had been applied to freeing the "stuck" pipe that rig personnel suspected that the casing hanger might have latched in. A check against the pipe-length correction showed that 528 mbsf was the correct landing depth for that assumption. The VIT frame then was lowered and provided visual confirmation that the casing hanger was down inside the reentry cone. String weight was slacked off until the casing string (29,500 kg [65,000 lb]) was supported by the cone and surface casing. When torque was applied to the drill string, the DrilQuip running tool functioned perfectly and released after four quick revolutions of the pipe. A dense plume of effluent was then observed on the VIT image, flowing freely from the reentry cone.

The actuating ball for the circulating sub then was dropped and allowed to fall freely in the pipe while the bit/underreamer was pulled above the screened section of the casing. It then was circulated into place at a low pumping rate (so as to avoid actuation of the underreamer arms). The pin in the sub was sheared at 12.4 MPa (1800 psi) to open the drill string to circulation above the PDM and to avoid a "wet trip."

Some drag and backflow were noted while the stinger BHA was being withdrawn from the casing string. That was attributed to packing of clay and cuttings around the lower BHA. When the BHA was recovered, those suspicions were borne out, as the two stands of drill collars near the bottom of the BHA were found to be tightly caked with clay.

To facilitate the testing and flushing of the PDM/underreamer with fresh water, the top drive was picked up. While the top drive was in place, it was blanked off and a pressure test of the rig's surface equipment was conducted in preparation for the forthcoming packer experiments. A logging/packer BHA then was assembled and tripped to reentry depth. Though the string-length discrepancy finally had been traced to a math error in the 12.7-cm (5-in.) drill-pipe tally, the entire drill string was remeasured during the trip to dispel all doubts. A "pig" was inserted into the drill string, and the circulating head was attached to the top stand of drill pipe as it was picked up for reentry. While the vessel was maneuvered into position for reentry, the pig was pumped down the drill string to clean rust scale and pipe dope, which could have interfered with the operation of the packer, from the interior of the string. Strong and variable currents interfered with positioning for reentry, and more than 4 hr was consumed before a successful stab was made into the cone. It was noted that there was little or no flow from the hole at this time.

Upon its reentry, the BHA was run into the hole and knobby drilling joints were picked up in preparation for logging. The Schlumberger ASI was deployed for a second VSP in the lower section of cased hole. When the seismic array had been run to 240 mbsf, it came to a stop unexpectedly. The seismic array was lightweight, and an obstruction in the cased hole had not been anticipated. Those factors resulted in the tool's being "overrun," with the excess slack placed in the cable immediately upon its landing. When the ASI would go no deeper, it was tested for functionality with a few air-gun shots and then retrieved to the surface. Some drag was noted during its retrieval, which became "jerky" at a shallower depth. Upon its recovery, the lower portion of the ASI was found to be knotted, with resultant kinking and abrasion. Subsequent repair and testing determined that the array was operational.

The drill string then was lowered to check the obstruction. Resistance was met at 227 mbsf, and circulation was used to wash out the accumulation in the casing. After the second stand of pipe was circulated downhole, we noted that the hole was flowing vigorously with billowing clouds of sediment-laden water. We inferred that the hole had filled in with sediment and that the obstruction had been cleared by the pipe. The top drive was picked up, and the BHA was circulated to total depth to ensure a clean hole for the packer experiments. Circulation was maintained while the string was advanced, and the slight drag noted was attributed to friction in the casing string and/or slight misalignment at the reentry cone. The hole was circulated at total depth for 30 min at 32.3 L/s (500 gpm). As the string was raised to position the packer above the screened-casing interval, a drag of 9100 to 13,600 kg (20,000–30,000 lb) was noted.

With the TAM International straddle packer (TSP) positioned at 474 mbsf, near the center of the first casing joint above the screened interval, the instrumented go-devil was introduced into the pipe at the rig floor and pumped into place. The motion compensator then was activated and, upon landing of the go-devil, a sequence of permeability experiments was conducted. The initial setting of the TSP was routine, except that the expected release of drill-string pressure to the isolated formation interval below the packer was not reflected on the standpipe pressure gauges—there was only a slow decline in pressure. A mechanical set was indicated by the weight indicator and behavior of the drill string, and the standpipe pressure steadied at about 1.4 MPa (200 psi). Those factors indicated an otherwise-normal packer set, so the experiment continued without resetting. The first set of experiments involved "negative" pulses generated by opening the standpipe valve to bleed small amounts of water into the cementing tanks and then monitoring the aquifer's pressure-recovery curves. It was noted that the pulses and recoveries were superimposed on a steady increase in shut-in pressure. The packer was found to be slipping during these tests, however, and this stopped only when the element reached the depth of a tool joint in the casing.

With the initial series of tests complete, a wireline trip was made to retrieve the go-devil. When the data had been checked and determined to be of good quality, the hole was cleaned to the bottom by circulating seawater, and the go-devil was redressed and pumped back into place for a second series of tests. Positive pulse or "slug" tests, followed by a series of constant-rate injections, completed the permeability experiments, and a second trip with the coring line was made to retrieve the go-devil. The retrieval tool struck an obstruction in the drill pipe about 235 m above the TSP setting depth. Attempts to pass the obstacle were unsuccessful, and the wireline sinker bars were recovered. It was concluded that, because the hydraulic seal of the packer had not been broken completely, the go-devil had been unseated and forced up the drill string by material flowing from the formation. Failure of the retrieving tool to engage the go-devil was attributed to sand or debris in the pipe above the go-devil. A second run then was made with the coring line. The winch was stopped short of the previous set-down depth, the rams of the wireline blowout preventer (BOP) were closed, and pump circulation was applied until the pressure reading showed that the go-devil had returned to the packer. That operation had to be repeated before the go-devil was engaged successfully for retrieval. When it was recovered to the surface, the go-devil assembly was found to be clean and undamaged.

Because of the suspicion of sand/silt in the hole and because an unobstructed hole was needed for subsequent installation of the

CORK sensor string, the coring-line sinker bars were run back down the drill string and through the TSP into cased hole. The depth meter indicated that the sinker bars reached to within 3 or 4 m of total depth before setting down.

After recovering the drill string, rig personnel noted that the TSP was in exceptionally good condition, although the element had not "relaxed" in diameter to the usual degree. The packer later was found to be filled with silt, sand, and clay, with sediment packed into the element, the control valve assembly, and all internal spaces. This meant that at some time before either the first or second packer set, mud must have gotten up inside the drill pipe above the go-devil seal and inflation ports.

The "stinger" for the CORK assembly was expanded to 12 used drill collars to provide sufficient weight to seat the CORK against a projected flowing pressure of at least 2.1 (and possibly 3.4) MPa (300–500 psi). When the stinger had been made up and hung off at the rig floor, the CORK and its running tool were assembled into the string. Two stands of drill collars above the running tool completed the BHA. After the pipe trip, a fairly routine reentry was made. Again, it was noted that the hole had ceased to flow.

During the reentry operation, the wireline sinker bars had been run down to the BHA. As soon as reentry had been accomplished, they were run out into the cased hole to recheck the amount of hole available for the CORK sensor string. The bars came to rest at 301 mbsf. It then became apparent that the hole was being filled in by the formation and that sediment slurry had twice accumulated in the borehole until it had stopped the influx of water. It also was evident that the sensor string could not be emplaced under the existing conditions.

Few options were available because the CORK assembly did not permit our running the string into the hole or any circulation beyond the running tool. Setting a 300-m sensor string was scientifically unacceptable; thus, it was necessary to trip the drill string before any further action could be taken. As no casing plugs were available, the best chance of emplacing a full-length sensor array successfully was judged to involve "killing" the hole with weighted drilling mud to arrest the influx of sediment-laden water. Because that action would consume most of the remaining stock of barite, however, operational capabilities for subsequent Site 947 would be compromised.

A round trip of the drill string was made, the CORK assembly was laid out, and reentry was performed with an open-ended BHA of two stands of drill collars. The hole was "washed" clean without difficulty from the top of fill, which had risen to 231 mbsf. To avoid the possibility of reopening the casing/hole annulus to flow, the reentry/cleanout bit was positioned 4 m above the casing shoe for hole conditioning by circulation. The decision was made to commit the heavy mud to the successful completion of Hole 948D and to start mixing the freshwater/bentonite/barite suspension to 1.6 kg/L (14 lb/gal). After the bit had been advanced to total depth and after a total of 10.5 hr of circulation, the hole was displaced with 57,000 L (350 bbl) of mud. The rig personnel pulled back the BHA to 92 mbsf, where the trip was interrupted for slipping and cutting the drilling line. No flow from the cone occurred while the hole was observed by TV for 1 hr during that operation.

Again, the drill string was tripped. The stinger, shortened to four drill collars because it was thought that additional weight was unnecessary, and CORK assemblies were incorporated into the BHA. Reentry was made with the stinger after 45 min of positioning, and the coring-line sinker bars, which had been run to the upper BHA, were lowered into the cased hole. The bars descended unimpeded to total depth, indicating that the hole was ready to receive the full CORK sensor string.

The string of thermistors and pressure transducers provided by IFREMER had been prepared for deployment, and the drill floor was rigged for handling the string. Initial handling of the sensor array was straightforward, as the spacing of the instrument nodes provided attachment points that enabled the crew to handle 25-m sections of the string. The sensors were spaced at 50-m intervals in the upper portion of the string, which entered the pipe last. That spacing exceeded the working height in the derrick, and the crew found it necessary to use a large sheave so that the cable could be handled in a doubled configuration. Two 50-m sections of the cable were damaged by a sharp edge on the sheave frame when tension was transferred between handling winches. The damaged sections were replaced with spare sections totaling 85 m in length and, after 5.5 hr, the array was hung off in the drill pipe. A 10.2-cm (4-in.) overshot then was used to connect the sinker bars of the coring line to the data logger at the top of the array for lowering into the hole.

To avoid "floating" or damage to the sensor string, the load was lowered slowly and cautiously. The weight indicator showed that the data logger landed approximately at the proper depth, but depth and tension indications were ambiguous as a result of the length/weight of the line and of the vessel's motion. Because the crew did not see the normal amount of overpull required to shear the pins to release the overshot, they tried numerous times to latch the data logger into the CORK, with some efforts involving downward jarring with the sinker bars. They finally decided that some weight had been lost (but less than the weight of the sensor array) and retrieved the coring line. Upon its arrival on deck, the overshot was found to have released the array and the pin had sheared. To verify that the data logger had been latched in, the redressed overshot was run back to engage the data logger. Upon landing the overshot, an overpull of 1800 kg (4000 lb) was taken before the pin was sheared by jarring, and the wireline again was recovered.

The top drive then was picked up, and knobby drilling joints were added to land the CORK in the reentry cone. With the CORK landed and the motion compensator in operation, the 10.2-cm-diameter (4-in.) setting ball was dropped and pumped down to the running tool. When the ball landed, the pump was stopped momentarily with drill-string pressure holding at 1.7 MPa (250 psi). Pressure then was increased to 6.9 MPa (1000 psi) to be held for 20 to 40 s to actuate the hydraulic latching mechanism. After only a few seconds, however, pressure abruptly fell to zero. The probable cause of the premature release of pressure was considered to be shearing out of the seat in the running tool at less than the design pressure of 12.4 MPa (1800 psi). On the slim chance that the ball had become temporarily fouled at a tool joint or other pipe restriction, circulation was continued for several minutes with no results. A final attempt to latch was made by pumping a second ball down the drill string, again with no pressure indication of landing. While further actions were considered, the wireline sinker bars were run to confirm that the balls had reached the depth of the running tool.

Inability to achieve mechanical latching left only two operational choices. The CORK could be released with only the weight of the stinger and CORK to maintain the seal by gravity, or the entire CORK and sensor-string assembly could be recovered to the drill floor, the sensor string removed, the running tool redressed, and the entire deployment procedure repeated. The principal drawback to the former choice was that the hydraulic seal of the CORK would be lost if/when the hole pressure at the CORK exceeded hydrostatic pressure sufficiently to lift the CORK. In addition to the impact of the latter option on operating time and on the remaining scientific objectives, a very high risk of further damage to the French sensor array was possible when pulling it clear of the reentry cone. The rig crew could not retrieve the IFREMER string without first bringing the CORK back to the ship because the setting balls prevented engagement of the data logger with the wireline. After the alternatives had been considered, the decision was to release the CORK and to continue with the operational plan of the leg. The final configuration of the IFREMER sensor string in Hole 948D is listed in Table 2 and shown relative to casing and screen positions in Figure 5.

The moonpool doors were opened, and the ROV landing platform was installed around the drill string and dropped freely. Immediately, the VIT was installed and run down the pipe to observe the position of the platform and the unjaying operation. When the VIT arrived at

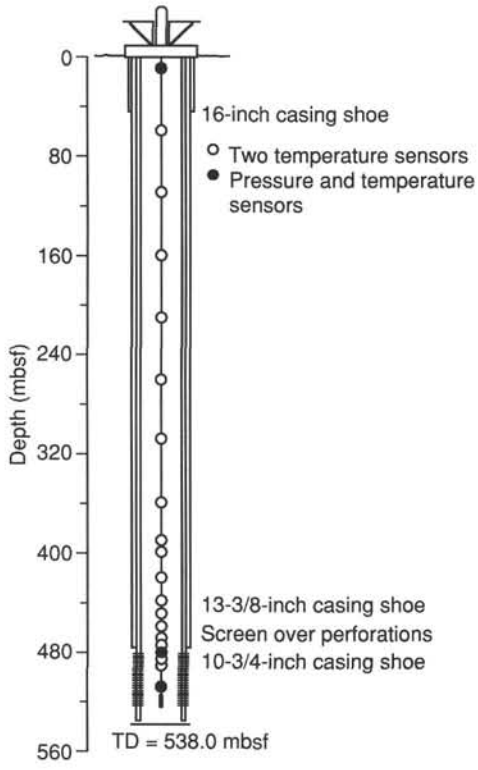

Figure 5. Final configuration of IFREMER sensor string, casing, and screen deployed as part of a long-term borehole observatory (CORK) in Hole 948D.

viewing depth, the platform was seen to be slightly off center; thus, the CORK was raised out of its seat sufficiently to reposition the platform. The CORK then was reseated, the drill string was slacked off and turned slightly to the right, and the CORK assembly was released.

During the final pipe trip at Site 948, both "live" positioning beacons were recovered. We attempted to call up a third beacon, which had ceased transmitting several days earlier, but the beacon did not surface. As plans to occupy site NBR-3 had been canceled, the vessel was offset to that location during the trip to reactivate and recover the beacon launched there on 28 May and subsequently switched to standby mode. No response was received from that beacon, which failed to surface.

LITHOSTRATIGRAPHY AND SEDIMENTOLOGY

Lithologic Units

The sediments recovered at Site 948 comprise three lithologic units (Table 3; Fig. 6). Divisions between units and subunits are based on visual core descriptions, smear slide analyses, fossil content, carbonate content, and bulk X-ray mineralogy. We adhere to the first-order unit divisions identified at Site 671 during Leg 110 (Shipboard Scientific Party, 1988), but we identified subunits differently. The stratigraphic intervals cored at Site 948 include 0 to 10.08 mbsf (Cores 156-948B-1H and 948C-1H) and 420.80 to 592.72 mbsf (Cores 156-948C-2X through -19X). Core recovery was good to excellent (68% to 106%).

Unit I (0–10.08 mbsf; 156-948B-1H and 948C-1H)

Only the top 10.08 m of this unit was cored. Based on analogy with similar strata at Site 671 (Shipboard Scientific Party, 1988), Unit I is probably about 400 m thick. The most common type of sediment consists of light brownish gray, mottled, and moderately bioturbated Pleistocene clay, with trace to abundant amounts of nannofossils and foraminifers. Intervals having increased foraminifer concentrations occur in Sections 156-948C-1H-1 and -1H-3. In addition, several thin beds and patches of gray to grayish brown vitric and crystal-rich volcanic ash are present. The carbonate content in Unit I ranges from 0.5 to 33.5 wt% (Fig. 7), and the mean value for 16 samples is 15.6 wt% (Table 4).

Table 2. Configuration of IFREMER sensor string deployed below CORK in Hole 948D.

Depth (mbsf)	Component type
8.4	TP
58.5	TT
108.5	TT
158.6	TT
208.6	TT
258.7	TT
308.8	TT
358.8	TT
388.8	TT
398.8	TT
418.8	TT
438.8	TT
448.8	TT
458.8	TT
468.8	TT
473.7	TT
478.8	TP
483.8	TT
488.7	TT
508.8	TP
513.8	SB

Note: TT = two temperature sensors; TP = one temperature and one pressure sensor; SB = sinker bar.

Unit II (420.80–513.87 mbsf; 156-948C-2X through -11X-5, 17 cm)

The cored interval of Unit II measures 93.07 m thick and has been divided into six subunits on the basis of subtle to dramatic changes in lithology and fossil content (Table 1). Most of the lithologic variations are manifested by changes in color and are further supported by bulk X-ray analyses, carbon-carbonate content, and logging data.

Subunit IIA (420.80–443.65 mbsf; 156-948C-2X through -4X-3, 55 cm) consists of gray, olive gray, and grayish brown claystone of late Miocene age. Bioturbation is minor to heavy; the more strongly bioturbated intervals appear slightly darker gray or olive gray in color (Fig. 8). *Zoophycos* burrows occur in Cores 156-948C-3X and -4X. Local intraformational breccias break up the general homogeneity of this subunit. The upper boundary was not cored (above 420.8 mbsf), and the lower boundary is defined by an increase in carbonate content (Fig. 7). Carbonate content within Subunit IIA ranges from 0.2 to 7.8 wt%, and the mean value for 19 samples is 1.0 wt% (Table 4).

Subunit IIB (443.65–460.90 mbsf; 156-948C-4X-3, 55 cm, through -6X-1) is also late Miocene in age, but consists of three different lithologies: (1) mottled, slightly to heavily bioturbated light brownish gray claystone with coccoliths and distinctive silicified discoasters; (2) interbeds of mottled gray claystone without significant microfauna; and (3) mottled and bioturbated gray claystone with nannofossils. *Zoophycos* burrows are common. The location of the lower boundary of this subunit is based on the disappearance of abundant nannofossils within the claystone and a sharp reduction in carbonate content. Weight percentages of total carbonate within Subunit IIB range from 0.2 to 25.8 wt% and the mean for 21 samples is 9.5 wt% (Table 4).

Subunit IIC (460.90–479.50 mbsf; 156-948C-6X-2 through -8X-1, 80 cm) is barren of microfossils and consists of gray, olive gray, and olive mottled, slightly bioturbated claystone of indeterminate age. The claystone is fairly homogeneous throughout. Small lithoclasts (mud chips) and *Zoophycos* burrows are rare. The lower boundary of this subunit is defined by a change in color from shades of gray or olive gray to light brown. The carbonate content varies between 0.2 and 2.5 wt%, and the mean value for 17 samples is 0.7 wt% (Table 4).

Subunit IID (479.50–498.10 mbsf; 156-948C-8X-1, 80 cm, through -9X) consists of light yellowish brown, brownish gray, brown, and

reddish gray claystone of indeterminate age. The claystone is mottled throughout. Local thin beds of altered tuffaceous siltstone and altered volcanic ash display irregular upper and lower contacts. A distinctive matrix-supported tuff-pebble layer occurs in interval 156-948C-9X-5, 114–125 cm (Fig. 9). The tuff pebbles in this layer are 1.5 to 2.0 cm in diameter and subrounded. The lower boundary of Subunit IID coincides with the first appearance of claystone beds containing abundant radiolarians. The mean carbonate content (22 samples) is 0.4 wt%, and individual values range from 0.1 to 1.7 wt% (Table 4).

Subunit IIE (498.10–507.70 msbf; 156-948C-10X) is early to middle Miocene in age. Strata consist of pinkish gray, light brownish gray, and light gray mottled, variegated silty claystone and claystone with radiolarians. Some intervals contain unusually large radiolarians that are clearly visible with the naked eye. Dark gray color bands occur locally. A scaly deformation fabric is well developed throughout most of Subunit IIE. The lower subunit boundary is marked by a color change, but is defined most clearly by the disappearance of radiolarians. The carbonate content ranges between 0.1 and 0.2 wt% (Table 4).

Subunit IIF (507.70–513.87 mbsf; 156-948C-11X-1 through -11X-5, 17 cm) is made up of variegated claystone of early to middle Miocene age; the color varies from grayish brown to olive brown and light brownish gray. Scaly deformation fabric is well developed, and the lower boundary of this subunit coincides with a color change that begins at the top of the first significant greenish gray claystone layer. The carbonate content is consistently very low and ranges from 0.1 to 0.3 wt% (Table 4).

Unit III (513.87–592.72 mbsf; 156-948C-11X-5, 17 cm, through -19X)

The cored interval of Unit III is 78.85 m thick and extends to the total depth of the hole. The boundary between Units II and III is in the middle of the décollement zone. Based on correlation with the stratigraphy at Site 671, Unit III probably continues to about 675 mbsf. We recognized two subunits on the basis of internal sedimentary structures and rhythmic alternations of lithologies.

Subunit IIIA (513.87–523.78 mbsf; 156-948C-11X-5, 17 cm, through -12X-5, 38 cm) consists of variegated claystone of early to middle Miocene age. Color bands alternate from greenish gray to olive gray, dark grayish brown, dark gray, and reddish brown. Thin white veins occur locally, and a scaly deformation fabric is common. The lower boundary occurs at the top of the first silty claystone to display well-defined horizontal laminae. The carbonate content is low throughout the subunit, ranging from 0.1 to 0.4 wt% (Table 4).

Subunit IIIB (523.78–592.72 mbsf; 156-948C-12X-5, 38 cm, through -19X) includes three different types of rhythmically interbedded sediment: (1) light greenish gray to light gray carbonate-rich beds, ranging from nannofossil chalk with clay to silty claystone with nannofossils; (2) gray siliciclastic-rich beds, ranging in texture from silty claystone to clayey siltstone; and (3) mottled light greenish gray claystone, which forms the background sediment. Some of the claystones with nannofossils and nannofossil chalks are structureless, but most display horizontal laminae and cross-laminae near their bases (Fig. 10A); normal size grading is also common. The bases are sharp, and bioturbation near the tops has resulted in mixing with the background sediment of greenish gray claystone (Fig. 10B). The gray silty claystones and clayey siltstones similarly display normal size grading, sharp bases, horizontal laminae, low-angle ripple cross-laminae, and bioturbated tops. Deposits of this type are probably turbidites and can be described as base-missing Bouma sequences with T_{c-e} and T_{de} divisions. The carbonate content fluctuates considerably (Fig. 7); the range is 0.1 to 83.8 wt%, and the mean for 85 samples is 14.7 wt% (Table 4). Most of the samples having carbonate contents above 10 wt% are light gray nannofossil-rich turbidites; a few of the darker gray beds also contain elevated carbonate contents, and in rare instances, significant amounts of carbonate have been disseminated into the background of greenish gray claystone.

Table 3. Lithostratigraphic units and subunits recovered at Site 948.

Lithologic unit/subunit	Depth (mbsf)	Core interval (cm)	Age	General lithology	Depositional processes
I	0–10.08	948B-1H; 948C-1H	Pleistocene	Light brownish gray clay with nannofossils and foraminifers	Hemipelagic; air-fall ash; turbidity currents
IIA	420.80–443.65	948C-2X to 948C-4X-3, 55	? late Miocene	Gray, olive gray, and grayish brown bioturbated claystone with local intraformational breccia	Hemipelagic settling
IIB	443.65–460.90	948C-4X-3, 55, to 948C-6X-1	late Miocene	Gray claystone and claystone with nannofossils	Hemipelagic settling
IIC	460.90–479.50	948C-6X-2 to 948C-8X-1, 80	Indeterminate	Gray, olive gray, and olive bioturbated claystone	Hemipelagic settling
IID	479.50–498.10	948C-8X-1, 80, to 948C-9X	Indeterminate	Yellowish brown, brownish gray, brown, and reddish gray claystone with local tuff interbeds and altered volcanic ash	Hemipelagic settling; air-fall ash
IIE	498.10–507.70	948C-10X	early to middle Miocene	Pinkish gray and brownish gray claystone with radiolarians	Hemipelagic settling
IIF	507.70–513.87	948C-11X-1 to 948C-11X-5, 17	early to middle Miocene	Grayish brown and olive brown claystone	Hemipelagic settling
IIIA	513.87–523.78	948C-11X-5, 17, to 948C-12X-5, 38	early to middle Miocene	Greenish gray and dark grayish brown, banded, variegated claystone	Hemipelagic settling
IIIB	523.78–592.72	948C-12-5, 38, to 948C-19X	early Miocene–upper Oligocene	Rhythmic interbeds of greenish gray claystone, gray silty claystone, light gray claystone with nannofossils, and nannofossil chalk	Hemipelagic settling; dilute turbidity currents

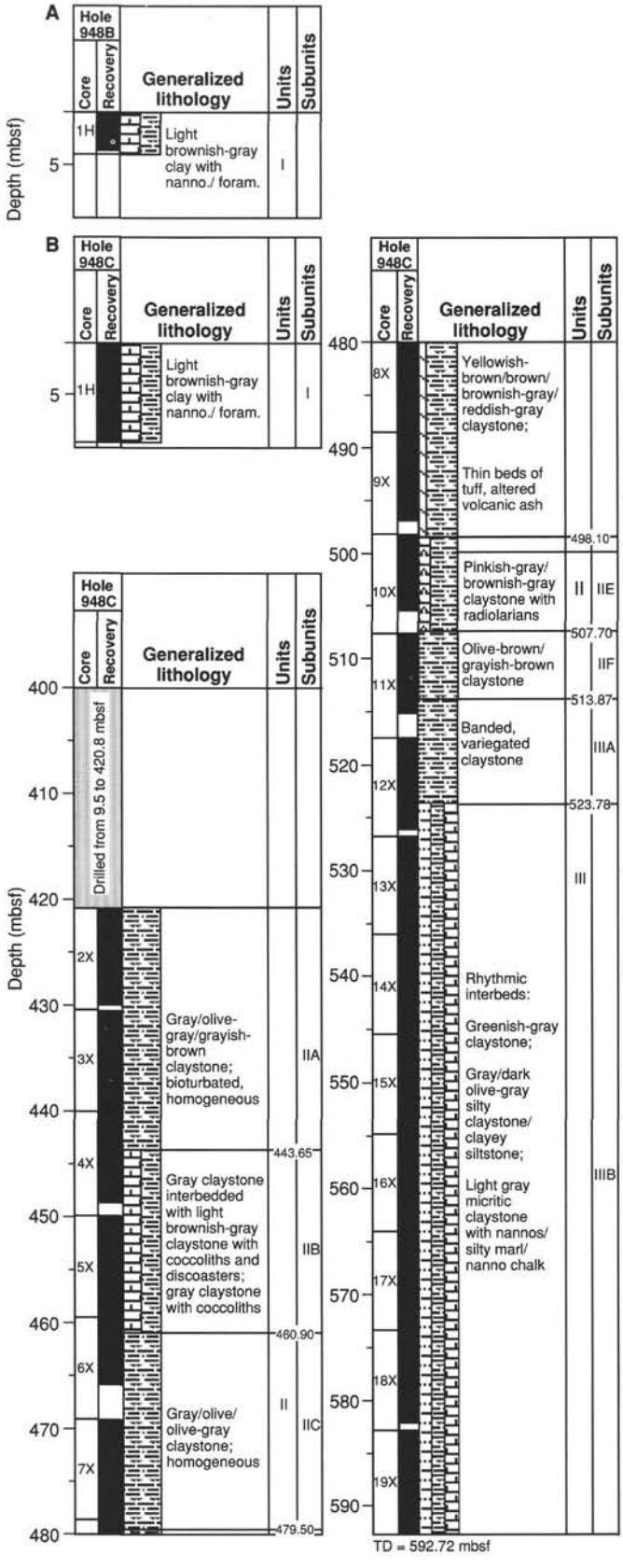

Figure 6. Lithostratigraphic summary for Site 948, showing core recovery, generalized lithology, and boundaries of lithologic units and subunits. **A.** Hole 948B. **B.** Hole 948C.

Table 4. Ranges and mean values of total carbonate ($CaCO_3$) for units and subunits recovered at Site 948.

Lithologic unit	Number	Range (wt%)	Mean (wt%)
I	16	0.5–33.5	15.6
IIA	19	0.2–7.8	1.0
IIB	21	0.2–25.8	9.5
IIC	17	0.2–2.5	0.7
IID	22	0.1–1.7	0.4
IIE	10	0.1–0.2	0.2
IIF	8	0.1–0.3	0.2
IIIA	10	0.1–0.4	0.2
IIIB	85	0.1–83.8	14.7

Notes: Measurements were performed with a Coulometrics analyzer. See Tables 5 through 13 for individual sample results and comparable estimates of wt%-calcite using X-ray diffraction techniques.

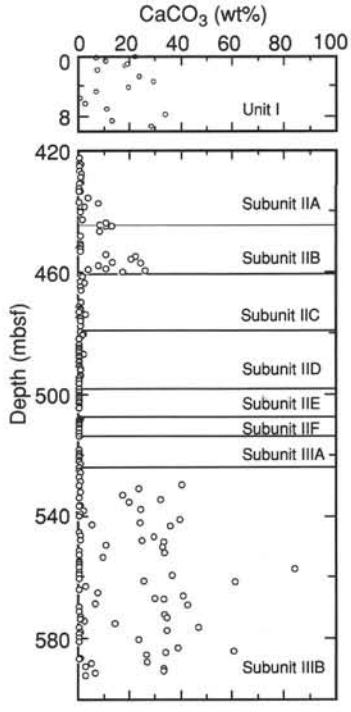

Figure 7. Plot of carbonate content ($CaCO_3$) vs. depth for Hole 948C. Measurements from a Coulometrics analyzer.

Inferred Depositional Environments

Strata of Unit I are bioturbated clay-rich sediments having varying amounts of nannofossils, foraminifers, and volcaniclastic debris. We have interpreted this unit to be mostly hemipelagic in origin. Unit I contains a great range in carbonate content, with values as high as 33.5 wt%. Deposition evidently occurred near the calcite compensation depth (CCD), such that slight shifts in the CCD resulted in transitions from carbonate preservation to carbonate dissolution. Sedimentation was dominated by a steady fallout of terrigenous mud and biogenic constituents from suspension in the surface waters and bottom nepheloid layer. This tranquil background sedimentation was punctuated by occasional influxes of silt- and sand-sized debris. The coarser grained material was transported as either air-fall tephra or in fine-grained turbidity currents. The vitric and crystal-rich ash layers probably originated from explosive eruptions in the nearby Lesser Antilles volcanic arc (to the west), whereas terrigenous constituents in the background clay came from multiple sources, including the Lesser Antilles and continental South America.

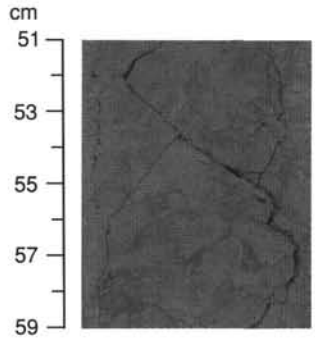

Figure 8. Bioturbated claystone typical of lithologic Subunit IIA (interval 156-948C-3X-4, 51–59 cm).

The portions of Unit II recovered at Site 948 consist mostly of deep-water hemipelagic claystones. Ash layers (probable air-fall deposits) are common only within Subunit IID. Characteristics of Unit II include moderate to intense bioturbation and *Zoophycos* trace fossils; these features are consistent with relatively low rates of sedimentation. The general depletion of calcium carbonate indicates that deposition occurred below the CCD, except for the time interval represented by the nannofossil-rich Subunit IIB.

Unit III is typified by recurrent graded sequences having sharp erosive bases, horizontal laminae, and cross-laminae; the normally graded intervals typically are overlain by bioturbated hemipelagic claystones. We interpreted these rhythmic sequences to be fine-grained base-missing turbidites (mostly T_{c-e} and T_{de} Bouma divisions) together with interbeds of hemipelagic claystone. Reconstructions of paleobathymetry indicate that deposition occurred within an abyssal plain environment and along the flanks of the Tiburon Rise (Dolan et al., 1990). Bioturbation is almost exclusively confined to the background hemipelagic claystones. In addition, the hemipelagic background has been cut out locally between amalgamated muddy turbidites; turbidity currents, therefore, evidently were triggered on a fairly regular basis. Some remobilization of mud also may have been caused by sluggish movement of thermohaline bottom currents.

Most of the hemipelagic claystones of Unit III include contents of calcium carbonate of less than 1 wt%. On the other hand, carbonate values of some graded turbidites are as high as 83 wt%. This partitioning of calcium carbonate indicates that nannofossil oozes were remobilized from sources located above the CCD. Transport, deposition, and burial below the CCD were rapid enough to inhibit dissolution of nannofossils. Conversely, only traces of carbonate debris were physically mixed into the hemipelagic background; nannofossils introduced into the bottom nepheloid layer were dissolved either prior to or shortly after deposition. Likely sources for the carbonate turbidites include shallower portions of nearby bathymetric highs, such as the Tiburon Rise. The darker gray terrigenous turbidites were probably transported from South America; some of these turbidity currents also entrained significant quantities of carbonate debris as they moved down the continental slope and rise. Quartz-rich sandstones of Oligocene and Eocene age (cored deeper in the sedimentary section at Site 672) were also derived from South America (Dolan et al., 1990).

Bulk X-ray Mineralogy

Relative proportions of quartz, plagioclase, calcite, and total clay minerals were calculated from X-ray diffraction (XRD) analysis of air-dried, randomly oriented bulk powders following the techniques of Fisher and Underwood (this volume). Samples were taken from the trimmings of interstitial-water "squeeze cakes" (Tables 5, 6, and 7), trimmings from whole-round specimens (Tables 8, 9, and 10), and residues of selected physical properties specimens (Tables 11, 12, and 13). Peak intensities (counts/s), integrated peak areas (total counts),

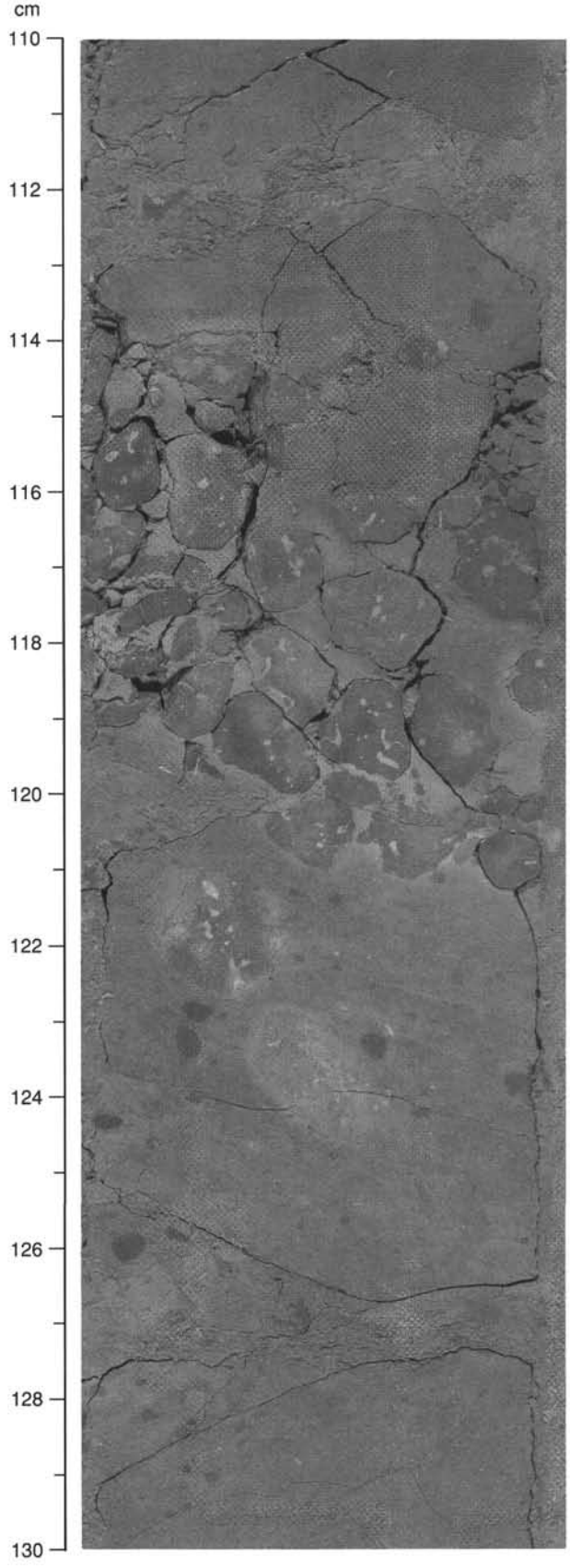

Figure 9. Matrix-supported tuff-pebble conglomerate within Subunit IID (interval 156-948C-9X-5, 110–130 cm).

Table 5. Values of X-ray diffraction peak intensity for specimens trimmed from interstitial-water "squeeze cakes," Hole 948C.

Core, section, interval (cm)	Depth (mbsf)	$CaCO_3$	Peak intensity above background (counts/s)					
			Smec.	Ill.	Kaol.	Qtz.	Plag.	Calc.
156-948C-								
1H-4, 143–150	5.93	29.4	17.4	9.6	8.4	271.5	62.7	613.5
2X-4, 130–150	426.60	0.4	28.7	21.3	26.5	367.5	31.4	9.5
4X-5, 110–150	447.20	2.2	21.0	21.9	25.4	230.0	41.0	46.0
5X-2, 120–150	452.50	0.7	41.8	9.9	32.9	323.3	44.2	0.0
6X-4, 118–150	465.08	1.2	22.6	25.9	15.8	234.5	53.6	9.8
7X-6, 120–150	477.70	0.8	51.7	6.7	18.1	271.2	36.7	0.0
8X-3, 110–150	482.80	1.6	67.1	9.5	27.7	381.3	66.5	10.0
8X-6, 120–150	487.40	0.1	42.8	5.6	20.9	298.7	174.9	0.0
9X-4, 115–150	494.05	0.3	47.1	0.0	16.8	209.1	108.3	0.0
10X-3, 110–150	502.20	0.2	43.7	10.6	23.7	262.4	139.6	0.0
11X-3, 120–150	511.90	0.2	19.5	17.1	34.7	426.0	33.8	0.0
11X-4, 110–150	513.30	0.2	41.2	15.6	38.4	401.5	26.7	0.0
12X-4, 110–150	523.00	0.4	22.2	23.8	46.6	387.3	16.4	0.0
13X-4, 115–150	532.45	1.2	12.2	33.8	58.8	550.0	20.5	0.0
14X-3, 110–150	540.20	0.7	20.9	34.1	56.9	680.6	19.6	20.4
14X-5, 120–150	543.30	0.8	15.1	30.2	57.7	752.0	28.9	0.0
15X-6, 110–150	554.00	0.2	7.6	20.2	59.1	677.0	25.8	0.0
16X-2, 110–150	557.40	19.2	17.2	11.4	35.0	840.6	18.8	624.0
17X-2, 120–150	566.80	7.3	22.1	9.9	50.7	335.6	17.6	207.6
17X-5, 0–40	570.10	0.4	28.7	22.7	37.9	706.7	27.3	0.0
18X-4, 110–150	578.90	1.0	22.4	19.0	44.6	657.2	29.0	25.7
19X-4, 110–150	588.40	1.0	13.5	28.0	38.3	899.8	34.2	0.0

Notes: Smec. = smectite; Ill. = illite; Kaol. = kaolinite + chlorite; Qtz. = quartz; Plag. = plagioclase; and Calc. = calcite.

Table 6. Values of X-ray diffraction integrated peak areas (total counts) for specimens trimmed from interstitial-water "squeeze cakes," Hole 948C.

Core, section, interval (cm)	Depth (mbsf)	$CaCO_3$	Integrated area after peak fitting (total counts)					
			Smec.	Ill.	Kaol.	Qtz.	Plag.	Calc.
156-948C-								
1H-4, 143–150	5.93	29.4	86.1	4.4	5.4	48.0	26.7	142.3
2X-4, 130–150	426.60	0.4	119.9	17.3	13.8	54.6	15.5	5.4
4X-5, 110–150	447.20	2.2	96.5	25.8	15.1	47.3	42.6	9.4
5X-2, 120–150	452.50	0.7	168.7	3.0	19.3	47.1	35.2	0.0
6X-4, 118–150	465.08	1.2	93.0	29.5	7.8	40.1	59.8	6.2
7X-6, 120–150	477.70	0.8	177.4	3.0	10.8	45.4	65.9	0.0
8X-3, 110–150	482.80	1.6	192.5	5.2	13.5	52.4	34.3	1.2
8X-6, 120–150	487.40	0.1	160.1	1.3	10.7	47.7	60.9	0.0
9X-4, 115–150	494.05	0.3	255.7	0.0	8.2	49.9	74.6	0.0
10X-3, 110–150	502.20	0.2	298.2	5.0	11.6	58.2	50.3	0.0
11X-3, 120–150	511.90	0.2	73.4	16.7	17.0	58.4	23.6	0.0
11X-4, 110–150	513.30	0.2	270.9	9.4	17.5	73.1	34.2	0.0
12X-4, 110–150	523.00	0.4	92.4	20.7	26.6	70.3	4.9	0.0
13X-4, 115–150	532.45	1.2	52.7	43.6	29.4	96.9	3.9	0.0
14X-3, 110–150	540.20	0.7	101.9	29.2	29.2	126.8	8.7	1.0
14X-5, 120–150	543.30	0.8	59.8	26.9	26.6	111.6	15.5	0.0
15X-6, 110–150	554.00	0.2	62.2	17.1	30.1	146.5	4.5	0.0
16X-2, 110–150	557.40	19.2	77.6	9.5	15.9	120.8	5.0	114.9
17X-2, 120–150	566.80	7.3	93.9	6.0	24.5	49.6	29.8	35.6
17X-5, 0–40	570.10	0.4	132.0	18.4	18.5	139.2	2.8	0.0
18X-4, 110–150	578.90	1.0	106.1	19.9	22.4	122.5	41.2	3.4
19X-4, 110–150	588.40	1.0	65.9	25.9	19.4	164.9	39.5	0.0

Note: See Table 5 for explanation of abbreviations.

and normalized mineral abundances (wt%) are listed separately for each type of specimen. We did not attempt to quantify the amount of amorphous solids nor of minerals other than those of the four primary constituent groups.

The total clay-mineral contents reported here are based on the sum of the values for individual clay minerals (smectite, illite, and [kaolinite + chlorite]). We caution that the estimates of weight percentages for individual clay minerals probably suffer from significant inaccuracies owing to peak interference. For example, the broad response of the smectite (001) peak cannot be discriminated from chlorite (001) and mixed-layer illite/smectite. A broadening of the smectite peak also may cause overlap with the discrete illite (001) peak (approximately 10 Å). In addition, the "kaolinite" peak (approximately 7 Å) is really a composite response of the kaolinite (001) plus chlorite (002) reflections. All of the data, therefore, should be viewed as semiquantitative estimates of relative, rather than absolute, abundances.

Error analysis and rigorous comparisons among different sets of peak-intensity and peak-area weighting factors are discussed by Fisher and Underwood (this volume). As an independent measure of accuracy, we compared the estimates of percentage of calcite from XRD vs. the weight percentage of total carbonate from Coulometrics analyses (Fig. 11). In general, the differences are less than 5 wt%. Most of the larger deviations indicate that the XRD method slightly underestimates the carbonate content. For some samples, this could result from the presence of carbonate minerals in addition to calcite. However, incompatibilities in XRD response also exist between naturally occurring, fine-grained biogenic calcite and the highly crystalline sparry calcite standards that were used to calibrate the model for estimating mineral abundances.

The sediment composition within Unit I, Hole 948C, fluctuates significantly (Fig. 12). Total clay-mineral content, for example, ranges from 36% to 59% and averages 48%. The relative percentage of quartz is 16% to 33% (mean = 25%), and plagioclase varies between 6% and 25% (mean = 13%). Estimates for calcite are consistent with total carbonate data from Coulometrics measurements (traces to 31%, with a mean of 15%).

Table 7. Estimates of relative mineral abundances for specimens trimmed from interstitial-water "squeeze cakes," Hole 948C.

Core, section, interval (cm)	Depth (mbsf)	$CaCO_3$	Normalized mineral abundances (wt%)						
			Smec.	Ill.	Kaol.	Clay	Qtz.	Plag.	Calc.
156-948C-									
1H-4, 143–150	5.93	29.4	31.5	8.4	3.8	43.7	24.0	8.1	24.1
2X-4, 130–150	426.60	0.4	37.5	25.8	5.6	68.9	27.8	1.7	1.7
4X-5, 110–150	447.20	2.2	28.1	34.6	5.2	67.9	22.5	7.1	2.5
5X-2, 120–150	452.50	0.7	49.1	5.4	9.2	63.8	28.7	7.6	0.0
6X-4, 118–150	465.08	1.2	27.5	37.6	1.6	66.7	21.2	9.9	2.2
7X-6, 120–150	477.70	0.8	49.4	5.1	5.0	59.4	27.3	13.2	0.0
8X-3, 110–150	482.80	1.6	51.0	7.6	5.5	64.1	29.9	6.0	tr
8X-6, 120–150	487.40	0.1	49.5	3.1	5.7	58.3	27.8	13.8	0.0
9X-4, 115–150	494.05	0.3	55.9	0.0	3.1	59.0	29.4	11.6	0.0
10X-3, 110–150	502.20	0.2	55.1	5.4	3.2	63.7	30.3	6.0	0.0
11X-3, 120–150	511.90	0.2	27.9	31.5	9.6	69.0	25.8	5.2	0.0
11X-4, 110–150	513.30	0.2	51.4	9.4	4.9	65.7	30.6	3.7	0.0
12X-4, 110–150	523.00	0.4	28.0	32.5	12.5	73.1	26.9	tr	0.0
13X-4, 115–150	532.45	1.2	12.5	54.2	9.7	76.4	23.6	tr	0.0
14X-3, 110–150	540.20	0.7	24.0	35.6	10.6	70.2	28.9	tr	0.9
14X-5, 120–150	543.30	0.8	16.8	41.9	12.5	71.2	27.6	1.2	0.0
15X-6, 110–150	554.00	0.2	17.7	30.8	17.9	66.3	33.7	tr	0.0
16X-2, 110–150	557.40	19.2	23.8	16.6	9.8	50.2	31.6	0.4	17.8
17X-2, 120–150	566.80	7.3	33.1	12.1	15.6	60.8	24.5	9.2	5.5
17X-5, 0–40	570.10	0.4	34.5	24.0	7.4	65.9	34.1	tr	0.0
18X-4, 110–150	578.90	1.0	28.0	26.6	9.5	64.1	29.0	6.8	tr
19X-4, 110–150	588.40	1.0	17.8	36.5	8.6	62.9	31.1	6.0	0.0

Notes: "tr" indicates that traces of the mineral were detected, but calculated abundance is less than 0%. Clay = total relative abundances of clay minerals. Significant errors may exist in the percentages of individual clay minerals, and particularly in the illite/smectite ratio. See Fisher and Underwood (this volume) for a complete description of how calculations were performed. See Table 5 for explanation of other abbreviations.

Table 8. Values of X-ray diffraction peak intensity for specimens trimmed from whole-round samples, Hole 948C.

Core, section, interval (cm)	Code	Depth (mbsf)	Peak intensity above background (counts/s)					
			Smec.	Ill.	Kaol.	Qtz.	Plag.	Calc.
156-948C-								
7X-6, 63–74	PH	477.13	67.1	0.0	8.4	217.1	45.5	0.0
12X-1, 91–106	PB	518.31	18.2	30.4	42.4	947.3	81.2	0.0
12X-3, 40–57	HT	520.80	22.2	34.3	38.9	438.5	23.5	0.0
12X-4, 47–63	GZ	522.37	9.5	14.9	38.4	453.6	2.6	0.0
12X-CC, 4–15	AM	525.77	12.1	24.9	27.0	443.2	13.3	0.0
13X-3, 60–70	AF	530.40	14.2	33.3	58.8	485.7	18.0	0.0
13X-5, 26–42	HT	533.40	16.2	20.0	56.7	378.6	13.1	0.0
13X-7, 36–51	GZ	536.16	7.6	7.3	48.3	246.1	0.0	1080.3
14X-6, 36–52	GZ	543.96	17.5	14.0	50.3	549.6	16.6	592.9
14X-6, 52–70	AM	544.12	23.5	24.5	55.3	342.1	16.8	0.0
14X-6, 79–92	SP	544.39	15.9	10.2	31.5	205.0	0.0	768.9
15X-4, 61–77	GZ	550.51	16.0	26.8	24.5	379.7	19.3	0.0
15X-6, 55–61	PH	553.45	12.0	8.8	55.6	700.3	0.0	515.0
15X-6, 103–109	PH	553.93	29.9	24.1	83.2	328.5	11.8	0.0
16X-5, 119–135	PB	561.99	14.0	15.0	41.3	333.3	20.6	823.9
16X-6, 50–61	JA	562.80	21.7	28.0	51.0	447.1	27.4	1.4
16X-7, 15–31	HT	563.45	20.1	31.3	38.8	597.3	26.9	0.0
17X-6, 67–78	AM	572.27	14.9	24.4	37.0	800.5	25.3	0.0
18X-5, 139–150	PH	580.69	14.6	6.9	74.5	270.6	10.8	537.8
19X-6, 49–65	HT	590.79	15.0	34.6	44.4	375.0	15.8	274.9

Note: See Table 5 for explanation of abbreviations.

Claystone compositions are fairly uniform within Unit II (Fig. 12). Calcite percentages, for example, are low, except within nannofossil-rich Subunit IIB, where the maximum value is 16% and the mean is 6%. Quartz content is stable throughout Unit II. All averages for the respective subunits are between 28% and 31% quartz. Total clay-mineral content ranges from 53% to 75%. Subunit IIF, which is located within the upper part of the décollement zone, contains the highest amounts of total clay minerals, with an average of 65%. There is an obvious gradient of increasing percentage of clay minerals through the décollement zone from the top of Subunit IIE to the base of Subunit IIIA (Fig. 12). Plagioclase decreases dramatically over this same depth interval. Maximum values of about 20% plagioclase occur within Subunits IID and IIE. Mean plagioclase values for Subunits IIF and IIIA (décollement zone) are only 4% to 5%.

Overall, there is significantly less plagioclase in Unit III than in Unit II. Relative percentages of the remaining major minerals throughout Subunit IIIB scatter appreciably in response to pronounced variations in lithology and detrital provenance (Fig. 12). Calcite percentages are obviously linked to the abundance of nannofossils, and both quartz and total clay-mineral content fluctuate inversely with calcite. Total clay-mineral content varies between 0% and 83%, whereas quartz values range from 6% to 46%.

Figure 13 shows the composite of relative mineral abundances for Units II and III. The overall temporal trend is in agreement with previous XRD analyses of samples from Site 671 (Tribble, 1990). In particular, an obvious change to higher clay-mineral content and lower plagioclase content occurs within the upper part of the décollement zone. Percentages of quartz, calcite, and total clay minerals range widely within the turbidite succession of Subunit IIIB, in response to variations in provenance. Higher contents of smectite and plagioclase in Unit II are probably a response to increases in the flux of volcanic debris from the Lesser Antilles during the Miocene.

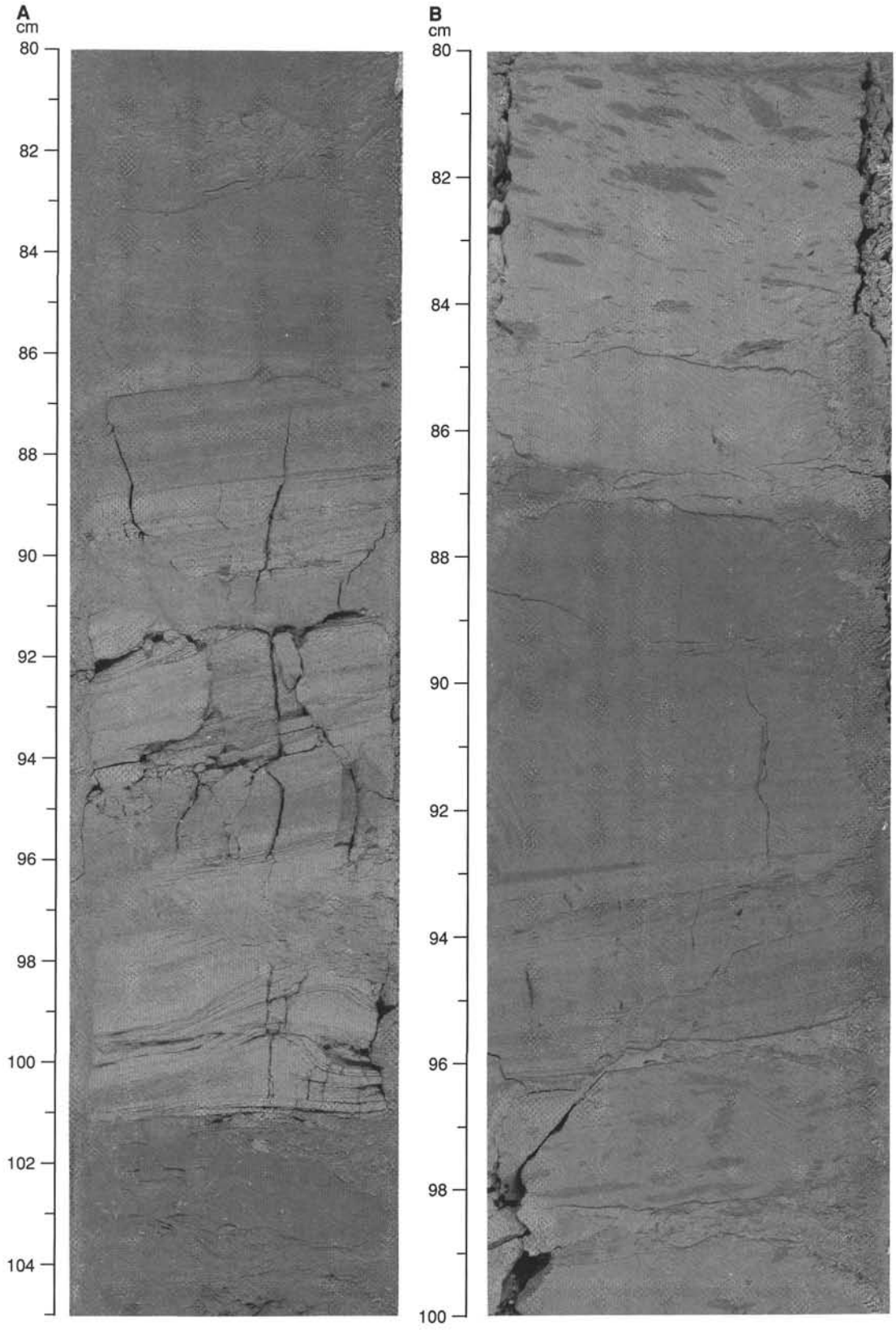

Figure 10. **A.** Normally graded carbonate-rich turbidite with sandy silt above a sharp base, ripple cross-laminae, and well-developed horizontal laminae (interval 156-948C-13X-3, 80–105 cm). **B.** Nannofossil-rich turbidite claystone; notice the sharp base above bioturbated background claystone, faint horizontal laminae, and gradation upward into bioturbated background claystone (interval 156-948C-17X-2, 80–100 cm).

Table 9. Values of X-ray diffraction integrated peak areas for specimens trimmed from whole-round samples, Hole 948C.

Core, section, interval (cm)	Code	Depth (mbsf)	Integrated area after peak fitting (total counts)					
			Smec.	Ill.	Kaol.	Qtz.	Plag.	Calc.
156-948C-								
7X-6, 63–74	PH	477.13	224.2	0.0	3.3	33.4	87.3	0.0
12X-1, 91–106	PB	518.31	86.8	23.5	20.3	198.4	44.2	0.0
12X-3, 40–57	HT	520.80	120.5	31.3	20.0	108.4	19.9	0.0
12X-4, 47–63	GZ	522.37	15.7	17.6	20.7	73.7	1.1	0.0
12X-CC, 4–15	AM	525.77	54.2	26.5	12.8	74.1	4.5	0.0
13X-3, 60–70	AF	530.40	55.2	35.0	29.5	98.2	6.9	0.0
13X-5, 26–42	HT	533.40	75.3	16.6	32.7	83.4	4.8	0.0
13X-7, 36–51	GZ	536.16	21.1	3.5	25.8	36.3	0.0	178.4
14X-6, 36–52	GZ	543.96	96.4	4.2	24.8	92.0	7.2	116.0
14X-6, 52–70	AM	544.12	127.5	27.8	31.1	67.2	2.5	0.0
14X-6, 79–92	SP	544.39	78.2	6.8	17.9	43.8	0.0	204.8
15X-4, 61–77	GZ	550.51	72.8	30.1	11.4	64.1	12.7	0.0
15X-6, 55–61	PH	553.45	53.3	6.6	28.5	99.0	0.0	87.3
15X-6, 103–109	PH	553.93	164.3	27.3	45.2	328.5	10.9	0.0
16X-5, 119–135	PB	561.99	73.0	4.2	24.0	67.8	11.3	192.1
16X-6, 50–61	JA	562.80	100.6	20.8	27.9	96.8	34.8	1.0
16X-7, 15–31	HT	563.45	109.7	30.9	22.2	169.8	9.4	0.0
17X-6, 67–78	AM	572.27	67.3	21.7	18.8	125.7	14.3	0.0
18X-5, 139–150	PH	580.69	73.3	4.8	39.4	39.3	1.3	108.6
19X-6, 49–65	HT	590.79	62.9	33.7	22.4	62.5	9.9	53.1

Note: See Table 5 for explanation of abbreviations.

Table 10. Estimates of relative mineral abundances for specimens trimmed from whole-round samples, Hole 948C.

Core, section, interval (cm)	Code	Depth (mbsf)	Normalized mineral abundances (wt%)						
			Smec.	Ill.	Kaol.	Clay	Qtz.	Plag.	Calc.
156-948C-									
7X-6, 63–74	PH	477.13	55.4	0.0	1.6	57.0	27.7	15.3	0.0
12X-CC, 4–15	AM	518.31	20.5	47.0	5.4	72.9	27.1	tr	0.0
12X-1, 91–106	PB	520.80	21.4	30.2	8.7	60.2	33.5	6.3	0.0
12X-3, 40–57	HT	522.37	28.9	35.7	6.1	70.7	28.4	0.9	0.0
12X-4, 47–63	GZ	525.77	4.0	50.9	18.6	73.5	26.5	tr	0.0
13X-3, 60–70	AF	530.40	14.1	49.1	11.8	75.1	24.9	tr	0.0
13X-5, 26–42	HT	533.40	23.4	30.2	18.9	72.4	27.6	tr	0.0
13X-7, 36–51	GZ	536.16	tr	10.1	26.8	36.9	13.5	0.0	49.6
14X-6, 36–52	GZ	543.96	28.7	7.8	15.1	51.5	28.6	2.3	17.6
14X-6, 52–70	AM	544.12	30.4	33.1	10.7	74.1	25.9	tr	0.0
14X-6, 79–92	SP	544.39	22.8	11.8	10.5	45.1	21.2	0.0	33.8
15X-4, 61–77	GZ	550.51	30.9	35.0	5.0	71.0	26.9	2.1	0.0
15X-6, 55–61	PH	553.45	15.9	15.2	22.5	53.6	29.1	0.0	17.3
15X-6, 103–109	PH	553.93	25.4	23.7	13.2	62.3	37.7	tr	0.0
16X-5, 119–135	PB	561.99	19.6	7.6	15.1	42.3	22.0	4.6	31.2
16X-6, 50–61	JA	562.80	26.7	28.6	12.0	67.3	26.5	6.0	0.2
16X-7, 15–31	HT	563.45	25.1	35.2	7.4	67.7	32.3	tr	0.0
17X-6, 67–78	AM	572.27	21.6	36.2	9.6	67.4	31.8	0.9	0.0
18X-5, 139–150	PH	580.69	20.8	10.2	26.8	57.8	19.5	2.3	20.4
19X-6, 49–65	HT	590.79	16.5	44.9	7.9	69.4	21.5	tr	9.1

Notes: "tr" indicates that traces of the mineral were detected, but calculated abundance is less than 0%. See Fisher and Underwood (this volume) for a complete description of how calculations were made. See Tables 5 and 7 for explanation of abbreviations.

Color Reflectance Data

Some 3097 color-reflectance data points were collected at 5-cm intervals from the cores of Hole 948C (see "Explanatory Notes" chapter, this volume). Figure 14 shows reflectance percentage in the 550-nm wavelength of visible light from Cores 156-948C-2X through -19X (420.80–592.72 mbsf; Units II and III). Table 14 lists the range and reflectance percentage for each stratigraphic division.

Downhole variations in reflectance percentage result from distinct color and compositional changes; consequently, the data generally correlate with unit and subunit boundaries. For example, greenish gray, pinkish gray, and brownish gray claystones exhibit the highest reflectance in the 550-nm range; gray and olive gray claystones exhibit the lowest reflectance. Cored intervals having abundant microfossils (e.g., Unit I and Subunits IIB and IIE) have higher reflectance than intervals of fossil-barren claystone. The range of reflectance percentages shown by Unit III is particularly noteworthy (Fig. 14) and entirely consistent with the rhythmic alternations of greenish gray claystone, gray silty claystone, and light gray nannofossil chalk.

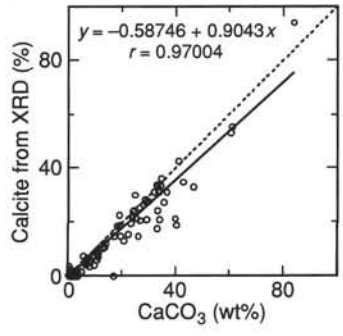

Figure 11. Linear regression of relative percentage of calcite from XRD analyses and weight percentage of $CaCO_3$ from Coulometrics analyses. r = correlation coefficient. Dashed line = reference slope equal to 1:1.

Table 11. Values of X-ray diffraction peak intensity for residues of physical properties specimens, Hole 948C.

Core, section, interval (cm)	Depth (mbsf)	$CaCO_3$	Peak intensity above background (counts/s)					
			Smec.	Ill.	Kaol.	Qtz.	Plag.	Calc.
156-948C-								
1H-1, 120–122	1.20	18.1	10.6	7.7	9.7	188.9	177.4	452.1
1H-1, 30–32	0.30	6.6	16.1	12.4	22.4	302.3	160.2	187.2
1H-1, 114–116	1.14	18.7	12.2	8.1	10.2	197.6	115.9	586.7
1H-2, 29–31	1.79	7.2	14.9	18.1	20.0	432.3	157.9	245.5
1H-2, 119–121	2.69	23.5	15.3	13.7	19.2	311.7	87.3	861.6
1H-3, 36–38	3.36	28.9	18.2	28.1	22.3	320.8	56.0	850.6
1H-3, 118–120	4.18	19.2	14.7	15.0	21.6	376.5	55.8	604.6
1H-4, 30–32	4.80	6.6	15.7	13.8	18.5	365.4	156.2	196.9
1H-4, 108–110	5.58	0.5	20.3	12.6	18.1	425.5	55.2	41.4
1H-5, 28–30	6.28	2.7	19.7	11.3	19.9	416.8	102.8	96.7
1H-5, 110–112	7.10	10.9	14.9	10.6	13.3	229.8	104.5	233.9
1H-6, 30–32	7.80	33.5	12.9	15.6	17.8	287.6	48.6	1016.7
1H-6, 120–122	8.70	13.1	18.2	13.6	20.6	404.4	64.3	391.9
1H-7, 34–36	9.34	28.2	11.3	11.8	10.8	231.5	158.3	828.1
2X-1, 140–142	422.20	0.2	17.9	19.0	13.9	247.3	35.7	0.0
2X-1, 146–148	422.26	0.2	23.3	21.3	22.3	302.5	52.8	0.0
2X-3, 30–32	424.10	0.2	36.2	12.8	15.2	255.0	118.8	0.0
2X-3, 72–74	424.52	0.3	26.4	21.9	14.5	208.1	67.0	0.0
2X-4, 3–5	425.33	0.2	25.1	13.8	16.9	243.6	72.4	0.0
2X-4, 116–118	426.46	0.2	16.1	27.4	17.8	253.3	53.6	0.0
2X-6, 52–54	428.82	0.3	40.5	12.2	20.5	275.0	52.1	0.0
3X-1, 6—8	430.56	0.2	23.9	19.4	17.8	253.5	76.5	0.0
3X-1, 55–57	431.05	0.2	34.1	9.9	15.9	273.9	76.7	0.0
3X-2, 16–18	432.16	0.2	38.6	13.1	20.2	252.6	80.4	0.0
3X-2, 139–141	433.39	0.3	27.4	15.2	14.0	257.8	76.9	0.0
3X-3, 1–3	433.51	0.2	51.4	12.9	16.6	256.2	66.1	0.0
3X-4, 69–71	435.69	3.5	32.8	18.6	23.5	365.9	21.6	0.0
3X-5, 48–50	436.98	0.2	29.6	31.1	31.2	266.4	38.8	0.0
3X-5, 95–97	437.45	7.8	28.8	8.8	22.3	290.1	36.5	185.2
3X-6, 47–49	438.47	2.0	37.0	14.2	26.7	227.5	35.7	22.3
4X-1, 16–18	440.26	0.5	35.2	12.0	16.1	310.0	77.7	0.0
4X-2, 108–110	442.68	1.2	30.9	14.0	28.2	302.9	28.7	0.0
4X-3, 55–57	443.65	10.7	23.8	13.6	20.6	265.6	21.4	319.4
4X-3, 142–144	444.52	8.1	23.3	17.4	24.5	267.4	36.4	196.0
4X-4, 12–14	444.72	12.7	26.5	14.1	26.6	283.2	40.5	454.7
4X-4, 25–27	444.85	10.6	21.5	14.9	22.9	257.8	37.4	284.7
4X-6, 44–46	448.04	0.4	49.1	3.4	19.5	199.5	40.5	0.0
5X-1, 63–65	450.43	0.4	30.1	7.0	22.3	168.9	43.1	0.0
5X-1, 146–148	451.26	0.4	34.7	7.9	24.1	270.2	90.1	34.7
5X-2, 43–45	451.73	0.3	31.3	14.0	34.6	259.5	54.2	0.0
5X-2, 93–95	452.23	0.3	39.0	11.2	27.9	240.8	35.1	0.0
5X-3, 31–33	453.11	0.3	43.9	4.8	18.3	194.9	72.1	0.0
5X-3, 127–129	454.07	10.8	31.8	7.7	19.4	185.7	42.3	328.7
5X-4, 47–49	454.77	22.1	27.2	10.5	20.3	151.0	31.3	459.4
5X-4, 110–112	455.40	20.5	27.3	5.7	21.9	243.9	26.0	531.7
5X-6, 32–34	457.62	7.8	39.9	8.3	22.9	292.4	40.1	258.9
5X-6, 148–150	458.78	10.7	28.3	6.5	18.3	223.3	42.9	321.8
5X-7, 8–10	458.88	3.4	35.0	10.0	21.6	229.7	47.2	85.3
5X-CC, 25–27	459.48	25.8	32.4	0.0	14.4	136.1	31.6	596.9
6X-1, 22–24	459.62	17.0	26.1	5.4	21.1	203.5	25.9	521.7
6X-1, 144–146	460.84	0.4	49.2	5.8	14.2	148.6	35.9	0.0
6X-2, 6–8	460.96	1.4	16.7	9.8	23.8	275.0	22.2	0.0
6X-3, 42–44	462.82	0.4	48.0	5.8	16.9	268.8	39.0	0.0
6X-3, 82–84	463.22	2.1	26.0	11.6	31.5	335.5	23.5	12.2
6X-4, 66–68	464.56	0.7	43.8	9.9	16.9	203.3	41.2	11.0
7X-1, 10–12	469.10		26.6	3.2	9.1	113.6	36.6	0.0
7X-1, 83–85	469.83	0.8	45.9	0.0	14.3	218.9	298.5	0.0
7X-2, 46–48	470.96	0.2	37.5	7.6	17.0	217.7	73.5	0.0
7X-2, 123–125	471.73	0.4	42.9	0.0	15.4	213.9	43.6	0.0
7X-3, 9–11	472.09	0.3	46.9	5.2	18.3	226.3	41.1	0.0
7X-3, 80–82	472.80	0.2	49.8	5.9	20.2	249.3	42.3	0.0
7X-4, 10–12	473.60	2.5	29.1	6.1	21.3	279.6	41.1	66.5
7X-4, 123–125	474.73	0.2	34.9	8.2	21.5	284.7	28.5	0.0
7X-5, 13–15	475.13	0.4	41.9	4.1	11.5	286.6	42.1	0.0
7X-5, 77–79	475.77	0.4	48.0	0.0	10.8	136.5	38.8	0.0
7X-6, 47–49	476.97	0.7	77.6	2.4	7.6	175.3	54.6	0.0
7X-6, 86–88	477.36	0.4	41.6	8.2	9.7	156.5	47.7	0.0
8X-1, 52–54	479.22	0.4	45.5	0.0	14.9	244.0	45.3	0.0
8X-1, 122–124	479.92	1.7	45.7	0.0	17.7	256.9	51.8	0.0
8X-2, 19–21	480.39	1.3	40.6	9.0	28.3	451.5	37.1	0.0
8X-2, 134–136	481.54	0.2	57.5	5.0	13.1	265.6	134.1	0.0
8X-3, 9–11	481.79	0.2	39.5	4.9	17.6	318.8	105.0	0.0
8X-4, 40–42	483.60	0.2	41.4	5.9	11.9	187.8	68.7	0.0
8X-4, 141–143	484.61	0.2	33.8	9.1	19.6	293.6	45.8	0.0
8X-5, 66–68	485.36	0.2	44.3	0.0	11.7	202.9	121.7	0.0
8X-6, 67–69	486.87	1.6	47.5	6.7	15.6	173.8	77.5	18.0
8X-6, 103–105	487.23	0.2	34.5	5.4	12.1	268.9	245.2	0.0
8X-7, 12–14	487.82	0.2	43.4	7.7	19.1	303.1	129.9	0.0
9X-1, 52–54	488.92	0.2	34.0	6.8	17.4	313.9	276.7	0.0
9X-1, 94–96	489.34	0.2	31.5	0.0	15.1	262.2	121.9	0.0
9X-2, 24–26	490.14	0.2	36.3	8.7	16.1	255.9	116.4	0.0
9X-2, 83–85	490.73	0.1	36.6	5.8	16.2	225.5	138.6	0.0
9X-3, 8–10	491.48	0.7	41.2	5.3	14.1	273.0	80.7	0.0
9X-3, 78–80	492.18	0.6	33.7	9.6	11.5	214.4	74.2	0.0
9X-4, 59–61	493.49	0.6	27.6	0.0	15.7	252.7	76.2	0.0
9X-4, 101–103	493.91	0.4	47.3	10.6	11.0	226.5	41.9	0.0
9X-5, 7–9	494.47	0.2	40.9	5.5	8.1	187.4	135.9	0.0

Table 11 (continued).

Core, section, interval (cm)	Depth (mbsf)	$CaCO_3$	Peak intensity above background (counts/s)					
			Smec.	Ill.	Kaol.	Qtz.	Plag.	Calc.
9X-5, 81–83	495.21	0.2	28.6	6.2	17.7	278.7	303.9	0.0
9X-6, 43–45	496.33	0.2	31.8	9.2	10.5	181.5	197.3	14.8
10X-1, 124–126	499.34	0.2	40.4	6.6	8.2	244.4	71.6	0.0
10X-2, 51–53	500.11	0.2	38.6	9.1	18.6	346.5	299.9	0.0
10X-2, 90–92	500.50	0.2	26.5	8.5	16.0	249.9	149.7	0.0
10X-3, 19–21	501.29	0.1	31.0	8.4	16.1	271.9	44.0	0.0
10X-4, 124–126	503.84	0.2	46.8	10.8	24.8	281.3	70.4	0.0
10X-5, 17–19	504.27	0.1	34.5	4.9	18.9	227.6	86.2	0.0
10X-5, 59–61	504.69	0.2	34.7	9.9	16.5	278.5	177.0	0.0
11X-1, 36–38	508.06	0.3	45.9	9.6	21.5	314.7	45.9	0.0
11X-1, 70–72	508.40	0.2	45.1	11.4	20.7	251.8	54.0	0.0
11X-1, 137–139	509.07	0.1	32.7	10.4	20.2	321.9	153.2	0.0
11X-2, 27–29	509.47	0.2	31.7	10.9	34.6	401.6	25.8	0.0
11X-2, 84–86	510.04	0.2	33.9	12.9	34.3	352.4	36.7	0.0
11X-3, 11–13	510.81	0.2	28.5	11.7	40.9	467.6	18.7	0.0
11X-4, 37–39	512.57	0.1	31.4	16.2	38.4	400.4	25.7	0.0
11X-4, 68–70	512.88	0.2	36.3	12.0	28.1	474.5	24.8	0.0
11X-5, 17–19	513.87	0.2	20.5	30.1	38.3	522.6	19.4	0.0
12X-1, 47–49	517.87	0.2	11.2	47.9	41.9	2038.0	100.3	0.0
12X-1, 79–81	518.19	0.2	21.9	31.7	45.8	460.8	21.4	0.0
12X-2, 29–31	519.19	0.2	31.6	25.2	37.7	519.4	25.0	0.0
12X-2, 93–95	519.83	0.2	35.0	25.9	36.6	459.8	20.5	0.0
12X-3, 27–29	520.67	0.2	16.3	17.4	31.7	397.0	21.7	0.0
12X-3, 107–109	521.47	0.1	14.5	50.9	58.5	2219.9	159.4	0.0
12X-4, 2–4	521.92	0.1	29.3	27.8	44.1	980.9	38.0	0.0
12X-4, 83–85	522.73	0.3	21.4	20.6	48.9	449.8	22.0	0.0
12X-5, 45–47	523.85	0.2	16.6	45.1	55.3	1807.8	74.6	0.0
13X-1, 14–16	526.94	0.2	16.1	27.8	52.2	883.1	37.4	0.0
13X-2, 14–16	528.44	0.6	11.7	30.9	73.7	1258.4	56.5	0.0
13X-2, 101–103	529.31	40.2	15.2	11.1	32.3	209.1	10.9	472.7
13X-3, 6–8	529.86	0.2	19.4	42.7	73.1	678.1	37.3	0.0
13X-3, 113–115	530.93	23.1	18.2	10.6	57.8	499.7	15.7	789.9
13X-5, 1–3	532.81	16.8	23.2	25.2	47.3	444.3	30.2	0.0
13X-5, 99–101	533.79	0.2	16.0	19.3	57.3	393.1	11.6	0.0
13X-6, 19–21	534.49	31.5	10.9	7.8	40.5	670.6	37.1	852.5
13X-6, 85–87	535.15	19.4	16.7	15.9	52.5	647.1	29.8	525.1
13X-7, 28–30	536.08	0.6	15.3	23.6	43.7	1041.6	38.5	0.0
14X-1, 42–44	536.52	0.2	16.2	33.6	58.8	616.3	24.7	0.0
14X-1, 146–148	537.56	24.2	15.3	0.0	64.9	176.1	0.0	595.4
14X-2, 43–45	538.03	1.9	17.4	30.3	47.6	696.9	29.2	28.6
14X-2, 100–102	538.60	0.1	18.5	23.3	49.6	790.9	31.7	0.0
14X-3, 9–11	539.19	0.3	13.3	20.0	32.5	336.1	8.8	0.0
14X-3, 70–72	539.80	0.2	2.1	15.3	29.7	409.3	22.7	0.0
14X-4, 19–21	540.79	39.4	13.9	10.4	20.4	142.8	0.0	499.1
14X-4, 116–118	541.76	23.7	13.0	9.8	87.6	325.2	0.0	807.2
14X-5, 61–63	542.71	5.3	8.8	28.6	51.9	514.8	22.5	203.9
14X-5, 92–94	543.02	35.3	15.3	0.0	21.0	225.2	0.0	601.7
14X-CC, 11–13	545.21	0.2	11.1	27.4	53.6	408.1	10.5	0.0
15X-1, 66–68	546.06	0.3	15.7	18.4	65.6	415.6	23.1	0.0
15X-1, 106–108	546.46	29.0	13.9	12.6	40.7	326.0	0.0	770.1
15X-2, 51–53	547.41	0.3	15.8	17.0	53.3	858.8	27.3	16.9
15X-2, 104–106	547.94	24.4	6.5	16.6	47.7	752.1	31.3	722.1
15X-3, 2–4	548.42	33.0	12.8	7.4	32.1	301.4	12.8	805.8
15X-3, 78–80	549.18	10.7	28.2	17.9	41.4	438.5	13.3	244.7
15X-4, 27–29	550.17	32.7	9.2	11.3	42.7	368.4	29.9	702.5
15X-4, 121–123	551.11	0.2	24.5	22.9	45.4	472.3	19.9	0.0
15X-5, 28–30	551.68	33.2	11.9	11.2	29.3	580.5	43.3	925.8
15X-5, 105–107	552.45	0.2	21.1	37.0	38.6	325.0	13.1	0.0
15X-6, 42–44	553.32	9.4	16.0	21.8	44.7	1640.4	62.0	287.2
16X-1, 12–14	554.92	0.2	8.7	27.6	34.6	435.9	26.7	0.0
16X-1, 106–108	555.86	0.2	8.4	32.2	37.3	976.3	59.9	0.0
16X-2, 24–26	556.54	0.2	0.0	38.4	54.6	414.1	16.3	0.0
16X-2, 91–93	557.21	83.8	5.2	0.0	0.0	123.3	0.0	1470.5
16X-3, 39–41	558.19	0.2	14.9	27.0	59.2	356.7	11.3	0.0
16X-3, 126–128	559.06	0.2	18.6	31.7	56.3	424.8	16.1	8.1
16X-4, 17–19	559.47	36.3	12.1	9.8	35.2	762.1	22.3	843.0
16X-4, 109–111	560.39	0.2	16.9	23.2	58.5	408.3	2.7	0.0
16X-5, 17–19	560.97	25.2	9.9	10.7	47.9	641.5	18.5	648.0
16X-5, 78–80	561.58	60.6	8.4	7.4	17.3	259.6	9.4	1341.6
16X-6, 29–31	562.59		16.3	31.7	51.6	810.4	22.8	0.0
16X-6, 72–74	563.02	2.7	16.5	22.5	44.9	757.9	32.2	64.7
16X-7, 56–58	563.86	0.2	17.5	26.8	33.8	530.7	24.3	0.0
17X-2, 33–35	565.93	40.7	5.7	15.6	28.4	156.8	0.0	881.5
17X-2, 101–103	566.61	29.6	10.9	23.4	28.8	359.7	16.1	759.7
17X-3, 138–140	568.48	6.3	11.3	19.7	31.0	444.6	24.3	116.6
17X-4, 21–23	568.81	42.4	9.1	9.4	21.7	401.6	0.0	698.7
17X-4, 114–116	569.74	0.2	21.4	30.5	30.8	609.3	29.5	0.0
17X-5, 83–85	570.93	0.2	14.1	31.7	37.5	662.4	20.0	0.0
17X-6, 38–40	571.98	33.2	14.6	9.4	55.8	161.1	0.0	728.8
17X-6, 138–140	572.98	0.6	14.8	28.3	34.5	787.2	42.5	0.0
17X-7, 12–14	573.22	34.4	10.2	9.4	56.1	244.3	0.0	814.0
18X-1, 97–99	574.27	2.3	24.0	41.6	62.4	756.5	30.5	24.6
18X-2, 28–30	575.08	14.1	15.8	22.9	51.7	455.9	20.6	387.8
18X-2, 145–147	576.25	46.4	14.7	12.4	32.4	445.9	17.3	922.5
18X-3, 25–27	576.55	0.2	15.2	27.4	29.3	484.6	23.7	0.0
18X-3, 126–128	577.56	34.1	11.6	10.1	44.9	187.9	0.0	772.1
18X-4, 17–19	577.97	0.3	14.1	21.3	29.2	1125.4	30.5	0.0
18X-4, 85–87	578.65	0.2	18.0	35.2	47.8	349.0	16.3	0.0
18X-5, 19–21	579.49	0.2	12.6	30.5	45.4	1035.9	41.9	0.0

Table 11 (continued).

Core, section, interval (cm)	Depth (mbsf)	$CaCO_3$	Peak intensity above background (counts/s)					
			Smec.	Ill.	Kaol.	Qtz.	Plag.	Calc.
18X-5, 86–88	580.16	23.4	11.8	15.5	27.7	319.6	16.5	589.5
18X-6, 11–13	580.91	0.2	18.2	36.1	27.6	382.5	19.6	0.0
19X-1, 134–136	584.14	60.2	7.8	4.6	14.8	71.3	0.0	982.1
19X-2, 15–17	584.45	33.8	21.2	11.0	28.9	156.1	0.0	639.5
19X-2, 92–94	585.22	26.2	18.1	7.6	60.9	167.2	0.0	679.0
19X-3, 44–46	586.24	0.3	23.7	35.7	48.2	448.7	29.2	0.0
19X-3, 104–106	586.84	0.1	21.0	34.0	40.5	504.1	31.8	0.0
19X-4, 47–49	587.77	26.7	13.5	13.0	54.2	279.1	15.2	716.3
19X-4, 97–99	588.27	4.6	28.1	24.0	33.7	644.3	32.4	116.9
19X-5, 33–35	589.13	2.7	0.0	30.5	48.3	1117.9	53.3	47.2
19X-5, 97–99	589.77	32.9	16.6	11.4	52.7	119.1	0.0	671.9
19X-6, 30–32	590.60	32.9	18.0	16.1	41.8	510.1	26.9	504.5
19X-6, 113–115	591.43	6.2	13.9	20.1	36.0	679.9	0.0	177.0
19X-7, 33–35	592.13	2.5	0.0	34.5	47.4	648.4	22.7	45.5

Note: See Table 5 for explanation of abbreviations.

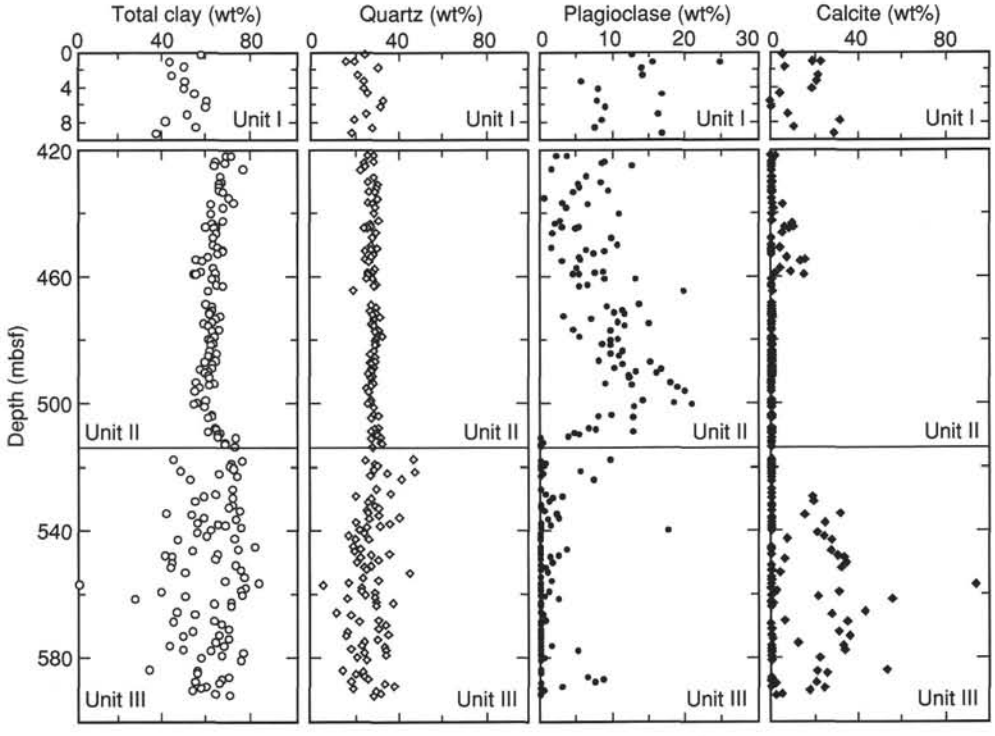

Figure 12. Values of relative abundances for major mineral groups from Hole 948C. Estimates were calculated from bulk-powder XRD data, following the technique of Fisher and Underwood (this volume).

Correlation with LWD Logs

The lithostratigraphic subdivisions identified in Hole 948C are based on clear differences in the character of cores. Physical changes in the cores are related to mineralogy, texture, physical properties, and sedimentary and tectonic structures; these same features should be expressed in the geophysical logs. Boundaries between units and subunits show up as changes in log character, electrofacies, or abrupt shifts in log values. LWD natural gamma-ray (GR) and photoelectric-effect (PEF) logs illustrate these relations most effectively (Fig. 15).

The increase in total clay-mineral abundance from Subunit IIE to the base of Subunit IIIA (Fig. 12) is expressed as a corresponding increase in natural gamma-ray values (Fig. 15). The most obvious feature in the logs, however, is the boundary between Units II and III. One way to explain this shift in log character is through an increase in the abundance of radioactive elements and higher densities down the section. These lithologic characteristics can be accommodated through increases in illite content and reductions in smectite. Illite is comparatively enriched in potassium, higher in bulk density (2.53 Mg/m^3), and higher in PEF (3.45 for pure illite). Subunit IIIB, furthermore, displays an electrofacies diagnostic of rhythmic lithologic variability; spikes in log response occur in addition to recurrent superposition of electrosequences with sharp bases and gradual upward changes in log values (Fig. 15).

STRUCTURAL GEOLOGY

Introduction

The primary goal of coring at Site 948 was to characterize the décollement zone as completely as possible. This site, adjacent to Site 671 drilled during Leg 110, was cored only from 420 to 592 mbsf, across the lowest 80 m of the accretionary prism, through the décollement, and approximately 60 m into the underthrust section. Core recovery was excellent. This, together with the limited interval cored and the ensuing ship time devoted to downhole experiments, allowed the shipboard structural geologists ample time to make an unusually

Table 12. Values of X-ray diffraction integrated peak areas for residues of phyiscal properties specimens, Holes 948B and 948C.

Core, section, interval (cm)	Depth (mbsf)	$CaCO_3$	Integrated area after peak fitting (total counts)					
			Smec.	Ill.	Kaol.	Qtz.	Plag.	Calc.
156-948B-								
1H-1, 120–122	1.20	18.1	27.2	8.1	4.7	37.5	56.8	78.3
156-948C-								
1H-1, 30–32	0.30	6.6	61.6	10.1	13.9	73.6	40.5	35.1
1H-1, 114–116	1.14	18.7	46.8	6.9	7.4	47.8	41.8	111.1
1H-2, 29–31	1.79	7.2	62.1	7.5	7.8	106.4	45.0	46.8
1H-2, 119–121	2.69	23.5	66.2	5.7	8.5	52.1	43.8	123.9
1H-3, 36–38	3.36	28.9	97.8	9.9	9.9	61.6	24.8	149.1
1H-3, 118–120	4.18	19.2	51.4	8.1	13.4	67.5	23.0	94.1
1H-4, 30–32	4.80	6.6	58.7	7.2	9.4	63.2	46.5	27.9
1H-4, 108–110	5.58	0.5	108.8	6.1	9.8	91.8	32.5	3.8
1H-5, 28–30	6.28	2.7	103.1	4.5	9.6	75.6	32.1	11.5
1H-5, 110–112	7.10	10.9	80.4	4.6	8.0	56.8	50.2	52.5
1H-6, 30–32	7.80	33.5	46.9	7.5	9.2	47.4	23.2	155.4
1H-6, 120–122	8.70	13.1	77.2	7.2	9.2	65.1	25.5	60.0
1H-7, 34–36	9.34	28.2	48.8	4.7	6.4	43.3	44.4	142.9
2X-1, 140–142	422.20	0.2	76.9	14.5	7.1	56.8	19.1	0.0
2X-1, 146–148	422.26	0.2	97.4	22.3	11.3	55.2	19.7	2.3
2X-3, 30–32	424.10	0.2	177.3	7.2	6.9	48.1	48.8	0.0
2X-3, 72–74	424.52	0.3	129.0	24.2	7.9	51.2	54.6	0.0
2X-4, 3–5	425.33	0.2	110.3	11.7	8.8	46.9	54.0	0.0
2X-4, 116–118	426.46	0.2	52.9	36.9	10.3	58.1	22.0	0.0
2X-6, 52–54	428.82	0.3	257.9	9.9	14.3	55.9	51.0	0.0
3X-1, 6–8	430.56	0.2	123.9	18.6	9.8	58.2	47.8	
3X-1, 55–57	431.05	0.2	161.0	4.4	7.8	40.9	25.7	0.0
3X-2, 16–18	432.16	0.2	205.2	5.4	10.5	49.1	33.1	0.0
3X-2, 139–141	433.39	0.3	112.7	12.5	5.9	42.4	41.8	0.0
3X-3, 1–3	433.51	0.2	371.8	10.8	9.6	46.1	52.7	0.0
3X-4, 69–71	435.69	3.5	170.3	13.5	15.2	66.2	10.8	0.0
3X-5, 48–50	436.98	0.2	142.8	25.9	17.8	59.9	27.8	0.0
3X-5, 95–97	437.45	7.8	141.3	5.4	13.5	52.1	29.2	39.1
3X-6, 47–49	438.47	2.0	244.8	14.0	15.7	68.5	32.9	6.8
4X-1, 16–18	440.26	0.5	151.6	4.4	7.5	51.1	49.1	0.0
4X-2, 108–110	442.68	1.2	149.6	6.4	15.2	58.8	16.1	0.0
4X-3, 55–57	443.65	10.7	110.1	9.1	11.8	46.9	11.2	58.0
4X-3, 142–144	444.52	8.1	127.4	13.1	14.1	61.3	19.5	43.2
4X-4, 12–14	444.72	12.7	119.4	8.6	13.4	51.1	24.1	69.9
4X-4, 25–27	444.85	10.6	100.2	17.0	11.6	53.1	26.7	54.3
4X-6, 44–46	448.04	0.4	229.3	0.9	10.4	34.8	57.9	0.0
5X-1, 63–65	450.43	0.4	145.0	4.8	11.9	44.1	46.0	0.0
5X-1, 146–148	451.26	0.4	157.1	3.8	11.8	40.9	9.7	26.9
5X-2, 43–45	451.73	0.3	162.5	11.1	18.4	59.8	36.1	0.0
5X-2, 93–95	452.23	0.3	155.8	15.3	17.0	44.7	52.0	0.0
5X-3, 31–33	453.11	0.3	223.8	2.5	12.8	34.3	42.8	0.0
5X-3, 127–129	454.07	10.8	177.1	4.3	10.0	38.6	28.2	60.2
5X-4, 47–49	454.77	22.1	135.9	6.1	11.8	40.5	25.2	117.9
5X-4, 110–112	455.40	20.5	145.0	4.1	10.7	35.0	13.5	95.6
5X-6, 32–34	457.62	7.8	241.4	4.0	12.1	47.2	34.3	43.4
5X-6, 148–150	458.78	10.7	112.6	5.0	8.8	38.2	32.1	58.0
5X-7, 8–10	458.88	3.4	201.3	6.3	12.3	46.5	45.5	17.6
5X-CC, 25–27	459.48	25.8	206.6	0.0	7.5	28.1	28.3	142.1
6X-1, 22–24	459.62	17.0	115.4	3.7	10.2	38.0	16.8	93.2
6X-1, 144–146	460.84	0.4	172.8	4.7	8.9	37.0	44.1	0.0
6X-2, 6–8	460.96	1.4	67.7	5.6	12.6	43.8	33.8	0.0
6X-3, 42–44	462.82	0.4	216.7	2.7	8.2	40.9	38.9	0.0
6X-3, 82–84	463.22	2.1	114.8	8.9	17.4	58.7	23.5	2.9
6X-4, 66–68	464.56	0.7	32.9	13.1	9.2	43.4	51.0	5.4
7X-1, 10–12	469.10		115.3	1.8	6.9	38.9	45.1	0.0
7X-1, 83–85	469.83	0.8	185.8	0.0	5.8	28.3	41.9	0.0
7X-2, 46–48	470.96	0.2	145.3	6.1	8.9	44.8	51.3	0.0
7X-2, 123–125	471.73	0.4	193.1	0.0	9.3	43.4	49.7	0.0
7X-3, 9–11	472.09	0.3	165.4	2.2	9.9	44.5	52.7	0.0
7X-3, 80–82	472.80	0.2	265.3	3.5	11.4	56.1	26.7	0.0
7X-4, 10–12	473.60	2.5	143.9	5.0	11.4	46.6	31.5	9.1
7X-4, 123–125	474.73	0.2	132.2	3.5	12.2	47.9	41.3	
7X-5, 13–15	475.13	0.4	130.6	1.1	5.3	40.7	54.7	0.0
7X-5, 77–79	475.77	0.4	229.2	0.0	5.9	34.9	67.2	0.0
7X-6, 47–49	476.97	0.7	230.5	1.6	3.7	28.5	29.0	0.0
7X-6, 86–88	477.36	0.4	163.5	1.2	6.1	34.5	41.9	0.0
8X-1, 52–54	479.22	0.4	149.5	0.0	7.3	40.0	21.0	0.0
8X-1, 122–124	479.92	1.7	155.4	0.0	10.5	47.2	42.5	0.0
8X-2, 19–21	480.39	1.3	164.1	3.3	14.1	64.8	46.4	0.0
8X-2, 134–136	481.54	0.2	200.4	2.2	5.6	44.9	46.4	0.0
8X-3, 9–11	481.79	0.2	155.8	1.7	9.6	48.5	41.6	0.0
8X-4, 40–42	483.60	0.2	166.9	2.9	7.4	50.1	53.6	0.0
8X-4, 141–143	484.61	0.2	131.7	8.9	10.5	49.7	43.8	0.0
8X-5, 66–68	485.36	0.2	206.5	0.0	4.8	36.3	56.4	0.0
8X-6, 67–69	486.87	1.6	195.2	2.6	7.8	37.5	42.4	0.9
8X-6, 103–105	487.23	0.2	133.8	2.0	6.6	40.6	57.5	0.0
8X-7, 12–14	487.82	0.2	212.9	5.7	8.7	48.0	70.1	0.0
9X-1, 52–54	488.92	0.2	144.2	3.6	9.2	48.4	42.8	0.0
9X-1, 94–96	489.34	0.2	140.6	0.0	10.3	52.9	64.1	0.0
9X-2, 24–26	490.14	0.2	172.1	1.9	8.9	42.9	62.2	0.0
9X-2, 83–85	490.73	0.1	152.3	3.9	7.0	42.4	71.6	0.0
9X-3, 8–10	491.48	0.7	172.8	3.6	7.1	52.9	60.1	0.0
9X-3, 78–80	492.18	0.6	159.9	7.2	6.2	56.4	62.9	0.0
9X-4, 59–61	493.49	0.6	119.9	0.0	6.4	48.9	59.8	0.0
9X-4, 101–103	493.91	0.4	249.0	5.9	7.8	48.5	63.3	0.0

Table 12 (continued).

Core, section, interval (cm)	Depth (mbsf)	$CaCO_3$	Integrated area after peak fitting (total counts)					
			Smec.	Ill.	Kaol.	Qtz.	Plag.	Calc.
9X-5, 7–9	494.47	0.2	187.4	4.5	4.8	42.1	68.2	0.0
9X-5, 81–83	495.21	0.2	136.2	2.9	9.6	54.9	79.3	0.0
9X-6, 43–45	496.33	0.2	143.9	0.7	4.0	54.7	82.8	1.4
10X-1, 124–126	499.34	0.2	156.4	2.0	4.2	37.8	60.9	0.0
10X-2, 51–53	500.11	0.2	137.8	2.7	6.7	61.8	78.3	0.0
10X-2, 90–92	500.50	0.2	96.9	4.1	8.8	67.0	72.3	0.0
10X-3, 19–21	501.29	0.1	109.1	3.3	9.4	59.9	44.8	0.0
10X-4, 124–126	503.84	0.2	186.3	3.2	11.9	56.6	52.0	0.0
10X-5, 17–19	504.27	0.1	163.7	1.7	9.2	56.6	36.4	0.0
10X-5, 59–61	504.69	0.2	140.4	5.9	7.3	52.8	57.5	0.0
11X-1, 36–38	508.06	0.3	193.3	5.3	11.0	70.1	39.9	0.0
11X-1, 70–72	508.40	0.2	172.9	7.6	10.3	59.2	42.8	0.0
11X-1, 137–139	509.07	0.1	118.7	5.2	9.9	55.1	49.8	0.0
11X-2, 27–29	509.47	0.2	128.8	6.9	19.2	68.1	21.7	0.0
11X-2, 84–86	510.04	0.2	175.2	5.7	17.1	71.3	29.8	0.0
11X-3, 11–13	510.81	0.2	126.6	4.1	17.1	72.9	16.9	0.0
11X-4, 37–39	512.57	0.1	175.8	7.5	17.8	73.5	7.9	0.0
11X-4, 68–70	512.88	0.2	243.1	8.4	13.7	77.5	5.3	0.0
11X-5, 17–19	513.87	0.2	84.7	26.9	19.0	93.0	5.4	0.0
12X-1, 47–49	517.87	0.2	4.2	15.4	16.6	311.3	43.6	0.0
12X-1, 79–81	518.19	0.2	104.4	33.0	23.9	71.0	11.5	0.0
12X-2, 29–31	519.19	0.2	190.4	22.2	19.8	80.8	16.2	0.0
12X-2, 93–95	519.83	0.2	209.5	22.2	20.0	101.8	8.6	0.0
12X-3, 27–29	520.67	0.2	62.6	15.3	15.8	66.3	1.9	0.0
12X-3, 107–109	521.47	0.1	5.2	15.9	22.9	321.6	31.1	0.0
12X-4, 2–4	521.92	0.1	184.2	13.5	23.5	162.9	13.0	0.0
12X-4, 83–85	522.73	0.3	94.1	18.8	25.0	68.8	4.3	0.0
12X-5, 45–47	523.85	0.2	4.8	15.2	24.1	253.4	31.8	0.0
13X-1, 14–16	526.94	0.2	82.3	27.8	26.3	132.2	7.2	0.0
13X-2, 14–16	528.44	0.6	113.6	9.2	40.3	190.2	8.1	0.0
13X-2, 101–103	529.31	40.2	48.6	10.8	14.7	34.9	9.5	81.0
13X-3, 6–8	529.86	0.2	94.4	28.7	37.2	138.7	19.6	0.0
13X-3, 113–115	530.93	23.1	101.1	4.5	28.2	73.9	2.5	129.7
13X-5, 1–3	532.81	16.8	138.2	15.8	22.7	100.4	8.7	0.0
13X-5, 99–101	533.79	0.2	67.0	15.2	32.2	67.9	5.4	0.0
13X-6, 19–21	534.49	31.5	51.2	3.6	19.4	86.1	3.4	153.7
13X-6, 85–87	535.15	19.4	96.0	5.5	29.9	130.8	8.6	111.6
13X-7, 28–30	536.08	0.6	78.6	12.3	21.9	205.5	18.9	0.0
14X-1, 42–44	536.52	0.2	58.9	22.2	31.7	101.5	11.3	0.0
14X-1, 146–148	537.56	24.2	90.3	0.0	38.8	34.6	0.0	132.6
14X-2, 43–45	538.03	1.9	71.8	19.2	26.1	179.6	11.1	4.4
14X-2, 100–102	538.60	0.1	85.3	14.6	24.3	109.3	12.0	0.0
14X-3, 9–11	539.19	0.3	39.8	20.8	17.1	60.9	2.7	0.0
14X-3, 70–72	539.80	0.2	18.2	8.9	14.3	52.9	31.7	0.0
14X-4, 19–21	540.79	39.4	81.8	6.2	10.8	28.7	0.0	103.7
14X-4, 116–118	541.76	23.7	61.2	9.4	45.6	43.1	0.0	136.2
14X-5, 61–63	542.71	5.3	17.2	31.9	27.9	83.4	10.3	32.2
14X-5, 92–94	543.02	35.3	86.2	0.0	11.1	41.0	0.0	131.7
14X-CC, 11–13	545.21	0.2	16.9	42.5	28.5	65.5	2.9	0.0
15X-1, 66–68	546.06	0.3	73.1	22.4	33.5	64.3	20.6	0.0
15X-1, 106–108	546.46	29.0	54.6	13.5	23.8	54.8	0.0	157.6
15X-2, 51–53	547.41	0.3	70.5	12.8	26.6	150.2	6.5	1.1
15X-2, 104–106	547.94	24.4	14.3	7.7	24.4	134.1	5.7	145.9
15X-3, 2–4	548.42	33.0	63.5	4.2	16.5	52.0	1.2	170.1
15X-3, 78–80	549.18	10.7	197.5	13.9	22.4	113.2	2.0	62.2
15X-4, 27–29	550.17	32.7	31.7	11.4	25.2	90.0	3.6	187.6
15X-4, 121–123	551.11	0.2	130.5	23.9	23.0	75.5	8.2	0.0
15X-5, 28–30	551.68	33.2	46.5	9.5	10.9	77.4	3.4	165.2
15X-5, 105–107	552.45	0.2	95.4	34.5	23.3	78.3	6.6	0.0
15X-6, 42–44	553.32	9.4	81.3	7.2	20.8	245.9	12.2	51.4
16X-1, 12–14	554.92	0.2	12.2	31.1	17.7	84.0	5.8	0.0
16X-1, 106–108	555.86	0.2	1.0	29.9	18.0	166.4	19.7	0.0
16X-2, 24–26	556.54	0.2	0.0	38.1	26.6	58.7	11.8	0.0
16X-2, 91–93	557.21	83.8	1.0	0.0	0.0	19.1	0.0	372.9
16X-3, 39–41	558.19	0.2	66.5	28.0	31.5	67.9	2.4	0.0
16X-3, 126–128	559.06	0.2	81.1	31.8	29.4	69.7	3.8	2.2
16X-4, 17–19	559.47	36.3	63.9	4.1	18.5	122.2	2.8	187.7
16X-4, 109–111	560.39	0.2	72.8	25.9	29.5	72.8	0.5	0.0
16X-5, 17–19	560.97	25.2	72.7	6.4	25.3	112.3	1.5	132.5
16X-5, 78–80	561.58	60.6	42.0	4.1	6.5	36.0	2.1	279.5
16X-6, 29–31	562.59		69.2	27.0	25.8	135.6	9.5	0.0
16X-6, 72–74	563.02	2.7	88.7	16.7	24.7	190.2	6.4	14.4
16X-7, 56–58	563.86	0.2	73.8	27.8	16.8	116.7	6.1	0.0
17X-2, 33–35	565.93	40.7	7.3	16.8	16.0	31.2	0.0	203.2
17X-2, 101–103	566.61	29.6	31.9	22.5	14.8	51.7	5.7	159.0
17X-3, 138–140	568.48	6.3	42.1	15.0	17.7	106.8	8.8	31.2
17X-4, 21–23	568.81	42.4	34.8	11.2	12.4	65.4	0.0	167.1
17X-4, 114–116	569.74	0.2	97.2	24.2	18.0	170.2	14.4	0.0
17X-5, 83–85	570.93	0.2	55.7	24.3	16.5	119.3	7.5	0.0
17X-6, 38–40	571.98	33.2	69.8	8.9	32.7	27.8	0.0	185.7
17X-6, 138–140	572.98	0.6	73.9	21.0	19.1	167.1	11.3	0.0
17X-7, 12–14	573.22	34.4	38.2	9.2	27.7	38.9	0.0	174.3
18X-1, 97–99	574.27	2.3	131.6	31.6	32.7	167.9	8.5	5.3
18X-2, 28–30	575.08	14.1	72.2	19.5	27.7	85.5	5.2	79.8
18X-2, 145–147	576.25	46.4	80.8	5.5	14.3	63.4	2.9	208.0
18X-3, 25–27	576.55	0.2	68.3	20.3	14.2	126.9	5.0	0.0
18X-3, 126–128	577.56	34.1	55.6	6.9	23.8	33.3	0.0	168.3
18X-4, 17–19	577.97	0.3	63.4	17.9	12.3	149.3	29.4	0.0
18X-4, 85–87	578.65	0.2	78.4	35.9	23.6	73.3	6.9	0.0

Table 12 (continued).

Core, section, interval (cm)	Depth (mbsf)	$CaCO_3$	Integrated area after peak fitting (total counts)					
			Smec.	Ill.	Kaol.	Qtz.	Plag.	Calc.
18X-5, 19–21	579.49	0.2	70.7	25.8	21.2	183.0	13.7	0.0
18X-5, 86–88	580.16	23.4	51.3	16.7	16.1	50.3	5.2	121.4
18X-6, 11–13	580.91	0.2	91.7	34.6	13.8	69.0	13.2	0.0
19X-1, 134–136	584.14	60.2	33.8	4.9	7.5	12.4	0.0	207.0
19X-2, 15–17	584.45	33.8	162.0	11.2	18.3	44.3	0.0	195.8
19X-2, 92–94	585.22	26.2	95.6	4.4	33.0	31.7	0.0	155.7
19X-3, 44–46	586.24	0.3	119.4	28.8	24.2	86.9	47.2	0.0
19X-3, 104–106	586.84	0.1	80.4	24.0	17.9	99.6	47.9	0.0
19X-4, 47–49	587.77	26.7	68.0	8.9	27.2	41.6	22.6	121.7
19X-4, 97–99	588.27	4.6	196.1	14.3	17.3	132.6	11.5	20.2
19X-5, 33–35	589.13	2.7	0.0	13.0	22.8	177.2	13.9	6.3
19X-5, 97–99	589.77	32.9	96.6	12.6	28.9	30.2	0.0	170.6
19X-6, 30–32	590.60	32.9	123.6	5.4	20.6	102.2	3.0	135.4
19X-6, 113–115	591.43	6.2	66.0	15.4	20.6	117.3	0.0	31.7
19X-7, 33–35	592.13	2.5	0.0	22.3	20.3	121.7	2.2	7.8

Note: See Table 5 for explanation of abbreviations.

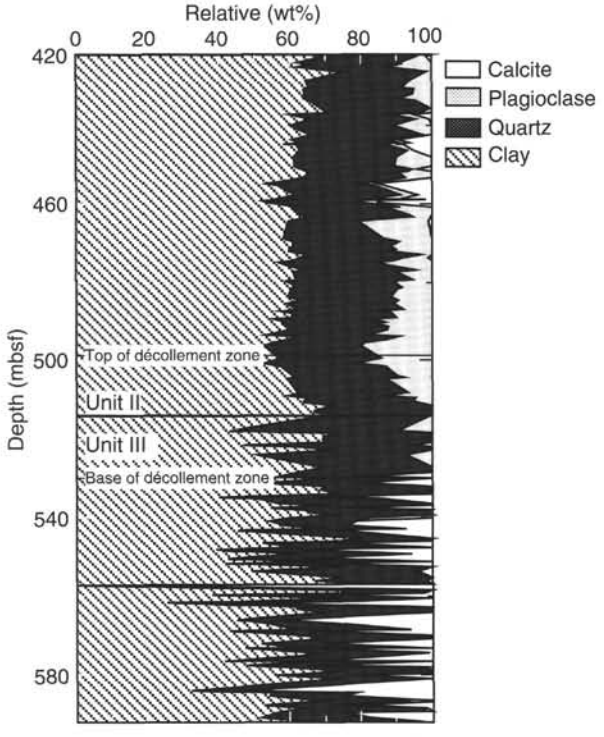

Figure 13. Relative mineral abundances for Units II and III, Hole 948C. Note the changes in sediment composition within the décollement zone and at the boundary between Units II and III.

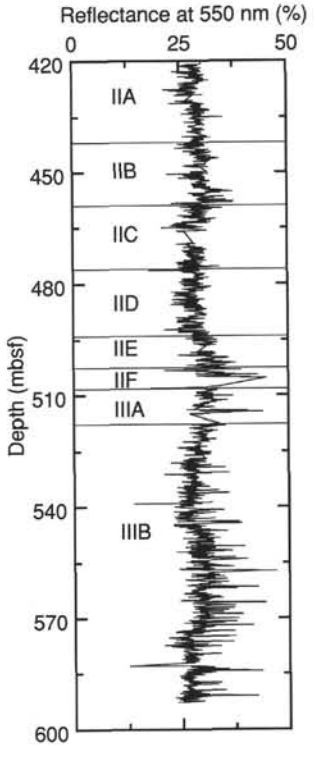

Figure 14. Color-reflectance spectrum (550 nm) for Cores 156-948C-2X through -19X (Units II and III, Hole 948C).

detailed record of the occurrence of core-scale structures. Thus, Site 948 marks the most completely studied section through a major plate-bounding fault zone at any accretionary prism. Full characterization of the geometry, strain history, and rheology of the décollement awaits detailed post-cruise microstructural study; in this section, we discuss the mesoscopic features of the cored interval. We distinguish three distinct structural domains (Fig. 16), referred to here, respectively, as the prism, décollement, and underthrust domains.

Within the cores at this site, we identified the following indicators of deformation: inclined bedding, core-scale faults with small offset (millimeter to centimeter), mineral veins, sediment-filled veins, brecciated zones, fracture networks, stratal disruption, and scaly fabric (see "Explanatory Notes" chapter, this volume, for definitions). Mud-filled veins have been interpreted as early extensional features not necessarily related to accretion (Ogawa et al., 1992), whereas scaly fabric and stratal disruption are typical features of shear zones in clay-rich sedimentary rocks. We use the term scaly fabric in its usual mesoscopic sense, based on visual observation of the cores, noting that scaly fabric may refer to any of several distinct microstructural textures (e.g., Agar et al., 1989). We have attempted to describe its relative intensity of development. Here, "intense" scaly fabric refers to a planar or semiplanar foliation that is penetrative at the mesoscopic scale. Intense scaly fabric generally occurs in zones of centimeter-scale thickness with sharp boundaries; the fabric is oblique to subparallel to the zone boundaries, and is commonly sigmoidal. Intervals of intense scaly fabric have been interpreted as zones of concentrated shear (Moore et al., 1986). While we debated little on the origin of intense scaly fabrics in the cores, it proved difficult to determine whether the incipient to weakly developed examples were artificial (drilling induced) or natural features (see "Explanatory Notes" chapter, this volume). Some of the incipient scaly fabric probably was

Table 13. Estimates of relative mineral abundances for residues of physical properties specimens, Holes 948B and 948C.

Core, section, interval (cm)	Depth (mbsf)	$CaCO_3$	Normalized mineral abundances (wt%)						
			Smec.	Ill.	Kaol.	Clay	Qtz.	Plag.	Calc.
156-938B-									
1H-1, 120–122	1.20	18.1	14.2	21.7	4.7	40.7	16.1	24.7	18.6
156-948C-									
1H-1, 30–32	0.30	6.6	24.7	21.3	9.9	55.9	25.8	12.6	5.7
1H-1, 114–116	1.14	18.7	19.8	15.7	6.2	41.7	20.0	15.5	22.8
1H-2, 29–31	1.79	7.2	25.7	16.1	6.5	48.3	30.9	14.0	6.8
1H-2, 119–121	2.69	23.5	24.8	11.4	6.3	42.5	21.5	14.2	21.8
1H-3, 36–38	3.36	28.9	29.0	15.1	5.0	49.0	24.2	5.7	21.1
1H-3, 118–120	4.18	19.2	19.9	18.2	10.4	48.5	24.5	8.0	19.0
1H-4, 30–32	4.80	6.6	27.8	17.4	7.9	53.1	25.7	16.8	4.5
1H-4, 108–110	5.58	0.5	40.8	11.8	6.3	58.9	33.1	7.9	tr
1H-5, 28–30	6.28	2.7	41.9	9.7	6.8	58.4	32.0	9.0	0.5
1H-5, 110–112	7.10	10.9	33.7	10.0	6.2	49.9	25.3	16.3	8.4
1H-6, 30–32	7.80	33.5	17.2	16.0	7.0	40.2	19.9	8.5	31.4
1H-6, 120–122	8.70	13.1	31.9	15.3	6.6	53.7	27.9	7.6	10.8
1H-7, 34–36	9.34	28.2	19.7	10.5	5.7	35.9	18.6	16.8	28.7
					Mean	48.3	24.7	12.7	15.4
Subunit IIA									
2X-1, 140–142	422.20	0.2	34.0	29.7	3.7	67.3	29.0	3.7	0.0
2X-1, 146–148	422.26	0.2	32.0	33.7	4.1	69.7	26.3	2.2	1.7
2X-3, 30–32	424.10	0.2	49.5	10.1	2.7	62.4	28.8	8.9	0.0
2X-3, 72–74	424.52	0.3	35.3	29.6	1.9	66.7	24.8	8.5	0.0
2X-4, 3–5	425.33	0.2	38.5	19.3	4.3	62.1	25.4	12.6	0.0
2X-4, 116–118	426.46	0.2	18.5	54.6	2.3	75.4	23.1	1.5	0.0
2X-6, 52–54	428.82	0.3	50.7	10.0	4.0	64.7	28.9	6.4	0.0
3X-1, 6–8	430.56	0.2	36.6	25.4	3.5	65.5	26.1	8.4	0.0
3X-1, 55–57	431.05	0.2	52.7	7.8	3.7	64.2	30.6	5.2	0.0
3X-2, 16–18	432.16	0.2	52.8	7.5	4.0	64.4	30.3	5.3	0.0
3X-2, 139–141	433.39	0.3	40.7	20.9	2.5	64.1	26.6	9.3	0.0
3X-3, 1–3	433.51	0.2	55.6	8.4	1.7	65.7	29.7	4.6	0.0
3X-4, 69–71	435.69	3.5	45.5	17.7	5.6	68.7	30.8	0.5	0.0
3X-5, 48–50	436.98	0.2	35.4	30.0	5.4	70.8	26.2	3.0	0.0
3X-5, 95–97	437.45	7.8	44.3	9.0	6.8	60.1	28.3	6.5	5.1
3X-6, 47–49	438.47	2	48.2	13.7	4.2	66.1	29.6	3.5	0.8
4X-1, 16–18	440.26	0.5	48.7	7.6	3.9	60.2	29.0	10.8	0.0
4X-2, 108–110	442.68	1.2	47.7	10.7	7.5	66.0	31.2	2.8	0.0
					Mean	65.8	28.0	5.8	0.4
Subunit IIB									
4X-3, 55–57	443.65	10.7	38.5	16.0	6.2	60.8	27.5	2.1	9.7
4X-3, 142–144	444.52	8.1	37.8	19.1	6.1	63.0	27.7	3.1	6.1
4X-4, 12–14	444.72	12.7	37.6	13.8	6.7	58.2	26.3	5.3	10.1
4X-4, 25–27	444.85	10.6	31.4	25.6	4.9	61.9	24.9	4.9	8.4
4X-6, 44–46	448.04	0.4	55.2	2.3	4.0	61.5	28.6	9.9	0.0
5X-1, 63–65	450.43	0.4	47.1	8.4	6.1	61.7	27.7	10.6	0.0
5X-1, 146–148	451.26	0.4	51.1	6.9	5.9	63.9	30.6	1.6	3.9
5X-2, 43–45	451.73	0.3	43.3	14.9	7.4	65.6	28.1	6.3	0.0
5X-2, 93–95	452.23	0.3	40.4	19.2	6.2	65.8	25.2	8.9	0.0
5X-3, 31–33	453.11	0.3	54.8	4.1	4.8	63.7	29.0	7.3	0.0
5X-3, 127–129	454.07	10.8	48.6	6.5	4.3	59.4	28.1	5.4	7.2
5X-4, 47–49	454.77	22.1	39.0	9.2	5.6	53.8	25.0	5.6	15.6
5X-4, 110–112	455.40	20.5	44.4	6.9	5.2	56.5	27.1	3.0	13.4
5X-6, 32–34	457.62	7.8	52.5	5.2	4.0	61.7	29.4	5.0	3.9
5X-6, 148–150	458.78	10.7	41.3	9.5	5.2	56.1	26.1	8.7	9.1
5X-7, 8–10	458.88	3.4	49.6	8.3	4.6	62.5	28.3	7.6	1.6
5X-CC, 25–27	459.48	25.8	49.5	0.0	3.1	52.6	26.9	5.4	15.0
6X-1, 22–24	459.62	17	40.7	7.1	6.1	53.9	26.4	4.6	15.1
6X-1, 144–146	460.84	0.4	51.2	7.5	4.0	62.7	28.4	8.9	0.0
					Mean	60.3	27.4	6.0	6.3
Subunit IIC									
6X-2, 6–8	460.96	1.4	34.8	15.1	10.9	60.8	26.0	13.2	0.0
6X-3, 42–44	462.82	0.4	55.6	4.4	3.2	63.2	30.2	6.6	0.0
6X-3, 82–84	463.22	2.1	40.1	16.0	9.6	65.7	28.8	5.3	0.2
6X-4, 66–68	464.56	0.7	18.0	34.1	7.4	59.5	19.8	19.8	0.9
7X-1, 10–12	469.10		48.5	4.7	5.0	58.2	28.1	13.7	0.0
7X-1, 83–85	469.83	0.8	58.0	0.0	2.9	60.9	30.0	9.1	0.0
7X-2, 46–48	470.96	0.2	46.7	10.0	4.4	61.1	27.5	11.4	0.0
7X-2, 123–125	471.73	0.4	55.4	0.0	4.5	59.9	30.0	10.2	0.0
7X-3, 9–11	472.09	0.3	50.7	4.3	5.0	60.0	28.4	11.6	0.0
7X-3, 80–82	472.80	0.2	56.7	4.7	3.6	65.0	31.8	3.3	0.0
7X-4, 10–12	473.60	2.5	48.0	8.9	5.9	62.8	29.2	7.1	0.8
7X-4, 123–125	474.73	0.2	46.9	7.0	7.1	61.0	28.4	10.6	0.0
7X-5, 13–15	475.13	0.4	50.1	3.2	3.7	56.9	28.1	15.0	0.0
7X-5, 77–79	475.77	0.4	56.8	0.0	2.5	59.3	29.0	11.7	0.0
7X-6, 47–49	476.97	0.7	59.8	3.2	1.3	64.3	31.2	4.6	0.0
7X-6, 86–88	477.36	0.4	54.5	3.1	3.3	60.9	29.4	9.7	0.0
8X-1, 52–54	479.22	0.4	57.4	0.0	4.6	62.0	32.7	5.3	0.0
					Mean	61.3	28.7	9.9	0.1
Subunit IID									
8X-1, 122–124	479.92	1.7	53.0	0.0	6.2	59.2	30.2	10.6	0.0
8X-2, 19–21	480.39	1.3	48.0	5.7	6.9	60.6	29.7	9.7	0.0
8X-2, 134–136	481.54	0.2	54.9	4.0	2.4	61.3	30.2	8.5	0.0
8X-3, 9–11	481.79	0.2	51.4	3.8	5.3	60.5	29.8	9.7	0.0
8X-4, 40–42	483.60	0.2	50.7	5.2	3.7	59.6	29.0	11.3	0.0
8X-4, 141–143	484.61	0.2	43.3	14.4	5.1	62.9	27.5	9.6	0.0
8X-5, 66–68	485.36	0.2	57.1	0.0	2.3	59.4	29.7	10.9	0.0

Table 13 (continued).

Core, section, interval (cm)	Depth (mbsf)	$CaCO_3$	Normalized mineral abundances (wt%)						
			Smec.	Ill.	Kaol.	Clay	Qtz.	Plag.	Calc.
8X-6, 67–69	486.87	1.6	54.5	4.6	3.4	62.4	29.5	8.0	tr
8X-6, 103–105	487.23	0.2	48.8	4.5	4.2	57.5	27.4	15.1	0.0
8X-7, 12–14	487.82	0.2	50.4	7.3	3.2	60.8	27.8	11.4	0.0
9X-1, 52–54	488.92	0.2	48.9	6.8	5.1	60.8	29.1	10.1	0.0
9X-1, 94–96	489.34	0.2	48.7	0.0	6.5	55.2	28.1	16.7	0.0
9X-2, 24–26	490.14	0.2	50.8	3.8	4.4	59.0	27.8	13.2	0.0
9X-2, 83–85	490.73	0.1	47.5	6.7	3.7	57.8	26.3	15.9	0.0
9X-3, 8–10	491.48	0.7	49.9	5.9	3.4	59.2	28.7	12.1	0.0
9X-3, 78–80	492.18	0.6	46.5	10.5	2.8	59.7	27.9	12.4	0.0
9X-4, 59–61	493.49	0.6	48.7	0.0	5.0	53.7	28.4	17.9	0.0
9X-4, 101–103	493.91	0.4	52.9	6.8	2.4	62.2	28.8	9.0	0.0
9X-5, 7–9	494.47	0.2	50.9	6.6	2.1	59.6	27.7	12.7	0.0
9X-5, 81–83	495.21	0.2	44.1	5.5	5.5	55.1	25.9	18.9	0.0
9X-6, 43–45	496.33	0.2	47.8	2.3	2.9	53.0	27.1	19.9	tr
					Mean	59.0	28.4	12.6	0.0
Subunit IIE									
10X-1, 124–126	499.34	0.2	51.5	4.2	2.4	58.1	27.8	14.1	0.0
10X-2, 51–53	500.11	0.2	45.1	5.2	4.1	54.3	27.2	18.5	0.0
10X-2, 90–92	500.50	0.2	37.9	8.5	6.3	52.8	26.3	20.9	0.0
10X-3, 19–21	501.29	0.1	43.8	7.3	6.6	57.7	29.3	13.0	0.0
10X-4, 124–126	503.84	0.2	50.4	5.2	5.3	60.9	29.2	9.9	0.0
10X-5, 17–19	504.27	0.1	52.2	3.7	4.9	60.9	31.2	8.0	0.0
10X-5, 59–61	504.69	0.2	45.7	9.8	3.8	59.3	27.8	12.9	0.0
					Mean	57.7	28.4	13.9	0.0
Subunit IIF									
11X-1, 36–38	508.06	0.3	50.3	7.5	4.5	62.3	31.0	6.7	0.0
11X-1, 70–72	508.40	0.2	47.9	10.7	4.3	62.9	29.4	7.7	0.0
11X-1, 137–139	509.07	0.1	43.4	9.9	6.0	59.2	27.9	12.9	0.0
11X-2, 27–29	509.47	0.2	42.5	12.1	10.4	65.0	30.3	4.7	0.0
11X-2, 84–86	510.04	0.2	47.9	8.5	7.5	63.9	30.8	5.3	0.0
11X-3, 11–13	510.81	0.2	45.1	8.2	10.3	63.7	32.4	3.9	0.0
11X-4, 37–39	512.57	0.1	48.6	10.9	7.6	67.1	32.5	0.4	0.0
11X-4, 68–70	512.88	0.2	53.1	9.6	4.2	66.9	33.1	tr	0.0
					Mean	63.9	30.9	5.9	0.0
Subunit IIIA									
11X-5, 17–19	513.87	0.2	25.1	39.0	7.5	71.6	28.4	tr	0.0
12X-1, 47–49	517.87	0.2	tr	29.6	13.4	43.0	47.4	9.6	0.0
12X-1, 79–81	518.19	0.2	26.6	40.3	7.8	74.6	25.4	tr	0.0
12X-2, 29–31	519.19	0.2	41.2	23.1	5.6	69.9	29.4	0.7	0.0
12X-2, 93–95	519.83	0.2	42.1	21.6	5.4	69.1	30.9	tr	0.0
12X-3, 27–29	520.67	0.2	26.9	33.5	10.3	70.7	29.3	tr	0.0
12X-3, 107–109	521.47	0.1	tr	29.7	17.1	46.8	47.7	5.5	0.0
12X-4, 2–4	521.92	0.1	40.5	15.3	8.5	64.3	35.3	0.4	0.0
12X-4, 83–85	522.73	0.3	29.7	30.6	12.2	72.5	27.5	tr	0.0
					Mean	64.7	33.5	4.1	0.0
Subunit IIIB									
12X-5, 45–47	523.85	0.2	tr	31.6	19.0	50.7	41.9	7.4	0.0
13X-1, 14–16	526.94	0.2	21.3	37.9	10.8	70.0	30.0	tr	0.0
13X-2, 14–16	528.44	0.6	27.7	14.1	20.5	62.3	37.0	0.7	0.0
13X-2, 101–103	529.31	40.2	20.4	25.5	10.9	56.9	21.0	3.1	19.0
13X-3, 6–8	529.86	0.2	20.8	35.1	14.2	70.2	28.2	1.7	0.0
13X-3, 113–115	530.93	23.1	28.7	8.0	16.2	52.9	26.2	1.3	19.6
13X-5, 1–3	532.81	16.8	37.3	21.6	9.5	68.5	31.5	0.0	0.0
13X-5, 99–101	533.79	0.2	22.5	30.5	20.5	73.5	26.0	0.5	0.0
13X-6, 19–21	534.49	31.5	15.7	8.2	16.0	40.0	26.5	2.2	31.4
13X-6, 85–87	535.15	19.4	25.2	9.3	17.1	51.6	31.0	2.2	15.1
13X-7, 28–30	536.08	0.6	22.9	20.9	13.2	57.1	40.4	2.5	0.0
14X-1, 42–44	536.52	0.2	16.7	38.1	17.1	71.9	27.1	1.0	0.0
14X-1, 146–148	537.56	24.2	27.5	0.0	27.0	54.5	21.5	0.0	24.5
14X-2, 43–45	538.03	1.9	19.5	30.5	13.8	63.9	36.0	0.1	tr
14X-2, 100–102	538.60	0.1	27.6	25.6	13.7	67.0	31.6	1.4	0.0
14X-3, 9–11	539.19	0.3	16.9	46.5	10.8	74.2	25.8	tr	0.0
14X-3, 70–72	539.80	0.2	9.5	32.8	17.7	60.1	22.3	17.6	0.0
14X-4, 19–21	540.79	39.4	33.6	13.4	7.3	54.2	24.5	0.0	21.3
14X-4, 116–118	541.76	23.7	12.8	17.6	28.2	58.7	17.2	0.0	24.2
14X-5, 61–63	542.71	5.3	2.4	55.0	14.1	71.5	20.9	0.1	7.4
14X-5, 92–94	543.02	35.3	36.4	0.0	9.2	45.5	27.0	0.0	27.5
14X-CC, 11–13	545.21	0.2	3.6	65.3	11.5	80.5	19.5	tr	0.0
15X-1, 66–68	546.06	0.3	20.9	35.9	16.6	73.3	22.9	3.8	0.0
15X-1, 106–108	546.46	29	14.4	24.0	13.8	52.2	20.3	0.0	27.5
15X-2, 51–53	547.41	0.3	22.2	24.4	17.1	63.7	36.3	tr	tr
15X-2, 104–106	547.94	24.4	tr	18.0	21.3	39.3	27.8	2.5	30.4
15X-3, 2–4	548.42	33	21.4	8.9	12.2	42.5	22.7	1.4	33.4
15X-3, 78–80	549.18	10.7	40.8	14.7	7.2	62.8	31.3	tr	6.0
15X-4, 27–29	550.17	32.7	3.9	21.8	16.9	42.7	21.4	1.7	34.2
15X-4, 121–123	551.11	0.2	33.7	30.1	8.2	72.0	28.0	tr	0.0
15X-5, 28–30	551.68	33.2	15.0	19.3	7.8	42.1	24.9	0.8	32.1
15X-5, 105–107	552.45	0.2	24.5	42.5	7.5	74.4	25.6	tr	0.0
15X-6, 42–44	553.32	9.4	22.5	12.6	13.9	49.0	45.8	1.1	4.1
16X-1, 12–14	554.92	0.2	3.5	62.8	9.4	75.7	24.3	tr	0.0
16X-1, 106–108	555.86	0.2	tr	56.7	10.4	67.1	31.3	1.6	0.0
16X-2, 24–26	556.54	0.2	0.0	69.5	13.1	82.6	17.4	tr	0.0
16X-2, 91–93	557.21	83.8	tr	0.0	0.0	0.0	5.9	0.0	94.1
16X-3, 39–41	558.19	0.2	18.7	43.2	14.3	76.2	23.8	tr	0.0
16X-3, 126–128	559.06	0.2	20.9	42.1	11.0	74.0	23.6	tr	2.4
16X-4, 17–19	559.47	36.3	17.2	7.7	13.0	37.9	29.7	1.3	31.2

Table 13 (continued).

Core, section, interval (cm)	Depth (mbsf)	$CaCO_3$	Normalized mineral abundances (wt%)						
			Smec.	Ill.	Kaol.	Clay	Qtz.	Plag.	Calc.
16X-4, 109–111	560.39	0.2	21.0	40.3	13.6	74.8	25.2	tr	0.0
16X-5, 17–19	560.97	25.2	20.3	11.9	16.4	48.6	29.4	0.5	21.5
16X-5, 78–80	561.58	60.6	12.0	8.0	5.3	25.3	16.8	2.5	55.4
16X-6, 29–31	562.59		18.6	39.6	11.5	69.7	30.3	tr	0.0
16X-6, 72–74	563.02	2.7	23.8	25.3	12.7	61.8	37.7	tr	0.5
16X-7, 56–58	563.86	0.2	22.2	40.9	6.7	69.9	30.1	tr	0.0
17X-2, 33–35	565.93	40.7	tr	34.7	10.4	45.1	11.9	0.0	43.0
17X-2, 101–103	566.61	29.6	8.1	38.1	7.2	53.4	18.3	0.4	27.9
17X-3, 138–140	568.48	6.3	15.4	33.5	12.9	61.8	31.3	0.8	6.1
17X-4, 21–23	568.81	42.4	10.1	23.9	8.9	43.0	22.2	0.0	34.9
17X-4, 114–116	569.74	0.2	25.8	32.3	7.4	65.4	34.6	tr	0.0
17X-5, 83–85	570.93	0.2	18.7	41.9	8.2	68.8	31.2	tr	0.0
17X-6, 38–40	571.98	33.2	17.4	15.5	18.9	51.8	17.0	0.0	31.2
17X-6, 138–140	572.98	0.6	21.8	33.0	9.6	64.4	35.6	tr	0.0
17X-7, 12–14	573.22	34.4	7.9	19.7	20.1	47.6	16.2	0.0	36.3
18X-1, 97–99	574.27	2.3	26.0	32.2	10.1	68.4	30.7	tr	0.9
18X-2, 28–30	575.08	14.1	19.1	30.1	13.5	62.7	24.9	0.0	12.4
18X-2, 145–147	576.25	46.4	23.7	9.4	8.6	41.7	23.6	1.5	33.2
18X-3, 25–27	576.55	0.2	23.6	35.3	7.4	66.2	33.8	tr	0.0
18X-3, 126–128	577.56	34.1	16.6	14.5	16.8	47.9	18.3	0.0	33.8
18X-4, 17–19	577.97	0.3	21.8	31.4	7.1	60.3	34.5	5.2	0.0
18X-4, 85–87	578.65	0.2	21.0	46.6	7.9	75.5	24.5	tr	0.0
18X-5, 19–21	579.49	0.2	18.8	36.9	9.6	65.3	34.7	tr	0.0
18X-5, 86–88	580.16	23.4	16.3	30.5	8.9	55.8	21.1	0.6	22.5
18X-6, 11–13	580.91	0.2	26.1	44.4	3.6	74.2	25.8	tr	0.0
19X-1, 134–136	584.14	60.2	12.7	12.5	6.9	32.1	14.5	0.0	53.4
19X-2, 15–17	584.45	33.8	35.4	12.7	6.4	54.5	24.3	0.0	21.2
19X-2, 92–94	585.22	26.2	26.9	8.1	19.2	54.1	20.5	0.0	25.4
19X-3, 44–46	586.24	0.3	28.0	32.6	7.9	68.6	24.9	6.5	0.0
19X-3, 104–106	586.84	0.1	23.6	34.1	7.6	65.3	26.1	8.7	0.0
19X-4, 47–49	587.77	26.7	19.8	16.5	16.6	52.9	18.8	7.5	20.8
19X-4, 97–99	588.27	4.6	43.0	15.7	5.8	64.4	33.8	0.1	1.7
19X-5, 33–35	589.13	2.7	0.0	35.7	22.7	58.4	38.5	3.1	tr
19X-5, 97–99	589.77	32.9	24.2	18.3	13.4	55.9	19.7	0.0	24.4
19X-6, 30–32	590.60	32.9	33.1	8.3	10.5	51.9	30.0	0.5	17.6
19X-6, 113–115	591.43	6.2	21.6	28.6	12.4	62.6	32.2	0.0	5.2
19X-7, 33–35	592.13	2.5	0.0	53.8	15.4	69.2	28.8	tr	2.1
					Mean	59.0	26.6	1.8	13.7

Notes: "tr" indicates that traces of the mineral were detected, but calculated abundance is less than 0%. See Fisher and Underwood (this volume) for a complete description of how calculations were made. See Tables 5 and 7 for explanation of abbreviations.

Table 14. Ranges and average values of reflectance percentage (550-nm wavelength interval of visible light) for each lithologic unit and subunit cored at Site 948.

Unit/subunit	General lithology	Range of 550-nm reflectance (%)	Average 550-nm reflectance (%)
I	Light brownish gray clay with nannofossils and foraminifers	23.72–38.53	32.23
IIA	Gray, olive gray, and grayish brown bioturbated claystone with local intraformational breccia	21.36–35.17	28.45
IIB	Gray claystone and claystone with nannofossils	14.19–37.68	30.13
IIC	Gray, olive gray, and olive bioturbated claystone	17.82–34.30	28.04
IID	Yellowish brown, brownish gray, brown, and reddish gray claystone with local tuff interbeds and altered volcanic ash	21.34–33.54	28.16
IIE	Pinkish gray and brownish gray claystone with radiolarians	21.24–44.92	32.04
IIF	Grayish brown and olive brown claystone	17.89–37.02	30.87
IIIA	Greenish gray and dark grayish brown, banded, variegated claystone	25.46–43.98	30.61
IIIB	Rhythmic interbeds of greenish gray claystone, gray silty claystone, light gray claystone with nannofossils, and nannofossil chalk	12.73–47.18	28.83

induced by rotational shear of the natural fissility of the claystones during XCB core cutting, but we also noted that much of it is spatially associated with zones of much more intense fabric, which we have attributed to tectonic deformation.

We were able to reorient a limited, but representative, sample of the structural measurements into true geographic coordinates, using paleomagnetic remanence directions (see "Paleomagetism" section, this chapter). The ubiquitous "biscuiting" of the cores (an effect of XCB core cutting in which individual core segments no more than a few centimeters long are rotated independently about a vertical axis) presented a major obstacle to reorientation of the structural measurements. Each biscuit from which we wanted a geographic orientation had to be passed independently through the cryogenic magnetometer to determine the appropriate rotation. Thus, although structures from critical intervals were analyzed, it was not possible to convert all orientation data.

Domain I: Accretionary Prism (420–498 mbsf)

The interval from Cores 156-948C-2X to -9X consists for the most part of homogeneous, bioturbated claystone, with scattered thin beds of altered volcanic ash. Bedding is variable in this interval (Fig. 17). Most dips are moderate to steep, from 20° to 60°, and locally in Cores 156-948C-7X and -9X they reach vertical. Some bedding orientations in this domain were determined using *Zoophycos* trace fossils, which are believed to reflect paleohorizontal (Ekdale et al., 1984). Although good indicators of younging direction were usually absent, all clear examples that were noted were upright.

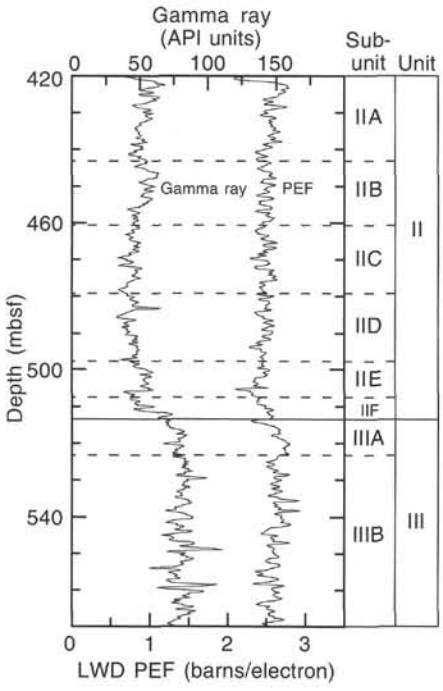

Figure 15. Correlation between lithostratigraphic units cored at Hole 948C and LWD data, Hole 948A.

Paleomagnetically reoriented data, presented in Figure 18, suggest that three structural subdomains occur within the prism. Cores 156-948C-2X and -3X exhibit variable dips toward the northeast, and a consistent strike that averages 347°, which agrees reasonably well with the overall strike of the plate margin. Cores 156-948C-4X and -5X show a similar strike, but bedding dips westward. At the base of Core 156-948C-3X, zones of scaly fabric, inclined about 30°, indicate a reverse sense of movement. The change of bedding dip therefore may indicate thrust-related folding, with a footwall flat and hanging wall cutoff geometry. These shear zones are the only ones that exhibit clear reverse movement in the cored interval. Cores 156-948C-6X through -9X show a considerably greater range of bedding orientations. This interval lies immediately above the décollement zone and thus may have been subject to more complex folding and thrusting than were shallower cores. Unfortunately, the resolution of the reoriented data does not permit interpretation of the detailed geometry of this subdomain.

Mineralized veins of two distinct types occur in Domain I (Fig. 16). Within intervals of scaly fabric (described below), several foliation-parallel veins have been identified by XRD as rhodochrosite (Table 15). In Cores 156-948C-2X (Fig. 19) and -7X, these appear to be structurally controlled. The second vein type, not associated with shear structures, is found in Cores 156-948C-7X and -9X, formed of semiplanar concentrations of rhodochrosite grains with green alteration haloes, and in Core 156-948C-9X, where a horizontal vein was identified by XRD as phillipsite (Table 15).

Several intervals of intense scaly fabric, 10 to 40 cm thick, are present in Cores 156-948C-2X and -3X. The zones of scaly fabric in Core 156-948C-2X have low dips and an unknown sense of displacement. The scaly fabric and associated rhodochrosite veins in Section 156-948C-2X-2 form a moderately tight recumbent fold. A veined zone of steeply inclined scaly fabric is seen in Section 156-948C-2X-5 (Fig. 19). The zones of scaly fabric in Core 156-948C-3X have been interpreted as a thrust fault, as discussed above. Intense scaly fabrics in Section 156-948C-6X-2 define another notable sheared interval, with low dip and indeterminate movement sense. This zone may correspond to the thrust fault identified at Site 671 at 455 mbsf based on the anomalous thickness of the late Miocene section (Thrust C; Mascle, Moore, et al., 1988). Only incipient to weak shear fabrics were identified in Cores 156-948C-7X and -8X.

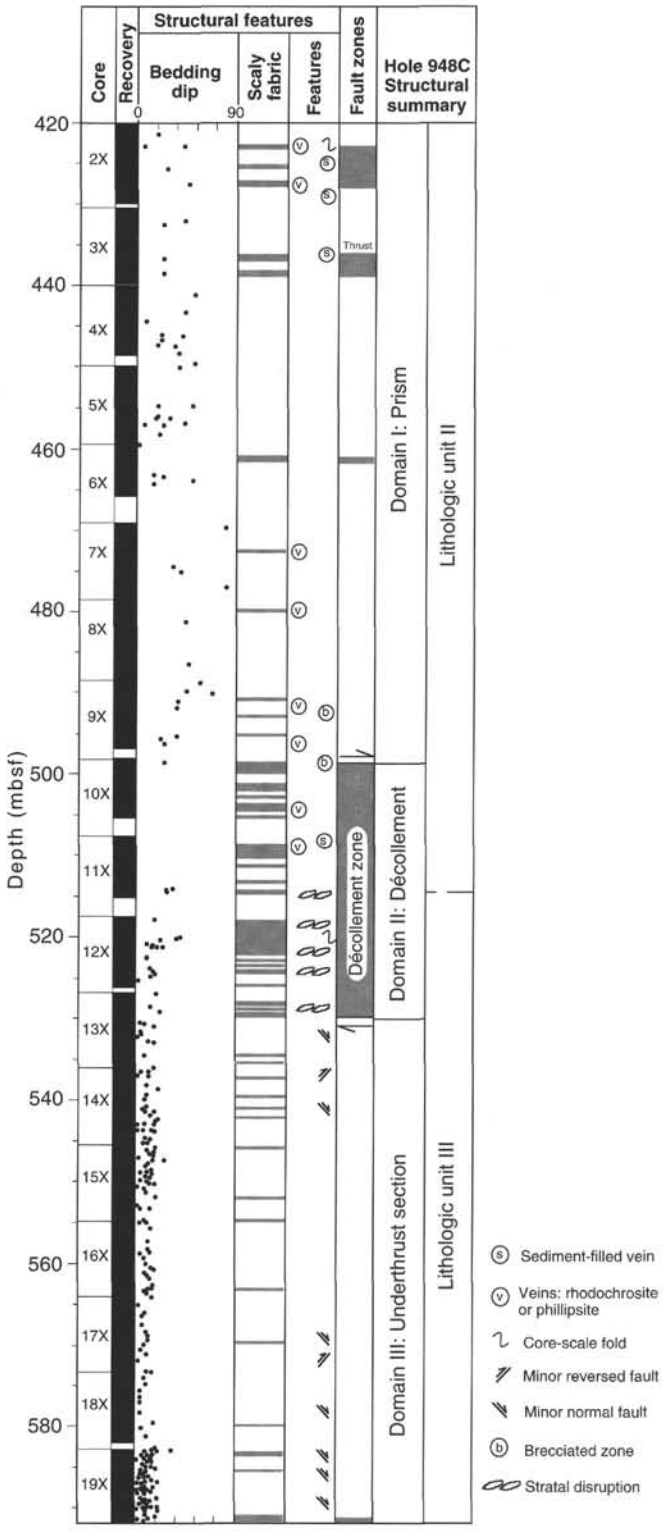

Figure 16. Summary diagram of major structural features recorded from Hole 948C. See Table 16 for data.

The base of the prism domain (Sections 156-948C-9X-2 through -5) exhibits several zones of intense scaly fabric as well as locally brecciated zones having steeply dipping boundaries (Fig. 20), which alternate with more intact intervals. These brecciated zones are charac-

Table 15. X-ray diffraction mineralogy of vein minerals and altered sediments from Hole 948C.

Core, section, interval (cm)	Depth (mbsf)	Sampled feature	Feldspar	Illite	Kaolinite/ chlorite	Mg-kutnohorite	Phillipsite	Quartz	Rhodochrosite	Smectite
156-948C-										
2X-2, 88	423.18	White mineral vein parallel to scaly fabric + matrix		#	##			###	###	##
3X-CC, 1–2	439.51	Light green halo in sediment		#	##		###	##		###
7X-3, 87	472.87	Encasing sediment of vein sampled at 88 cm	###	#	##			###		###
7X-3, 88	472.88	Light green halo in sediment around vein sampled at 88 cm	##	#	##			##	##	###
7X-3, 89	472.89	Mineral vein of mm-scale, pink crystals + matrix			#			#	####	##
9X-5, 24–25	494.64	Light green halo in sediment			#		####	##		##
9X-5, 119–120	495.59	Light green halo in sediment around ash nodules			#		####	##		###
9X-CC, 32–33	496.88	Mineral vein + matrix with light green halo					####			##
11X-1, 102–103	508.73	White, soft mineral vein along zone of scaly fabric		#	##		###	##		####
11X-1, 103–104	508.73	Same as above		#	##		###	##		###
12X-5, 0–2	523.4	Crystals in residues of paleontological sample				####				

Note: Relative major peak intensities are indicated as follows: # = very low; ## = low; ### = high; #### = very high.

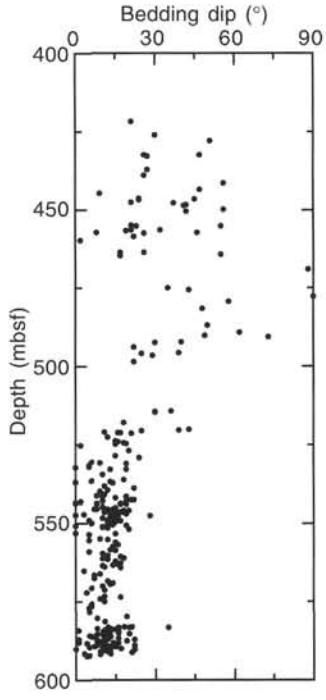

Figure 17. Plot of bedding dip vs. depth in Hole 948C, showing structurally rotated layers above ~521 mbsf and shallow to subhorizontal beds below.

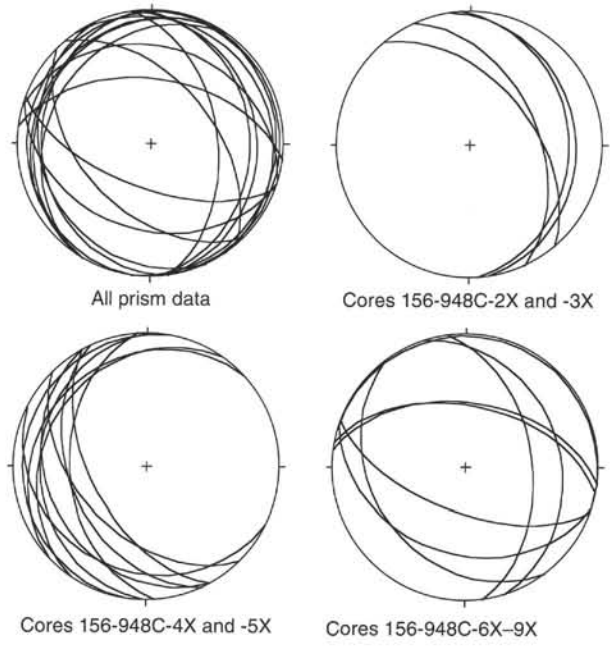

Figure 18. Bedding orientation in geographic reference frame for the accretionary prism domain, Hole 948C. Reorientation was accomplished by using the paleomagnetic remanence direction.

terized by fragmentation of the claystone into millimeter- to submillimeter-scale chips, which are loose, yet appear undisturbed by drilling (that is, the fragments still are interlocked and the matrix is intact). Within some of these breccias there is a weak planar fabric. The claystone in this core is sufficiently lithified to fracture readily, in contrast to much of the material just below in the décollement zone. Minimum values of chloride concentration and other pore-water geochemical anomalies occur in Section 156-948C-9X-5 (see "Inorganic Geochemistry" section, this chapter), possibly indicating that fracture porosity is important at the top of and immediately above the décollement zone.

We interpreted the prism domain as the immediate hanging wall and adjacent overlying sediments of the main décollement zone. It contains several shear zones that represent faults that may be splays or oblique ramps derived from the décollement. Evidently, folding on a scale of tens of meters and faulting has taken place in this interval, as might be expected for the hanging wall block of a décollement fault.

Domain II: Décollement Zone (498–529 mbsf)

Beginning at the top of Core 156-948C-10X and continuing to Core 13X, a zone dominated by scaly fabric and fracture networks or stratal disruption interleaved with intact intervals of sediment marks the décollement zone imaged in the MCS data. The uppermost boundary of this zone may be in the unrecovered interval between Cores 156-948C-9X and -10X (about 1 m). The transition into the fault zone is sharp, with thick scaly intervals at the top of Core 10X at 498 mbsf (Fig. 21; Table 16). Throughout Cores 156-948C-11X and -12X, zones of scaly fabric are dominant, although still separated by intact intervals. In Section 156-948C-12X-3, intact intervals in which shallowly dipping bedding can be discerned are common, and the lowest zone of intense scaly foliation in this domain is in interval 156-948C-13X-2, 116–129 cm (529.5 mbsf). The lower boundary of the décollement zone thus is gradational over about 8 m, with the spacing between the zones of intensely developed scaly fabric increasing downward.

The décollement is developed across and centered on the major boundary between lithologic Units II and III, which marks the contact between the siliceous pelagic and hemipelagic sections above and the interbedded turbiditic and hemipelagic deposits below (see "Lithostratigraphy" section, this chapter). Interestingly, at the core scale, the actual lithological contact is in a zone of relatively weak strain. From 498 to 514 mbsf, the fault fabric is within lithologic Subunits IIE and IIF, a radiolarian-rich yellowish-brown to brownish claystone that

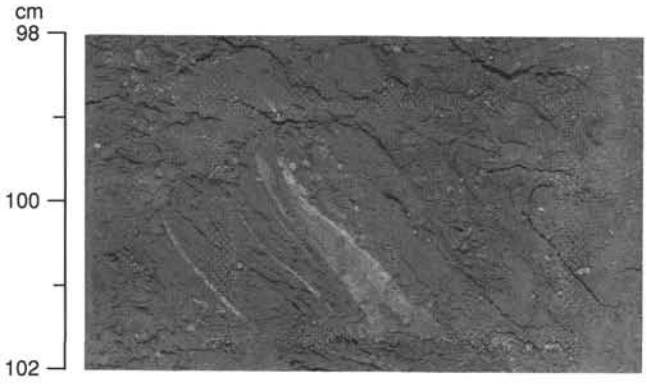

Figure 19. Close-up of scaly foliation with rhodochrosite veins, interval 156-948C-2X-5, 98–102 cm (Domain I).

exhibits a friable and fractured aspect when observed in the split core face (Figs. 22 and 23). Zones of closely spaced fractures, which break the core into angular polished chips, grade into zones of well-defined scaly fabric. In places, this interval exhibits blotchy purplish-black manganese staining, which, in at least one case, occurs along the foliation planes of the scaly fabric (Fig. 22). In Sections 156-948C-10X-5 (504.7 mbsf) and -11X-1 (508.7 mbsf) are small foliation-parallel veins, the latter of which have been identified by XRD analysis as phillipsite (Table 15).

Below Section 156-948C-11X-5 (513.7 mbsf), the sediment is interbedded greenish-gray, olive-gray, and reddish-gray claystone of lithologic Unit III, which is more plastic and less friable than the units above. When split cores exhibiting scaly fabric in this zone are scraped clean, the sediment shows a discontinuous subhorizontal banding and intense stratal disruption, which suggests a ductile shear fabric (Figs. 23B, -C, and 24). Where the presence of relatively coarse, silty layers renders bedding visible, one can see that the stratal disruption is associated with zones of intense scaly fabric. We found no veins in this lower half of the fault zone.

All of the sediments in which the décollement zone has formed are poorly lithified to completely unlithified, notwithstanding the use of the term "claystone" to describe them. All are soft enough to cut with a knife; thus, the deformation has taken place in an essentially unlithified state. Within the décollement, the lithologic boundary appears to mark a plasticity contrast, which implies that the two sediment types had differing rheologies during deformation. Intense scaly fabrics from above and below the boundary are mesoscopically similar; however, the structurally massive and more weakly foliated zones appear dissimilar. The upper half of the décollement (within lithologic Unit II) has a blocky appearance with more widely spaced discrete fractures, whereas the lower half (within lithologic Unit III) has well-defined zones of scaly fabric and stratal disruption and few discrete fractures in the more intact intervals, which have a plastic and sticky consistency. The intact intervals are mostly dark gray silty turbidites, indicating a lithologic control on rheology between beds as well as between lithologic units. Some nonfoliated intervals display extensive folding, associated with minor reverse faults, and other flow structures (Figs. 23B through 25) which were not observed in the upper half of the fault zone. Further elucidation of the lithologic control of rheology awaits microstructural study.

Detailed recording of the occurrence of scaly vs. relatively intact intervals in Cores 156-948C-10X through -13X indicates that intense scaly shear zones are not evenly distributed throughout the décollement. Three zones of relatively concentrated shear-zone formation were identified (Fig. 21B): the first from Section 156-948C-10X-1, 16 cm, to -10X-2, 10 cm (498.3–499.8 mbsf); the second in Section 156-948C-11X-2, from 4 to 150 cm (509.2–510.2 mbsf); and the third from Section 156-948C-12X-1, 14 cm, to -12X-2, 64 cm (517.5–519.5 mbsf). Within the décollement, the longest weakly deformed to

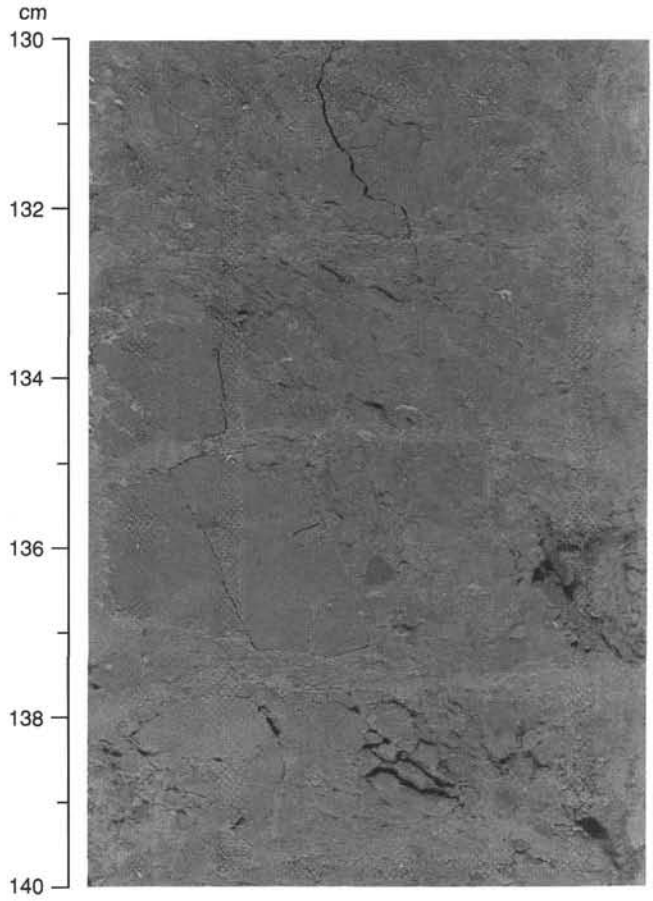

Figure 20. Brecciated zone with steeply dipping boundary in interval 156-948C-9X-3, 130–140 cm (Domain I).

intact interval is from the top of Section 156-948C-11X-3 (510.7 mbsf) to -11X-5, 57 cm (514.3 mbsf) and contains the lithologic Unit II/III boundary. The alternation of intervals of scaly fabric and less deformed, locally intact strata indicates a heterogeneous distribution of strain within the décollement zone which comprises discrete shear zones (intense scaly fabric) that bound intervals with fracture networks, stratal disruption, incipient to weak scaly fabric, and structurally intact sediment. The intervals of stratal disruption involve mainly low-angle extensional disruption of beds, but some contractional faults and associated folds also are present (Fig. 23).

Bedding dips were difficult to obtain in the upper half of the décollement zone because of the homogeneous and bioturbated nature of the sediments and the presence of extensive fracture networks. In the lower half the intact intervals are more clearly bedded. From 514.2 to 520.5 mbsf, bedding dips are variable (Fig. 17), ranging from 18° to 39°. From 521 mbsf to the base of the décollement zone, bedding is much more shallowly inclined, mostly 10° to 20°, identical to the inclination of the underthrust section of Domain III below. This change in dip, together with the decreasing frequency of scaly fabric zones over the interval between 520.5 and 529 mbsf, marks the gradational lower boundary of the décollement. Furthermore, reoriented bedding data from the décollement zone lie within the same field as the underthrust section (Fig. 26).

Within the fault zone, the boundary between zones of scaly fabric and less deformed material is generally subhorizontal where discernible; rarely, it dips shallowly (less than 20°). Some of these boundaries coincide with the laminations between individual drilling biscuits and may be artificial. The foliation of the scaly fabric itself, on the other hand, is commonly inclined at a significant but variable angle to horizontal (Fig. 22). In the interval from 521 to 529 mbsf, for which

Table 16. All structural measurements recorded for cores of Hole 948C.

Core, section, interval (cm)	Depth (mbsf)	ID	Thickness (cm)	Intensity	Apparent dip (°)	Apparent trend (°)	Strike (°)	Dip (°)	Reorient.	Geo. strike (°)	Geo. dip (°)	Comments
156-948C-												
1H-1, 23–23	0.23	B					180	2				Ash layer
1H-1, 31–32	0.31	B					270	12				Ash layer
1H-2, 73–73	2.23	B					14	8				Ash layer
1H-2, 92–92	2.42	B					180	2				Ash layer
1H-3, 26–26	3.26	B					112	5				Ash layer
1H-5, 123–124	7.23	B					121	6				Ash layer
1H-6, 3–3	7.53	B					108	3				Ash layer
2X-1, 93–99	421.73	B					45	21	Paleomag.	351	21	Aligned bioturbations
2X-2, 85–102	423.15	SFZ	17				231	13				Upper boundary
2X-2, 86–88	423.16	V	0.05				208	20				Rhodochrosite V parallel to SF, set
2X-2, 89–89	423.19	SF		3			19	45				Upper limb of small FO
2X-2, 90–90	423.20	FO			6	90						FO hinge surface trace
2X-2, 91–91	423.21	SF		3			211	46				Lower limb of small FO
2X-2, 91–91	423.21	FO					327	7				FO axial surface
2X-2, 96–99	423.26	SF		3			18	46				
2X-2, 99–102	423.29	SF		3			252	36				
2X-3, 23–39	424.03	SV	0.1				344	45				Mud-filled, set
2X-4, 26–33	425.56	SFZ	7									Low dip
2X-4, 30–30	425.60	SF		2			311	55				
2X-4, 78–78	426.08	B					305	30				Aligned coprolites
2X-5, 78–118	427.58	SFZ	40		37	270						Upper boundary
2X-5, 77–80	427.57	V	0.05									Rhodochrosite V parallel to SF, set
2X-5, 94–96	427.74	SF		3			13	47				
2X-5, 99–104	427.79	V	0.05				351	50				Rhodochrosite V parallel to SF, set
2X-5, 111–111	427.91	B					343	51	Paleomag.	320	51	*Zoophycos*
2X-6, 30–33	428.60	SV										Mud-filled, set
2X-CC, 27–27	429.13	SV	0.1				183	32				Mud-filled
3X-1, 30–36	430.80	SV										Mud-filled, set of trellis-type
3X-1, 42–45	430.92	SV										Mud-filled
3X-2, 29–32	432.29	B					34	26	Paleomag.	356	26	Aligned bioturbations
3X-2, 35–37	432.35	B					338	47	Paleomag.	335	47	Aligned bioturbations
3X-2, 80–80	432.80	B					153	27				Aligned bioturbations
3X-4, 112–117	436.12	SV	1				36	41				Clastic dike?
3X-4, 138–150	436.38	SFZ	12		47	270						Upper boundary, thrust
3X-4, 138–140	436.38	SF		3	88	270						
3X-4, 142–143	436.42	SF		3			135	39				
3X-5, 0–5	436.50	SFZ	5		11	90						Lower boundary
3X-5, 0–5	436.50	SF		3	60	270						
3X-5, 55–56	437.05	B					192	27				Aligned bioturbations
3X-5, 80–85	437.30	B			42	270						Aligned bioturbations
3X-5, 80–85	437.30	SV										Set at right angle to B
3X-6, 70–75	438.70	SFZ	1.5				211	32				Thrust
3X-6, 70–75	438.70	SF		3			211	32				
3X-6, 74–78	438.74	SFZ	1.5				180	28				Thrust
3X-6, 74–78	438.74	SF		3	48	270						
3X-6, 81–85	438.81	SFZ	1				253	43				Thrust
3X-6, 81–85	438.81	SF		3								
3X-6, 90–90	438.90	B					214	26				Color change
3X-6, 97–113	438.97	SFZ	13				220	28				Lower boundary, thrust
3X-6, 105–107	439.05	SF		3	37	270						
4X-1, 128–136	441.38	B					270	56	Paleomag.	151	56	Aligned bioturbations
4X-3, 43–47	443.53	B					204	47	Paleomag.	135	47	Ash layer
4X-4, 6–6	444.66	B					252	9				Aligned bioturbations
4X-4, 31–31	444.91	SFZ	0.5									Low dip
4X-4, 31–31	444.91	SF		3								
4X-4, 34–34	444.94	SFZ	0.1									Low dip
4X-4, 34–34	444.94	SF		3								
4X-5, 27–28	446.37	B					59	24				*Zoophycos*
4X-5, 38–48	446.48	B					180	45				*Zoophycos*
4X-5, 80–83	446.90	B					246	24	Paleomag.	214	24	*Zoophycos*
4X-6, 2–5	447.62	B					147	21				Aligned bioturbations
4X-6, 14–19	447.74	B					51	37				Aligned bioturbations
4X-CC, 20–24	448.48	B					180	42	Paleomag.	155	42	*Zoophycos*
4X-CC, 34–36	448.62	B					62	41				*Zoophycos*
5X-1, 7–10	449.87	B					61	56				*Zoophycos*
5X-1, 54–56	450.34	B					180	42	Paleomag.	176	42	*Zoophycos*
5X-4, 74–74	455.04	B					270	21	Paleomag.	181	21	*Zoophycos*
5X-4, 82–85	455.12	B					180	55				*Zoophycos*
5X-4, 84–85	455.14	B					238	23				*Zoophycos*
5X-5, 62–65	456.42	B					352	21	Paleomag.	351	21	*Zoophycos*
5X-5, 67–68	456.47	B					96	32				*Zoophycos*
5X-5, 72–72	456.52	B					243	19	Paleomag.	227	19	*Zoophycos*
5X-5, 142–145	457.22	B					164	46				*Zoophycos*
5X-5, 148–149	457.28	B					220	8	Paleomag.	189	8	*Zoophycos*
5X-6, 17–18	457.47	B					180	26	Paleomag.	151	26	*Zoophycos*
5X-6, 112–112	458.42	B					204	22	Paleomag.	116	22	*Zoophycos*
6X-1, 38–38	459.78	B					0	2	Paleomag.	286	2	*Zoophycos*
6X-2, 40–70	461.30	F		2								Fracture network, incipient SF
6X-2, 70–77	461.60	SFZ	7		5	270						Upper boundary
6X-2, 70–77	461.60	SF		3								
6X-2, 77–90	461.67	F		2								Fracture network, incipient SF
6X-2, 90–107	461.80	SFZ	17									Low dip
6X-2, 90–107	461.80	SF		3								
6X-2, 107–111	461.97	F		2								Fracture network, incipient SF
6X-2, 111–117	462.01	SFZ	6									Low dip
6X-2, 111–117	462.01	SF		3								
6X-2, 117–127	462.07	F		2								Fracture network, incipient SF
6X-2, 127–131	462.17	SFZ	4									Low dip

Table 16 (continued).

Core, section, interval (cm)	Depth (mbsf)	ID	Thickness (cm)	Intensity	Apparent dip (°)	Apparent trend (°)	Strike (°)	Dip (°)	Reorient.	Geo. strike (°)	Geo. dip (°)	Comments
6X-2, 127–131	462.17	SF		3								
6X-2, 131–137	462.21	F		2								Fracture network, incipient SF
6X-3, 115–120	463.55	F		3								Fracture network
6X-3, 118–118	463.58	B					107	17				Ash layer
6X-3, 124–124	463.64	B					210	26				Ash layer
6X-4, 24–31	464.14	B					39	55				Ash layer
6X-4, 78–79	464.68	B					31	17				Ash layer
7X-1, 2–8	469.02	B					0	88				*Zoophycos*
7X-3, 23–24	472.23	SFZ	0.4				306	34				
7X-3, 23–24	472.23	SF		3								
7X-3, 23–24	472.23	V					306	34				Rhodochrosite V parallel to SFZ
7X-3, 53–54	472.53	SFZ	0.4									Low dip
7X-3, 53–54	472.53	SF		3								
7X-3, 69–73	472.69	V	0.7				161	50				Rhodochrosite
7X-3, 73–73	472.73	SFZ	0.5									Low dip
7X-3, 73–73	472.73	SF		3								
7X-3, 87–89	472.87	V	0.5									Low dip, bifurcated, rhodochrosite V
7X-3, 132–135	473.32	F					358	81				Sense of movement unknown
7X-4, 129–130	474.79	B					186	35	Paleomag.	108	35	Aligned bioturbations
7X-5, 43–46	475.43	B					18	43				Color change
7X-6, 110–115	477.60	B					150	90				*Zoophycos*
8X-1, 53–57	479.23	B					0	58				*Zoophycos*
8X-2, 8–10	480.28	V										Low dip, diffuse rhodochrosite (?) V
8X-2, 27–37	480.47	F		3								Fracture network, incipient SF
8X-2, 37–38	480.57	SFZ	1									Low dip
8X-2, 37–38	480.57	SF		3								
8X-2, 38–44	480.58	F		3								Fracture network, incipient SF
8X-2, 44–44	480.64	SFZ	0.5									Low dip
8X-2, 44–44	480.64	SF		3								
8X-2, 44–67	480.64	F		2								Fracture network
8X-2, 67–67	480.87	SFZ	0.5									Low dip
8X-2, 67–67	480.87	SF		3								
8X-2, 67–78	480.87	F		3								Fracture network, incipient SF
8X-2, 131–136	481.51	B					26	48	Paleomag.	352	48	*Zoophycos*
8X-6, 59–65	486.79	B					316	50	Paleomag.	277	50	Aligned bioturbations
8X-7, 7–8	487.77	SFZ	0.1									Low dip
8X-7, 7–8	487.77	SF		3								
9X-1, 61–61	489.01	B					198	62	Paleomag.	110	62	Siltstone layer
9X-2, 9–18	489.99	B					347	49				Siltstone layer
9X-2, 49–54	490.39	B					182	73				Siltstone layer
9X-2, 54–133	490.44	F		2								Fracture network, incipient SF
9X-2, 120–127	491.10	BZ					0	52	Paleomag.	281	52	CTV with brecciated contact; B or F?
9X-2, 133–137	491.23	F		3								Fracture network, incipient SF
9X-2, 137–140	491.27	SFZ	1									Moderate dip
9X-2, 137–140	491.27	SF		3								
9X-2, 140–144	491.30	F		3								Fracture network, incipient SF
9X-2, 144–145	491.34	SFZ	1									Low dip
9X-2, 144–145	491.34	SF		3								
9X-2, 145–147	491.35	F		3								Fracture network, incipient SF
9X-2, 147–149	491.37	SFZ	2									Low dip
9X-2, 147–149	491.37	SF		3								
9X-2, 149–150	491.39	F		3								Fracture network
9X-3, 0–64	491.40	F		2								Fracture network, incipient SF
9X-3, 19–21	491.59	V	0.5									Low dip, rhodochrosite V
9X-3, 66–76	492.06	B					226	40				Siltstone layer
9X-3, 82–85	492.22	B					185	30	Paleomag.	143	30	
9X-3, 103–125	492.43	F	3									Fracture network
9X-3, 125–142	492.65	BZ	2									Inclined
9X-3, 142–146	492.82	F		3								Fracture network, phillipsite alteration
9X-4, 15–30	493.05	F		2								Fracture network, incipient SF
9X-4, 30–44	493.20	F		3								Fracture network, incipient SF
9X-4, 44–46	493.34	SFZ	2									Low dip, phillipsite alteration
9X-4, 44–46	493.34	SF		3								
9X-4, 46–49	493.36	F		3								Fracture network
9X-4, 49–52	493.39	SFZ	3									Low dip, phillipsite alteration
9X-4, 49–52	493.39	SF		3								
9X-4, 52–56	493.42	F		2								Fracture network
9X-4, 82–85	493.72	B					348	22				Aligned bioturbations
9X-5, 16–32	494.56	F		2								Fracture network, phillipsite alteration
9X-5, 68–74	495.08	F		2								Fracture network
9X-5, 84–105	495.24	F		2								Fracture network
9X-5, 120–127	495.60	B					54	39				
9X-5, 139–144	495.79	B					0	25				
9X-5, 144–150	495.84	SFZ	6									Low dip
9X-5, 144–150	495.84	SF		3								
9X-6, 4–17	495.94	F		1								Fracture network
9X-6, 17–19	496.07	SFZ	2									Low dip
9X-6, 17–19	496.07	SF		2								
9X-6, 19–27	496.09	F		1								Fracture network
9X-6, 54–56	496.44	B					15	29	Paleomag.	342	29	
9X-6, 56–66	496.46	F		2								Fracture network
9X-CC, 0–8	496.56	F		1								Fracture network
9X-CC, 33–33	496.89	V	0.5				0	0				Phillipsite
10X-1, 16–22	498.26	F		3								Mm-scale lenses bounded by slickenlined F
10X-1, 22–37	498.32	SFZ	15				255	22				
10X-1, 22–37	498.32	SF		3								
10X-1, 37–38	498.47	B					255	22				Silt layer, lower boundary of SFZ
10X-1, 38–57	498.48	F		3								Fracture network, incipient SF, narrow SFZ
10X-1, 57–63	498.67	SFZ	6									Low dip

Table 16 (continued).

Core, section, interval (cm)	Depth (mbsf)	ID	Thickness (cm)	Intensity	Apparent dip (°)	Apparent trend (°)	Strike (°)	Dip (°)	Reorient.	Geo. strike (°)	Geo. dip (°)	Comments
10X-1, 57–63	498.67	SF		3								
10X-1, 66–74	498.76	SFZ	8									Low dip
10X-1, 66–74	498.76	SF		3								
10X-1, 74–103	498.84	F		3								Fracture network, incipient SF, narrow SFZ
10X-1, 103–104	499.13	SFZ	1									Low dip
10X-1, 103–104	499.13	SF		3								
10X-1, 129–132	499.39	SFZ	3		32	90						Upper boundary, thrust
10X-1, 129–132	499.39	SF		3								
10X-1, 132–139	499.42	F		3								Fracture network, incipient SF
10X-1, 138–139	499.48	SFZ	1									Low dip
10X-1, 138–139	499.48	SF		3								
10X-1, 139–147	499.49	F		3								Fracture network, incipient SF, narrow SFZ
10X-1, 147–149	499.57	SFZ	2									Low dip
10X-1, 147–149	499.57	SF		3								
10X-1, 149–150	499.59	F		2								Fracture network, incipient SF
10X-2, 0–7	499.60	F		2								Fracture network, incipient SF
10X-2, 7–10	499.67	SFZ	3									Low dip
10X-2, 7–10	499.67	SF		3								
10X-2, 10–128	499.70	F		2								Fracture network, incipient SF
10X-2, 128–130	500.88	SFZ	1									Low dip
10X-2, 128–130	500.88	SF		3								
10X-2, 130–138	500.90	F		2								Fracture network, incipient SF
10X-2, 138–145	500.98	SFZ	0.3		30	90						Normal fault
10X-2, 138–145	500.98	SF		3								
10X-2, 145–150	501.05	F		2								Fracture network, incipient SF
10X-3, 0–1	501.10	F		2								Fracture network, incipient SF
10X-3, 1–2	501.11	SFZ	0.5									Low dip
10X-3, 1–2	501.11	SF		3								
10X-3, 2–5	501.12	F		3								Fracture network
10X-3, 5–5	501.15	SFZ	0.4									Low dip
10X-3, 5–5	501.15	SF		3								
10X-3, 5–20	501.15	F		3								Fracture network, incipient SF
10X-3, 25–26	501.35	SFZ	1									Low dip
10X-3, 25–26	501.35	SF		3								
10X-3, 26–33	501.36	F		3								Fracture network, incipient SF
10X-3, 33–34	501.43	SFZ	1									Low dip
10X-3, 33–34	501.43	SF		3								
10X-3, 34–51	501.44	F		3								Fracture network, incipient SF
10X-3, 51–58	501.61	SFZ	7									Low dip
10X-3, 51–58	501.61	SF		3								
10X-3, 58–75	501.68	F		3								Fracture network, incipient SF
10X-3, 75–83	501.85	SFZ	8									Low dip
10X-3, 75–83	501.85	SF		3								
10X-3, 83–110	501.93	F		3								Fracture network, incipient SF
10X-4, 0–15	502.60	F		3								Fracture network, incipient SF
10X-4, 15–15	502.75	SFZ	0.4									Low dip
10X-4, 15–15	502.75	SF		3								
10X-4, 15–16	502.75	F		3								Fracture network, incipient SF
10X-4, 16–17	502.76	SFZ	1									Low dip
10X-4, 16–17	502.76	SF		3								
10X-4, 17–44	502.77	F		3								Fracture network, incipient SF
10X-4, 23–30	502.83	B			38	270						
10X-4, 44–45	503.04	SFZ	1									Low dip
10X-4, 44–45	503.04	SF		3								
10X-4, 45–54	503.05	F		3								Fracture network, incipient SF
10X-4, 69–81	503.29	F		3								Fracture network, incipient SF
10X-4, 81–81	503.41	SFZ	0.4									Low dip
10X-4, 81–81	503.41	SF		3								
10X-4, 81–86	503.41	F		3								Fracture network, incipient SF
10X-4, 86–101	503.46	F		1								Fracture network
10X-4, 101–114	503.61	F		3								Fracture network, incipient SF
10X-4, 114–120	503.74	SFZ	5		29	270						Upper boundary
10X-4, 114–120	503.74	SF		3								
10X-4, 120–126	503.80	F		1								Fracture network
10X-4, 126–145	503.86	F		3								Fracture network, incipient SF
10X-4, 145–145	504.05	SFZ	0.2									Low dip
10X-4, 145–145	504.05	SF		3								
10X-4, 145–150	504.05	F		1								Fracture network
10X-5, 0–3	504.10	F		3								Fracture network, incipient SF
10X-5, 3–10	504.13	SFZ	7									Low dip, Mn oxide staining
10X-5, 3–10	504.13	SF		3			60	49				
10X-5, 10–29	504.20	F		3								Fracture network, incipient SF
10X-5, 44–63	504.54	F		3								Fracture network, incipient SF
10X-5, 63–68	504.73	SFZ	5		12	270						Moderate dip
10X-5, 63–68	504.73	SF		3								
10X-5, 66–66	504.76	V	0.1									Rhodochrosite (?) V along SFZ boundary
10X-5, 68–70	504.78	F		3								Fracture network, incipient SF
10X-5, 80–95	504.90	F		3								Fracture network, incipient SF
10X-CC, 0–10	505.03	F		3								Fracture network, incipient SF
10X-CC, 10–10	505.13	SFZ	0.5									Low dip
10X-CC, 10–10	505.13	SF		3								
10X-CC, 10–14	505.13	F		3								Fracture network, incipient SF
10X-CC, 14–14	505.17	SFZ	0.5									Low dip
10X-CC, 14–14	505.17	SF		3								
10X-CC, 14–23	505.17	F		3								Fracture network, incipient SF
11X-1, 17–32	507.87	SV	0.1				0	90				Mud-filled, bifurcated, set
11X-1, 32–65	508.02	F		3								Fracture network, incipient SF
11X-1, 76–90	508.46	F		3								Fracture network, incipient SF
11X-1, 94–96	508.64	SFZ	0.3				0	28				Normal fault

Table 16 (continued).

Core, section, interval (cm)	Depth (mbsf)	ID	Thickness (cm)	Intensity	Apparent dip (°)	Apparent trend (°)	Strike (°)	Dip (°)	Reorient.	Geo. strike (°)	Geo. dip (°)	Comments
11X-1, 94–97	508.64	SF		3								
11X-1, 100–108	508.70	SFZ	8									Low dip
11X-1, 100–108	508.70	SF		3								
11X-1, 103–103	508.73	V	1		10	270						Phillipsite V along SFZ
11X-1, 108–115	508.78	F		3								Fracture network, incipient SF
11X-1, 115–132	508.85	F		2								Fracture network, incipient SF
11X-1, 132–133	509.02	SFZ	0.1									Low dip
11X-1, 132–133	509.02	SF		3								
11X-1, 133–134	509.03	F		2								Fracture network, incipient SF
11X-1, 134–134	509.04	SFZ	0.1									Low dip
11X-1, 134–134	509.04	SF		3								
11X-1, 134–150	509.04	F		2								Fracture network, incipient SF
11X-2, 0–4	509.20	F		3								Fracture network, incipient SF
11X-2, 4–12	509.24	SFZ	6									Low dip
11X-2, 4–12	509.24	SF		3								
11X-2, 18–24	509.38	SFZ	6									Low dip
11X-2, 18–24	509.38	SF		3			23	34				
11X-2, 24–30	509.44	F		3								Fracture network, incipient SF
11X-2, 30–34	509.50	SFZ	4									Low dip
11X-2, 30–34	509.50	SF		3			240	33				
11X-2, 34–38	509.54	F		3								Fracture network, incipient SF
11X-2, 38–45	509.58	SFZ	7									Low dip
11X-2, 38–45	509.58	SF		3								
11X-2, 48–50	509.68	SFZ	2									Low dip
11X-2, 48–50	509.68	SF		3								
11X-2, 50–57	509.70	F		3								Fracture network, incipient SF
11X-2, 57–59	509.77	SFZ	2									Low dip
11X-2, 57–59	509.77	SF		3								
11X-2, 59–66	509.79	F		3								Fracture network, incipient SF
11X-2, 66–75	509.86	SFZ	9									Low dip
11X-2, 66–75	509.86	SF		3			233	37				
11X-2, 75–82	509.95	F		3								Fracture network, incipient SF
11X-2, 82–82	510.02	SFZ	0.5									Low dip
11X-2, 82–82	510.02	SF		3								
11X-2, 86–87	510.06	F		3								Fracture network, incipient SF
11X-2, 87–87	510.07	SFZ	0.4									Low dip, bifurcated
11X-2, 87–87	510.07	SF		3								
11X-2, 87–89	510.07	F		3								Fracture network, incipient SF
11X-2, 89–97	510.09	SFZ	8									Low dip
11X-2, 89–97	510.09	SF		3								
11X-2, 97–99	510.17	F		3								Fracture network, incipient SF
11X-2, 99–100	510.19	SFZ	1									Low dip
11X-2, 99–100	510.19	SF		3								
11X-2, 100–102	510.20	F		3								Fracture network, incipient SF
11X-2, 102–102	510.22	SFZ	0.5									Low dip
11X-2, 102–102	510.22	SF		3								
11X-2, 102–104	510.22	F		3								Fracture network, incipient SF
11X-2, 104–104	510.24	SFZ	0.5									Low dip
11X-2, 104–104	510.24	SF		3								
11X-2, 104–106	510.24	F		3								Fracture network, incipient SF
11X-2, 106–106	510.26	SFZ	0.5									Low dip
11X-2, 106–106	510.26	SF		3								
11X-2, 106–106	510.26	F		2								Fracture network, incipient SF
11X-2, 108–108	510.28	SFZ	0.5									Low dip
11X-2, 108–108	510.28	SF		3								
11X-2, 108–109	510.28	F		3								Fracture network, incipient SF
11X-2, 109–109	510.29	SFZ	0.5									Low dip
11X-2, 109–109	510.29	SF		3								
11X-2, 109–112	510.29	F		3								Fracture network, incipient SF
11X-2, 112–113	510.32	SFZ	1									Low dip
11X-2, 112–113	510.32	SF		3								
11X-2, 113–115	510.33	F										Fracture network, incipient SF
11X-2, 115–120	510.35	SFZ	5									Low dip
11X-2, 115–120	510.35	SF		3								
11X-2, 120–126	510.40	F		3								Fracture network, incipient SF
11X-2, 126–126	510.46	SFZ	0.5									Low dip
11X-2, 126–126	510.46	SF		3								
11X-2, 126–128	510.46	F		3								Fracture network, incipient SF
11X-2, 128–150	510.48	SFZ	22									Low dip
11X-2, 128–150	510.48	SF		3								
11X-3, 0–43	510.70	F		1								Fracture network, incipient SF
11X-3, 68–68	511.38	SFZ	0.3									Low dip
11X-3, 68–68	511.38	SF		3								
11X-3, 84–108	511.54	F		3								Fracture network, incipient SF
11X-3, 108–110	511.78	SFZ	0.5									Moderate dip
11X-3, 108–110	511.78	SF		3								
11X-3, 110–120	511.80	F		3								Fracture network, incipient SF
11X-4, 0–67	512.20	F		3								Fracture network, incipient SF
11X-4, 78–104	512.98	F		3								Fracture network, incipient SF
11X-4, 104–104	513.24	SFZ	0.2									Low dip
11X-4, 104–104	513.24	SF		3								
11X-4, 104–110	513.24	F		3								Fracture network, incipient SF
11X-5, 48–50	514.18	B					229	36				Stratal disruption
11X-5, 57–63	514.27	SFZ	6									Low dip
11X-5, 57–63	514.27	SF		3								
11X-5, 66–71	514.36	B					45	30				
11X-5, 86–93	514.56	SD										
11X-5, 86–89	514.56	B					202	30				Disrupted silt layer
11X-5, 93–94	514.63	SFZ	1									Low dip

Table 16 (continued).

Core, section, interval (cm)	Depth (mbsf)	ID	Thickness (cm)	Intensity	Apparent dip (°)	Apparent trend (°)	Strike (°)	Dip (°)	Reorient.	Geo. strike (°)	Geo. dip (°)	Comments
11X-5, 93–94	514.63	SF		3								
11X-5, 94–98	514.64	F		3								Fracture network, incipient SF
11X-5, 98–100	514.68	SFZ	2									Low dip
11X-5, 98–100	514.68	SF		3								
11X-5, 100–104	514.70	F		3								Fracture network, narrow SFZ
11X-5, 104–106	514.74	SFZ	2									Low dip
11X-5, 104–106	514.74	SF		3								
11X-5, 110–111	514.80	SD										
11X-CC, 0–25	514.87	SD										
11X-CC, 25–25	515.12	SFZ	0.3									Low dip
11X-CC, 25–25	515.12	SF		3								
12X-1, 15–62	517.55	SD										
12X-1, 53–51	517.93	B					276	18	Paleomag.	155	18	
12X-1, 62–70	518.02	SFZ	8									Low dip
12X-1, 62–70	518.02	SF		3								
12X-1, 70–76	518.10	SD										
12X-1, 76–87	518.16	SFZ	11									Low dip
12X-1, 76–87	518.16	SF		3								
12X-1, 90–92	518.30	SFZ	2									Low dip
12X-1, 90–92	518.30	SF		3								
12X-1, 106–114	518.46	SFZ	8									Low dip
12X-1, 106–114	518.46	SF		3								
12X-1, 114–120	518.54	SD										
12X-1, 120–132	518.60	SFZ	12									Low dip
12X-1, 120–132	518.60	SF		3								
12X-1, 137–146	518.77	SFZ	9		20	270						
12X-1, 137–146	518.77	SF		3								
12X-2, 3–120	518.93	FO										Several FO and Fr after extensional SD
12X-2, 10–10	519.00	SFZ	0.4									Low dip, folded
12X-2, 10–10	519.00	SF		3								
12X-2, 80–85	519.70	SFZ	5									Low dip
12X-2, 80–85	519.70	SF		3								
12X-2, 118–120	520.08	SFZ	1.5									Moderate dip, thrust
12X-2, 118–120	520.08	SF		3								
12X-2, 134–135	520.24	B					234	43				Silt layer at hanging wall of Fr
12X-2, 135–140	520.25	Fr					200	65				Offset 5 cm on core face
12X-2, 140–150	520.30	SFZ	10									Low dip
12X-2, 140–150	520.30	SF		3			201	48				
12X-3, 0–16	520.40	SD										
12X-3, 5–8	520.45	B					186	39				Disrupted silt layer
12X-3, 12–15	520.52	B					135	25				Disrupted silt layer
12X-3, 16–20	520.56	SFZ	4									Low dip
12X-3, 19–19	520.59	SF		3			219	57				
12X-3, 20–39	520.60	SD										
12X-3, 57–59	520.97	SFZ	2									Low dip
12X-3, 57–59	520.97	SF		3								
12X-3, 59–68	520.99	B					206	11				Turbidite
12X-3, 67–70	521.07	SFZ	3									Low dip
12X-3, 67–70	521.07	SF		3								
12X-3, 81–81	521.21	SFZ	0.1									Low dip
12X-3, 81–81	521.21	SF		3								
12X-3, 82–82	521.22	B					209	16				
12X-3, 90–90	521.30	B					293	17				
12X-3, 101–101	521.41	B					63	21				
12X-3, 109–114	521.49	SFZ	5									Low dip
12X-3, 109–114	521.49	SF		3								
12X-3, 114–122	521.54	SD										
12X-3, 137–150	521.77	SFZ	13									Low dip
12X-3, 145–145	521.85	SF					330	39				
12X-4, 0–3	521.90	SD										
12X-4, 3–11	521.93	SFZ	8									Low dip
12X-4, 3–11	521.93	SF		3								
12X-4, 68–68	522.58	B					166	12				
12X-4, 90–92	522.80	SFZ	2									Low dip
12X-4, 92–92	522.82	SF					288	47				
12X-5, 1–1	523.41	SFZ	0.1									Low dip
12X-5, 1–1	523.41	SF		3								
12X-5, 4–7	523.44	SFZ	3									Low dip
12X-5, 4–7	523.44	SF		3								
12X-5, 59–61	523.99	SFZ	2									Low dip
12X-5, 59–61	523.99	SF					260	40				
12X-5, 61–61	524.01	B					23	15	Paleomag.	210	15	
12X-5, 80–80	524.20	B					187	16				
12X-5, 117–117	524.57	B					40	18				
12X-5, 120–120	524.60	B					218	19				
12X-5, 121–125	524.61	SFZ	4									Low dip
12X-5, 122–122	524.62	SF					310	23				
12X-5, 140–144	524.80	Fn					331	39				
12X-5, 145–145	524.85	B					59	15				
12X-5, 148–148	524.88	SFZ	0.2									Low dip
12X-5, 148–148	524.88	SF		3								
12X-6, 14–14	525.04	Fn					182	80				
12X-6, 45–45	525.35	B					270	2				
12X-CC, 21–22	525.94	SFZ	0.1									Low dip
12X-CC, 21–22	525.94	SF		3								
12X-CC, 32–32	526.05	SFZ	0.2									Low dip
12X-CC, 32–32	526.05	SF		3								
13X-1, 23–25	527.03	B					163	20				
13X-1, 78–87	527.58	SFZ	9									Low dip

Table 16 (continued).

Core, section, interval (cm)	Depth (mbsf)	ID	Thickness (cm)	Intensity	Apparent dip (°)	Apparent trend (°)	Strike (°)	Dip (°)	Reorient.	Geo. strike (°)	Geo. dip (°)	Comments
13X-1, 78–78	527.58	SF		3	0	0						
13X-1, 110–115	527.90	P										Plastically deformed gray mudstone
13X-1, 120–124	528.00	P										Plastically deformed gray mudstone
13X-1, 115–115	527.95	SFZ	0.3				33	21				
13X-1, 115–115	527.95	SF		3			12	45				
13X-1, 131–131	528.11	SFZ	0.5									Low dip
13X-1, 131–131	528.11	SF		3								
13X-1, 145–147	528.25	SFZ	2									Low dip
13X-1, 145–147	528.25	SF		3								
13X-2, 8–8	528.38	SFZ	0.1									Low dip
13X-2, 8–8	528.38	SF		3								
13X-2, 29–36	528.59	SFZ	2									Moderate to steep dip
13X-2, 29–36	528.59	SF		3								
13X-2, 35–41	528.65	B					349	15				
13X-2, 92–92	529.22	SFZ	0.2									Low dip
13X-2, 92–92	529.22	SF		3								
13X-2, 93–117	529.23	B					0	24				
13X-2, 117–128	529.47	SFZ	11									Low dip
13X-2, 118–118	529.48	SF		3			233	15				
13X-3, 86–86	530.66	B					329	6				
13X-3, 101–101	530.81	B					212	9				Upright
13X-3, 132–150	531.12	B					333	19				
13X-4, 11–39	531.41	B										
13X-4, 39–51	531.69	B					90	5				Fissility
13X-4, 81–81	532.11	B					180	5				
13X-4, 95–100	532.25	SFZ	0.1									Moderate dip, normal fault
13X-4, 95–100	532.25	SF		3								
13X-4, 105–105	532.35	B						0				
13X-5, 5–5	532.85	B					274	13	Paleomag.	213	13	
13X-5, 24–24	533.04	B					52	19				
13X-6, 6–6	534.36	SFZ	0.1									Low dip
13X-6, 6–6	534.36	SF		3								
13X-6, 35–35	534.65	B					246	10				
13X-6, 43–43	534.73	SFZ	0.5									Low dip
13X-6, 43–43	534.73	SF		3								
13X-6, 128–129	535.58	SFZ	1									Low dip
13X-6, 128–129	535.58	SF		3								
13X-7, 33–33	536.13	B					213	18				
14X-1, 48–48	536.58	B					108	6	Paleomag.	8	6	
14X-1, 98–100	537.08	Fr					0	30				Offset 6 mm on core face
14X-1, 99–99	537.09	B					0	0				
14X-1, 58–58	536.68	B					324	13				
14X-1, 105–105	537.15	B					348	14				
14X-1, 144–147	537.54	SFZ	0.1				137	36				
14X-1, 144–147	537.54	SF		3								
14X-2, 71–71	538.31	B					26	11				
14X-2, 115–117	538.75	B					322	22				Upright
14X-3, 35–36	539.45	B					270	12				
14X-3, 37–38	539.47	SFZ	0.3		8	270						
14X-3, 37–38	539.47	SF		3								
14X-3, 49–49	539.59	B					261	12				
14X-3, 64–64	539.74	SFZ	0.3		1	270						
14X-3, 64–64	539.74	SF		3								
14X-3, 87–87	539.97	B					238	9				
14X-3, 104–105	540.14	SFZ	0.5		8	90						
14X-3, 104–105	540.14	SF		3	8							
14X-4, 27–28	540.87	B					326	11				
14X-4, 47–47	541.07	B			3	90						
14X-4, 63–63	541.23	B					230	8				
14X-4, 68–70	541.28	SFZ	2									Low dip
14X-4, 68–70	541.28	SF		3								
14X-4, 86–86	541.46	B					270	10				
14X-4, 95–99	541.55	B					25	19				
14X-4, 126–126	541.86	B			3	90						
14X-4, 137–147	541.97	B					40	15				
14X-5, 11–11	542.21	B			8	270						
14X-5, 42–44	542.52	B					20	22				
14X-5, 48–48	542.58	SFZ	0.3		1	90						
14X-5, 48–48	542.58	SF		3								
14X-5, 54–54	542.64	B					111	21				
14X-5, 78–79	542.88	B					29	10				
14X-5, 90–94	543.00	B					195	19	Paleomag.	175	19	
14X-5, 94–98	543.04	B					0	2				
14X-5, 101–105	543.11	Fn					180	71				
14X-6, 5–8	543.65	B					0	0				
14X-6, 12–12	543.72	B					40	8				
14X-6, 24–26	543.84	B					128	17				
14X-6, 26–28	543.86	B					32	19				
14X-6, 116–117	544.76	B					331	10				
14X-6, 135–136	544.95	B					270	15				
14X-CC, 28–29	545.38	B					360	11				
14X-CC, 30–32	545.40	B					343	14				
14X-CC, 32–34	545.42	B					214	7				
14X-CC, 34–35	545.44	B					121	12				
14X-CC, 35–37	545.45	B					270	8				
15X-1, 45–46	545.85	B			5	90						
15X-1, 47–47	545.87	SFZ	0.3									Low dip
15X-1, 47–47	545.87	SF		3								
15X-1, 49–49	545.89	B					40	18				

Table 16 (continued).

Core, section, interval (cm)	Depth (mbsf)	ID	Thickness (cm)	Intensity	Apparent dip (°)	Apparent trend (°)	Strike (°)	Dip (°)	Reorient.	Geo. strike (°)	Geo. dip (°)	Comments
15X-1, 52–52	545.92	B					14	20				
15X-1, 83–83	546.23	B					26	11				
15X-1, 87–87	546.27	B					212	19				
15X-1, 90–90	546.30	B					28	17				
15X-1, 93–98	546.33	B					318	15				
15X-1, 102–102	546.42	B					112	11				
15X-1, 107–107	546.47	B					219	13				
15X-1, 111–111	546.51	B					45	18				
15X-1, 116–116	546.56	B					222	15				
15X-1, 121–121	546.61	B					347	13				
15X-1, 141–141	546.81	B					180	16				
15X-1, 144–144	546.84	B					45	19				
15X-2, 23–30	547.13	B					0	3	Paleomag.	355	3	
15X-2, 31–31	547.21	B						0				
15X-2, 58–58	547.48	B					119	16				
15X-2, 61–61	547.51	B					105	28				
15X-2, 87–87	547.77	B					21	14				
15X-2, 94–97	547.84	B					53	13				
15X-2, 98–102	547.88	B					45	14				
15X-2, 126–126	548.16	B					90	10				
15X-3, 8–8	548.48	B					282	14				
15X-3, 25–25	548.65	B					302	16				
15X-3, 57–57	548.97	B					90	5				
15X-3, 59–59	548.99	B					329	12				
15X-3, 66–66	549.06	B					40	17				
15X-3, 83–83	549.23	B					90	12				
15X-3, 109–109	549.49	B					21	14				
15X-3, 118–118	549.58	B					301	15				
15X-4, 10–10	550.00	B					9	6				
15X-4, 25–35	550.15	B					180	12				
15X-4, 43–50	550.33	B					180	14				
15X-4, 55–60	550.45	B					118	19				
15X-4, 87–87	550.77	B						0				
15X-4, 107–107	550.97	B					90	10				
15X-4, 122–122	551.12	B					73	10				
15X-5, 7–14	551.47	B					312	12				
15X-5, 45–45	551.85	B					82	20				
15X-5, 64–65	552.04	SFZ	0.2									Low dip
15X-5, 64–65	552.04	SF		3								
15X-6, 11–11	553.01	B						0				
15X-6, 37–37	553.27	B					270	15				
15X-6, 42–48	553.32	B					180	5				
15X-7, 36–36	554.76	B					32	9				
15X-CC, 12–12	555.00	B					55	12				
15X-CC, 16–20	555.04	SFZ	1									Moderate dip
15X-CC, 16–20	555.04	SF		3								
16X-1, 41–41	555.21	B					323	5				
16X-1, 95–95	555.75	B					191	15				
16X-2, 47–47	556.77	B					209	16				Color change
16X-2, 111–111	557.41	B					4	14				
16X-3, 55–55	558.35	B					292	13				
16X-3, 84–84	558.64	B					344	15				
16X-3, 112–112	558.92	B					205	5				
16X-4, 17–17	559.47	B					174	10				
16X-4, 52–52	559.82	SFZ	0.3									Low dip
16X-4, 52–52	559.82	SF		3								
16X-4, 88–88	560.18	B					294	12				
16X-4, 138–138	560.68	B					40	17				
16X-5, 8–8	560.88	B					220	18				
16X-5, 46–46	561.26	B					11	10	Paleomag.	326	10	
16X-5, 72–72	561.52	B					284	12				
16X-5, 114–114	561.94	B					16	15				
16X-6, 1–1	562.31	SFZ	0.2									Low dip
16X-6, 1–1	562.31	SF		3								
16X-6, 39–39	562.69	B					149	17				
16X-6, 41–42	562.71	SFZ	1				225	7				
16X-6, 41–42	562.71	SF		3								
16X-6, 74–74	563.04	B					104	16				
16X-6, 97–97	563.27	B					120	14				
16X-7, 12–12	563.42	B					323	10				
16X-7, 46–46	563.76	B					124	11				
16X-CC, 38–39	564.29	SFZ	1									Low dip
16X-CC, 38–39	564.29	SF		3								
17X-1, 6–6	564.16	B					43	17				
17X-1, 111–111	565.21	B					270	3				
17X-2, 58–59	566.18	B					342	9				
17X-2, 88–88	566.48	B					90	7				
17X-3, 48–48	567.58	B					45	7				
17X-3, 130–130	568.40	B					166	12				
17X-4, 27–27	568.87	B					192	14				
17X-4, 76–76	569.36	B					189	13				
17X-4, 96–96	569.56	SFZ	0.3									Low dip
17X-4, 96–96	569.56	SF		3								
17X-4, 103–109	569.63	Fn					222	50				Offset 2 cm
17X-4, 141–142	570.01	Fr			90	45						
17X-4, 143–143	570.03	B					343	10				
17X-5, 57–57	570.67	B					270	6				
17X-5, 111–111	571.21	B					206	11				
17X-6, 50–50	572.10	B					207	4				

Table 16 (continued).

Core, section, interval (cm)	Depth (mbsf)	ID	Thickness (cm)	Intensity	Apparent dip (°)	Apparent trend (°)	Strike (°)	Dip (°)	Reorient.	Geo. strike (°)	Geo. dip (°)	Comments
17X-6, 90–90	572.50	SFZ	0.2									Low dip
17X-6, 90–90	572.50	SF		3								
17X-7, 18–18	573.28	B					260	11				
18X-1, 11–11	573.41	B					225	17				
18X-1, 86–86	574.16	B					49	9				
18X-2, 18–18	574.98	B					112	11				
18X-2, 95–95	575.75	B					99	6				
18X-3, 27–27	576.57	B					99	6				
18X-3, 80–80	577.10	B					0	5				
18X-4, 18–21	577.98	Fn					339	50				Healed
18X-4, 48–48	578.28	B					158	5				
18X-5, 24–25	579.54	SFZ	1									Low dip
18X-5, 24–25	579.54	SF		3								
18X-5, 31–31	579.61	B					212	19				
18X-5, 83–86	580.13	SFZ	0.2									Moderate dip
18X-5, 83–86	580.13	SF		3								
18X-5, 97–97	580.27	B					83	8				
18X-6, 50–50	581.30	B					304	11				
19X-1, 4–8	582.84	B					327	21				
19X-1, 4–8	582.84	Fn					174	65				Offset 5 mm on core face
19X-1, 19–21	582.99	B					57	18				
19X-1, 19–21	582.99	Fn			50	270						Offset 11 mm on core face
19X-1, 28–33	583.08	B					0	20				
19X-1, 28–33	583.08	Fn					213	52				Offset 35 mm on core face
19X-1, 33–36	583.13	B					180	35				
19X-1, 39–42	583.19	B					64	16				
19X-1, 43–48	583.23	B					222	12				
19X-1, 72–77	583.52	SFZ	5									Low dip
19X-1, 72–77	583.52	SF		3								
19X-1, 79–81	583.59	B					214	16				
19X-1, 81–83	583.61	B					210	8				
19X-1, 84–86	583.64	B					9	13				
19X-1, 97–100	583.77	B					45	15				
19X-1, 106–106	583.86	B					206	16				
19X-1, 122–122	584.02	B					64	11				
19X-1, 127–132	584.07	Fn					233	33				
19X-1, 134–138	584.14	B					231	13				
19X-1, 142–142	584.22	B					0	1				
19X-2, 11–30	584.41	B					56	16				
19X-2, 32–32	584.62	B					209	10				
19X-2, 43–43	584.73	B					0	12				
19X-2, 65–65	584.95	B					25	16				
19X-2, 74–74	585.04	B					20	12				
19X-2, 88–91	585.18	B					238	20				
19X-2, 105–105	585.35	B					166	8				
19X-2, 109–111	585.39	B					29	10				
19X-2, 119–122	585.49	B					34	11				
19X-2, 123–123	585.53	SFZ	0.5									Low dip
19X-2, 123–123	585.53	SF		3								
19X-2, 126–129	585.56	B					174	10				
19X-2, 141–141	585.71	B					270	10				
19X-2, 143–146	585.73	B					135	11				
19X-3, 8–10	585.88	B					270	5				
19X-3, 14–18	585.94	B					0	11				
19X-3, 30–32	586.10	B					206	13				
19X-3, 36–38	586.16	B					315	11				
19X-3, 40–41	586.20	B					153	7				
19X-3, 43–46	586.23	B					26	11				
19X-3, 50–52	586.30	B					0	6				
19X-3, 80–83	586.60	B					56	16				
19X-3, 90–92	586.70	B					180	12				
19X-3, 103–105	586.83	B					208	12				
19X-3, 113–115	586.93	B					180	1				
19X-3, 123–123	587.03	B					90	22				
19X-3, 139–150	587.19	B					225	8				
19X-4, 10–12	587.40	B					90	10				
19X-4, 25–27	587.55	B					52	19				
19X-4, 34–39	587.64	B					210	8				
19X-4, 46–50	587.76	B					35	9				
19X-4, 64–66	587.94	B					231	14				
19X-4, 66–68	587.96	Fn			42	90						Offset 5 mm on core face
19X-4, 66–68	587.96	B					180	1				
19X-4, 78–78	588.08	B					206	11				
19X-4, 79–82	588.09	B					288	16				
19X-4, 87–89	588.17	B					146	4				
19X-4, 102–106	588.32	B					299	10				
19X-5, 7–11	588.87	B					355	22				
19X-5, 7–11	588.87	Fn			45	270						Offset 9 mm on core face
19X-5, 11–12	588.91	B					220	8				
19X-5, 25–25	589.05	B					132	12				
19X-5, 40–40	589.20	B					274	15				
19X-5, 48–50	589.28	B					315	7				
19X-5, 56–62	589.36	B					132	13				
19X-5, 63–66	589.43	B					281	10				
19X-5, 81–81	589.61	B					112	5				
19X-5, 83–90	589.63	B					28	12				
19X-5, 112–112	589.92	B					153	13				
19X-5, 113–113	589.93	B					152	12				

Table 16 (continued).

Core, section, interval (cm)	Depth (mbsf)	ID	Thickness (cm)	Intensity	Apparent dip (°)	Apparent trend (°)	Strike (°)	Dip (°)	Reorient.	Geo. strike (°)	Geo. dip (°)	Comments
19X-5, 120–120	590.00	B					130	17				
19X-5, 126–126	590.06	B					296	22				
19X-5, 132–132	590.12	B					0	10				
19X-5, 139–145	590.19	B					180	0				
19X-6, 3–8	590.33	B					145	12				
19X-6, 8–14	590.38	B					290	22				
19X-6, 23–26	590.53	B					244	11				
19X-6, 26–30	590.56	Fn			42	90						Offset 1 cm on core face
19X-6, 29–40	590.59	B					17	10				
19X-6, 67–72	590.97	B					294	12				
19X-6, 72–74	591.02	B					180	9				
19X-6, 89–97	591.19	B					69	21				
19X-6, 117–117	591.47	B					309	13				
19X-6, 128–128	591.58	B					270	3				
19X-6, 146–146	591.76	B					145	9				
19X-7, 20–29	592.00	SFZ	9									Low dip
19X-7, 20–29	592.00	SF		3								
19X-CC, 1–1	592.27	B					270	5				
19X-CC, 16–16	592.42	B					214	4				

Notes: ID = structural identifier; thickness = thickness of structure measured normal to boundaries on the cut core face; intensity = intesity of development of scaly fabric. For more detailed information see "Explanatory Notes" chapter (this volume). Intensity is indicated by a 3-point numerical scale: 1 (incipient), 2 (moderate), and 3 (intense).

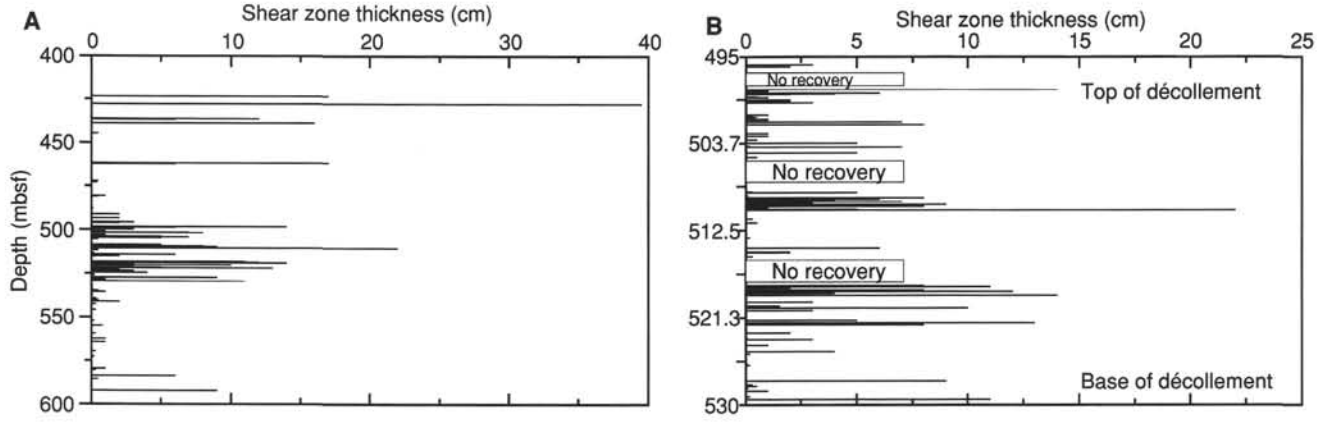

Figure 21. **A.** Frequency and thickness of intense scaly fabric zones (i.e., shear zones) plotted vs. depth, Hole 948C, entire cored interval (420–592 mbsf). **B.** Frequency and thickness of scaly fabric zones, décollement region only.

we obtained a large number of measurements, the foliation is oblique to both bedding and shear-zone boundaries (Table 16).

We interpreted the scaly fabric, stratal disruption, and locally intense fracturing of the décollement domain as the expression of a brittle-ductile shear zone. The zone is 31 m thick, but has a core of intense shear-induced fabric 15 to 20 m thick, with a sharp boundary at the top and a gradational boundary at the bottom. Our interpretation of the thickness of this domain agrees reasonably well with that of the structural geologists on Leg 110 at Site 671. They reported the top of the décollement at very nearly the same depth in meters below seafloor, but described a 40-m-thick zone (Mascle, Moore, et al., 1988). It is unclear from the Leg 110 *Initial Reports* volume whether the discrepancy in thicknesses is attributable to actual differences in the structures recovered, to the more complete core recovery in Hole 948C, or to differences in the definition of features, given the gradational lower boundary.

Domain III: Underthrust Section (529–592 mbsf)

Beginning in Section 156-948C-13X-3 (529.8 mbsf) and continuing to the total depth of 592 mbsf, the bedding in the claystone is consistently shallowly inclined (Figs. 17 and 26) and shows little evidence of deformation, except in a few narrow intervals (Fig. 16). This domain comprises well-bedded hemipelagic sediments and distal turbidites, the same lithology as in the lower part of the décollement, and has higher density than that of the prism (see "Physical Properties" and "Logging" sections, this chapter). The claystones show some fissility; that is, they have a bedding-parallel parting. Beds in this domain incline consistently from 0° to 20°, and those in which the orientation could be determined paleomagnetically strike about north-south, parallel to the deformation front.

Immediately below the décollement, in Sections 156-948C-13X-3 and -13X-4, the sediments appear to have no structures whatsoever and lack even the fissility and weak fracturing that is characteristic farther downhole in this domain. Cores 156-948C-14X through -19X exhibit several very thin, intensely scaly zones, never more than 0.5 to 1 cm thick, with sharply defined boundaries (Fig. 27). These zones contrast with all surrounding material and cannot easily be explained as drilling induced. In the last section of the hole, 156-948C-19X-7, a zone of intense scaly fabric several tens of centimeters thick is interpreted as a noteworthy low-angle shear zone of unknown sense and magnitude of displacement.

Cores 156-948C-18X and -19X exhibit a number of small normal faults, with displacements of a few millimeters to a few centimeters, which apparently were not drilling induced (many other normal faults that are present in these cores cut across drill biscuits and must be artifacts). The normal faults are associated with coarser intervals, and we interpreted them as early structures, possibly predating passage of the sediment under the deformation front. The faults may be related to compaction before the package entered the trench, to downgoing

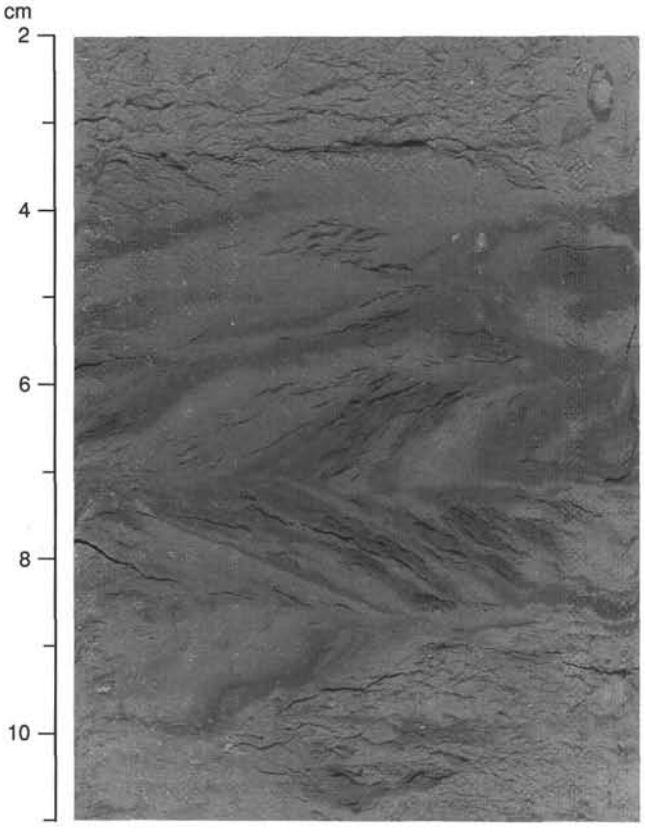

Figure 22. Detail of interval 156-948C-10X-5, 2–11 cm, intense scaly fabric with manganese staining of foliation, dipping at a moderate angle. The fabric has been rotated by biscuiting along horizontal planes into several different orientations in the core face.

plate flexure, or to loading by the prism. Similar minor extensional features were described in the reference section at Site 672, seaward of the deformation front (Mascle, Moore, et al., 1988).

The foregoing observations suggest that this domain has experienced no folding and probably only minor faulting during underthrusting beneath the accretionary prism. Mesoscopically, the underthrust section appears to have experienced mainly vertical compaction from burial and/or loading by the prism and little horizontal strain.

Magnetic Anisotropy

Anisotropy of magnetic susceptibility (AMS) measurements of discrete samples provide additional information about the geometry of structures and finite-strain orientations at this site. The orientations of the principal AMS axes are sensitive indicators of the orientations of the principal strains in deformed sediments (Borradaile, 1991), and in certain cases, finite-strain magnitudes may also be obtained from AMS results. The samples measured were collected for shipboard paleomagnetic analysis, so many of the AMS data from the XCB cores have been reoriented into true geographic coordinates using the paleomagnetic results. All the reoriented AMS data from Domain I (Fig. 28) have maximum susceptibility axes that are well-grouped about a mean of 349°/18° (declination/inclination), with a precision parameter (k) = 65.7 and confidence limits (α_{95}) = 4.8°. From 420 to 478 mbsf, the minimum susceptibility axes are also well-clustered, with a mean of 260°/1.2° with k = 17 and α_{95} = 12.1° (Fig. 28A). From 478 to 498 mbsf in Unit I, the minimum susceptibility axes change orientation from trending east-west with shallow inclinations in samples above 492 mbsf, to south-trending, steeply inclined orientations in samples from 492 to 497 mbsf (Fig. 28B). The steeply inclined minimum susceptibility axes match the orientations of the minimum

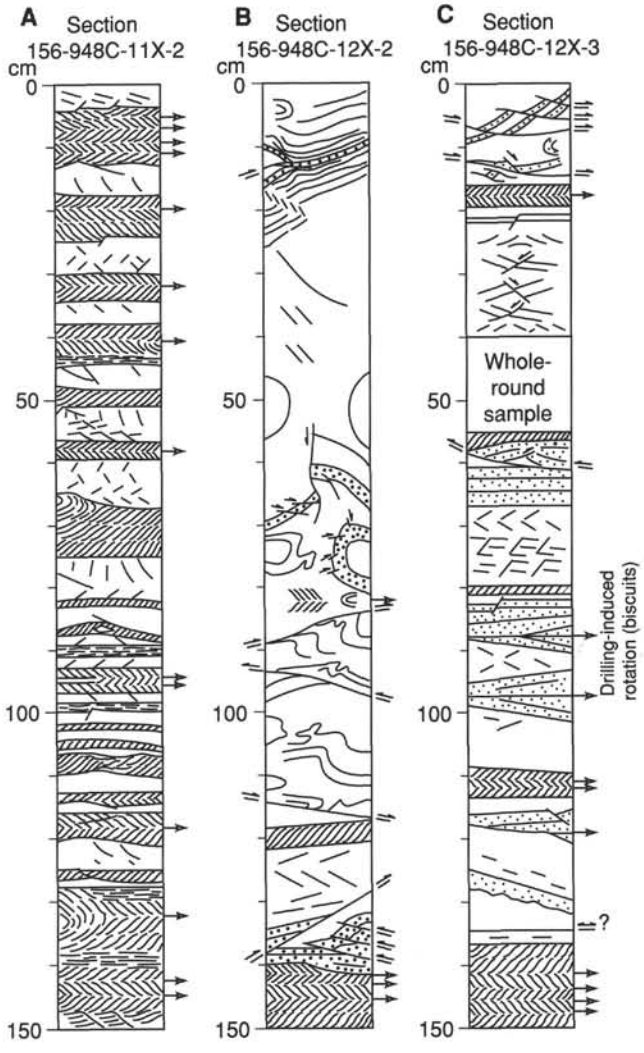

Figure 23. Representative sketches of the structures within the décollement zone, Hole 948C. **A.** Meter-scale fault zone defined by closely spaced shear zones having intense scaly fabric alternating with fractured intervals, Section 156-948C-11X-2. **B.** Folds and reverse faults, postdating extensional stratal disruption, Section 156-948C-12X-2 (see photo, Fig. 25). **C.** Spaced shear zones bounding intervals having stratal disruption or intact sediments, Section 156-948C-12X-3 (see photo, Fig. 24). Note that disproportional width of core drawings introduces slight distortion.

susceptibility axes of samples from the décollement zone (Fig. 28C). Below the décollement, the minimum susceptibility axes are near vertical, and match the orientations of bedding poles measured in the underthrust domain (Fig. 28D; compare with Fig. 26B). The shapes of the susceptibility ellipsoids are predominantly triaxial to weakly oblate in the samples from 421 to 478 mbsf (Fig. 29A). Samples from 478 to 498 mbsf have triaxial to prolate susceptibility ellipsoid shapes (Fig. 29B). Within the décollement, the samples have susceptibility ellipsoid shapes that are weakly oblate to triaxial (Fig. 29C). The underthrust domain samples (530–591 mbsf) have predominantly oblate susceptibility ellipsoid shapes (Fig. 29D).

Summary

The cored interval from 420 to 592 mbsf in Hole 948C presents an excellent section through the active décollement of the Barbados accretionary prism. Three domains are evident in the cores. The first is an upper domain of accreted deep-water sediments (420–498 mbsf),

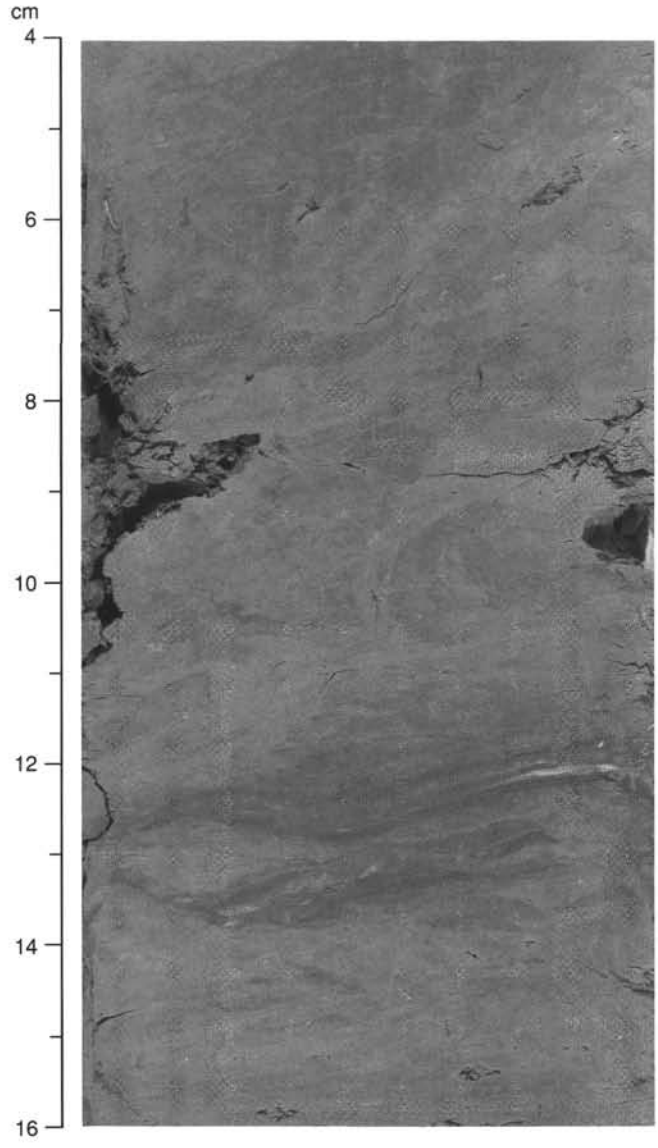

Figure 24. Detail of interval 156-948C-12X-3, 4–16 cm, illustrating stratal disruption and scaly fabric within lithologic Unit III sediments of the décollement domain (see sketch, Fig. 23C).

with variable strike of bedding, predominantly near north-south (averaging 347°), and generally dipping 40°–60°. We identified several intervals having shear zones, the most important between 423 and 428, 436 and 439, and 461 and 462 mbsf. The second is a 30°-dipping thrust zone, while the others have low dips. At 425 and 472 mbsf, rhodochrosite veins fill the scaly foliation. A few brecciated zones occur at 492 mbsf, immediately above the décollement. From 498 to 529 mbsf, zones of semipenetrative scaly fabric, interleaved with zones of fracture networks or stratal disruption and structurally intact intervals, delineate the décollement zone. This brittle-ductile shear zone coincides with the lithologic boundary between pelagic clays above and hemipelagic and turbidites below, and shear-induced fabrics are developed in both lithologies. The upper half of the décollement zone is locally stained with black manganese-rich diagenetic material, which, in one case, is foliation-parallel. The zone of intense scaly fabric gradually disappears between 520 and 529 mbsf, and bedding dips become shallow to subhorizontal. The interval from 529 to the total depth of 592 mbsf is the third domain—the underthrust turbidite and hemipelagic section. Bedding in this domain dips shallowly and strikes generally north-south. Little deformation is evident,

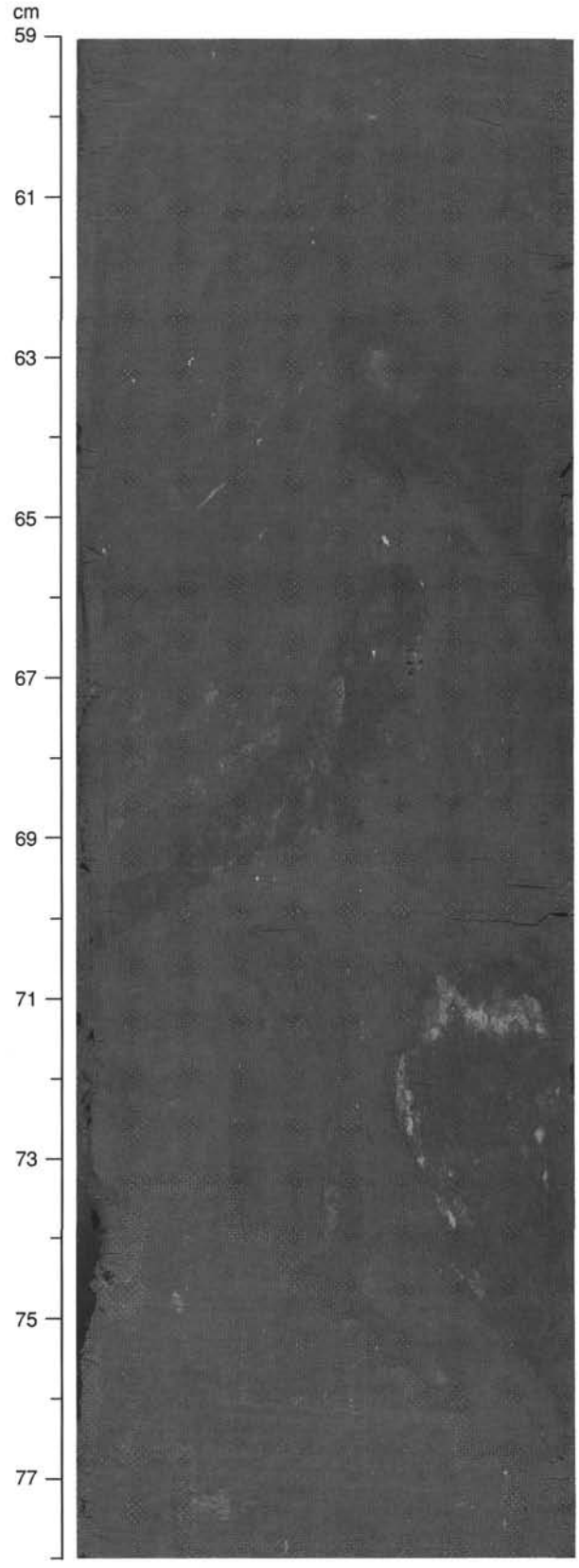

Figure 25. Folding within décollement domain, interval 156-948C-12X-2, 59–78 cm (see sketch, Fig. 23B).

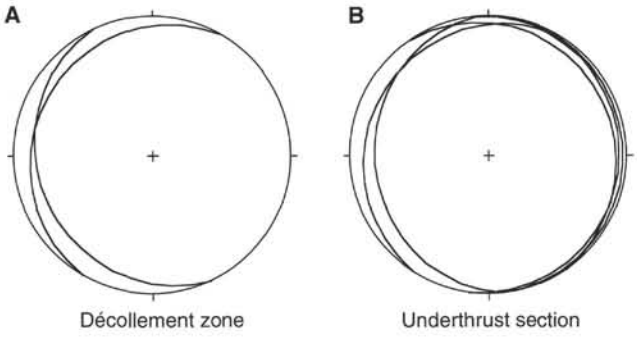

Figure 26. Bedding orientations from the décollement (**A**), and from the underthrust domains (**B**), Hole 948C, oriented into the geographic reference frame using paleomagnetic remanence directions.

Figure 27. Interval exhibiting a very thin zone of scaly fabric, interval 156-948C-16X-6, 40–42 cm.

except for a few very thin scaly zones, a 10-cm or thicker shear zone at the bottom of the hole (592 mbsf), and minor extensional faults.

BIOSTRATIGRAPHY

A biostratigraphic summary of Hole 948C for nannofossils, radiolarians, and foraminifers is given in Figure 30. The biostratigraphy described here is based on shipboard investigations.

Calcareous Nannofossils

Hole 948C was drilled without coring from 9.5 down to 420.80 mbsf. The uppermost mud-line core is of Pleistocene age. Sediments of late Miocene and late Oligocene age are found above and below the décollement respectively. Floras are moderately well preserved, with the exception of those in the Miocene interval found near the décollement, which show significant dissolution.

Sections 156-948C-1H-1 through -1H-4 belong to the late Pleistocene *Gephyrocapsa oceanica* Zone on the basis of the absence of both *Emiliania huxleyi* and *Pseudoemiliania lacunosa.* Samples 156-948C-1H-5, 140–141 cm, to -CC were assigned to the early Pleistocene *Pseudoemiliania lacunosa* Zone, owing to the presence of *P. lacunosa* without the occurrence of older markers.

Core 156-948C-2X through Sample 156-948C-4X-2, 25–26 cm, are barren.

Sample 156-948C-4X-2, 134–135 cm, has a poorly to moderately preserved assemblage, but forms in Samples 156-948C-4X-3, 30–31 cm, through 156-948C-5X-5, 45–46 cm, are well preserved. This interval contains *Discoaster berggrenii,* but lacks *Amaurolithus primus.* Therefore, it has been placed in Subzone CN9a. However, *Discoaster surculus,* another marker for the base of Subzone CN9a, was not found. *Minylitha convallis* is common.

Samples 156-948C-5X-5-CC through -6X-1, 131–132 cm, do not contain any of the above marker species nor other age-diagnostic species. Possible *Discoaster neohamatus* forms are broken and could not be identified with certainty. The interval may belong to Subzone CN8a because of the absence of both *Discoaster hamatus* and *D.*

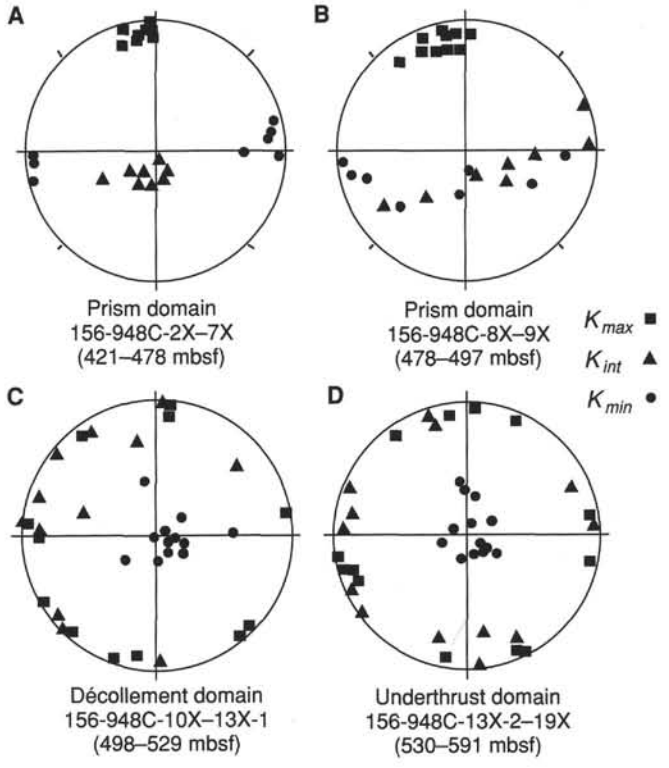

Figure 28. **A–D.** Lower hemisphere, equal-area projections of principal susceptibility axes of samples from Hole 948C reoriented into geographic coordinates using paleomagnetic results. Solid circles = minimum axes; solid triangles = intermediate axes; solid squares = maximum axes. See text for discussion.

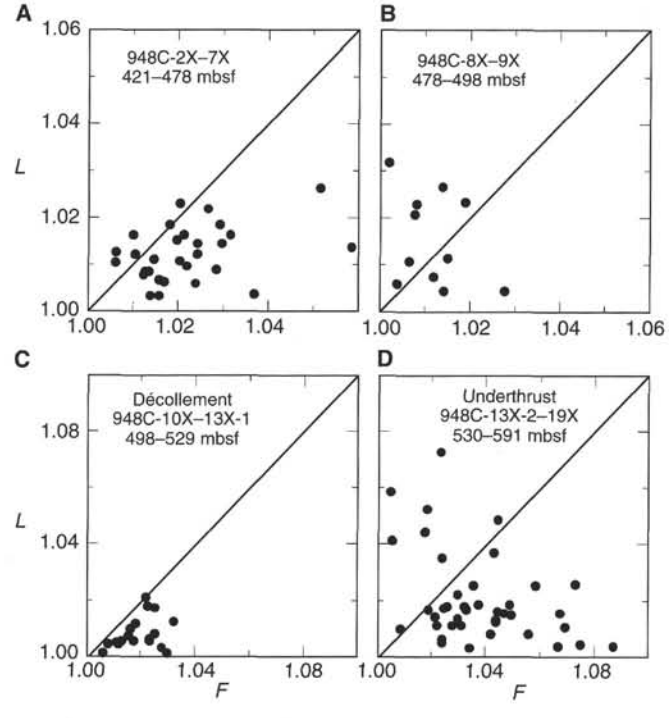

Figure 29. **A–D.** Flinn-type diagrams of the shapes of the susceptibility ellipsoids, Hole 948C. The vertical axes are values of magnetic lineation ($L = K_{max}/K_{int}$), and the horizontal axes are magnetic foliation ($F = K_{int}/K_{min}$). Points plotting in the fields above and below the diagonal line correspond to prolate and oblate ellipsoid shapes, respectively. Points on or near the line correspond to a triaxial ellipsoid shape.

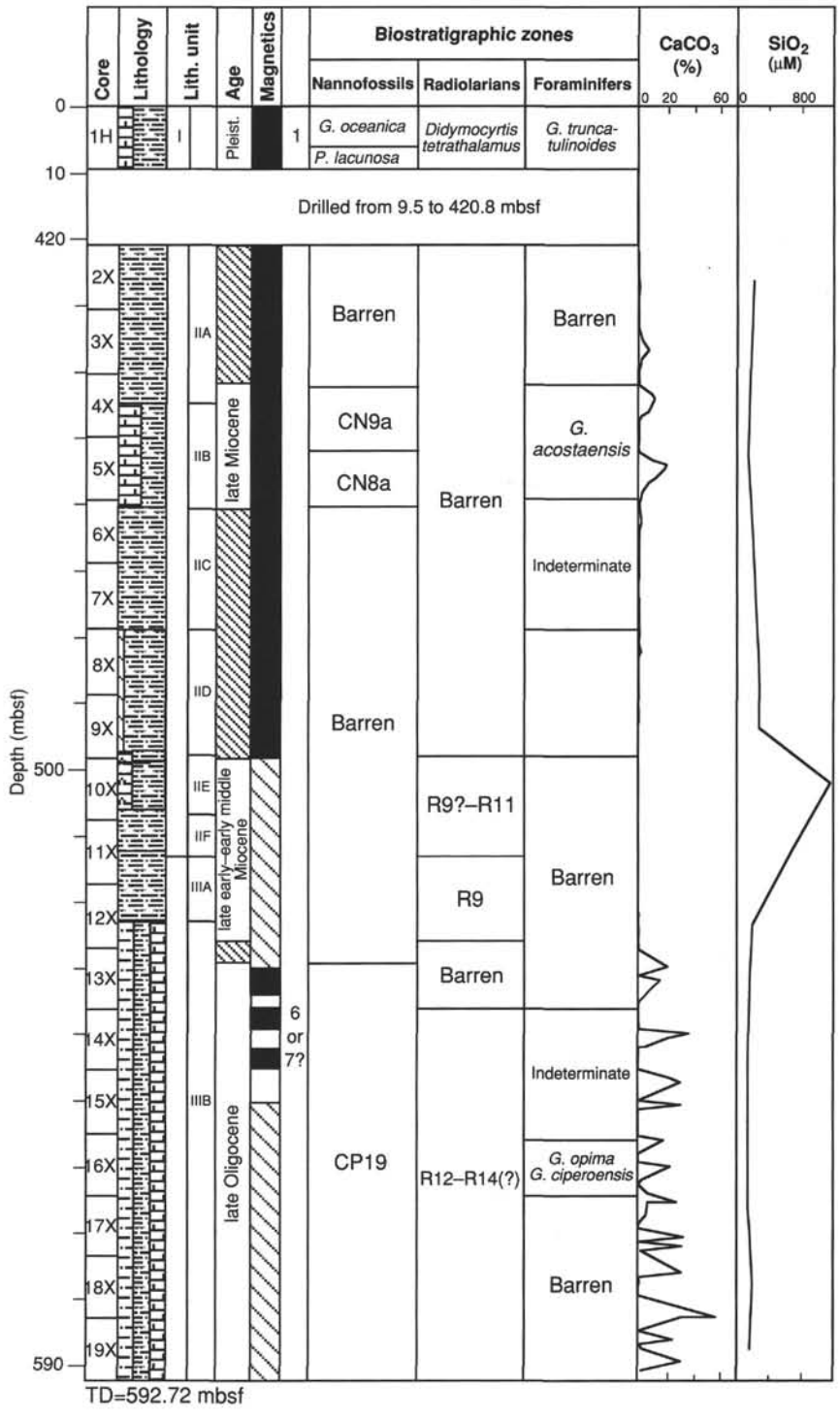

Figure 30. Biostratigraphic summary for Hole 948C.

neorectus. The presence of *D. bellus* and *D. bollii* as well as the absence of *Minylitha convallis* is a further indication of the zonal range of this interval.

Samples 156-948C-6X-2, 46–47 cm, through -13X-2, 139–140 cm, are devoid of calcareous nannofossils. Therefore, the material within the décollement zone, which occurs within this interval, could not be dated.

Below the long barren interval is a thick section of upper Oligocene sediments. Well-preserved nannofossils are found in the grayish-brown claystones in this section. Samples 156-948C-13X-3 through -19X-CC have been placed within Zone CP19 as a result of the presence of the range marker *Sphenolithus ciperoensis*.

Planktonic Foraminifers

Planktonic foraminifers first occur in mud-line Core 156-948C-1H. The entire core contains forms of the *Globorotalia truncatulinoides* Zone (N22–N23).

Above the décollement zone in Sections 156-948C-4X-3 through -5X-CC, planktonic foraminifers of late Miocene age occur. These

alternate with intervals that are rich in benthic foraminifers. The association of planktonic foraminifers can tentatively be assigned to the *Globorotalia acostaensis* Zone (N16). Common species are *Globigerinoides bollii, Globigerina decoraperta, Globigerina nepenthes,* and *Sphaeroidinellopsis simulina.* The biostratigraphic marker is rare.

Between Sections 156-948C-5X-CC and -9X-CC, the sediments of the accretionary prism, which consist in part of yellowish brown hemipelagic claystones, contain large planktonic foraminifers. Identification of these foraminifers was not possible because their fragile tests, resulting from advanced diagenetic alteration, were broken during the washing procedure. In general, these belong to the genus *Globorotalia.*

The low content of calcium carbonate indicates that the pinkish gray and greenish gray claystones in the décollement zone are barren. Below the décollement zone in Cores 156-948C-13X through Section 948C-16X-1, the sediments of the underthrust section lack planktonic foraminifers. In Section 156-948C-16X-2 a well-preserved foraminiferal fauna is present. It comprises planktonic foraminifers (mostly globigerinids, 20%) and benthic foraminifers (80%). The specimens are generally small. *Globigerina* species are *G. praebulloides praebulloides, G. praebulloides occlusa, G. ciperoensis ciperoensis, G. ciperoensis angulisuturalis, G. ciperoensis angustiumbilicata,* and *G. ouachitaensis ouachitaensis.* A further common biostratigraphic marker is *Globorotalia opima opima.* The age of the association is late Oligocene. It can be assigned to the *Globorotalia opima* Zone (P21) and the *Globigerina ciperoensis* Zone (P22).

Radiolarians

Mud-line Core 156-948C-1H contains a well-preserved modern radiolarian fauna. The specimens belong to a high-diversity association. *Didymocyrtis tetrathalamus, Euchitonia furcata, Dictyocoryne profunda, Spongaster tetras, Dictyocoryne truncatum, Stylodictya validispina,* and *Lophospyris pentagona* are the most common species. Because the fauna lacks markers, it cannot be assigned to a specific Quaternary zone. The most significant species, *Didymocyrtis tetrathalamus,* accords with the age shown in Figure 30.

In the Neogene sediments of the accretionary prism, between Cores 156-948C-2X and -9X, radiolarians are absent. From the top of the décollement zone (Section 156-948C-10X-1), radiolarians are present in varying abundances, through Core 156-948C-12X (base of the décollement). The fauna has an age of late early Miocene to early middle Miocene (Fig. 30). Biostratigraphically important markers are *Calocycletta virginis, Cyrtocapsella tetrapera, Stichocorys wolffii, Stichocorys delmontensis, Cyrtocapsella cornuta, Didymocyrtis prismatica, Liriospyris stauropora, Liriospyris parkerae, Dorcadospyris dentata, Dorcadospyris forcipata,* and *Cyclampterium leptetrum.*

Starting from Section 156-948C-10X-1, the youngest age of the radiolarian interval is late early Miocene (*Stichocorys wolffii* Zone, Zone R10 of Riedel and Sanfilippo, 1978) because *Calocycletta costata* (marker of Zone R9) was not determined with certainty. However, as the radiolarian sequence contains the transition between *Liriospyris parkerae,* which is a characteristic feature of the *Calocycletta costata* Zone (R9), the presence of this zone is possible. The lower boundary of the radiolarian association was considered to be not older than the *Stichocorys delmontensis* Zone (Zone R11 of Riedel and Sanfilippo, 1978) because the markers of the earlier *Calocycletta serrata* Zone (R12) and *Lychnocanoma elongata* Zone (R13) were not detected.

Sample 156-948C-11X-2, 16–19 cm, contains indications of reworking of late Eocene radiolarians on the basis of the presence of rare specimens of *Lithochytris vespertilio.*

In Sections 156-948C-10X-1 through -10X-2, and from the base of Section 156-948C-11X-2 through -11X-4, radiolarians are highly recrystallized (Fig. 31) and the radiolarian diversity decreases to 5 to 10 species. In Sections 156-948C-11X-2 through -11X-4, large spherical forms of *Orosphaera* type are embedded in tectonically undisturbed grayish yellowish brown claystone (the "fat rad zone"). In this interval, the radiolarians are cemented and overgrown by quartz crystals. Below the zone of strong recrystallization in Section 156-948C-10X-2 and in the "fat rad zone" in Section 156-948C-11X-2, radiolarians are well preserved, and diversity and abundance increase. Between the two zones of strong recrystallization, alteration of radiolarian skeletons changes gradually, depending on specific morphotypes (Fig. 31).

In Sections 156-948C-11X-5 through -12X-CC, radiolarians are rare. Nevertheless, the association belongs to the *Calocycletta costata* Zone.

Sections 156-948C-14X-1 through -19X-CC, beneath the décollement, contain traces of radiolarians. These are species of *Tholospyris* and *Calocycletta.* All the specimens of the latter genus are broken, and it is possible that these radiolarians were derived from the drilling slurry. Therefore, the zonal assignment remains questionable, although these cores have been tentatively identified as late Oligocene (Zone R14?) to early early Miocene (Zone R12) in age (Fig. 30).

Comparison with Holes 671B and 671C

The depth below seafloor of the upper boundary of the décollement zone, identified in Holes 948C, 671B, and 671C, differs by only 2 m, whereas in Hole 948C, the base of the décollement is structurally and lithologically placed 12 m above that recognized in Holes 671B and 671C (Fig. 32).

The radiolarian associations within the décollement have been attributed to different biostratigraphic zones because of the varying occurrence of distinct markers. For Hole 948C, the association tends toward the base of Zone R9 in terms of the abundance of *Calocycletta costata* (which is rare), the presence of *Dorcadospyris dentata* together with *Liriospyris stauropora,* and the absence of *Lychnocanoma elongata.*

In Holes 671B and 671C, the association was assigned to Zones R10 and R12, based on the occurrence of *Stichocorys wolffii, Cyrtocapsella tetrapera, Cyrtocapsella cornuta, Lychnocanoma elongata, Stichocorys delmontensis,* and *Carpocanopsis cingulata* (R10 = *Stichocorys wolffii* Zone) in the upper part of the radiolarian interval, and *Cyrtocapsella tetrapera, Cyrtocapsella cornuta,* and *Dorcadospyris ateuchus* (R12 = *Cyrtocapsella tetrapera* Zone) in the lower part. An association defining Zone R11 (*Stichocorys delmontensis* Zone) was not found (Shipboard Scientific Party, 1988).

PALEOMAGNETISM

Natural Remanence

The remanent magnetization of the sediments from Site 948 is stable throughout most of the cored section. Both the archive half of the split cores and discrete samples were demagnetized using alternating fields (AF) of up to 20 mT, with 5-mT steps being the standard treatment. A steep, downward magnetization component was removed with the initial 3- to 5-mT AF step (Fig. 33). This component is the drilling-induced magnetization that is nearly ubiquitous in ODP paleomagnetic studies. This drilling-induced remanence is thought to be an isothermal remanent magnetization (IRM), rather than a viscous remanent magnetization (VRM) (Musgrave et al., 1993). After removal of the drilling overprint, a stable, single component remanence was isolated with the remaining demagnetization steps in about 60% of the samples (Fig. 33). The remaining samples display either curved demagnetization trajectories from 5 to 20 mT (Fig. 33E), which indicate simultaneous removal of two or more directions, or are unstable during AF treatment. For the discrete samples, the stable behavior of remanence has enabled us to use the paleomagnetic results to reorient individual (single drilling biscuits) portions of the XCB core at this site. Additional measurements were performed on half biscuits temporarily exhumed from the working half of the core for reorienting individual structures (see "Structural Geology" section, this chapter).

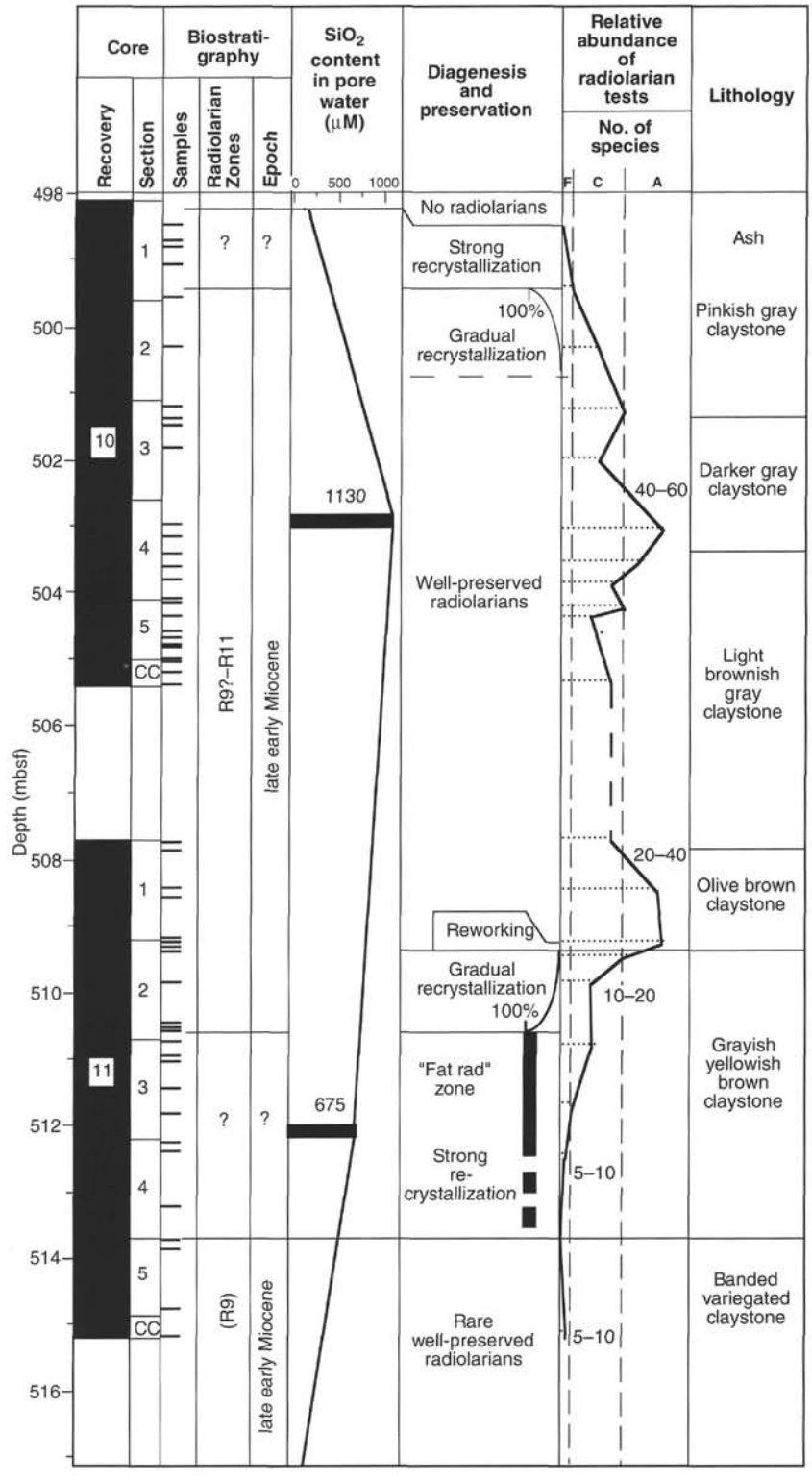

Figure 31. Radiolarian preservation compared with lithologic units, silica content, abundance of radiolarian tests (F = few, C = common, A = abundant), and taxonomic diversity in the décollement of Hole 948C.

The construction of a reliable magnetostratigraphy for this site is complicated by several factors. First is the effect of drilling disturbance on the split-core data. The cores throughout the drilled interval have been broken into 1- to 5-cm-long (downcore) biscuits, which have been rotated differentially during drilling. Each measurement made with the cryogenic magnetometer averages over a 10-cm interval; thus, the (rotated) directions of several biscuits are incorporated into each measurement. This will oversteepen the measured inclination of intervals of biscuits having a single polarity and shallow the measured inclination of mixed-polarity intervals. For a more complete treatment of the effect of drilling biscuits on split-core remanence, see the "Explanatory Notes" chapter in Taira, Hill, Firth, et al. (1991). Because the length of the biscuits is much less than the length measured by the magnetometer, the declinations obtained from the split cores are also averaged, and so cannot be used to reorient the XCB cores. These measurements also are affected by the relatively

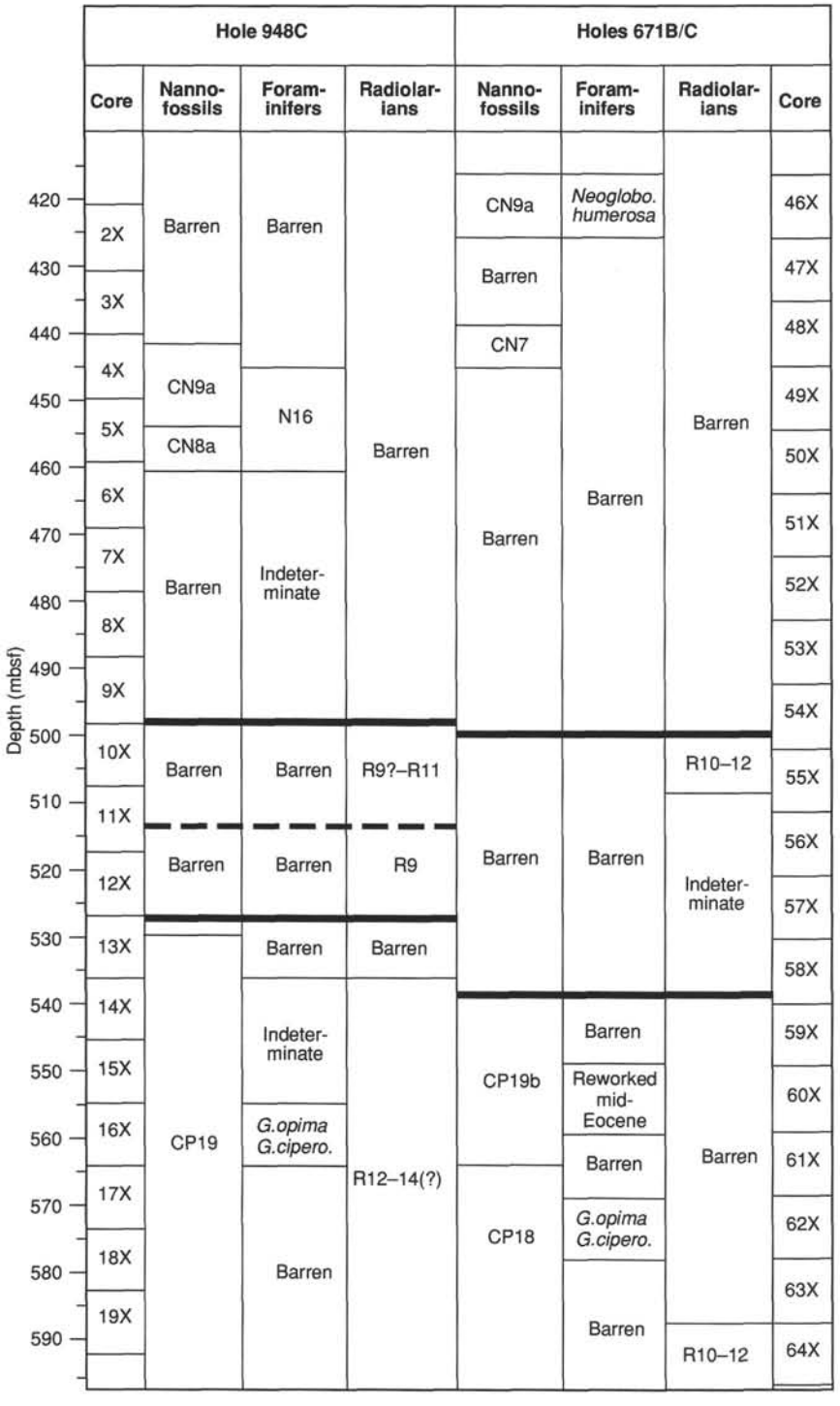

Figure 32. Comparison of biostratigraphic summaries of Holes 948C, 671B, and 671C. Heavy lines indicate location of top and base of the décollement zone; dashed line marks the major lithologic change within the décollement zone. Data for Holes 671B and 671C are from Shipboard Scientific Party (1988).

large number of whole-round samples removed from the cores. After the whole-round samples were extracted, they were replaced with foam spacers in the split cores. The magnetometer control software is currently unable either to suspend measurement over the foam spacers or to allow for subsections of a single core section to be measured. The split-core data, therefore, contain measurements taken on intervals of foam where whole-round samples were collected. These measurements will be subtracted from the data during shore-based study. Another effect on these data is bedding tilt. In the interval from 421 to 498 mbsf (structural Domain I), bedding dips from 0° to 62° were measured (see "Structural Geology" section, this chapter). The remanence data have not yet been corrected for bedding tilts, but this will be completed during shore-based work. A further complicating factor is the weak remanence of the samples from below 555 mbsf (Cores 156-948C-16X to -19X). The intensity of remanence after 5-mT AF demagnetization is less than 1 mA/m throughout this interval, and is not significantly higher than the magnetization of the sample boat in some cases. More reliable results from these weakly magnetized samples will be obtained during shore-based study. The final complication to consider is the effect of deformation on natural remanence. In strained sediments such as many of those at Site 948, remanence directions that were acquired before deformation (in this case, any

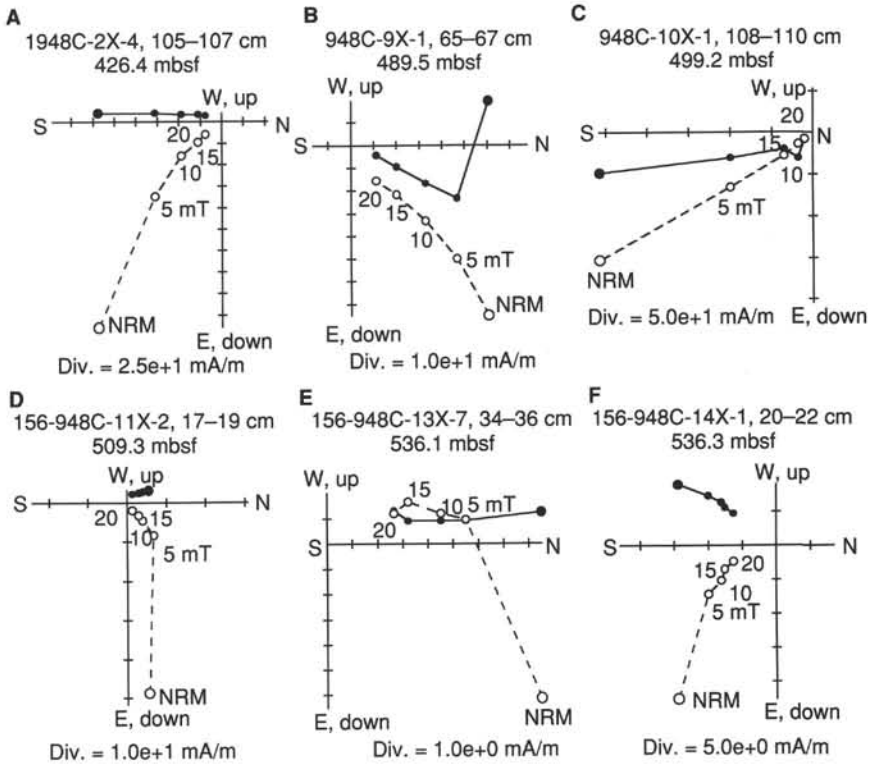

Figure 33. Orthogonal vector projections of demagnetization behavior of discrete samples from Hole 948C. Solid circles = projections of remanence vector on a horizontal plane; open circles = projections of remanence vector on a vertical plane. Intensity of remanence (mA/m) of each axis is denoted, and AFs used for each demagnetization step are given next to open circles. **A–D, F.** Single-component behavior after removal of the drilling overprint by the 5-mT step. **E.** Nonlinear demagnetization behavior, which indicates simultaneous removal of two (or more) directions in this sample.

remanence except for a recent present-day field overprint, and the drilling-induced IRM) will be rotated into the plane of flattening, away from the direction of shortening (Kodama, 1988). Efforts to collect the discrete samples in relatively undeformed areas of core were made to minimize this effect. Post-cruise remanence anisotropy studies will be performed to determine the magnitude of expected remanence deflection (Jackson et al., 1991).

With these complications in mind, a rudimentary magnetostratigraphy has been constructed. Both the split-core data (Fig. 34A) and the discrete-sample data (Fig. 34B), after 20-mT AF demagnetization, can be divided into three intervals that correspond to lithologic units or subunits (see "Lithostratigraphy" section, this chapter). The upper interval (420–498 mbsf, Unit II to Subunit IIE) is characterized by high remanence intensities and is predominantly of normal polarity. The second interval (498–514 mbsf, Subunits IIE through IIF) is characterized by decreasing remanence intensities (from 10 to 1 mA/m) and has mixed polarity. The third interval (514–593 mbsf, Unit III) is characterized by weak remanence and mixed polarity from 514 to 555 mbsf and predominantly reversed polarity from 555 to 593 mbsf. Remanence results of the discrete samples from 555 to 593 mbsf are biased toward the declination of the empty sample boat (180°) and thus are not reliable. The predominantly normal polarity of the upper interval may indicate that this portion of the hole has been remagnetized (pending correction for bedding tilts). Given the unknown effect of deformation within the décollement zone, the second interval (and the upper 16 m of the third interval) will be considered to have an indeterminate polarity. The third interval, because it occurs within the underthrust section, may contain a reliable portion of magnetostratigraphy from 530 to 555 mbsf. The biostratigraphic age of the sediments in Cores 156-948C-13X to -15X is late Oligocene (see "Biostratigraphy" section, this chapter). Comparison between the magnetostratigraphy of the interval from 530 to 555 mbsf with the geomagnetic time scale of Cande and Kent (1992) indicates possible ages of 24 to 26 Ma, if the normal-polarity interval from 530 to 534 mbsf is the first normal-polarity subchron of Chron 6 or is the top of Chron 7n1 (Fig. 35). This correlation should be regarded as highly speculative, pending shore-based refinement.

Rock Magnetism

Rock-magnetic experiments were conducted (1) to identify the magnetic minerals in the sediments from this site, (2) to identify the carriers of the natural remanence, and (3) to note any changes in magnetic mineralogy related to differences in lithology. Thermal demagnetization of multicomponent isothermal remanent magnetization (mIRM) (Lowrie, 1990) was used as the primary means of identifying minerals. For these experiments, orthogonally applied fields of 1.2, 0.3, and 0.05 T were used to generate the IRM components. The samples then were thermally demagnetized using 28 thermal steps from 60° to 625°C. For all samples, the 0.05-T component carried the vast majority of the mIRM. The intensities of the mIRM agree well with those observed in the natural remanence. Magnetizations with intensities >10,000 mA/m were obtained in samples from 420 to 498 mbsf. The 0.05-T component carried >80% of the mIRM in these samples. Thermal treatment revealed two unblocking temperatures (T_{ub}), one between 175° and 225°C, the other at 570° to 590°C (Fig. 36). A T_{ub} of 175° to 225°C was observed only in the 0.05- and 0.3-T components, and so is most likely carried by (titano)-maghemite. The T_{ub} of 570° to 590°C for the portions of the mIRM remaining after 225°C, carried mostly by the 0.05-T component, indicates that relatively pure (<10% ulvospinel) magnetite is the dominant magnetic mineral in these sediments. In samples from 498 to 514 mbsf, mIRM intensities ranged from 5000 to 10,000 mA/m. The mIRM results from this interval indicate a distinct difference in magnetic mineralogy between the pinkish gray claystone in Subunit IIE (Fig. 37A) and the grayish brown claystone in Subunit IIF (Fig. 37B). The pinkish gray claystone (Sample 156-948C-10X-5, 48–50 cm) has two distinct values of T_{ub} carried by all three mIRM components. The first is at about 250°C and is most likely carried by (titano)maghemite. In contrast to the samples from 420 to 498 mbsf, more than half of the magnetization carried by the 0.05-T component is lost after 250°C, indicating that (titano)maghemite is more abundant in the pinkish gray claystones. The mIRM remaining above 250°C has a T_{ub} of 570° to 590°C, indicating magnetite. The grayish brown claystone (Sample 156-948C-11X-2, 147–149 cm, Fig. 37B)

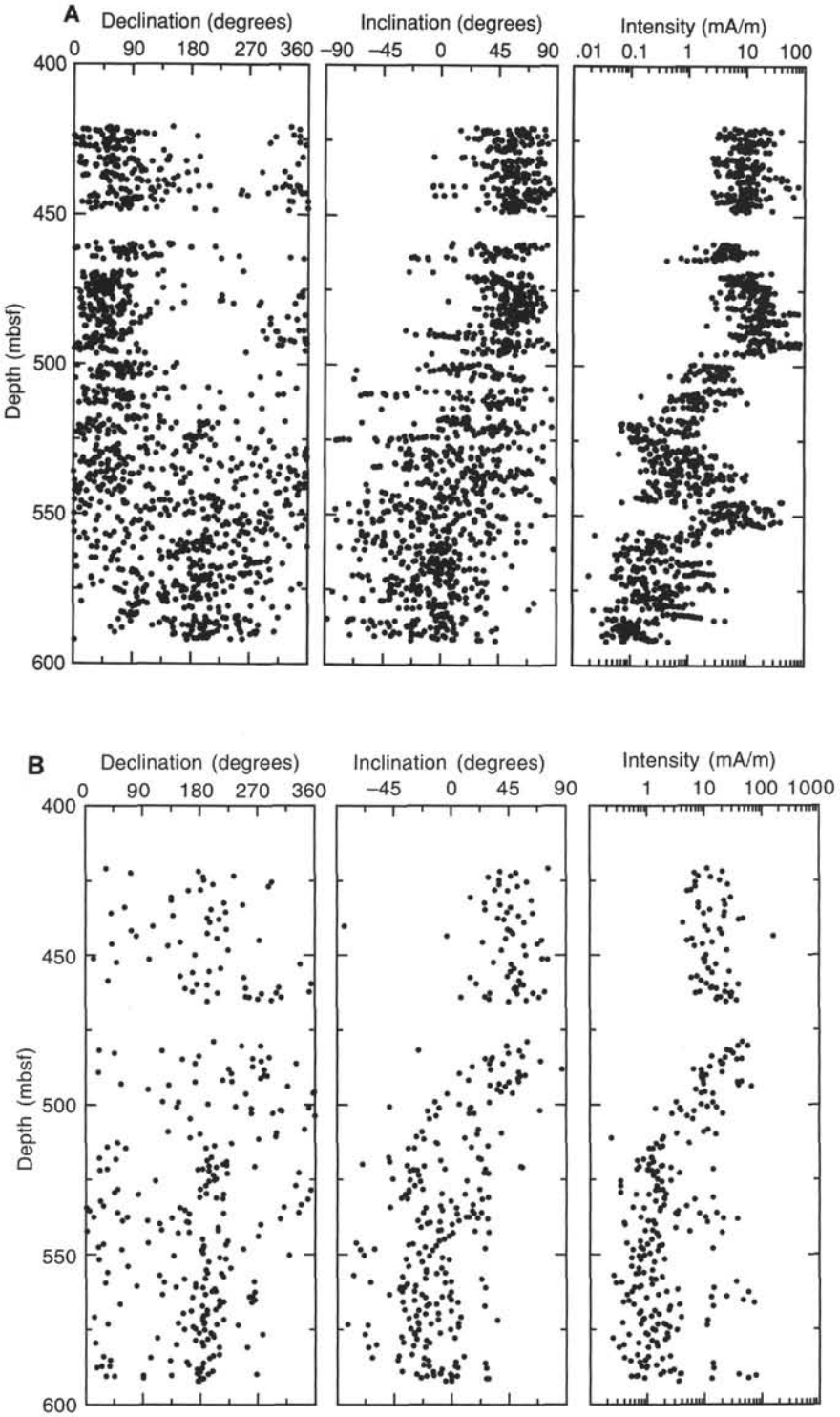

Figure 34. **A.** Remanence results from split cores after 20-mT AF demagnetization plotted vs. depth. **B.** Remanence results from the discrete samples after 20-mT AF demagnetization plotted vs. depth.

has an mIRM carried almost entirely by the 0.05-T component and having a single T_{ub} of 590°C. This indicates that magnetite is the only significant magnetic mineral in this sample. Samples from Unit III (below 514 mbsf) have much lower mIRM intensities (40 to 300 mA/m). Sample 156-948C-14X-5, 76–78 cm (Fig. 38A) is a greenish-gray claystone with two values of T_{ub}, one at 290° to 310°C and carried only by the 0.05-T component, the other at 530° to 580°C and carried by the remaining components. Below 320°C, the 0.05-T component is the largest mIRM component; above 320°C, the 1.2-T component is the largest. The almost total loss of the 0.05-T component at 320°C is most characteristic of greigite, although (titano)-maghemite and titanomagnetite with about 50% ulvospinel are also possible. The presence of greigite is supported by the occurrence of pyrite in Core 156-948C-14X (see "Lithostratigraphy" section, this chapter). A T_{ub} of 530° to 580°C and high coercivity of the magnetization remaining after 320°C indicate that fine-grained magnetite carries this portion of the mIRM. Sample 156-948C-18X-3, 115–117 cm (Fig. 38B) is a light gray silty claystone having low (40 mA/m) mIRM intensity. Although the behavior of this sample is noisy, a T_{ub} of 225°C was observed in the 0.05- and 1.2-T components, indicating

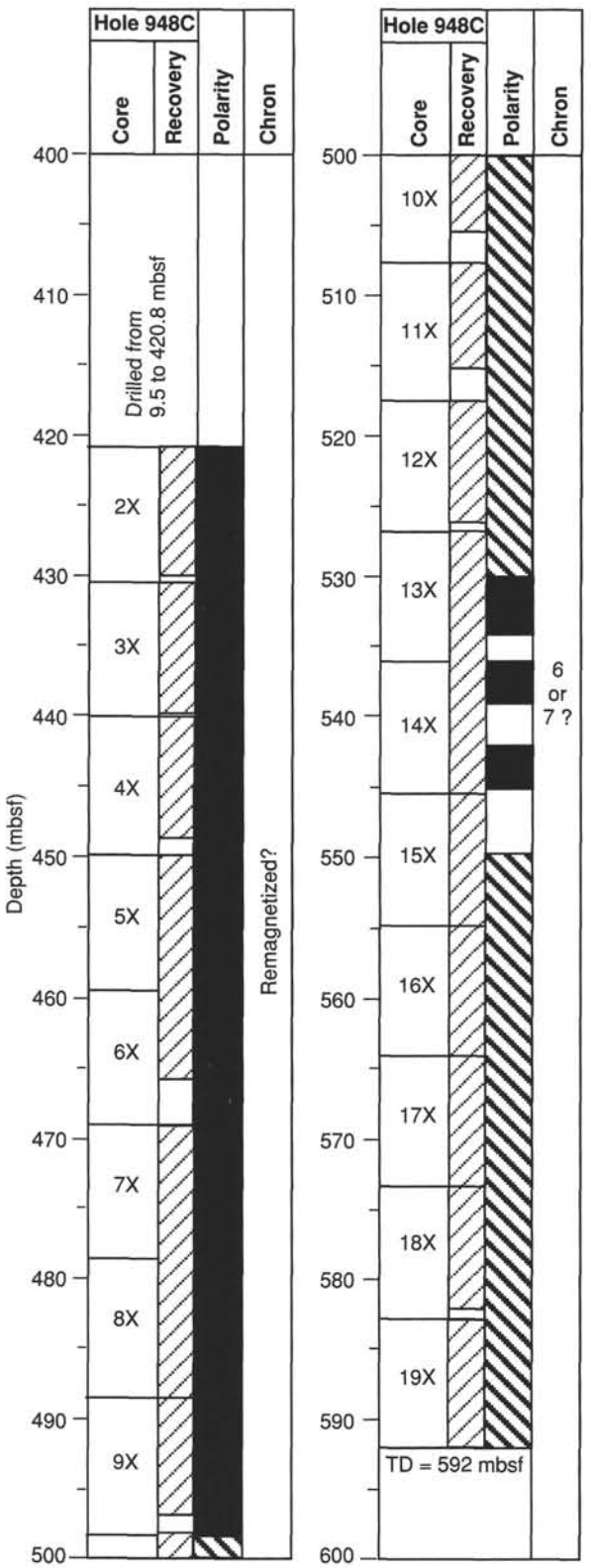

Figure 35. Summary magnetostratigraphy for Site 948. Black intervals denote normal polarity; white intervals, reversed polarity; and intervals with heavy diagonal lines, polarity of indeterminate nature. The interval from 530 to 550 mbsf has been tentatively assigned to either Chron 6 or Chron 7.

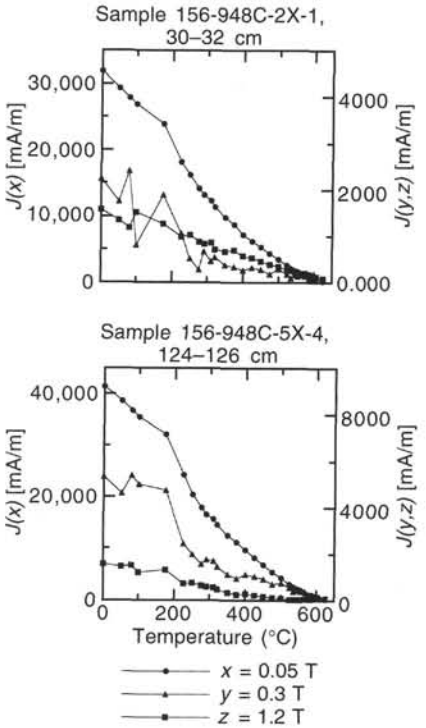

Figure 36. Multicomponent IRM (mIRM) thermal demagnetization results from grayish brown claystones of lithologic Unit II. Left axis = intensity of magnetization of the 0.05-T component (solid circles); right axis = intensity of magnetization of the 0.3-T (solid triangles) and 1.2-T (solid squares) components. Horizontal axis is oven temperature (°C). The loss of intensity of 0.05-T and 0.3-T components between 175° and 225°C signifies the presence of (titano)maghemite, whereas the loss of remanence at 570° to 590°C indicates the presence of magnetite.

(titano)maghemite. After the 520°C thermal step, sharp changes in intensity and direction were measured in the sample. This is most likely the result of formation of a new magnetic phase during heating.

To determine the average grain sizes of the magnetite, partial anhysteretic remanent magnetization (pARM) experiments were conducted. The pARMs were generated with a 10-mT-wide window over which the DC field was applied simultaneously with the AF. The center of the window was moved from 5 to 95 mT in 10-mT steps to generate the pARM curves. Samples from lithologic Unit II acquired stable pARMs, while those from Unit III would not acquire a stable pARM. All the pARM peaks for the Unit II samples (Fig. 39) are between 15 and 35 mT, which indicates an average magnetite grain size of 3 to 5 µm in these samples (Jackson et al., 1988).

Magnetic Susceptibility

Magnetic susceptibilities measured on whole cores with the multisensor track (MST) and on discrete samples using the KLY-2 show a good correlation between susceptibility and lithologic units. Unit II has high (>1 × 10^{-3} SI) susceptibility, with small-scale variations correlative with ash layers in the sediment (Fig. 40). Unit III has a much lower susceptibility (1–4 × 10^{-4} SI) and less small-scale variation (Fig. 40). The high quality of the susceptibility data, especially in Unit II, will aid in shore-based correlations with susceptibility stratigraphy determined for Leg 110, Site 671 (Hounslow, 1990). Additional shore-based work will determine the mineralogic sources of the susceptibility in these sediments, which will provide a better understanding of what changes in sediment composition are responsible for the observed variations in magnetic susceptibility.

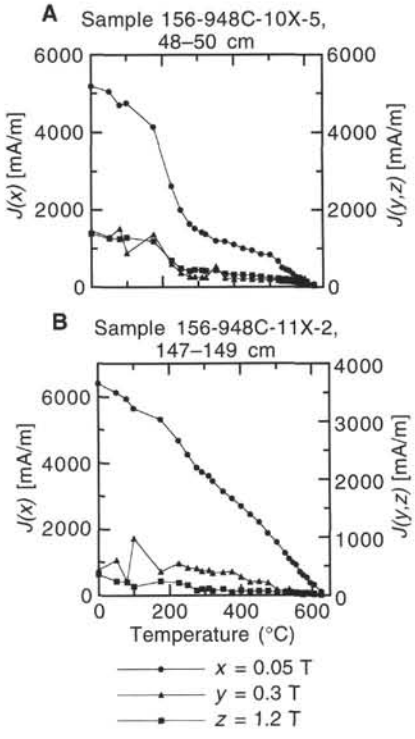

Figure 37. mIRM thermal demagnetization results from (**A**) pinkish gray claystone of Subunits IIE and IIB and (**B**) grayish brown claystone of Subunit IIF. Axes and symbols as in Figure 36. The loss of intensity of the 0.05- and 0.3-T components between 175° and 225°C signifies the presence of (titano)maghemite in (**A**), while the loss of remanence at 570° to 590°C indicates the presence of magnetite. Linear decrease in remanence to 590°C in (**B**) indicates that only magnetite is present in this sample.

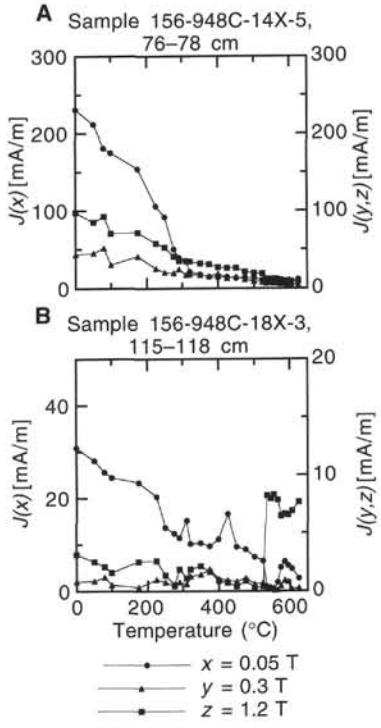

Figure 38. mIRM thermal demagnetization results from greenish gray claystone of Unit III (**A**) and light gray silty claystone of Unit III (**B**). Axes and symbols as in Figure 37. **A.** The T_{ub} of 290° to 320°C occurs in the 0.05-T component, which indicates the likely occurrence of greigite. **B.** The formation of a new magnetic phase during heating is indicated by the large increase in magnetization after 520°C.

ORGANIC GEOCHEMISTRY

Overview

Organic carbon contents in the sediments above and in the décollement zone are low, usually less than 0.05 wt%. Below the décollement zone, organic carbon content varies between 0.00 and 1.83 wt%, and high organic carbon contents are mainly associated with relatively thin layers of gray to dark gray material, presumably turbidite deposits. Organic matter consists of mainly marine and marine/terrestrial material of relatively low maturity. However, various parameters related to hydrocarbon generation indicate that some hydrocarbons may have been formed. The concentration of hydrocarbon gases in the sediments, mainly methane, is low, and the highest concentration of methane, 44 ppm by volume, was observed at 494.4 mbsf, just above the décollement zone. Very low concentrations of ethane and propane were also found, and the methane-to-ethane ratio varies from 20 to 60.

Headspace Hydrocarbon Gases

Headspace gas analyses are routinely conducted during ODP drilling for safety reasons, but information obtained at Site 671, not far from Site 948, showed that only trace quantities of methane are present in those sediments. Most interestingly, the highest methane concentrations were observed in the décollement zone (Mascle, Moore, et al., 1988, p. 102), and stable carbon isotopic analyses of methane pointed to a thermogenic source for the gas (Vrolijk et al., 1990). However, as a result of sampling procedure and small quantities of gas available for analysis, the authors emphasized that interpretation based on their isotopic results should be regarded as tentative. Therefore, an effort was made to obtain gas samples for better isotopic analyses, in addition to the routine headspace analyses.

Soon after the cores were retrieved in transparent core liners, they were carefully inspected for any sign of the presence of free gas. Gas was extracted from the core liners using 60-mL syringes, which were pushed into 4-mm holes drilled in the liner. The syringes were equipped with a spring to overcome the friction of the piston. In most cases, only a few milliliters of gas were recovered, and the gas was transferred to 20-mL vacutainers. The gas chromatographic system on board the ship requires 5 mL of gas for analyses; thus, most samples were not analyzed immediately, but were stored for analysis later onshore. Analysis of one larger sample (60 mL) showed only 63 ppm by volume of methane and 1.4 ppm of ethane, indicating that the hydrocarbon content in most samples is probably low. The concentrations of hydrocarbons in the samples collected by syringes are not directly comparable to those in a headspace sample, as the volumes of sediments and gas phase involved are unknown.

Samples for routine headspace analysis were taken at the top of the core section, just below the sample used for analyzing interstitial waters. Headspace gas was analyzed as described in the "Explanatory Notes" chapter (this volume), and results are reported in Table 17. Methane concentrations are very low, just above atmospheric background level in most samples. The highest concentration of methane, 44 ppm by volume, was observed at 494.4 mbsf, just above the décollement zone (498–526 mbsf, Fig. 41). This peak in methane concentration agrees with the observations made during drilling of Site 671; however, the maximum concentration found at Site 948 is an order of magnitude lower than that found earlier. For direct comparison of the two sets of results, the values in Table 17 may be multiplied by a factor of 0.25 to obtain the concentrations in micromoles per liter of interstitial water. Low concentrations of C_2 to C_3 were also found in a number of samples (Table 17), and the methane-to-ethane ratio varies from 20 to 30 in most samples. For comparison, it should be mentioned that no higher hydrocarbons were measured

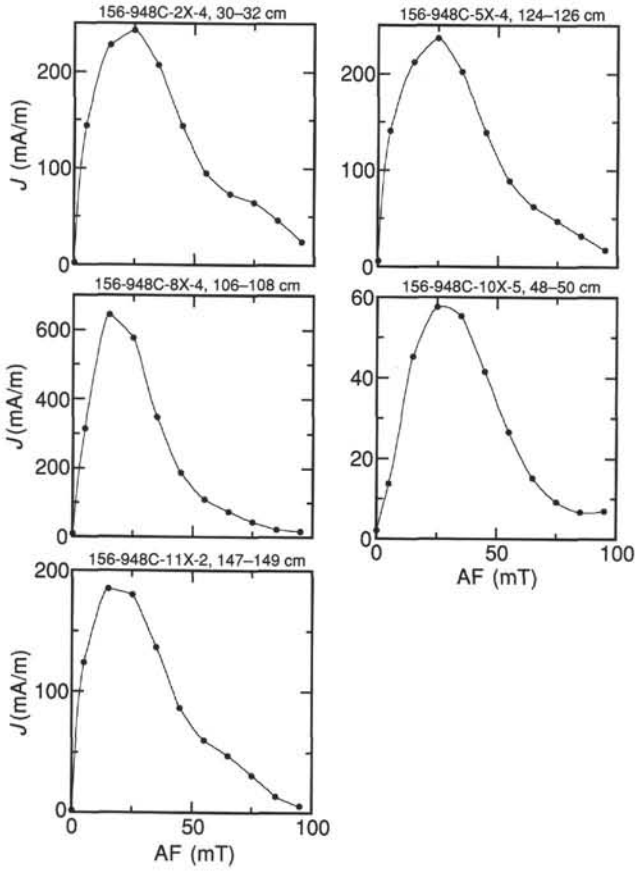

Figure 39. pARM results from samples of Unit II. Vertical axes are magnetization intensities; horizontal axes are AFs of the center of the (10-mT-wide) pARM window used in each step. The peak in the pARM curves at 10 to 30 mT indicates an average magnetite grain size of 3 to 5 μm in these samples.

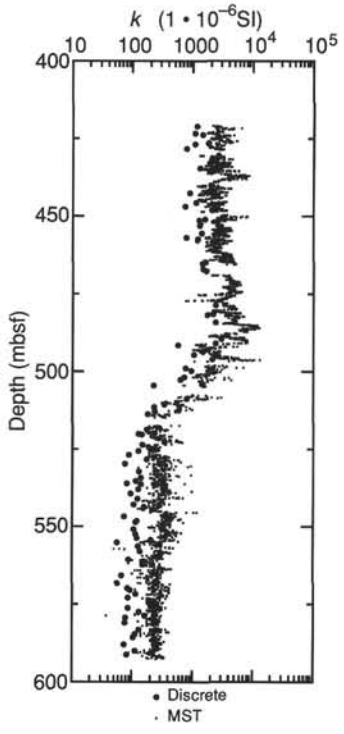

Figure 40. Magnetic susceptibility from the MST (small dots) and from discrete samples (solid circles). Susceptibilities are plotted in 10^{-6} SI volume units. High (>1^{-3} [SI units]) susceptibilities characterize lithologic Unit II, while Unit III is characterized by much lower susceptibilities.

in the headspace samples at Site 671. The peak in methane concentration observed just above the décollement zone corresponds to a minimum in chloride concentration at this depth, and one is tempted to conclude that this peak results from fluid flow (see "Inorganic Geochemistry" section, this chapter). Note, however, that even the peak level of methane represents a very low concentration, which could have resulted from drilling artifacts, the so-called "drill-bit metamorphism." In favor of an increase in indigenous methane concentration is that no problems or changes in drilling operations at this depth point to an artificial origin of the gas.

It is difficult to interpret the origin of the hydrocarbon gases because of the very low concentrations; however, the slight increase in ethane and the presence of propane in the samples having the highest methane concentration (Table 17) point to a thermogenic source. Better interpretation of hydrocarbon gas origin awaits further shore-based isotopic analyses.

Organic Carbon

Organic carbon contents, defined as the difference between total carbon and carbonate carbon (see "Explanatory Notes" chapter, this volume), were determined in all samples taken for interstitial-water analysis and in most samples for physical properties analyses (Table 18). The organic carbon content of the sediments was low, mostly below 0.1 wt%, in the interval from 422 to 510 mbsf, and scattered from 0.00 to 1.83 wt% from 510 to 592 mbsf (Fig. 42). Inspection of Cores 156-948C-12X to -19X below 510 mbsf showed that the higher organic carbon contents are mainly associated with gray to dark gray

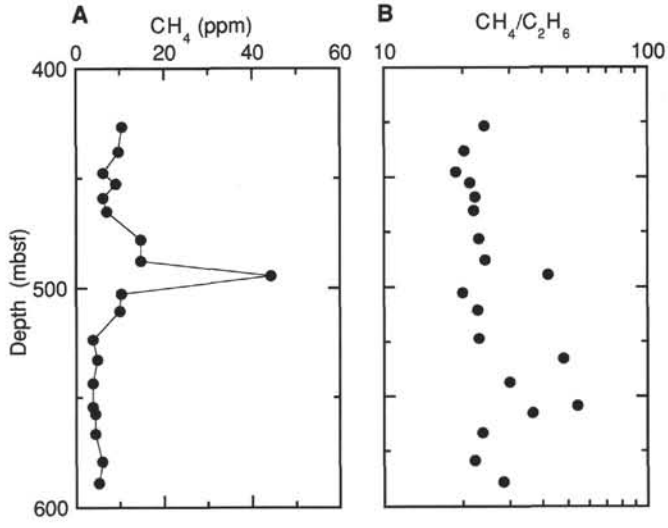

Figure 41. Results of headspace gas analyses vs. depth in Hole 948C. **A.** Methane. **B.** Methane/ethane ratio.

intervals, 2 to 30 cm thick. These layers were interpreted as representing turbidite deposits (see "Sedimentology and Lithostratigraphy" section, this chapter). More systematic sampling of these layers for further organic geochemical analysis confirmed that the organic contents of these deposits generally were considerably higher (>0.4 wt%), compared to the background greenish gray clays that make up most of the sedimentary column below the décollement zone (Fig. 42).

Organic carbon was also determined by Rock-Eval pyrolysis on these samples, and the results of the two methods show good agreement for most samples (Fig. 43).

Table 17. Hydrocarbons in headspace gas at Site 948.

Core, section, interval (cm)	Depth (mbsf)	C_1 (ppm)	C_2 (ppm)	$C_{2=}$ (ppm)	C_3 (ppm)	C_1/C_2
156-948B-						
1H-3, 0–5	3.03	3.0				
1H-5, 0-5	6.03	2.0				
156-948C-						
2X-5, 0–5	426.83	10.6	0.44			24
3X-6, 0–5	438.03	9.7	0.48			20
4X-6, 0–5	447.63	6.2	0.33	0.07		19
5X-3, 0–5	452.83	9.1	0.43			21
5X-7, 38–43	459.21	6.2	0.28	0.05		22
6X-5, 0–5	465.43	7.0	0.32			22
7X-7, 0–5	478.03	14.7	0.64			23
8X-7, 0–5	487.73	14.8	0.61		0.28	24
9X-5, 0–5	494.43	44.4	1.06		0.33	42
10X-4, 0–5	502.63	10.4	0.52		0.16	20
11X-3, 0–5	510.73	10.0	0.44			23
12X-5, 0–5	523.43	3.9	0.17			23
13X-5, 0–5	532.83	4.8	0.10			48
14X-6, 0–5	543.63	3.9	0.13	0.14		30
15X-7, 0–5	554.43	3.8	0.07			54
16X-3, 0–5	557.83	4.4	0.12			37
17X-2, 115–120	566.78	4.5	0.19	0.17		24
18X-5, 0–5	579.33	6.0	0.27			22
19X-5, 0–5	588.83	5.1	0.18	0.12		28

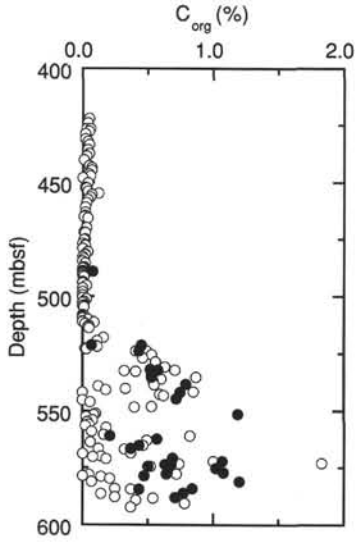

Figure 42. Organic carbon contents determined as total carbon minus carbonate carbon by Coulometric analysis vs. depth in Hole 948C. Open circles = samples for physical properties and interstitial water. Solid circles = samples for organic geochemical analyses.

Nitrogen and Sulfur

Total nitrogen contents were determined (see "Explanatory Notes" chapter, this volume) in the samples on which organic carbon was analyzed (Table 18). The crossplot of carbon and nitrogen shows fairly scattered data points (Fig. 44); however, samples having the highest nitrogen content relative to carbon content probably contain higher proportions of marine organic matter.

Sulfur analyses were not performed on the samples analyzed early during Leg 156 because of an intrinsic problem with the Carlo Erba instrument. This problem results from H_2O produced during combustion of the sample for total carbon, nitrogen, and sulfur; it totally obscures the SO_2 peak. The decision not to perform sulfur analyses was also based on the fact that very low organic contents were expected on the basis of information obtained previously at Site 671. When we realized that some of the samples had relatively high carbon contents, we decided to perform sulfur analyses by inserting an H_2O trap consisting of $MgClO_4$. Problems with high H_2O still occurred, and reliable results were obtained on relatively few samples (Table 18). The relatively high sulfur content of Core 156-948C-19X is consistent with the occurrence of pyrite crystals in this core.

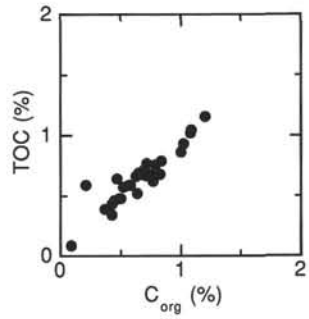

Figure 43. Crossplot of organic content determined by two methods in Hole 948C: total carbon minus inorganic carbon (TC – IC) and Rock-Eval (TOC).

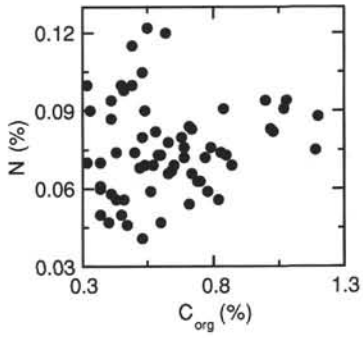

Figure 44. Crossplot of organic carbon and total nitrogen from Hole 948C samples. The highest nitrogen-to-carbon ratios are found in marine OM.

Kerogen Analyses

Organic matter is particularly sensitive to changes in temperature in the range expected in the cored interval, and samples having high organic contents were selected for further analyses. Thirty-two samples, mostly from the layers below the décollement, were analyzed with respect to kerogen type and maturity using the Rock-Eval pyrolysis technique (see "Explanatory Notes" chapter, this volume). The amount of volatile hydrocarbons, S_1, and the amount of hydrocarbons released by cracking of the kerogen, S_2, are given in Table 19. S_3 shows the amount of CO_2 produced during pyrolysis, and T_{max} gives the temperature at which the maximum of hydrocarbons is released by cracking. S_1, S_2, and S_3 are used to calculate a number of indices useful for characterizing type and maturity of organic matter: hydrogen index (HI) = $100 \cdot S_2/TOC$; oxygen index (OI) = $100 \cdot S_3/TOC$; production index (PI) = $S_1/(S_1 + S_2)$ and pyrolyzed carbon (PC) = $0.083 \cdot (S_1 + S_2)$ (Table 19).

Rock-Eval data are not considered reliable for sediments having total organic carbon (TOC) contents below 0.5 wt% because of matrix effects; therefore, these data have been omitted in the plots used to characterize type and maturity of organic matter. The organic matter in the gray to dark gray sediments below the décollement zone consists mainly of type III and mixtures of type II + type III kerogens (Fig. 45). The three types of kerogens marked in Figure 45 are commonly related to different types of organic matter (OM): I = algal OM; II = marine OM; and III = terrestrial OM. Thus, the data indicate mainly terrestrial or very degraded (oxidized) marine organic matter in the Hole 948C samples. However, interpretation of organic matter type based on Rock-Eval data alone may be uncertain, especially for clay-rich sediments

Table 18. Carbon, nitrogen, and sulfur data from Hole 948C.

Core, section, interval (cm)	Depth (mbsf)	Inorg. C (%)	$CaCO_3$ (%)	Total C (%)	Org. C (%)	Nitrogen (%)	Sulfur (%)
156-948C-							
1H-1, 37–39	0.37	1.66	13.8	1.85	0.19	0.03	NA
1H-1, 120–122	1.20	2.17	18.1	NA	NA	NA	NA
1H-1, 69–71	0.69	1.27	10.6	1.43	0.16	0.04	NA
1H-2, 20–22	1.70	0.61	5.1	0.82	0.21	0.04	NA
1H-2, 120–122	2.70	2.86	23.8	NA	NA	NA	NA
1H-3, 28–30	3.28	1.97	16.4	2.10	0.13	0.02	NA
1H-1, 8–10	0.08	2.60	21.7	2.78	0.18	0.04	NA
1H-1, 30–32	0.30	0.79	16.4	0.95	0.16	0.04	NA
1H-1, 114–116	1.14	2.24	18.7	NA	NA	NA	NA
1H-2, 29–31	1.79	0.87	7.2	1.00	0.13	0.04	NA
1H-2, 119–121	2.69	2.82	23.5	NA	NA	NA	NA
1H-3, 36–38	3.36	3.47	28.9	3.65	0.18	0.06	NA
1H-3, 118–120	4.18	2.31	19.2	NA	NA	NA	NA
1H-4, 30–32	4.80	0.79	6.6	0.90	0.11	0.04	NA
1H-4, 108–110	5.58	0.06	0.5	NA	NA	NA	NA
1H-4, 143–150	5.95	3.53	29.4	3.76	0.23	0.03	NA
1H-5, 28–30	6.28	0.33	2.7	0.43	0.10	0.04	NA
1H-5, 110–112	7.10	1.31	10.9	1.47	0.16	0.03	NA
1H-6, 30–32	7.80	4.02	33.5	4.15	0.13	0.03	NA
1H-6, 120–122	8.70	1.57	13.1	NA	NA	NA	NA
1H-7, 34–36	9.34	3.38	28.2	3.58	0.20	0.06	NA
2X-1, 140–142	422.20	0.02	0.2	0.07	0.05	0.04	0.00
2X-1, 146–148	422.26	0.03	0.2	0.09	0.06	0.04	NA
2X-3, 30–32	424.10	0.03	0.2	0.07	0.04	0.03	NA
2X-3, 72–74	424.52	0.04	0.3	0.09	0.05	0.04	NA
2X-4, 3–5	425.33	0.03	0.2	NA	NA	NA	NA
2X-4, 116–118	426.46	0.03	0.2	0.06	0.03	0.04	NA
2X-4, 130–150	426.60	0.05	0.4	0.11	0.06	0.06	NA
2X-5, 95–97	427.75	0.12	1.0	0.17	0.05	0.05	NA
2X-6, 52–54	428.82	0.04	0.3	0.06	0.02	0.03	NA
3X-1, 6–8	430.56	0.05	0.4	0.11	0.06	0.04	NA
3X-1, 55–57	431.05	0.03	0.2	0.05	0.02	0.03	NA
3X-2, 16–18	432.16	0.03	0.2	0.07	0.04	0.05	NA
3X-2, 139–141	433.39	0.04	0.3	0.07	0.03	0.03	NA
3X-3, 1–3	433.51	0.02	0.2	0.07	0.05	0.03	NA
3X-4, 69–71	435.69	0.42	3.5	0.46	0.04	0.04	NA
3X-5, 48–50	436.98	0.03	0.2	0.09	0.06	0.05	NA
3X-5, 95–97	437.45	0.94	7.8	0.99	0.05	0.03	NA
3X-6, 47–49	438.47	0.24	2.0	0.27	0.03	0.03	NA
4X-1, 16–18	440.26	0.06	0.5	0.07	0.01	0.03	NA
4X-2, 108–110	442.68	0.14	1.2	0.19	0.05	0.04	NA
4X-3, 55–57	443.65	1.29	10.7	1.36	0.07	0.04	NA
4X-3, 142–144	444.52	0.97	8.1	1.06	0.09	0.05	NA
4X-4, 12–14	444.72	1.52	12.7	1.59	0.07	0.04	NA
4X-4, 25–27	444.85	1.27	10.6	NA	NA	NA	NA
4X-5, 42–44	446.52	0.95	7.9	1.00	0.05	0.04	NA
4X-5, 110–150	447.20	0.26	2.2	0.32	0.06	0.05	NA
4X-6, 44–46	448.04	0.05	0.4	0.05	0.00	0.02	NA
5X-1, 63–65	450.43	0.05	0.4	0.09	0.04	0.03	NA
5X-1, 146–148	451.26	0.05	0.4	0.09	0.04	0.03	NA
5X-2, 43–45	451.73	0.03	0.2	0.09	0.06	0.03	NA
5X-2, 93–95	452.23	0.04	0.3	0.06	0.02	0.03	NA
5X-2, 120–150	452.50	0.08	0.7	0.11	0.03	0.05	NA
5X-3, 31–33	453.11	0.04	0.3	NA	NA	NA	NA
5X-3, 127–129	454.07	1.30	10.8	1.34	0.04	0.03	NA
5X-4, 47–49	454.77	2.65	22.1	2.77	0.12	0.03	NA
5X-4, 110–112	455.40	2.46	20.5	2.53	0.07	0.03	NA
5X-5, 63–65	456.43	1.58	13.2	1.64	0.06	0.03	NA
5X-5, 99–101	456.79	2.90	24.2	NA	NA	NA	NA
5X-6, 32–34	457.62	0.94	7.8	0.98	0.04	0.03	NA
5X-6, 148–150	458.78	1.29	10.7	NA	NA	NA	NA
5X-7, 8–10	458.88	0.41	3.4	0.44	0.03	0.03	NA
5X-CC, 25–27	459.48	3.10	25.8	NA	NA	NA	NA
6X-1, 22–24	459.62	2.04	17.0	2.15	0.11	0.03	NA
6X-1, 144–146	460.84	0.05	0.4	0.07	0.02	0.02	NA
6X-2, 6–8	460.96	0.17	1.4	1.30	1.13	0.04	NA
6X-3, 42–44	462.82	0.05	0.4	NA	NA		NA
6X-3, 82–84	463.22	0.25	2.1	0.27	0.02	0.04	NA
6X-4, 66–68	464.56	0.09	0.7	0.11	0.02	0.03	NA
6X-4, 118–150	465.08	0.15	1.2	0.16	0.01	0.02	NA
6X-CC, 15–17	465.81	0.11	0.9	0.15	0.04	0.03	NA
7X-1, 10–12	469.10	NA	NA	NA	NA	NA	NA
7X-1, 83–85	469.83	0.10	0.8	0.13	0.03	0.02	NA
7X-2, 46–48	470.96	0.03	0.2	NA	NA	NA	NA
7X-2, 123–125	471.73	0.05	0.4	0.06	0.01	0.03	NA
7X-3, 9–11	472.09	0.04	0.3	0.06	0.02	0.03	NA
7X-3, 80–82	472.80	0.03	0.2	NA	NA	NA	NA
7X-4, 10–12	473.60	0.30	2.5	NA	NA	NA	NA
7X-4, 123–125	474.73	0.03	0.2	0.05	0.02	0.03	NA
7X-5, 13–15	475.13	0.05	0.4	0.06	0.01	0.02	NA
7X-5, 77–79	475.77	0.05	0.4	NA	NA	NA	NA
7X-6, 47–49	476.97	0.09	0.7	0.07	0.00	0.01	NA
7X-6, 86–88	477.36	0.05	0.4	0.07	0.02	0.02	NA
7X-6, 120–150	477.70	0.10	0.8	0.12	0.02	0.02	NA
8X-1, 52–54	479.22	0.05	0.4	0.05	0.00	0.03	NA
8X-1, 122–124	479.92	0.20	1.7	NA	NA	NA	NA
8X-2, 19–21	480.39	0.16	1.3	0.20	0.04	0.03	NA
8X-2, 134–136	481.54	0.03	0.2	0.05	0.02	0.03	NA

Table 18 (continued).

Core, section, interval (cm)	Depth (mbsf)	Inorg. C (%)	$CaCO_3$ (%)	Total C (%)	Org. C (%)	Nitrogen (%)	Sulfur (%)
8X-3, 9–11	481.79	0.02	0.2	0.04	0.02	0.03	NA
8X-3, 110–150	482.80	0.19	1.6	0.17	0.00	0.03	NA
8X-4, 40–42	483.60	0.03	0.2	0.04	0.01	0.02	NA
8X-4, 141–143	484.61	0.03	0.2	NA	NA	NA	NA
8X-5, 66–68	485.36	0.02	0.2	0.04	0.02	0.02	NA
8X-5, 115–117	485.85	0.01	0.1	NA	NA	NA	NA
8X-6, 67–69	486.87	0.19	1.6	NA	NA	NA	NA
8X-6, 103–105	487.23	0.03	0.2	0.04	0.01	0.03	NA
8X-6, 120–150	487.40	0.01	0.1	0.02	0.01	0.02	NA
8X-7, 12–14	487.82	0.03	0.2	0.03	0.00	0.03	NA
9X-1, 52–54	488.92	0.02	0.2	0.02	0.00	0.03	NA
9X-1, 70–71	489.10	0.03	0.2	0.02	0.00	0.00	NA
9X-1, 94–96	489.34	0.02	0.2	NA	NA	NA	NA
9X-2, 24–26	490.14	0.02	0.2	0.02	0.00	0.03	NA
9X-2, 83–85	490.73	0.01	0.1	NA	NA	NA	NA
9X-3, 8–10	491.48	0.08	0.7	0.09	0.01	0.03	NA
9X-3, 78–80	492.18	0.07	0.6	NA	NA	NA	NA
9X-4, 59–61	493.49	0.07	0.6	0.06	0.00	0.02	NA
9X-4, 101–103	493.91	0.05	0.4	NA	NA	NA	NA
9X-4, 115–150	494.05	0.04	0.3	0.04	0.00	0.02	NA
9X-5, 7–9	494.47	0.02	0.2	NA	NA	NA	NA
9X-5, 81–83	495.21	0.02	0.2	0.05	0.03	0.03	NA
9X-6, 43–45	496.33	0.03	0.2	0.02	0.00	0.02	NA
10X-1, 11–13	498.21	0.02	0.2	NA	NA	NA	NA
10X-1, 124–126	499.34	0.03	0.2	0.02	0.00	0.02	NA
10X-2, 51–53	500.11	0.02	0.2	NA	NA	NA	NA
10X-2, 90–92	500.50	0.02	0.2	0.02	0.00	0.03	NA
10X-3, 19–21	501.29	0.01	0.1	0.04	0.03	0.04	NA
10X-3, 99–101	502.09	0.02	0.2	NA	NA	NA	NA
10X-3, 110–150	502.20	0.02	0.2	0.03	0.01	0.03	NA
10X-4, 25–27	502.85	0.02	0.2	NA	NA	NA	NA
10X-4, 124–126	503.84	0.03	0.2	0.04	0.01	0.03	NA
10X-5, 17–19	504.27	0.01	0.1	NA	NA	NA	NA
10X-5, 59–61	504.69	0.03	0.2	0.04	0.01	0.03	NA
11X-1, 36–38	508.06	0.04	0.3	NA	NA	NA	NA
11X-1, 70–72	508.40	0.03	0.2	0.04	0.01	0.03	NA
11X-1, 137–139	509.07	0.01	0.1	NA	NA	NA	NA
11X-2, 27–29	509.47	0.02	0.2	NA	NA	NA	NA
11X-2, 84–86	510.04	0.03	0.2	0.07	0.04	0.07	NA
11X-3, 11–13	510.81	0.02	0.2	NA	NA	NA	NA
11X-3, 55–57	511.25	0.03	0.2	0.12	0.09	0.05	NA
11X-3, 120–150	511.90	0.02	0.2	0.04	0.02	0.06	NA
11X-4, 37–39	512.57	0.01	0.1	0.06	0.05	0.07	NA
11X-4, 68–70	512.88	0.02	0.2	NA	NA	NA	NA
11X-4, 110–150	513.30	0.03	0.2	0.07	0.04	0.06	NA
11X-5, 17–19	513.87	0.03	0.2	0.08	0.05	0.08	NA
12X-1, 47–49	517.87	0.02	0.2	0.18	0.16	0.04	NA
12X-1, 79–81	518.19	0.03	0.2	NA	NA	NA	NA
12X-2, 29–31	519.19	0.02	0.2	0.13	0.11	0.07	NA
12X-2, 93–95	519.83	0.03	0.2	NA	NA	NA	NA
12X-3, 27–29	520.67	0.02	0.2	NA	NA	NA	NA
12X-3, 80–81	521.20	0.02	0.2	0.47	0.45	0.10	NA
12X-3, 83–84	521.23	0.02	0.2	0.09	0.07	0.03	NA
12X-3, 107–109	521.47	0.01	0.1	0.11	0.10	0.07	NA
12X-3, 133–135	521.73	0.03	0.2	NA	NA	NA	NA
12X-4, 2–4	521.92	0.01	0.1	0.12	0.11	0.07	NA
12X-4, 83–85	522.73	0.04	0.3	0.06	0.02	0.07	NA
12X-4, 110–150	523.00	0.05	0.4	0.08	0.03	0.06	NA
12X-5, 45–47	523.85	0.02	0.2	0.43	0.41	0.09	NA
12X-5, 45–46	523.85	0.02	0.2	0.51	0.49	0.12	NA
12X-5, 145–147	524.85	0.02	0.2	NA	NA	NA	NA
12X-6, 59–61	525.49	0.09	0.7	0.62	0.53	0.11	NA
13X-1, 14–16	526.94	0.02	0.2	0.48	0.46	0.10	NA
13X-1, 142–144	528.22	0.07	0.6	NA	NA	NA	NA
13X-2, 14–16	528.44	0.07	0.6	0.63	0.56	0.06	NA
13X-2, 101–103	529.31	4.82	40.2	NA	NA	NA	NA
13X-3, 6–8	529.86	0.03	0.2	NA	NA	NA	NA
13X-3, 113–115	530.93	2.77	23.1	3.40	0.63	0.07	NA
13X-4, 58–59	531.88	0.84	7.0	0.62	0.00	0.08	NA
13X-4, 73–75	532.03	0.04	0.3	0.75	0.71	0.08	NA
13X-4, 73–74	532.03	0.02	0.2	0.60	0.58	0.08	NA
13X-4, 115–150	532.45	0.15	1.2	0.47	0.32	0.10	NA
13X-5, 1–3	532.81	2.02	16.8	2.43	0.41	0.09	NA
13X-5, 99–101	533.79	0.03	0.2	NA	NA	NA	NA
13X-6, 19–21	534.49	3.78	31.5	4.31	0.53	0.08	NA
13X-6, 46–47	534.76	NA	NA	NA	NA	NA	NA
13X-6, 85–87	535.15	2.33	19.4	3.20	0.87	0.07	NA
13X-7, 28–30	536.08	0.07	0.6	0.67	0.60	0.07	NA
14X-1, 42–44	536.52	0.03	0.2	0.57	0.54	0.07	NA
14X-1, 146–148	537.56	2.91	24.2	NA	NA	NA	NA
14X-2, 43–45	538.03	0.23	1.9	NA	NA	NA	NA
14X-2, 69–70	538.29	0.14	1.2	0.93	0.79	0.08	NA
14X-2, 100–102	538.60	0.01	0.1	0.56	0.55	0.12	NA
14X-3, 9–11	539.19	0.04	0.3	0.16	0.12	0.08	NA
14X-3, 70–72	539.80	0.03	0.2	NA	NA	NA	NA
14X-3, 110–150	540.20	0.09	0.7	0.42	0.33	0.09	NA
14X-4, 19–21	540.79	4.73	39.4	4.91	0.18	0.03	NA
14X-4, 116–118	541.76	2.85	23.7	3.70	0.85	0.07	NA
14X-4, 135–136	541.95	2.78	23.2	3.53	0.75	0.06	NA
14X-5, 61–63	542.71	0.64	5.3	1.23	0.59	0.07	0.36

Table 18 (continued).

Core, section, interval (cm)	Depth (mbsf)	Inorg. C (%)	$CaCO_3$ (%)	Total C (%)	Org. C (%)	Nitrogen (%)	Sulfur (%)
14X-5, 92–94	543.02	4.24	35.3	NA	NA	NA	NA
14X-5, 120–150	543.30	0.10	0.8	0.72	0.62	0.12	NA
14X-6, 108–109	544.68	0.05	0.4	0.77	0.72	0.08	NA
14X-CC, 11–13	545.21	0.03	0.2	NA	NA	NA	NA
15X-1, 66–68	546.06	0.04	0.3	0.10	0.06	0.06	NA
15X-1, 106–108	546.46	3.48	29.0	NA	NA	NA	NA
15X-2, 51–53	547.41	0.04	0.3	NA	NA	NA	NA
15X-2, 104–106	547.94	2.93	24.4	3.46	0.53	0.04	1.76
15X-3, 2–4	548.42	3.96	33.0	4.36	0.40	0.05	0.50
15X-3, 78–80	549.18	1.28	10.7	1.97	0.69	0.08	NA
15X-4, 27–29	550.17	3.92	32.7	4.37	0.45	0.05	NA
15X-4, 121–123	551.11	0.03	0.2	0.13	0.10	0.06	0.04
15X-5, 12–13	551.52	1.22	10.2	2.41	1.19	0.08	NA
15X-5, 28–30	551.68	3.98	33.2	4.07	0.09	0.03	0.08
15X-5, 105–107	552.45	0.03	0.2	0.06	0.03	0.05	NA
15X-6, 42–44	553.32	1.13	9.4	1.73	0.60	0.05	NA
15X-6, 110–150	554.00	0.03	0.2	0.11	0.08	0.07	NA
15X-7, 44–46	554.84	0.02	0.2	0.06	0.04	0.05	0.05
16X-1, 12–14	554.92	0.02	0.2	NA	NA	NA	NA
16X-1, 106–108	555.86	0.02	0.2	0.07	0.05	0.05	0.08
16X-2, 24–26	556.54	0.03	0.2	0.05	0.02	0.08	NA
16X-2, 91–93	557.21	10.06	83.8	NA	NA	NA	NA
16X-2, 110–150	557.40	2.38	19.8	2.56	0.18	0.02	NA
16X-3, 39–41	558.19	0.03	0.2	NA	NA	NA	NA
16X-3, 126–128	559.06	0.02	0.2	0.09	0.07	0.05	0.04
16X-4, 17–19	559.47	4.36	36.3	NA	NA	NA	NA
16X-4, 109–111	560.39	0.03	0.2	0.19	0.16	0.05	0.05
16X-5, 17–19	560.97	3.03	25.2	3.85	0.82	0.06	NA
16X-5, 25–26	561.05	2.38	19.8	2.59	0.21	0.02	NA
16X-5, 78–80	561.58	7.28	60.6	NA	NA	NA	NA
16X-6, 14–15	562.44	0.02	0.2	0.59	0.57	0.07	NA
16X-6, 72–74	563.02	0.32	2.7	0.81	0.49	0.10	0.27
16X-7, 56–58	563.86	0.03	0.2	0.09	0.06	0.06	0.07
17X-1, 1–3	564.11	0.03	0.2	NA	NA	NA	NA
17X-1, 104–106	565.14	0.87	7.2	1.33	0.46	0.06	0.58
17X-1, 107–108	565.17	1.10	9.2	1.53	0.43	0.06	NA
17X-2, 33–35	565.93	4.88	40.7	NA	NA	NA	NA
17X-2, 78–79	566.38	0.04	0.3	0.41	0.37	0.06	NA
17X-2, 101–103	566.61	3.55	29.6	3.67	0.12	0.07	NA
17X-2, 120–150	566.80	0.88	7.3	1.20	0.32	0.07	NA
17X-3, 20–22	567.30	3.95	32.9	NA	NA	NA	NA
17X-3, 138–140	568.48	0.76	6.3	1.13	0.37	0.06	0.79
17X-4, 21–23	568.81	5.09	42.4	NA	NA	NA	NA
17X-4, 114–116	569.74	0.03	0.2	0.17	0.14	0.06	0.08
17X-5, 0–40	570.10	0.05	0.4	0.13	0.08	0.06	NA
17X-5, 49–50	570.59	0.03	0.2	0.72	0.69	0.07	NA
17X-5, 83–85	570.93	0.03	0.2	0.21	0.18	0.06	0.22
17X-6, 38–39	571.98	3.99	33.2	NA	NA	NA	NA
17X-6, 38–40	571.98	4.22	35.2	5.29	1.07	0.09	NA
17X-6, 38–39	571.98	3.99	33.2	4.99	1.00	0.09	NA
17X-6, 122–124	572.82	0.06	0.5	0.74	0.68	0.08	NA
17X-6, 138–140	572.98	0.07	0.6	1.90	1.83	0.08	NA
17X-7, 5–7	573.15	3.82	31.8	4.65	0.83	0.07	NA
17X-7, 12–14	573.22	4.13	34.4	4.87	0.74	0.06	0.72
18X-1, 9–11	573.39	0.05	0.4	NA	NA	NA	NA
18X-1, 23–24	573.53	0.08	0.7	0.71	0.63	0.08	NA
18X-1, 96–97	574.26	0.26	2.2	0.76	0.50	0.07	NA
18X-1, 97–99	574.27	0.28	2.3	0.80	0.52	0.07	0.24
18X-2, 28–30	575.08	1.69	14.1	2.72	1.03	0.08	NA
18X-2, 31–32	575.11	1.69	14.1	2.71	1.02	0.08	NA
18X-2, 145–147	576.25	5.57	46.4	NA	NA	NA	NA
18X-3, 25–27	576.55	0.03	0.2	NA	NA	NA	NA
18X-3, 45–46	576.75	0.03	0.2	0.68	0.65	0.07	NA
18X-3, 98–99	577.28	1.13	9.4	2.21	1.08	0.09	NA
18X-3, 122–123	577.52	3.79	31.6	4.43	0.64	0.07	NA
18X-3, 126–128	577.56	4.09	34.1	4.81	0.72	0.07	NA
18X-4, 17–19	577.97	0.04	0.3	0.09	0.05	0.07	NA
18X-4, 60–61	578.40	4.56	38.0	5.03	0.47	0.05	NA
18X-4, 85–87	578.65	0.03	0.2	NA	NA	NA	NA
18X-4, 110–150	578.90	0.12	1.0	0.26	0.14	0.08	NA
18X-5, 19–21	579.49	0.02	0.2	0.23	0.21	0.05	0.21
18X-5, 86–88	580.16	2.81	23.4	NA	NA	NA	NA
18X-6, 11–13	580.91	0.03	0.2	0.10	0.07	0.06	0.56
18X-6, 35–36	581.15	0.51	4.2	1.71	1.20	0.09	NA
19X-1, 43–45	583.23	4.62	38.5	NA	NA	NA	NA
19X-1, 120–121	584.00	0.98	8.2	1.82	0.84	0.09	NA
19X-1, 134–136	584.14	7.23	60.2	7.48	0.25	0.03	0.26
19X-2, 8–9	584.38	0.03	0.2	0.46	0.43	0.07	NA
19X-2, 15–17	584.45	4.06	33.8	4.43	0.37	0.05	NA
19X-2, 92–94	585.22	3.15	26.2	NA	NA	NA	NA
19X-3, 36–37	586.16	0.73	6.1	1.50	0.77	0.07	NA
19X-3, 44–46	586.24	0.04	0.3	0.18	0.14	0.06	0.60
19X-3, 104–106	586.84	0.01	0.1	NA	NA	NA	NA
19X-4, 47–49	587.77	3.20	26.7	3.45	0.25	0.04	NA
19X-4, 66–67	587.96	0.08	0.7	0.79	0.71	0.05	NA
19X-4, 97–99	588.27	0.55	4.6	NA	NA	NA	NA
19X-4, 110–150	588.40	0.12	1.0	0.66	0.54	0.09	NA
19X-5, 33–35	589.13	0.32	2.7	0.73	0.41	0.06	0.42
19X-5, 97–99	589.77	3.95	32.9	NA	NA	NA	NA
19X-6, 30–32	590.60	3.95	32.9	4.73	0.78	0.06	2.94
19X-6, 113–115	591.43	0.74	6.2	NA	NA	NA	NA
19X-7, 33–35	592.13	0.30	2.5	0.67	0.37	0.07	NA

Note: NA = not analyzed.

Table 19. Summary of Rock-Eval pyrolysis for Hole 948C.

Core, section, interval (cm)	Depth (mbsf)	T_{max}	S_1	S_2	S_3	PI	PC	HI	OI	TOC
156-948C-										
9X-1, 70–72	489.10	444	0.25	0.79	0.00	0.24	0.08	987	0	0.08
9X-4, 115–150	494.05	439	0.19	0.95	0.18	0.17	0.09	791	150	0.09
12X-3, 80–81	521.20	415	0.26	0.67	0.22	0.28	0.07	145	47	0.46
12X-3, 83–84	521.23	439	0.15	0.37	0.00	0.29	0.04	411	0	0.09
12X-5, 45–46	523.85	454	0.22	0.68	0.06	0.24	0.07	141	12	0.48
13X-4, 58–59	531.88	461	0.14	0.84	0.44	0.14	0.08	147	77	0.57
13X-4, 73–74	532.03	450	0.16	0.80	0.54	0.17	0.08	135	91	0.59
13X-6, 103–106	535.33	456	0.19	1.02	0.42	0.16	0.10	192	79	0.53
14X-2, 69–70	538.29	486	0.21	0.65	2.14	0.24	0.07	85	281	0.76
14X-4, 134–135	541.94	405	0.19	0.43	1.81	0.31	0.05	63	266	0.68
14X-6, 108–109	544.68	458	0.24	1.22	0.54	0.16	0.12	158	70	0.77
15X-5, 12–13	551.52	411	0.36	0.85	2.13	0.30	0.10	80	202	1.05
16X-5, 25–26	561.05	464	0.13	0.12	0.97	0.54	0.02	20	164	0.59
16X-6, 14–15	562.44	448	0.14	0.88	0.43	0.14	0.08	149	72	0.59
17X-1, 107–108	565.17	411	0.06	0.18	2.02	0.25	0.02	54	594	0.34
17X-2, 78–79	566.38	452	0.15	0.75	0.49	0.17	0.07	192	125	0.39
17X-5, 49–50	570.59	441	0.20	0.83	0.42	0.20	0.08	116	59	0.71
17X-6, 38–39	571.98	412	0.25	1.01	2.06	0.20	0.10	117	239	0.86
17X-6, 122–124	572.82	427	0.16	0.71	0.52	0.19	0.07	104	76	0.68
17X-7, 5–7	573.15	402	0.39	0.77	2.72	0.34	0.09	113	400	0.68
18X-1, 23–24	573.53	429	0.18	0.76	0.63	0.19	0.07	115	95	0.66
18X-1, 96–99	574.26	586	0.09	0.71	3.24	0.11	0.06	147	675	0.48
18X-2, 31–32	575.11	414	0.22	0.67	2.61	0.25	0.07	609	2372	0.11
18X-3, 45–46	576.75	422	0.25	0.81	0.67	0.24	0.08	117	97	0.69
18X-3, 98–99	577.28	439	0.35	0.94	3.37	0.27	0.10	92	330	1.02
18X-3, 122–123	577.52	408	0.29	0.46	3.02	0.39	0.06	88	518	0.52
18X-4, 60–61	578.40	392	0.20	0.19	1.31	0.53	0.03	29	204	0.64
18X-6, 36–37	581.16	413	0.22	0.74	1.27	0.23	0.08	63	109	1.16
19X-1, 120–121	584.00	407	0.28	0.79	2.88	0.26	0.08	100	364	0.79
19X-2, 8–9	584.38	453	0.16	0.76	0.54	0.17	0.07	176	125	0.43
19X-3, 36–37	586.16	410	0.15	0.30	1.24	0.34	0.03	48	200	0.62
19X-4, 66–67	587.96	396	0.33	0.53	0.67	0.38	0.07	79	100	0.67

Notes: S_1 and S_2 in milligrams hydrocarbons per gram of dry sediment, S_3 in milligrams carbon dioxide per gram of dry sediment. PI = production index; PC = pyrolyzed carbon; TOC = total organic carbon; HI = hydrogen index; OI = oxygen index. For definition of indexes, see text.

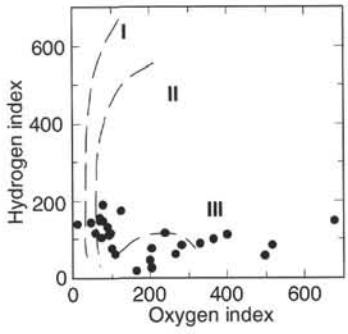

Figure 45. Hydrogen and oxygen indices (HI and OI) obtained from Rock-Eval analyses of samples from Hole 948C, plotted on a modified van Krevelen diagram (Tissot and Welte, 1984). Kerogen type: I = highly oil prone; II = oil prone; III = gas prone.

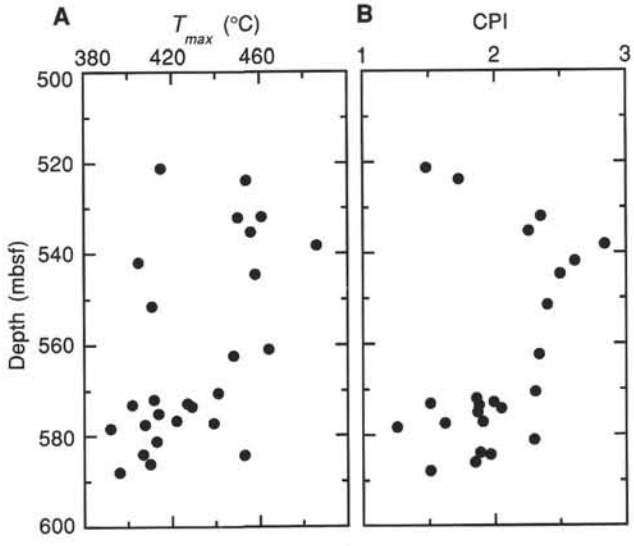

Figure 46. OM maturity indicators vs. depth from Hole 948C. **A.** T_{max}. **B.** CPI = $(C_{25} + C_{27} + C_{29} + C_{31} + C_{33/2} + C_{23/2})/(C_{24} + C_{26} + C_{28} + C_{30} + C_{32})$; equation from Waples (1985).

having relatively low organic carbon contents, such as the sediments in this study, because of adsorption of pyrolyzates on the clays (Peters, 1986). Organic matter types were also investigated with bitumen analyses of the sediments (see following text).

Given the similarity of the types of sediment analyzed by Rock-Eval pyrolysis (gray to dark gray layers), T_{max} may be used as an indicator of thermal maturity because, in many cases, variations in T_{max} grossly parallel variation in other maturity parameters (e.g., vitrinite reflectance). From the temperature gradient measured at Site 948 (see "Heat Flow" section, this chapter), the temperatures of the sediments below the décollement should be about 40° to 50°C. Immature organic matter, with T_{max} below 430°C thus is to be expected, and this is indeed the case for most samples below 570 mbsf. However, most samples between 520 and 560 mbsf have considerably higher T_{max} values (Fig. 46A), suggesting a higher thermal maturity near the décollement, compared to that of the deeper sediments. The PI is expected to increase with increasing T_{max} as more and more hydrocarbons are generated with increasing maturity; however, the opposite appears to be the case with the sediments cored at Site 948 (Fig. 47). The decrease in PI with increasing T_{max} may be explained by matrix effects. S_1 is more affected compared to S_2 by the clay content in sediments with low organic carbon content (Peters, 1986). Therefore, PI tends to be underestimated. T_{max}, on the other hand, tends to be overestimated for such types of sediments. Therefore, conclusions

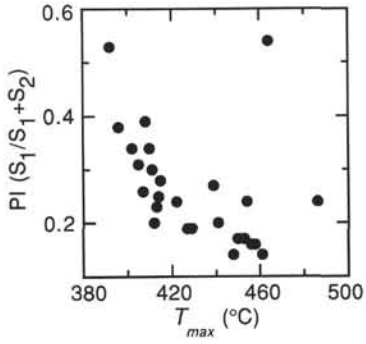

Figure 47. Plot of PI vs. T_{max}, Hole 948C.

with respect to higher temperatures near the décollement zone compared to the underlying sediments should not be based on T_{max} alone.

Bitumen Analyses

The composition of hydrocarbons generated at fairly low maturities may provide useful information on the type of organic matter and may reflect even slight changes in its thermal maturity. Therefore, bitumen was analyzed in the 32 samples also examined by Rock-Eval pyrolysis. Hydrocarbons were extracted from about 500 mg of dry sediment using a hexane/methanol mixture (see "Explanatory Notes" chapter, this volume), and the concentrated extract in hexane was analyzed by gas chromatography (GC). When splitting Core 156-948C-13X, a petroliferous smell was noted in Section 156-948C-13X-6, and a sample from that particular depth was included in the 32 samples for extract analyses. The result of the GC analysis for this particular sample is shown in Figure 48, together with the chromatogram of an *n*-alkane standard. The *n*-alkanes above C_{13} and the two isoprenoids pristane and phytane were easily identified by their retention times, but the most prominent peak between C_{16} and C_{17} and the numerous minor peaks in the chromatogram could not be identified in the shipboard laboratory. The chromatograms of the total extracts of most samples had the same overall appearance, but distinct differences in the relative concentrations of the *n*-alkanes also were obvious. The concentration of each *n*-alkane was determined by its peak height relative to the *n*-alkane standard (40 ng/μL), and the concentrations of *n*-alkanes (ng/g) in the sediments of each sample are presented in Figure 49. The HP Chemstation software (see "Explanatory Notes" chapter, this volume) was particularly useful for scaling the axes of chromatograms and for merging standard chromatograms and sample chromatograms to avoid confusion of peaks, and for checking the software integration of the peaks. For the heavier hydrocarbons, those above C_{23}, the concentrations of *n*-alkanes having an odd number of carbon atoms are significantly higher than even-numbered ones, which shows that the organic matter is immature or only marginally mature. With increasing maturity, the predominance of odd over even will disappear (Tissot and Welte, 1984), and a carbon preference index ($CPI = \Sigma C_{odd}/\Sigma C_{even}$) for the heavier *n*-alkanes is often used to indicate the changes in maturity with depth. CPI values calculated for the alkanes of most samples have been plotted vs. depth (Fig. 46B). The results are scattered, but may indicate a slight general increase in maturity with depth. The distribution of *n*-alkanes generated at low maturity depends on the type of OM. Marine OM mainly produces lighter hydrocarbons, with a maximum of about 15 to 18, whereas terrestrial OM mainly generates heavier homologues, with a maximum of about 27 to 31. The distribution of *n*-alkanes probably reflects the origin of the OM better than does the crossplot of HI and OI in Figure 45.

The pristane-to-phytane ratios vary from 0.5 to 1.7, but range mostly from 0.8 to 1.2, which also points to a type II kerogen (Tissot and Welte, 1984). With increasing maturity, the amount of *n*-alkanes will increase relative to the pristane and phytane. On the other hand, bacterial degradation mainly affects the *n*-alkanes and thus will decrease the alkane-to-isoprenoid ratio. Considering the relatively low maturity of the OM, the alkane-to-isoprenoid ratios in the crossplot of Figure 50 do not suggest extensive degradation of the hydrocarbons in the organic-rich layers below the décollement zone.

Among the samples analyzed for kerogen and bitumen, two were from above and two from within the décollement. Three of these samples had very low OM contents of less than 0.1 wt%. Still, two of the samples contained sufficient extractable matter for GC analyses, and the results of these analyses suggest that the OM becomes more marine at shallower depth. The third sample, collected at the depth of the chloride minimum (see "Inorganic Geochemistry" section, this chapter) contained little extractable organic matter, and no *n*-alkanes were observed in the gas chromatogram; this suggests biodegradation of the hydrocarbons. The shallowest sample analyzed was taken from an approximately 10-cm-thick brown layer at 489.10 mbsf, which appears to be highly unusual in its color and consistency (see "Structural Geology" section, this chapter). The chromatogram of this sample differs from those of the other samples in that it contains almost no *n*-alkanes above C_{20} (Fig. 49). This suggests that the hydrocarbons derive from either an entirely marine type of OM or from a much more mature source rock, compared to those of the other hydrocarbons.

Overall, the analyses of bitumens in the samples from Site 948 suggest that most of these hydrocarbons have been generated in situ. Hydrocarbons that migrated from a deeper source would not be expected to give such a large variation in the distribution of *n*-alkanes (Fig. 49) and CPI values (Fig. 46B), as is seen for the bitumens from this study.

INORGANIC GEOCHEMISTRY

Overview of Results

Interstitial waters were squeezed from whole-round cores and analyzed for salinity, pH, alkalinity, sulfate, ammonia, chloride, calcium, magnesium, lithium, potassium, sodium, and silica. The sediments also were analyzed for organic and inorganic carbon contents. The concentration-depth profiles indicate that, overall, the interstitial waters in the accreted sediments have been more diluted by a freshwater source than those in the subducted sediments. A fluid conduit, characterized by lower-than-seawater chloride concentration (~18% dilution) and enriched in manganese and methane, was intersected at about 4 m above the structurally defined décollement, at 498 to 529 m. The concentration-depth profiles of the major elements analyzed indicate the importance of horizontal fluid advection at this site. The calculated maximum vertical fluid flux rate below the décollement, assuming steady-state conditions, is ≤1.0 mm/yr. Diagenesis is widespread; the most important diagenetic reactions are volcanic matter and oceanic basement alteration to hydrous silicates at low-to-moderate temperatures, carbonate recrystallization, and sulfate reduction coupled with organic-matter decomposition.

Methods

Sample Retrieval

In every whole-round core sample, any material potentially contaminated with drilling fluid (surface seawater with various admixtures of drilling mud and churned-up sediment) must be removed before squeezing. At this site, to obtain an acceptable quality of interstitial water data, it was necessary to retrieve, thus squeeze, relatively small volumes of undisturbed "pristine biscuits" of sediments from the whole-round core samples characterized by drilling disturbances. This necessitated taking whole-round samples of up to 40 cm long, even above the décollement where sediment porosities are ~55%. Between 460 and 500 mbsf, these longer-than-usual whole-round samples yielded just 6 to 8 mL of interstitial water, after squeezing at 205 MPa for approximately 1.5 hr. Below the décollement, however, despite the lower porosities of 47% to 50%, the yield

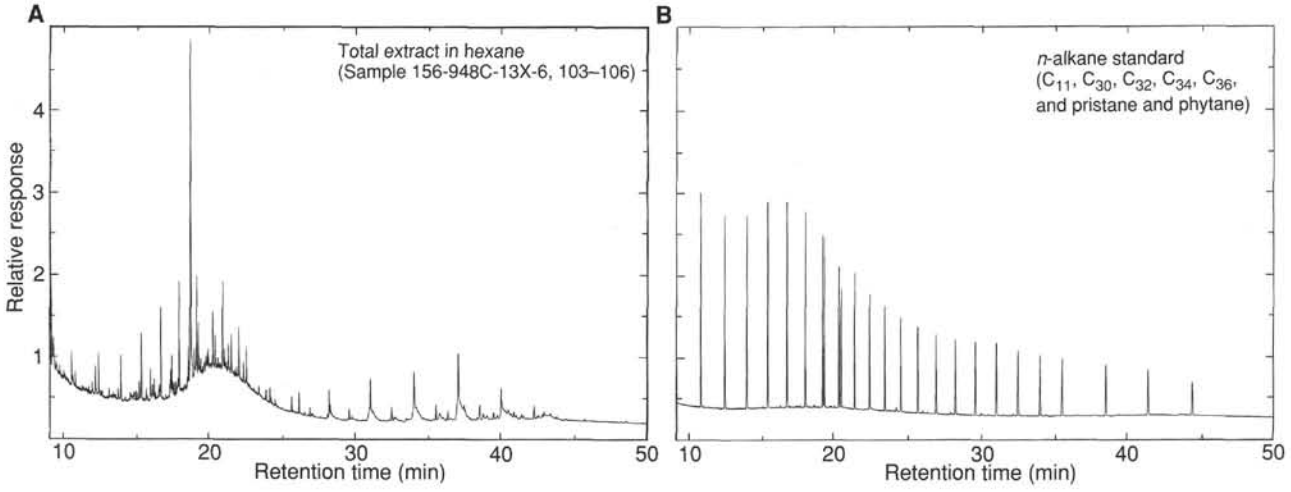

Figure 48. Gas chromatograms of total extract of (**A**) Sample 156-948C-13X-6, 103–106 cm, in hexane (a petroliferous smell was noted when this core section was split), and (**B**) a standard alkane mixture (40 ng/μL) in hexane.

of interstitial water per unit volume of sediment squeezed was significantly higher, by about 30%, most probably because of the different lithology of these sediments (see "Lithostratigraphy and Sedimentology" section, this chapter).

Analyses

Except for manganese, essentially the same methodologies as those described in Gieskes et al. (1991) were used for analyzing the interstitial waters. Concentrations of chloride, potassium, calcium, and magnesium were determined by two methods, as described in the "Explanatory Notes" chapter (this volume). Results from the more accurate and precise method are reported in Table 20. Because of the high concentrations of dissolved Ca, minor amounts of a Ca phase seem to have precipitated in the samples squeezed after refrigeration (probably a carbonate or a sulfate phase), affecting slightly the salinity, dissolved Ca, and therefore also Mg concentrations. These data are reported in Table 20 (marked by #), but are not plotted in these three figures. Four 40-cm-long whole-round cores were immediately squeezed, and the interstitial waters promptly sealed in special gas-tight Cu-tubes for shore-based analyses of helium isotope ratios. Excess interstitial waters from the samples taken for helium were also analyzed with shipboard methods. These samples are marked by an asterisk in Table 20.

Results

The shipboard interstitial-water chemical data are given in Table 20 and plotted vs. burial depth in Figures 51 through 55.

Chloride and Salinity

The concentration-depth profile of dissolved chloride (Fig. 51A) is dominated by the distinct Cl minimum (461 mM, ~18% seawater dilution) at 494 mbsf, situated about 4 m above the structurally defined décollement, at 498 to 529 mbsf (see "Structural Geology" section, this chapter). Concentration-depth profiles of other components, especially of Na, SO_4, and NH_4, indicate dilution with a fresher, significantly lower-Cl solution, which must have been advected from deeper in the accretionary complex. In situ production of such a low-Cl solution at 55% porosity at 40° to 50°C is implausible. The low-Cl solution, however, is enriched in dissolved manganese and methane. For detailed discussion of the methane-concentration spike (Fig. 51C), see "Organic Geochemistry" section (this chapter). The origin of a low-Cl solution above the décollement zone, first observed during Leg 110 (Gieskes et al., 1990), is still being debated; based on Leg 110 geochemical data that indicated only 10% seawater Cl dilution, Gieskes et al. (1990) suggested clay-membrane ion filtration or clay-mineral dehydration as possible origins.

The dissolved-Cl concentration gradients increase gradually but asymmetrically above vs. below this distinct Cl-minimum horizon. Also, above it, Cl concentrations remain lower than the seawater value throughout the depth interval drilled at Hole 948C. In contrast, below the Cl-minimum horizon, higher-than-seawater Cl concentrations are observed just 25 m deeper.

In addition, above the Cl-minimum horizon, the Cl gradient is diffusive for only 20 m; but below it, within and below the décollement, the diffusion profile extends for about 40 m. Can this discrepancy in diffusional path lengths be attributed to a lower diffusion coefficient in the more porous clay-rich section immediately above the décollement? Indeed, the preliminary calculated sediment diffusion coefficients from the wireline-log formation factors and porosity measurements (see "Downhole Logging" and "Core Physical Properties" sections, respectively, this chapter) are 3.3×10^{-6} cm^2/s above the Cl-minimum horizon and ~4.0×10^{-6} cm^2/s in the lower porosity section below it. Accordingly, based on the former calculated sediment diffusion coefficient for above the Cl-minimum horizon and a diffusive path length of 20 m equal to $\sqrt{2Dt}$ (D = diffusion coefficient and t = time), the low-Cl fluid advected into this horizon at least 20,000 yr ago. The same calculation over the diffusive path length of 40 m below the Cl-minimum horizon and a sediment diffusion coefficient of 4.0×10^{-6} cm^2/s, however, indicate that an advective "pulse" of low-Cl fluid occurred at least 60,000 yr ago. The discrepancy in the calculated timing of the low-Cl advective "pulse," together with the persistence of lower-than-seawater Cl concentrations above the décollement, suggest that, in this section, the advected low-Cl-fluid flows not only along the Cl-minimum horizon, but that additional fluid-flow horizons must exist above the décollement. This conclusion is supported by the Cl concentration-depth profile obtained at Site 671 during Leg 110 (Gieskes et al., 1990).

The Cl concentration-depth profile (Fig. 51), together with the Ca and Mg depth profiles (Fig. 52), indicate the greater importance of horizontal relative to vertical fluid flow at this site, especially in the accreted sediments. Also, assuming steady-state conditions, preliminary one-dimensional vertical flux calculations (using a diffusion coefficient calculated from the depth-dependent formation factor, a porosity of 50%, and various vertical flux rates) were performed. The Cl-concentration data within and below the décollement (498–548 mbsf) fall between the curves of 0.8 and 1.0 mm/yr, indicating a maximum vertical advective flux rate of ≤1.0 mm/yr. However, based on one-dimensional calculations of porosity reduction from Sites 672

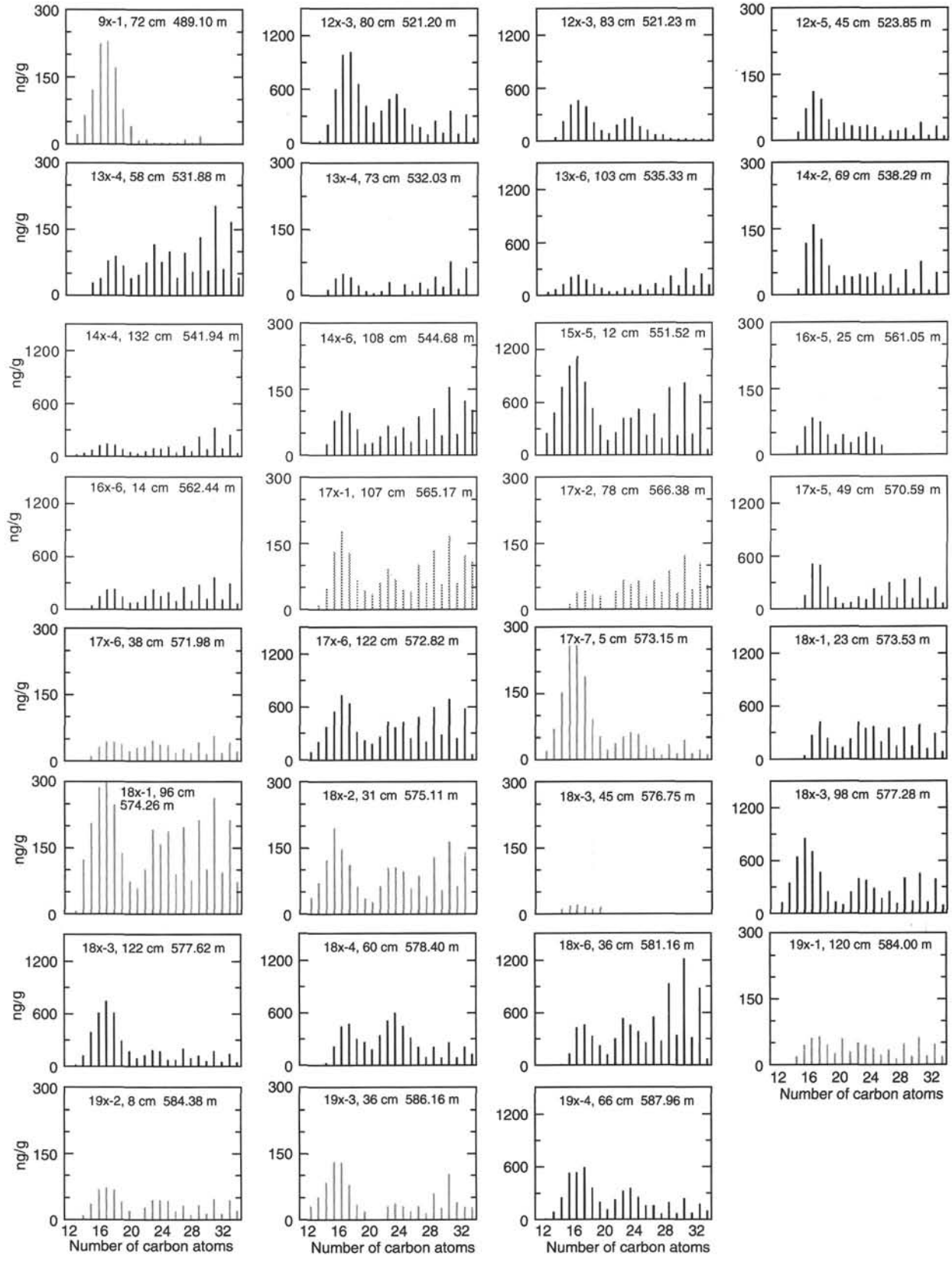

Figure 49. Concentrations of *n*-alkanes in Hole 948C sediments (ng/g), based on GC–flame ionization detector (FID) analysis of total sediment extracts. Note that two different scales on the *y*-axes have been used.

Table 20. Interstitial-water chemical data of major constituents, Hole 948C.

Core, section interval (cm)	Depth (mbsf)	IW volume (mL)	pH	Alk. (mM) (Gran.)	Sal. (Refr.)	Cl^- (mM) (Titrn.)	Ca^{2+} (mM) (Titrn.)	Mg^{2+} (mM) (Titrn.)	Mg/Ca	SO_4^{2-} (mM) (IC)	NH_4^+ (μM) (Spec.)	SiO_2 (μM) (Spec.)	Li^+ (μM) (AES)	K^+ (mM) (AES)	Na^+ (mM)	Na/Cl	Mn^{2+} (μM) (AAS)
156-948C-																	
1H-4, 143–150	6.0	84	7.30	3.62	35.1	559	12.5	50.2	4.01	27.8	22	483	25.6	11.3	481	0.86	130.3
2X-4, 130–150	426.7	10			30.2	523	42.8	19.8	0.46	15.3	206	187	50.8	2.8	426	0.81	65.5
3X-5, 120–150	437.9	18	7.07	0.51	30.4	538	43.1	19.2	0.45	16.0	242	154	56.4	3.4	443	0.82	63.2
4X-5, 110–150[a]	447.4	21			30.8												
5X-2, 120–150[b]	452.7	10			32.5	510	44.2	20.3	0.46	15.9	218	125	65.6	3.2	409	0.80	93.4
6X-4, 118–150[b]	465.2	8			32.0	516	43.6	18.8	0.43	16.2	220	173	82.6	3.1	420	0.81	123.8
7X-6, 120–150	477.8	8			30.8	511	45.3	18.5	0.41	15.0	183	224	80.8	2.8	411	0.80	139.6
8X-3, 110–150[b]	483.0	8			31.8	512	44.7	14.4	0.32		196	237	69.6				137.6
8X-6, 120–150	487.6	6			30.6	488	46.3	16.2	0.35	14.4	169	266	80.7	2.6	389	0.80	
9X-4, 115–150	494.2	6				461	42.5	18.7	0.44	13.9	174	257	107.0	2.8	364	0.79	207.5
10X-3, 110–150	502.4	12	6.90	1.43	30.8	511	42.3	24.1	0.57	14.2	205	1140	177.8	3.4	405	0.79	611.6
11X-3, 120–150	512.1	11			31.8	538	42.4	31.5	0.74	14.8	251	676	215.2	3.8	416	0.77	440.5
12X-4, 110–150[b]	523.2	30	7.54	2.62	35.0	564	42.2	33.2	0.79	14.1	321	184	173.6	4.3	440	0.78	142.0
13X-4, 115–150	532.6	20	7.45	3.01	35.2	571	42.6	34.3	0.80	13.8	335	136	188.2	4.4	444	0.78	89.2
14X-3, 110–150[a]	540.4	22			35.0												
14X-5, 120–150[b]	543.5	19	7.39	2.93	35.2	572	44.0	35.7	0.81	13.0	342	123	170.0	4.3	437	0.76	57.9
15X-6, 110–150	554.2	16	7.42	2.68	34.2	560	43.1	37.5	0.87	11.9	355	121	242.6	3.9	422	0.75	51.0
16X-2, 110–150	557.1	15	7.52	1.91	34.1	560	44.9	37.1	0.83	11.9	320	123	244.3	4.8	417	0.74	37.5
17X-2, 120–150[b]	567.0	22	7.39	1.92	34.2	559	45.7	35.6	0.78	11.7	419	134	251.4	4.1	418	0.75	30.6
17X-5, 0–40[a]	570.3	25			34.0	553	48.5	37.6	0.77	10.7	365	136	273.6	3.5	399	0.72	32.4
18X-4, 110–150	579.1	24	7.40	2.55	34.0	554	48.7	35.3	0.72	9.8	375	180	283.7	3.7	405	0.73	26.2
19X-4, 110–150	588.6	12			34.1	554	51.1	35.4	0.69	10.2	392	136	302.8	3.6	398	0.72	22.6

Notes: Abbreviations for methods used: Gran. = Gran titration; Refr. = hand-held refractometer; Titrn. = titration; IC = ion chromatograph; Spec. = spectrophotometer; AES = atomic emission spectrometry; AAS = atomic absorption spectrometry.

[a] He sample excess interstitial water.

[b] Squeezed after sealing and up to 24-hr storage in refrigerator.

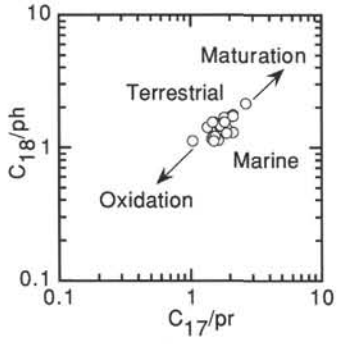

Figure 50. Crossplot of C_{17}/pristane (C_{17}/pr) and C_{18}/phytane (C_{18}/ph) based on GC-FID analyses of total sediment extracts in hexane, Hole 948C.

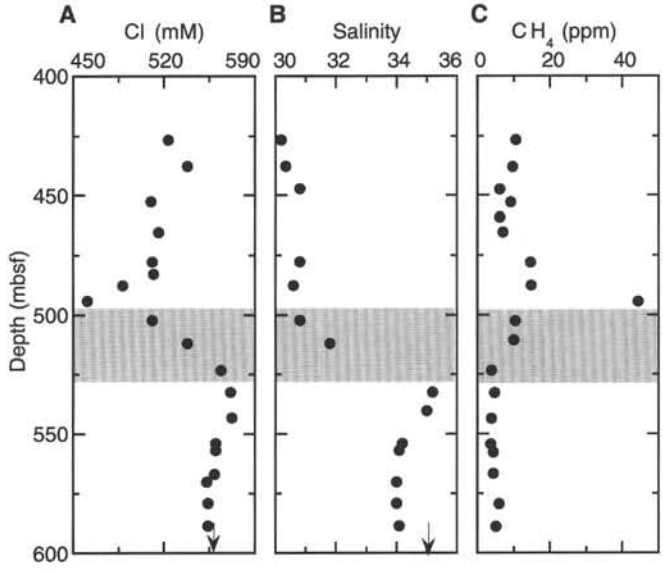

Figure 51. Concentration-depth profiles. **A.** Chloride. **B.** Salinity. **C.** Methane. In Figures 51–55, arrow indicates seawater concentration (where appropriate), and shaded area delineates décollement zone.

to 671, Leg 110, the minimum vertical advection rate is 0.2 mm/yr. Assuming that the error in both calculations is small, the lower vertical advection rates in the latter calculation suggest that some lateral flow also exists below the décollement.

Volcanic-ash hydration reactions to clay minerals and/or zeolites are probably responsible for the slightly elevated Cl concentrations of 2.5% higher than the seawater value at 520 to 550 mbsf.

Like the Cl concentration-depth profile, the salinity-depth profile (Fig. 51B) divides the section drilled at this site into a low-salinity zone (13% to 15% lower than seawater salinity) above the décollement, and a higher salinity zone in the décollement and underthrust sediments. The latter consists of a slightly higher than seawater salinity interval within the décollement zone (2.5% above seawater salinity), underlined by a slightly lower than seawater salinity zone (4%–5% below seawater). No salinity measurement is available for interval 156-948C-9X-4, 115–150 cm, at 494 mbsf, which has the distinct minimum-Cl concentration.

Calcium and Magnesium

Dissolved Ca concentrations are four to five times higher and dissolved Mg concentrations are 30% to 60% lower than seawater concentrations at the depth interval drilled at Site 948 (Fig. 52). In addition, the Ca concentrations are somewhat higher and the Mg concentrations somewhat lower than those at equivalent burial depths at Sites 541 and 671. The high Ca and low Mg concentrations have been attributed to volcanic ash or basement alteration reactions (Gieskes et al., 1990), which is supported by lower-than-contemporary-seawater strontium isotopic composition, observed at Site 541. The large increase in dissolved Ca concentrations is especially noticeable because of the presence of active sulfate reduction, hence, of in situ alkalinity production, which promotes diagenetic carbonate formation. The low alkalinities measured in much of this section are most likely controlled by the coupling of mainly two types of diagenetic reactions: low-to-moderate temperature alteration of volcanic matter and/or oceanic basement, and carbonate diagenesis. The latter is indicated by

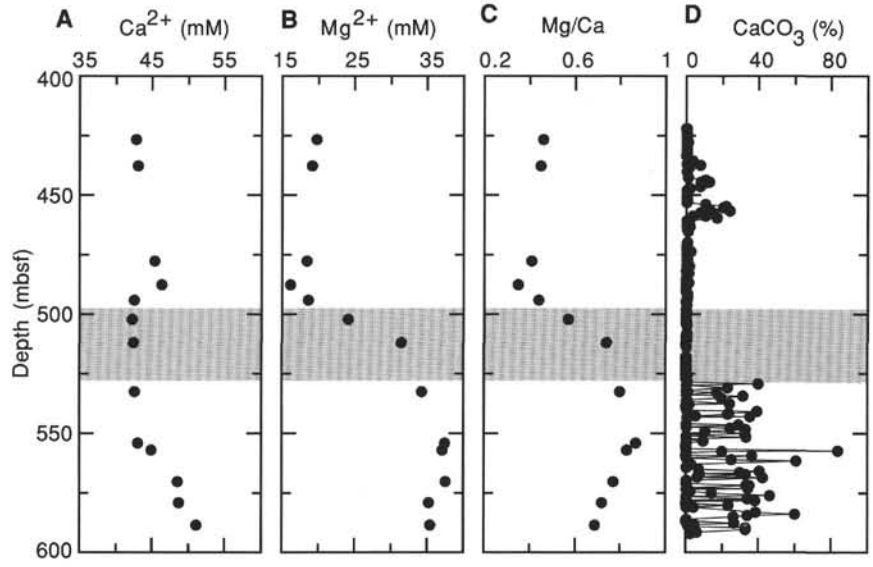

Figure 52. Concentration-depth profiles. **A.** Ca. **B.** Mg. **C.** Mg/Ca. **D.** Sediment inorganic carbon.

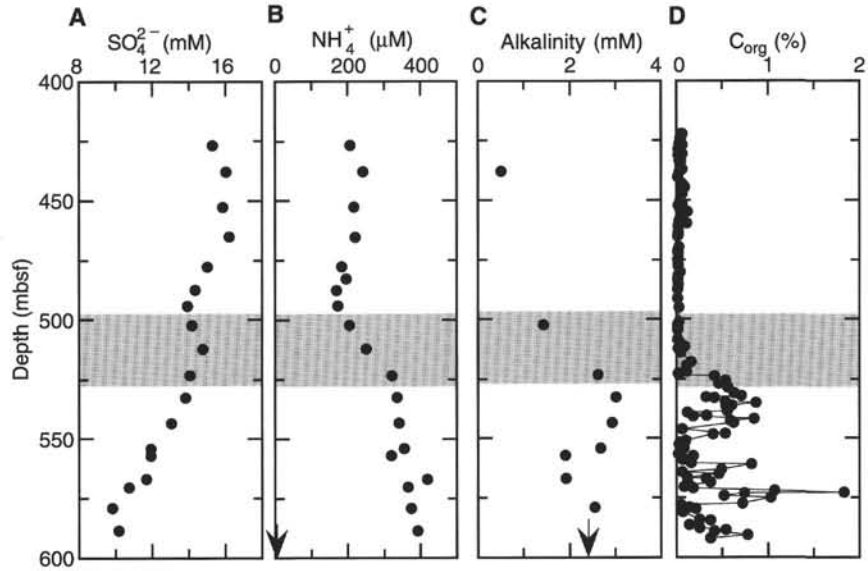

Figure 53. Concentration-depth profiles. **A.** Sulfate. **B.** Ammonia. **C.** Alkalinity. **D.** Sediment organic carbon.

the presence of recrystallized foraminifers and nannofossils and rhodochrosite veins (see "Lithostratigraphy and Sedimentology" section, this chapter). Dolomite is absent; it cannot precipitate at Mg/Ca ratios of <1, which prevail throughout the section drilled at this site (Fig. 52C).

The most interesting features of the depth profiles of dissolved Ca and Mg concentrations and Mg/Ca ratios (Fig. 52) are (1) similar to the dissolved-Cl and salinity-depth profiles, and overall, the Mg concentrations and Mg/Ca ratios are significantly lower above the décollement than within and below it, reflecting the greater dilution by H_2O of the accreted sediment section relative to the underthrusted section; and (2) these Ca and Mg depth profiles consist of three geochemically distinct sections: (a) above the minimum-Cl fluid-flow horizon, (b) between 495 and 555 mbsf, and (c) below 555 mbsf. The first is characterized by increasing Ca and decreasing Mg concentrations with depth at an approximately 1:1 ratio, suggesting a simple exchange reaction between the two cations (Ca <==> Mg), most frequently observed in association with volcanic-matter alteration or dolomite formation from calcite. However, dolomite is probably not important because of the low Mg/Ca ratios. This depth interval, indeed, contains more volcanic ash than the two deeper ones (see "Lithostratigraphy and Sedimentology" section, this chapter). In the middle section, between 495 and 555 mbsf, located in the lower porosity clay-rich section, the Ca and Mg concentration-depth profiles have been decoupled. Ca remains almost constant with depth, while the Mg concentration-depth profile is diffusive, similar to that of the Cl profile. This interval is also marked by more intense sulfate reduction and higher alkalinity values. These observations are consistent with little volcanic-matter alteration reactions in this interval, and with some carbonate formation maintaining the constant Ca concentration (and most probably also of Mn carbonate, rhodochrosite, formation), but not affecting the Mg concentration profile. This agrees with a near absence of ash layers in these sediments (see "Lithostratigraphy and Sedimentology" section, this chapter), indicating lower volcanic activity during this time interval. In the lowermost section, below 555 mbsf, Ca concentrations increase steeply, while Mg concentrations decrease gradually at a ratio of 4:1. The charge balance is compensated by decreases in the concentrations of Na and K (Ca <==> Mg + Na + K) with depth. This exchange reaction is typical of oceanic-basement alteration and/or more extensive volcanic-matter alteration involving seawater, at low to moderate temperatures (McDuff, 1981). The dissolved-Ca concentration-depth profile indi-

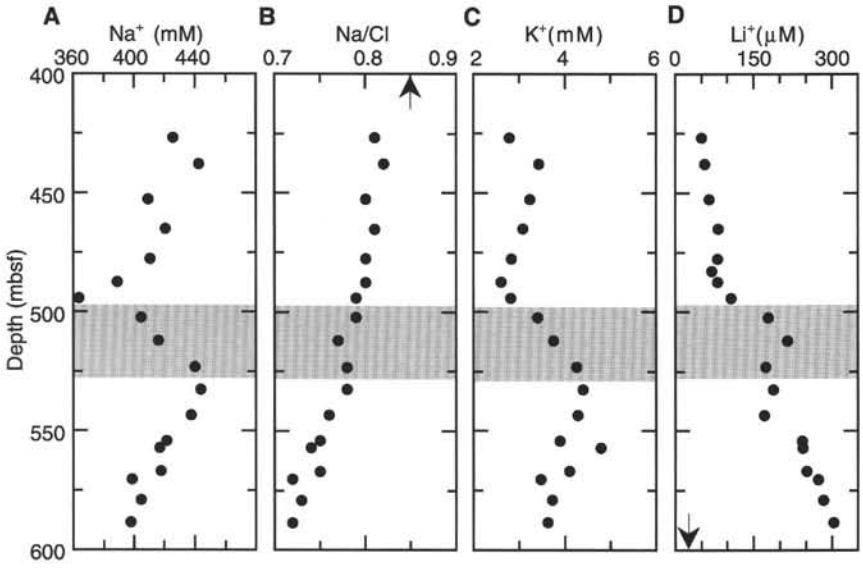

Figure 54. Concentration-depth profiles. **A.** Na. **B.** Na/Cl. **C.** K. **D.** Li.

cates active diagenesis within the décollement, involving Ca, but not Mg, removal. Therefore, only the Mg concentration-depth profile, similar to the Cl profile, indicates fluid flux across the décollement.

Sulfate, Ammonia, and Alkalinity

Probably the result of moderate sedimentation rates, coupled with low organic-matter content (TOC of <0.6%, except for a few higher values below 550 mbsf), and possibly also influenced by the nature of the organic matter, sulfate reduction has not reached completion within the section drilled at this site (Fig. 53A). Below the décollement, the dissolved-sulfate concentration profile is diffusional and indicates more intense sulfate reduction at greater depth. It suggests that sediments richer in organic matter most probably are present deeper, below the depth interval drilled at this site. The extrapolated dissolved sulfate profile to zero sulfate concentration occurs at 700 to 750 mbsf, in late Oligocene (or older?) sediments. Even within the depth interval drilled at this site, already in the late Oligocene section below 530 mbsf, the average TOC content is considerably higher than that in the younger section, as shown in Figure 53D. (For a more detailed discussion of the TOC profile, see "Organic Geochemistry" section, this chapter.)

The clear minimum in the dissolved-sulfate concentration-depth profile, situated at 494 mbsf, indicates dilution by the advected low-Cl fluid. This suggestion is confirmed by the dissolved-ammonia concentration-depth profile (Fig. 53B), which, except for the minimum concentration at 494 mbsf reflecting the intimate relationship between sulfate reduction and ammonia production, is essentially a mirror image of the dissolved-sulfate profile.

Despite the fewer data points in the alkalinity depth profile caused by the low yields of interstitial waters, especially above the décollement, a general trend of increasing alkalinity with depth below the décollement exists. There, sulfate reduction is more intense, particularly in the more organic-matter-rich sediments, as shown in Figure 53C. The coupling between intense volcanic-matter and/or oceanic-basement alteration reactions and carbonate diagenesis most likely is responsible for the generally low alkalinity values observed at this site, as well as at Sites 541 and 671, and for the good correlation of these low alkalinities with the steep Ca gradients (Fig. 52A), and the presence of carbonate (Fig. 52D). Between 495 and 555 mbsf, with little to no carbonate and volcanic ash, alkalinity values are elevated. Volcanic-matter alteration releases Ca and consumes alkalinity, and $CaCO_3$ dissolution releases Ca and produces alkalinity.

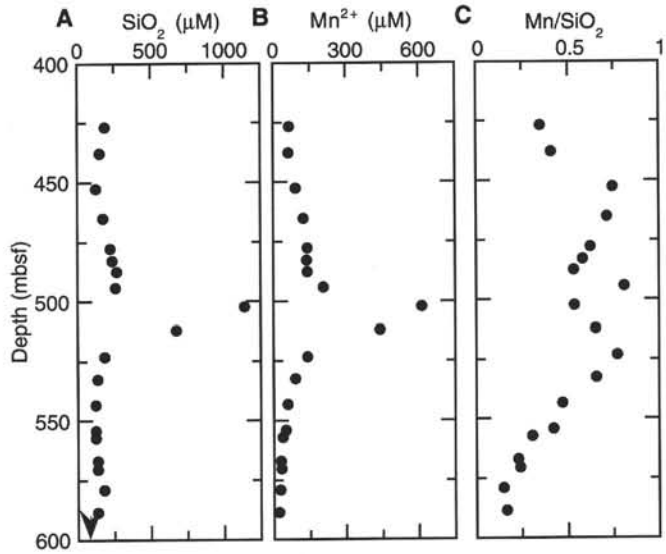

Figure 55. Concentration-depth profiles. **A.** Silica. **B.** Mn. **C.** Mn/Si.

Sodium, Potassium, and Lithium

Below 555 mbsf, where dissolved Ca concentrations increase steeply with depth but Mg concentrations only decrease gradually, the charge balance is compensated by concurrent depletions in dissolved Na and K concentrations. These coupled reactions have been documented in numerous marine interstitial-water profiles with active low to moderate temperature alteration of oceanic basement and/or volcanic matter, with minor diagenesis in the overlying sediments (McDuff, 1981).

Overall, the dissolved-Na concentration-depth profile (Fig. 54A) mimics that of dissolved Cl, including the distinct dilution minimum at 494 mbsf. The Na/Cl ratio depth profile, which is a typical diffusive exchange profile (Fig. 54B), indicates, however, that Na is being depleted relative to Cl at depth, with the main sink located below the interval drilled at this site. The Na/Cl profile does not have a minimum or maximum at the horizon of minimum dissolved-Cl concentration, at 494 mbsf, indicating that dissolved-Na is not being transported by the advected low-Cl fluid and that the minimum in the dissolved Na concentration profile simply reflects dilution with fresh

water. Dilution above the décollement is also seen in the dissolved K and Li concentration-depth profiles (Fig. 54C and -D, respectively).

The dissolved-K concentration-depth profile is most similar to the dissolved-Mg profile, and the dissolved-Li concentration-depth profile is extremely similar to that of dissolved Ca. As discussed above, the dissolved-Mg and -Ca concentration profiles are controlled by volcanic-matter alteration above the décollement and by volcanic-matter alteration and/or diffusive exchange reactions with oceanic basement below about 550 mbsf. At both depth intervals, K and Mg are being consumed and Li and Ca are being released through these reactions.

Silica and Manganese

Except for the very high dissolved-silica concentrations immediately below the upper "boundary" of the décollement, in Cores 156-948C-10X and -11X, at 498 to 514 mbsf, dissolved-silica concentrations are low throughout the section drilled, ranging between 120 and 270 µM (Fig. 55A). The high silica values encountered in Cores 156-948-10X and -11X, up to 1140 µM, reflect the special lithology of these sediments, a radiolarian-rich claystone, in which silica concentrations are controlled by the opal-A dissolution rate, solubility, and recrystallization rates.

Dissolved silica is not enriched in the advected low-Cl fluid, at 494 mbsf, ~4 m above the structurally defined décollement. The maximum in dissolved-silica concentrations clearly occurs at a greater depth (below 500 mbsf, in Core 156-948-10X) than the minimum in dissolved Cl at 494 mbsf (in Core 156-948C-9X), as seen in Figures 51A and 55A, respectively. Because of the significantly lower resolution of data points available during the cruise, Leg 110 geochemists incorrectly concluded that dissolved silica is being carried by the advected low-Cl fluid (Gieskes et al., 1990).

The dissolved-manganese concentration-depth profile is generally similar to that of dissolved silica (Fig. 55A, -B). Maximum Mn concentration of >600 µM occurs in Core 156-948-10X. Like silica, the high Mn concentrations reflect mostly an original depositional feature. The radiolarian-rich claystones of Cores 156-948C-10X and -11X contain dark gray to brownish gray bands, which are enriched in Mn oxides (see "Lithostratigraphy and Sedimentology" section, this chapter) that are being remobilized in this suboxic environment.

The advected low-Cl fluid at 494 mbsf, however, is enriched in dissolved Mn, as indicated in Figure 55C, which shows a distinct enrichment peak of Mn when normalized to silica. A similar clear enrichment peak is obtained when Mn is normalized to Cl.

CORE PHYSICAL PROPERTIES

Introduction

The objectives of the physical properties group for Site 948 are twofold:

1. To provide "ground truth" for special techniques applied during Leg 156 by providing data for correlating and calibrating downhole measurements, specifically LWD, standard wireline logging, VSP experiments, and packer tests.
2. To provide a comprehensive downhole profile of physical property measurements throughout the lower part of the accreted section, the upper part of the subducted section, and the décollement, especially within the critical interval that will be subject to long-term monitoring.

Both objectives were met. Supplemental information was available from previous drilling of Site 671 during Leg 110, which provided an additional measure of control for most index physical properties. A total of 240 samples of 15-cm^3 volume was recovered from split sections of the core; these were processed to yield an average distance of 75 cm between samples, a rate which yields a ratio of one laboratory value to five LWD measurements.

Density and Porosity

Two methods were used to determine sediment bulk density: the mass/volume method ("index properties") and gamma-ray attenuation method (GRAPE) (see "Explanatory Notes" chapter, this volume). Because of the smaller diameter and the "biscuited" nature of XCB cores, the GRAPE density data were highly scattered and significantly lower than the bulk densities by the mass/volume method (Fig. 56A–C) and those derived from the CDN tool in the LWD assembly (see "Downhole Logging" section, this chapter).

Samples for index and other physical property measurements were selected from intact drill biscuits at regularly spaced intervals at a rate of two per section (75-cm resolution). Efforts were made to sample representative lithologies of each section. Measurements of wet and dry volume and wet and dry mass were entered into program "IP/4D," which calculates water content, bulk density, grain density, porosity, void ratio, and "dry bulk density." The mud-line cores of Holes 948B and 948C show porosities of 70% to 75% and bulk densities of about 1.5 g/cm^3, typical for shallow marine mud (Table 21, Fig. 56D, -F). With the exception of one horizon at 1.2 mbsf, index properties in the shallow part of both Holes 948B and 948C closely match those measured from Site 671. Although the GRAPE bulk densities are on average 0.1 g/cm^3 lower than those determined from core samples, they exhibit the same relative downhole changes in both mud-line cores (Fig. 56A).

The XCB-cored section of Hole 948C (421–592 mbsf) shows four characteristic porosity and bulk-density intervals (Fig. 56). From 421 to 464 mbsf, the data display considerable scatter, with an average porosity value of 55% and a bulk density of 1.9 g/cm^3. This is followed by an interval of significantly less scatter that has an average porosity of 57% and a bulk density of 1.8 g/cm^3 down to 498 mbsf. These first two intervals show an anomalous trend of slightly increasing porosity. The third interval, from 498 to 518 mbsf, is characterized by a steep porosity decrease with a mean value of 54%. Below this, the fourth interval (the underthrust sediments in the lowermost part of Hole 948C) from 518 to 592 mbsf, displays again a considerable amount of scatter with porosities from 37% to 58%, with an average value of about 50%, without apparent downhole trend. This pattern is again mirrored by the downhole profile of wet bulk density that ranges from 1.8 to 2.2 g/cm^3, averaging about 2 g/cm^3 over the same depth intervals.

The boundaries of the intervals mentioned above are matched by those defining lithological subunits (see "Lithostratigraphy and Sedimentology" section, this chapter). In the accreted section (structural Domain I), the topmost cored interval (421–464 mbsf) corresponds to lithologic Subunits IIA and IIB, while the second interval identified comprises lithologic Subunits IIC and IID. The correlation of the third interval (498–518 mbsf) with lithologic Subunits IIE, IIF, and IIIA in structural Domain II, the décollement zone, is less clear cut: only the abrupt change in all index properties occurring over the lower 10 m of this interval (between 508 and 518 mbsf) coincides with lithologic Subunit IIF. A strong discontinuity in the downhole pattern of both porosity and bulk density is apparent at the boundary between lithologic Units II and III, while no offset is found at the boundary between structural Domains II and III (529 mbsf). Evidently, the downhole variation observed in porosity and density primarily reflects the lithological composition of the sediment, rather than its structural and deformational properties.

The GRAPE densities in the XCB-cored interval are highly scattered and significantly lower than those measured on discrete samples, most likely because the GRAPE sampled the strongly disturbed and biscuited sediment as well as appreciable amounts of low-density drill slurry. The GRAPE data were therefore processed by discarding data from the top 30 cm of the core and replacing each set of five adjacent measurements by the mean of the largest and second-largest values. Although this somewhat limited the scatter, the densities still vary by 0.2 g/cm^3 over a scale of a few meters, rendering them useless

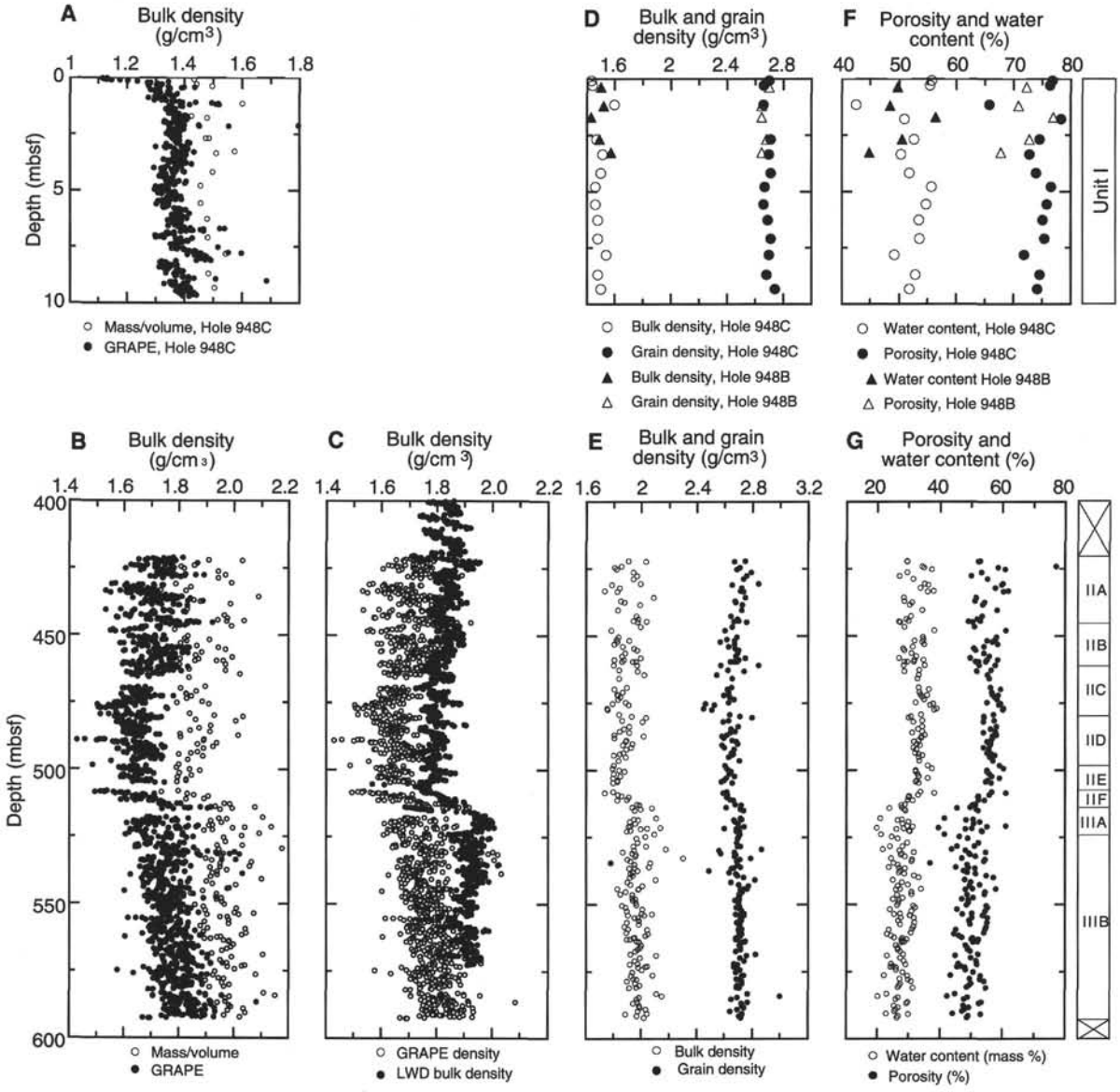

Figure 56. Site 948 density and porosity data. Smaller graphs (top row) present data from Holes 948B and 948C APC mud-line cores. Larger graphs (bottom row) present data from Hole 948C XCB section drilled through décollement. **A.** Comparison of GRAPE bulk densities with those measured on core samples in mud-line Cores 156-948C-1H and 948B-1H. **B.** Comparison of GRAPE bulk densities with those measured on core samples, Cores 156-948C-2X through -19X. **C.** Comparison of GRAPE densities with those derived from the LWD CDN tool, Hole 948C. **D.** Core-sample bulk and grain densities in mud-line Cores 156-948B-1H and 948C-1H. **E.** Core-sample bulk and grain densities in Hole 948C, XCB-cored section (Cores 156-948C-2X through -19X). **F.** Core-sample porosity and water content (percent of wet weight), in mud-line Cores 156-948B-1H and 948C-1H. **G.** Core-sample porosity and water content (percent of wet weight) in Hole 948C, XCB-cored section.

for any quantitative estimate of the actual sediment bulk density. Yet, the relative changes in bulk densities over the four intervals mentioned above are discernible, as well as the trend toward higher densities in the underthrust section.

The grain-density profile shows a less pronounced separation of the upper part of the accreted section. All grain densities calculated show a large degree of variation within a general trend of decreasing values between 420 and 508 mbsf, while no clear trend downhole is apparent between 508 and 515 mbsf, with average grain densities of 2.66 g/cm^3.

Compressional-wave Velocity

P-wave velocity was measured by three methods: the *P*-wave logger (PWL) on the MST, the digital sonic velocimeter (DSV), and the Hamilton Frame velocimeter.

P-*wave Velocity Logger*

The transverse (i.e., normal to the core-axis) *P*-wave velocity was measured at 10-cm intervals along all core sections with the PWL. Longitudinal (i.e., parallel to the core axis) velocities were measured with the DSV in the soft sediment of the mud-line (APC) cores. Three directions (V_{pl}, V_{pt1}, and V_{pt2}) were measured on cuboid samples cut from the split cores (Table 22) (see "Explanatory Notes" chapter, this volume).

Velocities from the PWL were compared with results from the DSV and the Hamilton Frame measurements on core samples (Fig. 57A, -B). PWL velocities are consistently lower. These are scattered, but show a gradual downhole increase below 530 m, in agreement with the core sample velocities. In mud-line Cores 156-948B-1H and 948C-1H, PWL velocities are lower than DSV velocities, but are less scattered than in XCB cores.

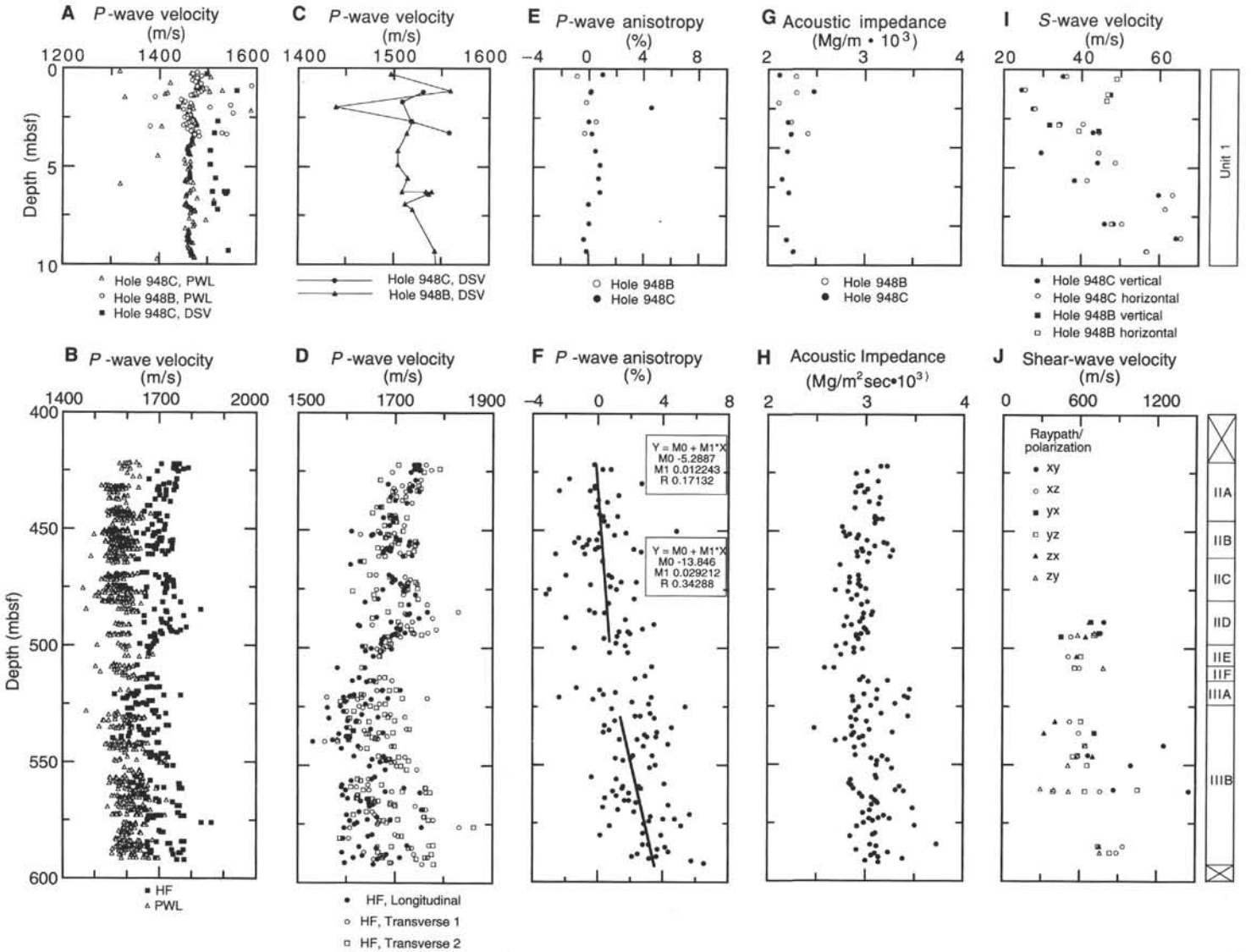

Figure 57. Site 948 velocity data. Smaller graphs (top row) present data from Holes 948B and 948C mud-line cores. Larger graphs (bottom row) present data from Hole 948C XCB section drilled through décollement. PWL = *P*-wave logger; DSV = digital sonic velocimeter; HF = Hamilton Frame. **A.** Comparison of PWL and DSV (vertical and horizontal) *P*-wave velocities in mud-line Cores 156-948B-1H and 948C-1H. **B.** Comparison of PWL and Hamilton Frame (horizontal) *P*-wave velocities in XCB cores from Hole 948C. **C.** Comparison of *P*-wave velocities in mud-line Cores 156-948B-1H and 948C-1H. **D.** Longitudinal and transverse compressional (*P*-wave) velocities, measured with the Hamilton Frame on core samples from Hole 948C. **E.** Transverse *P*-wave velocity anisotropy in mud-line Cores 156-948B-1H and 948C-1H. **F.** Transverse *P*-wave velocity anisotropy in XCB cores from Hole 948C. **G.** Acoustic impedance, based on longitudinal *P*-wave velocities in mud-line Cores 156-948B-1H and 948C-1H. **H.** Acoustic impedance, based on longitudinal compressional (*P*-wave) velocities in XCB cores from Hole 948C. **I.** Horizontal and vertical shear-wave velocities in mud-line Cores 156-948B-1H and 948C-1H. **J.** Shear-wave velocities measured on core samples from Cores 156-948C-9X through -19X. Symbols indicate propagation and polarization directions as defined in the inset diagram.

Table 21. Density and porosity data, Site 948.

Core, section	Depth (mbsf)	Wet bulk density (g/cm^3)	Dry bulk density (g/cm^3)	Grain density (g/cm^3)	Porosity B (%)	Porosity C (%)	Water content (% wet)	Water content (% dry)	Void ratio B	Void ratio C
156-948B-										
1H-1	0.37	1.50	1.49	2.70	72.57	72.28	49.69	98.78	2.65	2.61
1H-1	1.20	1.52	1.50	2.65	72.00	70.89	48.48	94.11	2.57	2.43
1H-2	1.70	1.43	1.40	2.65	78.54	77.01	56.43	129.49	3.66	3.35
1H-2	2.70	1.49	1.47	2.68	73.33	72.78	50.56	102.26	2.75	2.67
1H-3	3.28	1.57	1.55	2.65	68.97	67.85	44.89	81.46	2.22	2.11
156-948C-										
1H-1	0.08	1.43	1.41	2.70	77.83	76.83	55.68	125.63	3.51	3.32
1H-1	0.30	1.44	1.41	2.66	77.97	76.39	55.45	124.47	3.54	3.24
1H-1	1.14	1.60	1.58	2.66	66.54	65.79	42.54	74.02	1.99	1.92
1H-2	1.79	1.48	1.57	3.55	73.64	78.32	51.03	104.21	2.79	3.61
1H-2	2.69	1.47	1.45	2.71	75.82	74.62	52.68	111.32	3.14	2.94
1H-3	3.36	1.51	1.48	2.70	74.33	72.85	50.42	101.68	2.90	2.68
1H-3	4.18	1.50	1.46	2.71	75.82	73.98	51.83	107.60	3.13	2.84
1H-4	4.80	1.46	1.41	2.67	79.12	76.61	55.65	125.49	3.79	3.28
1H-4	5.58	1.46	1.42	2.66	77.86	75.88	54.79	121.20	3.52	3.15
1H-5	6.28	1.48	1.44	2.69	77.30	75.12	53.53	115.18	3.41	3.02
1H-5	7.10	1.48	1.44	2.71	77.62	75.42	53.67	115.85	3.47	3.07
1H-6	7.80	1.54	1.50	2.70	74.19	71.92	49.27	97.13	2.87	2.56
1H-6	8.70	1.48	1.44	2.68	76.59	74.60	52.92	112.40	3.27	2.94
1H-7	9.34	1.50	1.47	2.74	76.09	74.23	51.82	107.56	3.18	2.88
2X-1	422.20	1.91	1.84	2.75	54.94	52.88	29.49	41.82	1.22	1.12
2X-1	422.26	2.03	1.81	2.67	58.68	52.29	29.58	42.01	1.42	1.10
2X-3	424.10	1.86	2.30	6.58	62.31	77.08	34.36	52.35	1.65	3.36
2X-3	424.52	1.81	1.72	2.71	61.58	58.63	34.89	53.58	1.60	1.42
2X-4	425.33	1.82	1.67	2.69	66.34	60.98	37.34	59.58	1.97	1.56
2X-4	426.46	1.94	1.85	2.79	55.94	53.29	29.49	41.83	1.27	1.14
2X-5	427.75	1.97	1.89	2.76	52.13	50.03	27.10	37.18	1.09	1.00
2X-6	428.82	1.94	1.79	2.73	59.82	55.12	31.51	46.01	1.49	1.23
3X-1	430.56	1.99	1.75	2.85	68.37	60.10	35.15	54.21	2.16	1.51
3X-1	431.05	1.79	1.68	2.66	63.40	59.64	36.30	56.97	1.73	1.48
3X-2	432.16	1.84	1.74	2.72	60.86	57.62	33.83	51.13	1.55	1.36
3X-2	433.39	1.73	1.67	2.72	64.15	61.80	37.89	61.00	1.79	1.62
3X-3	433.51	1.83	1.71	2.74	64.47	60.21	36.15	56.63	1.81	1.51
3X-4	435.69	2.09	1.86	2.75	57.94	51.57	28.39	39.65	1.38	1.07
3X-5	436.98	1.85	1.83	2.68	51.76	51.14	28.60	40.06	1.07	1.05
3X-5	437.45	1.88	1.78	2.68	56.98	54.16	31.09	45.11	1.32	1.18
3X-6	438.47	1.99	1.81	2.73	58.92	53.73	30.36	43.59	1.43	1.16
4X-1	440.26	1.83	1.73	2.72	61.56	58.24	34.43	52.50	1.60	1.39
4X-2	442.68	1.97	1.78	2.65	58.92	53.37	30.71	44.32	1.43	1.14
4X-3	443.65	1.98	1.83	2.69	56.27	52.00	29.18	41.19	1.29	1.08
4X-3	444.52	1.94	1.82	2.70	56.55	52.86	29.82	42.49	1.30	1.12
4X-4	444.72	2.04	1.86	2.67	53.71	49.03	26.98	36.95	1.16	0.96
4X-4	444.85	1.98	1.89	2.76	52.72	50.33	27.35	37.64	1.12	1.01
4X-5	446.52	1.99	1.82	2.66	55.77	51.04	28.68	40.20	1.26	1.04
4X-6	448.04	1.78	1.64	2.60	66.66	61.16	38.27	62.00	2.00	1.57
5X-1	450.43	1.83	1.72	2.69	61.71	58.04	34.50	52.67	1.61	1.38
5X-1	451.27	1.82	1.70	2.62	61.84	57.63	34.76	53.28	1.62	1.36
5X-2	451.74	1.91	1.77	2.67	59.29	54.86	31.78	46.59	1.46	1.22
5X-2	452.23	1.83	1.69	2.57	61.14	56.64	34.28	52.15	1.57	1.31
5X-3	453.11	1.81	1.71	2.67	61.73	58.43	35.01	53.87	1.61	1.41
5X-3	454.06	1.87	1.76	2.63	57.07	53.95	31.33	45.62	1.33	1.17
5X-4	454.78	1.95	1.84	2.68	53.62	50.69	28.24	39.36	1.16	1.03
5X-4	455.41	1.97	1.84	2.70	54.96	51.37	28.58	40.01	1.22	1.06
5X-5	456.42	1.88	1.79	2.69	56.89	54.10	30.97	44.86	1.32	1.18
5X-6	457.61	1.86	1.76	2.68	58.94	55.69	32.43	48.00	1.44	1.26
5X-6	458.28	1.99	1.89	2.75	52.21	49.59	26.81	36.64	1.09	0.98
5X-6	458.80	1.87	1.77	2.68	58.15	55.01	31.82	46.68	1.39	1.22
5X-7	458.88	1.80	1.72	2.70	61.16	58.38	34.72	53.20	1.57	1.40
5X-CC	459.47	1.86	1.76	2.64	57.59	54.52	31.75	46.52	1.36	1.20
6X-1	459.62	1.96	1.84	2.69	54.82	51.32	28.65	40.15	1.21	1.05
6X-1	459.62	1.94	1.81	2.67	55.90	52.25	29.57	41.98	1.27	1.09
6X-1	460.84	1.80	1.68	2.57	61.74	57.59	35.10	54.08	1.61	1.36
6X-2	460.96	1.97	1.89	2.85	54.57	52.38	28.37	39.61	1.20	1.10
6X-3	462.82	1.84	1.73	2.63	59.89	56.21	33.37	50.09	1.49	1.28
6X-3	463.22	1.97	1.85	2.74	55.04	51.76	28.61	40.07	1.22	1.07
6X-4	464.56	2.02	1.70	2.54	65.63	55.25	33.24	49.79	1.91	1.23
6X-CC	465.81	1.84	1.74	2.66	58.82	55.83	32.78	48.77	1.43	1.26
7X-1	469.10	1.90	1.74	2.65	61.33	56.17	33.14	49.56	1.59	1.28
7X-1	469.83	1.81	1.67	2.62	64.05	59.34	36.33	57.06	1.78	1.46
7X-2	470.96	1.86	1.72	2.63	60.94	56.38	33.49	50.35	1.56	1.29
7X-2	471.73	1.83	1.72	2.63	60.25	56.67	33.78	51.02	1.52	1.31
7X-3	472.09	1.83	1.68	2.60	63.91	58.55	35.79	55.75	1.77	1.41
7X-3	472.80	1.85	1.71	2.64	61.94	57.42	34.38	52.40	1.63	1.35
7X-4	473.60	1.83	1.71	2.67	62.36	58.30	34.92	53.67	1.66	1.40
7X-4	474.73	1.89	1.75	2.63	59.31	54.93	32.22	47.54	1.46	1.22
7X-5	475.13	1.79	1.61	2.46	66.14	59.34	37.80	60.77	1.95	1.46
7X-5	475.77	1.91	1.64	2.52	68.42	58.82	36.70	57.99	2.17	1.43
7X-6	476.95	1.76	1.59	2.45	66.59	60.28	38.87	63.59	1.99	1.52
7X-6	477.36	1.76	1.62	2.51	65.44	60.14	38.12	61.60	1.89	1.51
8X-1	479.22	1.84	1.72	2.64	61.15	57.07	34.04	51.61	1.57	1.33
8X-1	479.92	1.93	1.80	2.71	57.84	53.96	30.72	44.33	1.37	1.17
8X-2	480.39	2.03	1.84	2.80	59.50	53.91	29.97	42.81	1.47	1.17
8X-2	481.54	1.86	1.71	2.63	62.29	57.23	34.26	52.12	1.65	1.34
8X-3	481.79	2.01	1.75	2.59	61.75	53.76	31.50	45.99	1.61	1.16
8X-4	483.62	1.92	1.73	2.70	64.32	58.00	34.40	52.45	1.80	1.38
8X-4	484.61	1.87	1.74	2.65	60.35	55.99	33.00	49.25	1.52	1.27

Table 21 (continued).

Core, section	Depth (mbsf)	Wet bulk density (g/cm^3)	Dry bulk density (g/cm^3)	Grain density (g/cm^3)	Porosity B (%)	Porosity C (%)	Water content (% wet)	Water content (% dry)	Void ratio B	Void ratio C
8X-5	485.36	1.84	1.72	2.68	61.65	57.69	34.29	52.19	1.61	1.36
8X-5	485.85	1.91	1.77	2.64	58.17	53.83	31.15	45.25	1.39	1.17
8X-6	486.87	1.80	1.69	2.62	61.89	58.05	35.15	54.21	1.62	1.38
8X-6	487.23	2.02	1.70	2.58	67.26	56.70	34.19	51.95	2.05	1.31
8X-7	487.82	1.81	1.70	2.59	60.09	56.66	34.07	51.68	1.51	1.31
9X-1	488.92	1.89	1.74	2.66	61.17	56.22	33.13	49.54	1.58	1.28
9X-1	489.34	1.89	1.77	2.69	58.38	54.85	31.66	46.33	1.40	1.21
9X-2	490.14	1.94	1.76	2.69	61.68	56.00	32.63	48.44	1.61	1.27
9X-2	490.73	1.87	1.71	2.58	61.14	55.98	33.54	50.48	1.57	1.27
9X-3	491.48	1.92	1.75	2.60	59.08	53.77	31.45	45.87	1.44	1.16
9X-3	492.18	1.89	1.76	2.67	59.79	55.54	32.40	47.93	1.49	1.25
9X-4	493.49	1.87	1.76	2.65	58.39	54.89	32.01	47.07	1.40	1.22
9X-4	493.91	1.84	1.74	2.66	59.89	56.43	33.27	49.86	1.49	1.30
9X-5	494.47	1.80	1.71	2.65	60.38	57.48	34.37	52.36	1.52	1.35
9X-5	495.21	1.89	1.73	2.63	60.98	55.94	33.09	49.45	1.56	1.27
9X-6	496.33	1.83	1.75	2.71	59.64	56.93	33.34	50.02	1.48	1.32
10X-1	498.21	1.80	1.67	2.61	63.31	58.89	36.04	56.34	1.73	1.43
10X-1	499.34	1.79	1.66	2.62	65.32	60.40	37.38	59.69	1.88	1.53
10X-2	500.11	1.84	1.75	2.63	57.73	54.86	32.16	47.40	1.37	1.22
10X-2	500.50	1.88	1.75	2.64	58.95	55.05	32.17	47.43	1.44	1.22
10X-3	501.29	1.80	1.74	2.63	57.74	55.68	32.82	48.86	1.37	1.26
10X-3	502.09	1.85	1.74	2.67	59.89	56.49	33.24	49.80	1.49	1.30
10X-4	502.85	1.80	1.68	2.61	63.08	58.92	35.99	56.24	1.71	1.43
10X-4	503.84	1.83	1.73	2.59	58.18	55.07	32.63	48.44	1.39	1.23
10X-5	504.27	1.83	1.73	2.58	57.60	54.54	32.30	47.72	1.36	1.20
10X-5	504.69	1.79	1.74	2.66	58.06	56.26	33.15	49.58	1.38	1.29
11X-1	508.06	1.80	1.72	2.62	59.20	56.56	33.75	50.94	1.45	1.30
11X-1	508.40	1.74	1.64	2.59	64.80	61.02	38.22	61.87	1.84	1.57
11X-1	509.07	1.83	1.73	2.62	58.94	55.73	32.99	49.24	1.44	1.26
11X-2	509.47	1.86	1.79	2.62	54.41	52.35	30.04	42.95	1.19	1.10
11X-2	510.04	1.91	1.79	2.62	55.65	52.13	29.89	42.62	1.25	1.09
11X-3	510.81	1.89	1.80	2.64	55.04	52.25	29.79	42.42	1.22	1.09
11X-3	511.25	1.83	1.77	2.66	55.84	54.25	31.32	45.60	1.26	1.19
11X-4	512.57	1.97	1.83	2.67	55.16	51.28	28.74	40.32	1.23	1.05
11X-4	512.88	1.99	1.87	2.72	53.53	50.30	27.61	38.14	1.15	1.01
11X-5	513.87	1.93	1.82	2.61	52.60	49.65	27.89	38.67	1.11	0.99
11X-5	514.01	2.08	1.95	2.71	48.55	45.48	23.95	31.49	0.94	0.83
11X-5	514.55	2.00	1.84	2.71	55.70	51.47	28.59	40.03	1.26	1.06
11X-CC	515.01	1.95	1.84	2.74	55.15	52.14	28.97	40.79	1.23	1.09
12X-1	517.87	2.11	2.02	2.72	43.16	41.36	21.00	26.59	0.76	0.71
12X-1	518.19	1.95	1.86	2.73	52.88	50.64	27.83	38.55	1.12	1.03
12X-1	518.45	1.98	1.87	2.67	51.04	48.38	26.46	35.99	1.04	0.94
12X-2	519.19	1.92	1.81	2.68	55.91	52.67	29.88	42.61	1.27	1.11
12X-2	519.83	1.96	1.85	2.70	53.64	50.71	28.10	39.08	1.16	1.03
12X-3	520.67	1.92	2.11	3.82	55.54	61.08	29.61	42.06	1.25	1.57
12X-3	520.96	1.91	1.80	2.74	58.30	54.91	31.28	45.52	1.40	1.22
12X-3	521.47	2.14	2.04	2.70	41.48	39.56	19.88	24.82	0.71	0.65
12X-3	521.73	2.04	1.81	2.60	56.67	50.22	28.46	39.78	1.31	1.01
12X-4	521.92	2.00	1.89	2.68	50.94	48.11	26.14	35.38	1.04	0.93
12X-4	522.52	1.92	1.81	2.71	56.45	53.20	30.08	43.01	1.30	1.14
12X-4	522.73	1.89	1.80	2.69	56.10	53.35	30.36	43.60	1.28	1.14
12X-5	523.85	2.09	2.01	2.71	43.16	41.51	21.14	26.80	0.76	0.71
12X-5	524.85	2.03	1.93	2.70	48.76	46.29	24.63	32.68	0.95	0.86
12X-6	525.49	1.96	1.88	2.70	51.02	48.85	26.62	36.28	1.04	0.95
13X-1	526.94	1.97	1.82	2.69	56.74	52.31	29.48	41.81	1.31	1.10
13X-1	528.22	2.03	1.94	2.69	47.59	45.35	23.99	31.56	0.91	0.83
13X-2	528.44	1.94	1.86	2.72	53.21	50.86	28.08	39.05	1.14	1.04
13X-2	529.31	2.18	2.06	2.87	46.09	43.68	21.71	27.73	0.86	0.78
13X-3	529.86	1.95	1.82	2.56	51.37	48.07	27.04	37.05	1.06	0.93
13X-3	530.49	1.87	1.77	2.67	57.56	54.61	31.58	46.15	1.36	1.20
13X-3	530.93	1.94	1.81	2.58	52.53	49.18	27.80	38.50	1.11	0.97
13X-4	531.43	1.96	1.86	2.68	52.39	49.68	27.37	37.69	1.10	0.99
13X-4	532.03	1.96	1.83	2.67	54.95	51.34	28.79	40.44	1.22	1.06
13X-5	532.81	2.30	1.96	2.79	54.92	46.85	24.45	32.37	1.22	0.88
13X-5	533.21	1.90	1.79	2.71	57.48	54.30	31.00	44.92	1.35	1.19
13X-5	533.79	1.92	1.79	2.69	57.96	54.01	30.92	44.76	1.38	1.17
13X-6	534.49	2.06	1.50	1.78	50.73	36.88	25.17	33.63	1.03	0.58
13X-6	535.15	1.95	1.88	2.69	50.36	48.59	26.44	35.94	1.01	0.95
13X-7	536.08	2.06	1.95	2.72	47.51	45.10	23.65	30.98	0.91	0.82
13X-7	536.30	1.95	1.86	2.67	51.34	49.01	26.97	36.93	1.05	0.96
14X-1	536.52	1.91	1.82	2.65	53.87	51.21	28.85	40.54	1.17	1.05
14X-1	537.56	1.98	1.79	2.48	52.45	47.54	27.20	37.37	1.10	0.91
14X-2	538.03	1.94	1.85	2.63	50.88	48.58	26.89	36.77	1.04	0.94
14X-2	538.60	1.92	1.83	2.68	53.77	51.28	28.67	40.19	1.16	1.05
14X-3	539.19	1.94	1.78	2.69	59.73	54.78	31.55	46.09	1.48	1.21
14X-3	539.80	1.92	1.76	2.74	62.05	57.02	33.17	49.63	1.63	1.33
14X-4	540.79	2.10	1.96	2.82	51.34	47.89	25.02	33.37	1.06	0.92
14X-4	541.76	1.90	1.84	2.65	51.52	49.82	27.77	38.44	1.06	0.99
14X-5	542.71	1.92	1.82	2.70	55.69	52.66	29.68	42.21	1.26	1.11
14X-5	543.02	2.01	1.91	2.77	51.95	49.38	26.50	36.06	1.08	0.98
14X-6	544.11	1.98	1.89	2.76	52.86	50.32	27.30	37.56	1.12	1.01
14X-6	544.12	1.83	1.75	2.73	60.49	57.82	33.93	51.36	1.53	1.37
14X-6	544.51	1.98	1.90	2.71	49.98	48.09	25.91	34.97	1.00	0.93
14X-CC	545.21	1.89	1.80	2.73	57.03	54.42	30.96	44.85	1.33	1.19
15X-1	546.06	1.85	1.80	2.71	55.68	54.18	30.91	44.75	1.26	1.18
15X-1	546.46	1.94	1.89	2.71	49.72	48.59	26.30	35.68	0.99	0.94
15X-2	547.41	1.94	1.85	2.70	52.86	50.60	27.98	38.86	1.12	1.02
15X-2	547.94	1.96	1.92	2.71	47.77	46.85	25.02	33.36	0.91	0.88

Table 21 (continued).

Core, section	Depth (mbsf)	Wet bulk density (g/cm^3)	Dry bulk density (g/cm^3)	Grain density (g/cm^3)	Porosity B (%)	Porosity C (%)	Water content (% wet)	Water content (% dry)	Void ratio B	Void ratio C
15X-3	548.42	1.94	1.87	2.68	50.81	48.98	26.87	36.74	1.03	0.96
15X-3	549.18	1.96	1.88	2.70	51.13	49.08	26.75	36.52	1.05	0.96
15X-4	550.17	1.97	1.89	2.70	50.36	48.42	26.25	35.59	1.01	0.94
15X-4	550.51	1.86	1.78	2.71	57.15	54.81	31.48	45.93	1.33	1.21
15X-4	551.11	1.89	1.77	2.68	58.99	55.21	32.00	47.06	1.44	1.23
15X-5	551.68	2.01	1.95	2.71	47.01	45.50	23.96	31.52	0.89	0.83
15X-5	552.45	1.90	1.80	2.72	57.14	54.27	30.87	44.65	1.33	1.19
15X-6	553.32	2.00	1.88	2.74	53.42	50.17	27.33	37.60	1.15	1.01
15X-6	553.50	2.07	1.90	2.68	51.53	47.20	25.45	34.14	1.06	0.89
15X-6	553.98	2.02	1.82	2.74	59.96	53.89	30.42	43.71	1.50	1.17
15X-6	553.99	1.90	1.81	2.72	56.27	53.55	30.29	43.46	1.29	1.15
15X-7	554.84	1.98	1.87	2.72	53.16	50.26	27.54	38.01	1.13	1.01
16X-1	554.92	1.95	1.78	2.72	60.26	55.13	31.66	46.32	1.52	1.23
16X-1	555.86	1.98	1.88	2.72	51.75	49.20	26.74	36.50	1.07	0.97
16X-2	556.54	1.89	1.77	2.69	58.76	55.00	31.78	46.59	1.42	1.22
16X-2	557.21	1.98	1.87	2.71	52.62	49.69	27.20	37.37	1.11	0.99
16X-3	558.19	1.88	1.78	2.71	57.72	54.80	31.46	45.90	1.36	1.21
16X-3	559.06	1.90	1.80	2.72	57.68	54.45	31.03	44.98	1.36	1.20
16X-4	559.47	2.04	1.95	2.70	47.14	44.98	23.64	30.97	0.89	0.82
16X-4	560.39	1.89	1.80	2.71	56.59	53.90	30.68	44.26	1.30	1.17
16X-5	560.97	2.05	1.97	2.72	46.12	44.40	23.10	30.05	0.86	0.80
16X-5	561.58	2.03	1.94	2.71	48.20	46.02	24.34	32.18	0.93	0.85
16X-5	562.14	1.95	1.91	2.69	48.17	47.02	25.27	33.82	0.93	0.89
16X-6	562.59	1.94	1.85	2.68	53.03	50.45	28.00	38.88	1.13	1.02
16X-6	562.90	1.89	1.82	2.70	54.37	52.30	29.40	41.65	1.19	1.10
16X-6	563.02	1.92	1.85	2.68	51.63	49.96	27.61	38.13	1.07	1.00
16X-7	563.60	1.96	1.87	2.75	53.49	50.98	27.92	38.73	1.15	1.04
16X-7	563.86	1.98	1.85	2.75	55.59	51.92	28.72	40.29	1.25	1.08
17X-1	564.11	1.98	1.87	2.73	53.65	50.55	27.73	38.38	1.16	1.02
17X-1	565.14	2.00	1.90	2.71	50.63	48.10	25.96	35.07	1.03	0.93
17X-2	565.93	1.99	1.89	2.71	51.33	48.74	26.42	35.90	1.05	0.95
17X-2	566.61	1.98	1.89	2.72	51.19	48.94	26.54	36.13	1.05	0.96
17X-3	567.30	1.96	1.86	2.68	52.11	49.55	27.28	37.52	1.09	0.98
17X-3	568.48	1.92	1.89	2.82	53.00	52.08	28.28	39.43	1.13	1.09
17X-4	568.81	2.11	1.98	2.76	47.53	44.76	23.12	30.07	0.91	0.81
17X-4	569.74	1.99	1.87	2.71	52.98	49.80	27.26	37.48	1.13	0.99
17X-5	570.93	1.95	1.86	2.74	54.13	51.53	28.42	39.70	1.18	1.06
17X-6	571.98	1.97	1.92	2.67	47.14	45.75	24.46	32.38	0.89	0.84
17X-6	572.37	1.92	1.83	2.69	54.04	51.66	28.90	40.65	1.18	1.07
17X-6	572.98	2.04	1.91	2.68	49.88	46.60	25.04	33.40	1.00	0.87
17X-7	573.22	2.03	1.92	2.67	48.06	45.50	24.26	32.03	0.93	0.83
18X-1	573.39	1.98	1.89	2.69	50.21	47.96	26.00	35.14	1.01	0.92
18X-1	574.27	2.00	1.90	2.71	50.85	48.16	26.00	35.14	1.03	0.93
18X-2	575.08	1.93	1.84	2.68	52.93	50.54	28.07	39.02	1.12	1.02
18X-2	576.25	2.08	2.00	2.74	45.08	43.27	22.20	28.53	0.82	0.76
18X-3	576.55	1.93	1.83	2.73	55.54	52.74	29.55	41.95	1.25	1.12
18X-4	577.97	1.96	1.82	2.71	56.94	52.74	29.69	42.23	1.32	1.12
18X-4	578.65	1.90	1.80	2.72	56.84	54.07	30.70	44.30	1.32	1.18
18X-5	579.49	1.96	1.88	2.72	51.96	49.85	27.21	37.39	1.08	0.99
18X-5	580.16	1.98	1.87	2.69	52.08	49.13	26.89	36.78	1.09	0.97
18X-5	580.79	1.96	1.88	2.68	50.66	48.48	26.42	35.91	1.03	0.94
18X-6	580.91	1.91	1.79	2.71	58.38	54.62	31.29	45.54	1.40	1.20
19X-1	583.23	2.11	1.99	2.77	47.65	44.85	23.14	30.11	0.91	0.81
19X-1	584.14	2.15	2.16	3.00	42.26	42.44	20.13	25.20	0.73	0.74
19X-2	584.45	1.99	1.88	2.69	51.79	48.93	26.72	36.46	1.07	0.96
19X-2	585.22	1.97	1.88	2.65	50.08	47.67	26.04	35.20	1.00	0.91
19X-3	586.24	1.97	1.84	2.77	57.19	53.31	29.71	42.28	1.34	1.14
19X-3	586.84	1.94	1.83	2.72	55.82	52.59	29.44	41.73	1.26	1.11
19X-4	587.77	1.98	1.92	2.73	49.01	47.42	25.30	33.86	0.96	0.90
19X-4	588.27	1.99	1.90	2.74	51.77	49.32	26.66	36.35	1.07	0.97
19X-5	589.13	2.04	1.89	2.69	51.41	47.84	25.87	34.90	1.06	0.92
19X-5	589.77	1.98	1.88	2.64	49.44	47.03	25.60	34.41	0.98	0.89
19X-6	590.60	2.04	1.98	2.73	45.54	44.09	22.85	29.62	0.84	0.79
19X-6	590.94	1.89	1.82	2.73	55.05	53.11	29.85	42.56	1.22	1.13
19X-6	591.43	1.97	1.88	2.71	51.29	49.08	26.73	36.48	1.05	0.96
19X-7	592.13	2.02	1.89	2.72	51.95	48.66	26.31	35.71	1.08	0.95

The low values of PWL velocity probably were caused by void space and layers of drilling-disturbed sediment between the core and the core liner; scatter in values from XCB cores may have resulted from the alternation of undisturbed "biscuits" and drilling-disturbed sediment at 1- to 5-cm intervals.

The DSV was used on the mud-line APC cores (156-948B-1H and 948C-1H; Fig. 57C) only, while the Hamilton Frame velocimeter was used for measurements on 15-cm^3 cube samples cut from XCB-cored semilithified sediments from Hole 948C (Fig. 57D). The compressional-wave velocities from core samples also display an unusually large degree of variation over most of the cored interval in Hole 948C (Fig. 57D). For sediments of lithologic Subunits IIA through IID, no apparent trend in *P*-wave velocities downhole is found, with values varying between 1766 and 1608 m/s. The upper part of the décollement zone shows an anomalous decrease in velocity from 1692 to 1581 m/s over a 25-m interval, coinciding with decreasing porosity and an increase in bulk and grain densities. The lower part of the décollement zone as well as lithologic Unit III below it is characterized by velocities scattering over a wide range from 1531 to 1755 m/s.

The overall pattern observed in the longitudinal *P*-wave velocities can also be found in the transverse velocities (Fig. 57D). In general, longitudinal and transverse *P*-wave velocities show a fair amount of separation from 421 to 495 mbsf; they match closely between 490 and 510 mbsf, while they are extremely variable between 508 and 592 mbsf. This pattern is also imaged in the downhole trend of transverse and absolute anisotropies (Fig. 57E, -F). Transverse anisotropy is defined as the difference between the average transverse velocity, V_{pt0} and longitudinal velocity, V_{pl}, expressed as a percentage of the mean velocity:

$$\text{Transverse anisotropy } Ap(\%) = [(V_{pt0} - V_{pl})/(V_{pt0} + V_{pl})] \cdot 200.$$

Table 22. *P*-wave velocities from DSV and Hamilton Frame measurements, Holes 948B and 948C.

Core, section, interval (cm)	Depth (mbsf)	*P*-wave velocity (m/s)			Transverse anisotropy (%)	Acoustic impedance, longitudinal (MPa·s/m)
		V_{pl}	V_{pt1}	V_{pt2}		
156-948B-						
1H-1, 37	0.37	1534	1521		−0.84	2.29
1H-1, 120	1.20	1531	1533		0.14	2.29
1H-2, 20	1.70	1509	1506		−0.17	2.11
1H-2, 120	2.70	1518	1527		0.56	2.24
1H-3, 27	3.27	1558	1554		−0.27	2.41
156-948C-						
1H-1, 30	0.30	1497	1512		1.00	2.11
1H-1, 114	1.14	1559	1562		0.17	2.47
1H-2, 46	1.96	1439	1506		4.54	
1H-2, 120	2.70	1520	1520		0.02	2.21
1H-3, 30	3.30	1514	1517		0.23	2.24
1H-3, 120	4.20	1504	1512		0.50	2.20
1H-4, 40	4.90	1504	1517		0.83	
1H-4, 110	5.60	1515	1526		0.72	2.15
1H-5, 30	6.30	1540	1553		0.84	2.21
1H-6, 40	7.90	1537	1538		0.07	
1H-5, 90	6.90	1512	1512		0.00	
1H-6, 120	8.70	1520	1515		−0.31	2.19
1H-7, 30	9.30	1543	1541		−0.14	2.26
2X-1, 140–142	422.20	1749	1745		−0.23	3.21
2X-1, 146–148	422.26	1738	1763	1707	−0.20	3.15
2X-3, 30–32	424.10	1740	1744		0.27	
2X-3, 72–74	424.52	1749	1774	1751	0.80	3.01
2X-4, 3–5	425.33	1732	1698	1746		2.90
2X-6, 52–54	428.82	1742	1753	1669	−1.78	3.12
3X-1, 6–8	430.56	1685	1730		2.67	2.95
3X-1, 55–57	431.05	1735	1714	1749	−0.20	2.92
3X-2, 16–18	432.16	1728	1697	1752	−0.19	3.02
3X-2, 139–141	433.39	1731	1700	1745	−0.47	2.89
3X-3, 1–3	433.51	1749	1722	1694	−2.37	2.98
3X-4, 69–71	435.69	1690	1721	1702	1.27	3.15
3X-5, 95–97	437.45	1700	1714	1688	0.03	3.04
3X-6, 47–49	438.47	1724	1734		0.58	3.13
4X-1, 16–18	440.26	1668	1662	1671	−0.10	2.89
4X-3, 55–57	443.65	1693	1700	1689	0.09	3.09
4X-3, 142–144	444.52	1701	1689	1724	0.32	3.09
4X-4, 12–14	444.72	1675	1701	1690	1.22	3.12
4X-5, 42–44	446.52	1695	1701	1703	0.38	3.09
4X-6, 44–46	448.04	1688	1719	1677	0.59	2.76
5X-1, 63–65	450.43	1611	1665	1716	4.83	2.78
5X-1, 147–149	451.27	1669	1698		1.72	2.83
5X-2, 44–46	451.74	1654	1628	1684	0.13	2.92
5X-2, 93–95	452.23	1652	1651	1688	1.03	2.80
5X-3, 31–33	453.11	1701	1682	1680	−1.20	2.91
5X-3, 126–128	454.06	1708	1703	1709	−0.08	3.01
5X-4, 48–50	454.78	1730	1700	1742	−0.54	3.18
5X-4, 111–113	455.41	1745	1734	1707	−1.44	3.21
5X-5, 62–64	456.42	1728	1693	1740	−0.67	3.09
5X-6, 8–10	457.38	1691	1688	1664	−0.93	
5X-6, 31–33	457.61	1682	1674	1691	0.01	2.96
5X-6, 98–100	458.28	1689	1686		−0.17	3.20
5X-6, 150–152	458.80	1677	1690	1739	2.21	2.97
6X-1, 22–24	459.62	1674	1710	1728	2.63	3.03
6X-1, 144–146	460.84	1734	1720		−0.80	2.91
6X-2, 6–8	460.96	1716	1666	1679	−2.59	3.25
6X-3, 82–84	463.22	1627	1628	1636	0.29	3.02
6X-4, 66–68	464.56	1608				2.74
7X-1, 10–12	469.10	1687	1661	1648	−1.97	2.93
7X-1, 83–85	469.10	1693	1720	1688	0.65	2.94
7X-2, 46–48	470.96	1700	1731	1698	0.86	2.93
7X-3, 9–11	472.09	1694	1727	1742	2.37	2.84
7X-3, 80–82	472.80	1710	1745	1726	1.44	2.93
7X-4, 10–12	473.60	1725	1714	1720	−0.46	2.95
7X-4, 123–125	474.73	1718	1718	1745	0.78	3.00
7X-5, 13–15	475.13	1674	1661	1725	1.14	2.69
7X-5, 77–79	475.77	1717	1721	1612	−2.99	2.82
7X-6, 86–88	477.36	1741	1718	1656	−3.19	2.81
8X-1, 52–54	479.22	1665	1658	1748	2.24	2.86
8X-2, 134–136	481.54	1728	1766	1712	0.65	2.96
8X-4, 141–143	484.61	1766	1830	1685	−0.51	3.07
8X-5, 66–68	485.36	1730	1720	1755	0.41	2.98
8X-5, 115–117	485.85	1727	1724	1742	−0.19	3.06
8X-6, 67–69	486.87	1662				2.81
8X-6, 103–105	487.23	1749	1777		−1.95	2.97
9X-1, 52–54	488.92	1692	1735	1706	1.68	2.94
9X-2, 24–26	490.14	1625	1653	1711	3.46	2.86
9X-3, 78–80	492.18	1711	1784	1733	2.76	3.00
9X-4, 59–61	493.49	1720	1767	1737	1.83	3.02
9X-4, 101–103	493.91	1700	1740	1705	1.31	2.95
9X-5, 7–9	494.47	1695	1703	1755	1.98	2.90
9X-5, 81–83	495.21	1678	1710	1685	1.17	2.91
9X-6, 43–45	496.33	1674	1672	1688	0.38	2.93
10X-1, 11–13	498.21	1671	1687	1692	1.10	2.80
10X-1, 124–126	499.34	1633	1639	1683	1.69	2.70
10X-2, 51–53	500.11		1651			
10X-2, 90–92	500.50	1693	1663	1675	−1.43	2.97
10X-3, 99–101	502.09	1656	1667	1668	0.73	2.88
10X-4, 25–27	502.85	1639	1669	1671	1.86	2.75
11X-1, 70–72	508.40	1582	1639	1632	3.33	2.59
11X-4, 37–39	512.57	1626	1668	1679	2.89	2.97
11X-5, 17–19	513.87	1612	1648	1651	2.31	2.94
12X-1, 47–49	517.87	1710	1674	1702	−1.31	3.45
12X-1, 79–81	518.19	1673	1662	1689	0.13	3.12
12X-2, 93–95	519.83	1616	1636	1631	1.09	2.99
12X-3, 27–29	520.67	1607	1614	1611	0.34	
12X-3, 107–109	521.47	1685	1767	1715	3.28	3.43
12X-4, 2–4	521.92	1651	1623	1601	−2.37	3.11
12X-4, 83–85	522.73	1598	1599	1588	−0.29	2.88
12X-5, 45–47	523.85	1640	1669	1680	2.09	3.30
12X-5, 145–147	524.85	1588	1626	1649	3.12	3.06
12X-6, 59–61	525.49	1561	1634	1661	5.38	2.93
13X-1, 14–16	526.94	1595	1601	1616	0.84	2.90
13X-1, 142–144	528.22	1631	1691	1679	3.23	3.16
13X-2, 101–103	529.31	1664	1721	1685	2.29	3.43
13X-3, 6–8	529.86	1564	1604	1608	2.61	2.85
13X-3, 113–115	530.93	1603	1621	1699	3.47	2.91
13X-4, 13–15	531.43	1620	1626	1647	1.04	3.01
13X-5, 99–101	533.79	1600	1607		0.42	2.86
13X-6, 19–21	534.49	1650	1723	1729	4.54	
13X-6, 85–87	535.15	1615	1637	1615	0.69	3.04
13X-7, 28–30	536.08	1675	1667	1696	0.36	3.27
14X-1, 42–44	536.52	1585	1646	1641	3.64	2.88
14X-1, 146–148	537.56	1599	1684	1608	2.87	2.86
14X-2, 43–45	538.03	1608	1662	1653	3.03	2.98
14X-2, 100–102	538.60	1604	1664	1660	3.57	2.94
14X-3, 9–11	539.19	1572	1582	1605	1.33	2.80
14X-3, 70–72	539.80	1532	1556	1583	2.42	2.70
14X-4, 116–118	541.76	1624	1693	1698	4.31	2.99
14X-5, 61–63	542.71	1590	1630	1642	2.82	2.89
15X-1, 66–68	546.06	1616	1676	1666	3.36	2.90
15X-1, 106–108	546.46	1677	1720	1707	2.16	3.17
15X-2, 51–53	547.41	1654	1686	1688	2.02	3.06
15X-2, 104–106	547.94	1682	1673	1728	1.09	3.23
15X-3, 2–4	548.42	1669	1699	1693	1.57	3.12
15X-4, 27–29	550.17	1648	1704	1711	3.54	3.12
15X-5, 28–30	551.68	1680	1745	1724	3.20	3.27
15X-7, 44–46	554.84	1658				3.10
16X-1, 106–108	555.86	1652	1646		−0.39	3.11
16X-2, 24–26	556.54	1611	1629	1640	1.14	2.86
16X-3, 39–41	558.19	1591	1644	1672	4.10	2.84
16X-3, 126–128	559.06	1590	1621	1609	1.58	2.86
16X-4, 17–19	559.47	1719	1763	1762	2.53	3.35
16X-4, 109–111	560.39	1599	1647	1635	2.63	2.88
16X-5, 17–19	560.97	1679	1693	1715	1.49	3.31
16X-5, 78–80	561.58	1751	1763	1772	0.92	3.39
16X-6, 29–31	562.59	1593	1622	1624	1.90	2.94
16X-7, 56–58	563.86	1603	1623	1621	1.15	2.97
17X-1, 1–3	564.11	1642	1646	1654	0.45	3.07
17X-1, 104–106	565.14	1630	1659	1664	1.91	3.09
17X-2, 33–35	565.93	1647	1659	1691	1.66	3.11
17X-2, 101–103	566.61	1654	1689	1699	2.36	3.13
17X-3, 20–22	567.30	1648	1742	1700	4.35	3.07
17X-4, 21–23	568.81	1755	1763	1757	0.30	3.48
17X-4, 114–116	569.74	1627	1653	1641	1.23	3.04
17X-5, 83–85	570.93	1601	1659	1615	2.22	2.97
17X-6, 38–40	571.98	1663	1759	1760	5.64	3.19
17X-6, 138–140	572.98	1643	1690	1705	3.25	3.13
17X-7, 12–14	573.22	1691	1778	1768	4.73	3.25
18X-1, 9–11	573.39	1607	1669	1677	4.02	3.04
18X-1, 97–99	574.27	1622	1666	1683	3.17	3.08
18X-2, 28–30	575.08	1617	1664		2.83	2.98
18X-2, 145–147	576.25	1754	1831	1862	5.11	3.50
18X-3, 25–27	576.55	1595	1607		0.72	2.92
18X-5, 19–21	579.49	1653	1700		2.78	3.10
18X-5, 86–88	580.16	1644	1706	1713	3.88	3.08
18X-6, 11–13	580.91	1593	1605	1587	0.16	2.85
19X-1, 134–136	584.14	1725	1769	1778	2.79	
19X-2, 15–17	584.45	1626	1664	1692	3.14	3.05
19X-2, 92–94	585.22	1661	1735	1728	4.14	3.12
19X-3, 44–46	586.24	1591	1636	1665	3.67	2.92
19X-3, 104–106	586.84	1591	1636	1665	3.67	2.91
19X-4, 47–49	587.77	1682	1739	1775	4.35	3.23
19X-4, 97–99	588.27	1633	1671	1677	2.45	3.10
19X-5, 33–35	589.13	1615	1673	1675	3.61	3.06
19X-5, 97–99	589.77	1664	1656	1744	2.11	3.13
19X-6, 30–32	590.60	1710	1767	1762	3.15	3.38
19X-6, 113–115	591.43	1596	1693	1690	5.77	3.00
19X-7, 33–35	592.13	1655	1755	1779	6.53	3.14

While only a small increase in anisotropy is evident above the décollement zone (421–498 mbsf), a stronger increase is apparent in the underthrust sequence (530–592 mbsf) (Fig. 57F).

The acoustic-impedance profile, based on the longitudinal compressional-wave velocities from Hamilton Frame measurements (Fig. 57G, -H), delineates a trend of decreasing values (3.27–2.59 $Mg/m^2s \times 10^3$) over the depth range of 421 to 508 mbsf. Below 508 mbsf, a sharp offset toward higher values and a larger degree of scattering occurs, separating the accreted sediment and the upper part of the décollement zone with a positive impedance contrast from the lower part of the décollement zone and the underthrust sediments. As the *P*-wave velocity offset across the décollement is reversed in the impedance profile, it is obvious that the observed impedance pattern is primarily controlled by variations in bulk density.

Shear-wave Velocities

We attempted to measure shear-wave (*S*-wave) velocities in mud-line Cores 156-948C-1H and -948B-1H with side-by-side transducers (Table 23). For the more consolidated sediments in the interval from 421 to 592 mbsf (Cores 156-948C-2X to -19X), we measured with end-to-end transducers on the specimens sawed for the Hamilton Frame *P*-wave velocity measurements (Table 24 and Fig. 57I, -J) (see "Explanatory Notes" chapter, this volume).

For the interval from 421 to 592 mbsf, we measured in three orthogonal directions on wet samples immediately after measuring the *P*-wave velocity. Two problems with the equipment affected measurements. The specimens from Cores 156-948C-2X to -9X were not grounded, thus the first break of the arrival of the *S* wave was contaminated by electrical noise. Repeated readings with and without grounding showed that the traveltime in the nongrounded specimen had been overestimated. We discarded all readings from the cores above 156-948C-9X (485 mbsf).

The other problem arose from having the transducer blades just touching the specimen, rather than being embedded in it. The transducer blades were not of equal length, and the vise had to be tightened until one blade indented the specimen before the other blade would make contact. Some specimens split or cracked under this ill-distributed stress. If the crack was near the edge of the specimen, readings were continued with the transducers on intact faces. Specimens cracked by the Hamilton Frame *P*-wave apparatus were not used for measuring *S* waves. We discarded traveltimes from the shorter pair of transducer blades because they were systematically lower than those from the pair that were in good contact with the specimen.

Apparent *S*-wave velocities in the mud-line cores were low and scattered (Fig. 57I), but the velocity of the horizontally traveling, vertically polarized wave was consistently greater than the velocity of the vertically traveling wave. The anisotropy is about 2%.

The apparent velocities from the 400–600-mbsf interval (Fig. 57J) are scattered, particularly in the interval at 530–560 mbsf. Vertical (*Z*-direction) velocities are consistently lower than horizontal ones below 530 mbsf, and horizontal velocities of horizontally polarized waves (*XY* and *YX*) are consistently highest. Apparent velocities range from 300 to 1000 m/s; anisotropy is 30% to 50% in the zone at 530–560 mbsf. The anisotropy coincides with the zone of low structural dip and probably results from horizontal grain and pore alignment caused by deposition and compaction.

Some representative elastic moduli calculated from the *P*- and *S*-wave velocities and the corresponding bulk-density data are listed in Table 25.

Thermal Conductivity

Thermal conductivity data were collected at one point per section, except for core catchers (Table 26 and Fig. 58). Thermal conductivity within the upper 10 mbsf (lithologic Unit I) is almost constant with depth (1.0 W/[m·K]). Below 420 mbsf, thermal conductivity varies between 1.0 and 1.7 W/(m·K), with a mean of 1.2 W/(m·K). No apparent trend with depth was observed. Porosity and thermal conductivity measurements have been crossplotted in Figure 58C. Although low thermal conductivity in lithologic Unit I coincides with high porosity (about 73%), thermal conductivity is highly scattered in porosity of less than 60%. The absence of obvious change in thermal conductivity at 500 mbsf, where density and porosity data show a distinct offset, probably results from drilling disturbance.

Resistivity Measurements and Formation Factor

The method used for resistivity measurements requires frequent calibration of the probe with standard seawater. Assuming that the pore fluid has the same conductivity as standard seawater, the formation factor is the ratio of the impedance readings in the core and in the standard (Fig. 59A). A correction was applied for temperature (see "Explanatory Notes" chapter, this volume).

To compare these results with the log data, the resistivity measured from electromagnetic wave attenuation with the LWD tool (see "Downhole Logging" section, this chapter) has been filtered by applying a 5-m sliding average and has been converted to a formation factor by assuming that the pore fluid is standard seawater and using linearly interpolated and extrapolated temperature from downhole measurements.

Ideally, a correction should also be applied for changes of the fluid chemical composition. In particular, the increase of salinity across the décollement could be taken into account. However, applying an approximate correction to the LWD data, assuming that conductivity is proportional to salinity, shows that this correction is small (Fig. 59D).

Resistivities in cores have not been measured systematically; only the mud-line cores (Cores 156-948B-1H and -948C-1H) and Cores 156-948C-7X, -11X through -16X, -18X, and -19X were measured. Thus, few measurements are available for lithologic Unit II, which makes comparison between the two major units difficult.

Measurements from the mud-line cores and Core 156-948C-7X are compatible with logging data; however, the measurements in lithologic Unit III give higher formation factors than the LWD data at the same depth (Fig. 59C). Unlike those from the log, formation factors measured on cores do not decrease significantly across the lithological boundary between Units II and III.

If the surface conductivity of clay particles (from conduction in the diffuse electrical double layer, which is thin in seawater) and effects of ion electrical interactions are disregarded, the formation factor is related to the molecular diffusivity of ions in the rock by the following equation,

$$F = \sigma_0/\sigma = d0/\phi d = \tau^2/\phi,$$

where σ_0 and σ are the conductivity of the fluid and of the rock, respectively, d_0 and d are the molecular diffusion coefficients of a given ion in seawater and in the rock, τ is the tortuosity, and ϕ is the porosity. The tortuosity squared graph from the log has a remarkably constant value of 3 from 300 mbsf depth to the décollement (a suitable value for clays of 50% porosity) and drops to 2 in the underthrust sequence (a value more usual for sands), while the measurements on the core are still higher (between 3 and 4) (Fig. 59D).

Shear Strength

The undrained shear strengths were measured using the motorized miniature vane-shear device described in the "Explanatory Notes" (this volume). Data were collected only from APC cores, where sample quality was high enough for measurements. No data are available from XCB cores because sediments below 400 mbsf were well consolidated and highly fractured by drilling disturbance and deformation.

A linear trend of increasing peak and residual strength with depth can be seen in Holes 948B and 948C (Table 27; Fig. 60). A linear

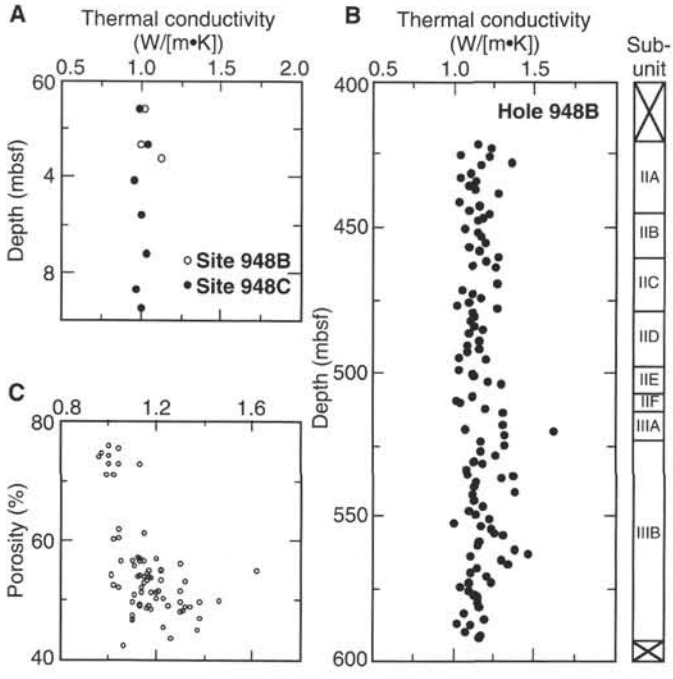

Figure 58. Thermal conductivity data for Site 948. **A.** Thermal conductivity vs. depth for mud-line Cores 156-948B-1H and 948C-1H. **B.** Thermal conductivity vs. depth for XCB cores from Hole 948C. **C.** Thermal conductivity vs. porosity calculated from core-sample measurements at Site 948.

least-squares regression of peak strength on depth results in the following correlation:

$$\text{Strength} = 5.2 + (2.7 \times \text{Depth}),\ r = 0.91,\ N = 19,$$

where depth is in meters and strength is in kilopascals, r is the correlation coefficient, and N is the number of samples. The effective overburden stress was calculated for the sedimentary section of Holes 948B and 948C using bulk-density measurements and assuming hydrostatic pore-pressure conditions (dashed line in Fig. 60).

Natural Gamma Rays

Natural gamma-ray radiation (NGR) was measured at a sampling rate of three per section and a sampling interval of 30 s. The results are presented in counts per seconds (cps) and corrected for background radiation (see "Explanatory Notes" chapter, this volume).

The curve of total counts of the MST NGR shows four characteristic intervals within the cored section from 421 to 592 mbsf (Fig. 61). The first is one of moderate to steep decline from about 22 to 13 cps between 421 and 478 mbsf (including a noteworthy peak of low counts at 440 mbsf), with a fair amount of scatter. The second interval from 478 to 500 mbsf is characterized by a constantly low count of about 13 cps, and considerably less scatter; the minimum in data scatter in this interval is compatible with other physical properties measurements. The third interval from 500 to 510 mbsf shows a sudden increase to about 20 cps, followed by a slight decrease and an even stronger, steep increase to more than 30 cps. The fourth interval extends from 510 mbsf to the bottom of the hole and has constant but highly scattered rates of 23 to 33 cps.

A comparison of the MST NGR data with downhole measurements from the LWD and wireline logging (WLL) NGT tools shows that MST and LWD data are in good agreement, while WLL data are mostly degraded by hole conditions (Fig. 61A). The three data sets have been resampled at 0.5-m intervals using a 2-m averaging boxcar filter. The indicator of poor open-hole log quality is lower counts from the WLL than from the LWD and limited imaging of the characteristic

Table 23. Shear-wave velocities in cores from Holes 948B and 948C.

Core, section, interval (cm)	Depth (mbsf)	Shear-wave velocity (m/s)	
		V_{sl}	V_{st}
156-948B-			
1H-1, 47–53	0.47	48.82	48.82
1H-1, 126–131	1.26	47.31	46.63
1H-2, 9.5–14.5	1.595	46.38	46.38
1H-2, 131.5–136.5	2.815	31.85	34.19
1H-3, 12.5–17.5	3.125	44.31	39.25
156-948C-			
1H-1, 33–35	0.33	35.13	36.08
1H-1, 104–106	1.04	24.62	25.51
1H-2, 50–52	2.00	27.44	28.09
1H-2, 126.5–128.5	2.77	34.50	40.37
1H-3, 21–23	3.21	42.89	44.42
1H-3, 123–125	4.23	29.68	44.27
1H-4, 23.5–25.5	4.74	44.12	48.55
1H-4, 115.5–117.5	5.66	38.19	41.33
1H-5, 39–41	6.39	59.68	63.31
1H-5, 112.5–114.5	7.13	61.37	61.37
1H-6, 36–38	7.86	48.27	50.33
1H-6, 36–38	7.86	45.99	47.66
1H-6, 110.5–112.5	8.61	64.25	65.38

Note: Measurements were made in both longitudinal (V_{sl}) and transverse (V_{st}) directions.

NGR intervals by the WLL. MST and LWD data are so close in character that we were able to identify differences in the depth reference used by the two methods of measuring. Within the décollement, the LWD depth is 2.5 m too deep relative to the MST depth. This shift is not linear, however. Between 490 and 500 mbsf, there seems to be no depth shift, whereas below 540 mbsf, the LWD log appears to be about 3 m too deep.

Gamma-ray emission is routinely recorded in five energy windows (see "Explanatory Notes" chapter, this volume, for details). Figure 61B illustrates that the total count curve in Figure 61A is mirrored more or less by all spectral window components. The main break in the décollement is characterized by a doubling of potassium and thorium count rates (Windows 3 and 5, respectively), whereas uranium (Window 4) increases slightly less. The total clay content of the formation increases at most by 5% to 10% at 510 mbsf (see "Lithostratigraphy and Sedimentology" section, this chapter) and, therefore, is not the main reason for the increase in NGR. Thus, the change must be related to a substantial increase in potassium content of the formation. An increase in the illite/smectite ratio is a possible explanation for the increase in potassium.

Figure 61C shows the relationship between the characteristic gamma-ray intervals, lithologic units, and structural domains. The first NGR interval corresponds to lithologic Subunits IIA to IIC. It is not clear what causes the gradual decrease of radioactivity downhole in these claystones. Clay content decreases only very slightly from ~65% to ~60% (see "Lithostratigraphy and Sedimentology" section, this chapter). The second interval of low counts spans lithologic Subunit IID, which is the lowermost part of the accretionary prism. The third NGR interval of drastically increasing counts corresponds to the uppermost décollement and lithologic Subunit IIE and the top of Subunit IIF. No sharp lithologic change is seen at this depth, but deformation increases suddenly from here downcore (see "Structural Geology" section, this chapter). The fourth interval of persistently high counts includes the lowermost décollement and the underthrust section, including lower lithologic Subunit IIF and Unit III. These variegated claystones and calcareous turbidites are composed of different lithologies at intervals near the resolution of the NGR device, which produces the high scatter in count rates.

Summary

A feature seen in all physical-property data sets is an apparent lack of correlation with recent physical processes generally thought to be associated with accretionary prism dynamics. Although an offset can

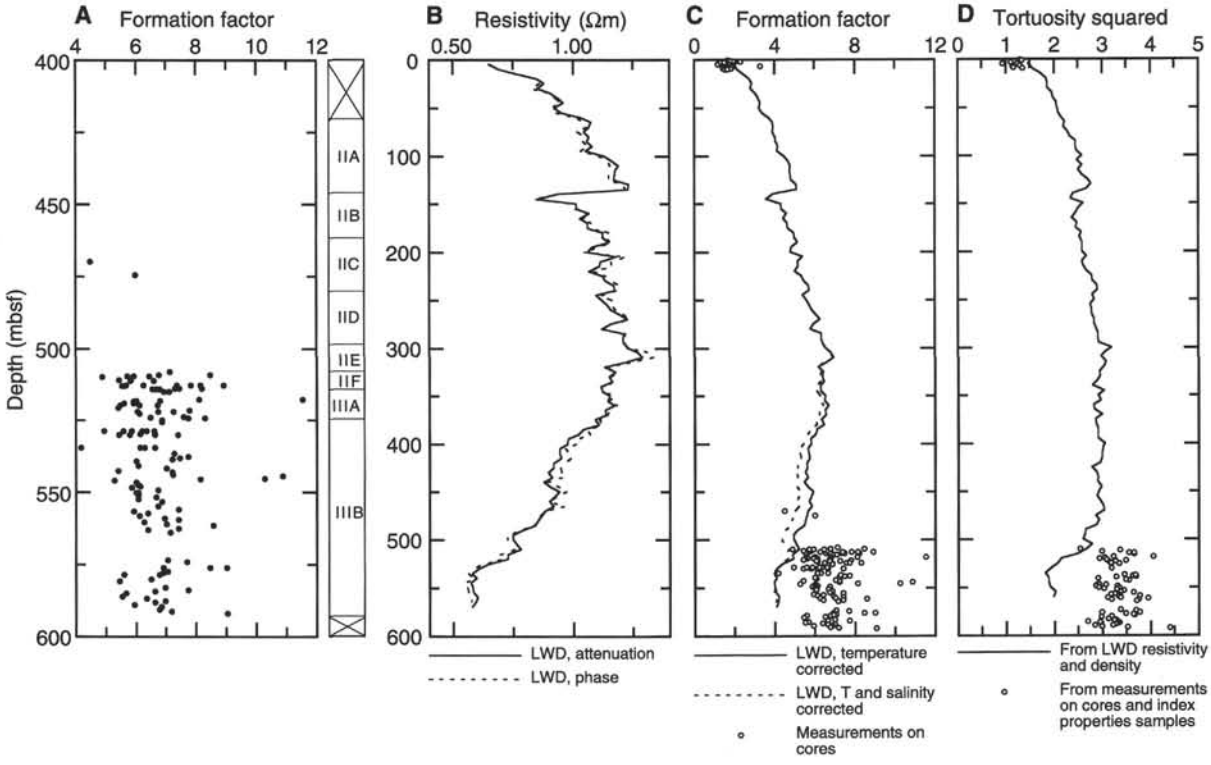

Figure 59. Resistivity data for Site 948. **A.** Formation factor from resistivity measurements on cores. **B.** LWD resistivity logs, filtered by applying a 5-m sliding average. **C.** Formation factors from measurements on cores and LWD. Temperature correction is explained in text. Salinity correction is assuming linear variation of conductivity with salinity, and with 35‰ for seawater. The salinity variation with depth is assumed linear from 35‰ at 300 m depth to 30.6‰ at 490 m depth. Below this level, the value from the nearest interstitial water sample is used for correction. **D.** Tortuosity from measurement on cores and LWD. Only the temperature correction has been applied.

Table 24. *S*-wave measurements for Hole 949B.

Core, section, interval (cm)	Depth (mbsf)	Shear-wave velocity (m/s)					
		xy	*xz*	*yx*	*yz*	*zx*	*zy*
156-949B-							
1X-1, 36–38	244.46		617.68		517.59		458.61
1X-CC, 26–28	246.20	600.16			640.40		653.08
2X-5, 31–33	260.11		693.13		554.89		537.54
3X-3, 50–52	267.00	548.02			708.78		650.12
3X-1, 108–110	264.58		517.43			500.94	
5X-1, 133–135	284.13		776.79		658.80		870.87
5X-2, 84–86	285.14	635.86			583.60		619.32
5X-5, 136–138	290.16		837.85		599.66	562.77	
5X-CC, 18–20	292.46		714.42		590.61	559.49	
5X-6, 23–25	290.53	604.45			671.98		566.95
7X-5, 136–138	309.46	571.02			504.01		562.77
7X-6, 22–24	309.82	493.45			395.76		512.09
13X-1, 18–20	350.38		772.53	618.76		733.82	
13X-2, 27–29	351.97		763.10		732.44		759.55
14X-3, 48–50	358.38	670.95		756.42			784.18
23X-8, 2–4	437.12	794.02		573.68			906.80
19X-1, 135–137	400.15	712.70		708.22			609.33
22X-3, 27–29	430.67	547.19		596.87			499.07
25H-2, 69–71	460.59		557.62		494.16		573.85

Note: Polarization convention: *xy* means wave traveling in *x* direction, polarized in *y* direction; *z* direction is parallel to core axis.

be found in all downhole profiles of physical properties across the décollement zone, this change is more likely to be governed by the difference in lithologic composition above and below the décollement than by changes in the in situ stress state or fluid-flow activity within this depth interval.

It is remarkable that the lithologically dominated change in the index physical properties toward lower porosity and higher density sediments across the décollement is not reflected in the acoustic properties. Although of a lower wet bulk density, Unit II sediments display significantly higher longitudinal *P*-wave velocities than Unit III sediments. The same is true for a comparison of average transverse velocities. The reasons for this inverse velocity-density correlation are not clear and remain to be resolved by shore-based post-cruise studies.

Table 25. Some representative elastic moduli calculated from measured *P*-wave and *S*-wave velocities.

Core, section	Depth (mbsf)	Density (g/cm^3)	Velocity (m/s)		Shear modulus (GPa)	Bulk modulus (GPA)	Poisson's ratio
			P-wave	*S*-wave			
156-948C-							
1H-2	2.80	1.47	1519	40.00	0.002	3.39	0.50
1H-5	7.10	1.44	1520	61.00	0.005	3.32	0.50
9X-5	495.21	1.89	1710	454.41	0.39	5.01	0.46
14X-1	536.52	1.91	1585	327.25	0.20	4.53	0.48
19X-2	585.22	1.97	1735	936.38	1.73	3.63	0.29

Table 26. Thermal conductivity data for Holes 948B and 948C.

Core, section, interval (cm)	Depth (mbsf)	Thermal conductivity (W/[m·K])
156-948B-		
1H-1, 120	1.20	1.02
1H-2, 120	2.70	1.00
1H-3, 27	3.27	1.13
156-948C-		
1H-1, 120	1.20	0.99
1H-2, 120	2.70	1.04
1H-3, 120	4.20	0.96
1H-4, 110	5.60	1.00
1H-5, 120	7.20	1.04
1H-6, 120	8.70	0.97
1H-7, 45	9.45	1.00
2X-1, 120	422.00	1.15
2X-2, 120	423.50	1.23
2X-3, 120	425.00	1.04
2X-4, 100	426.30	1.22
2X-5, 120	428.00	1.36
2X-6, 27	428.60	1.17
3X-1, 120	431.70	1.11
3X-2, 120	433.20	1.04
3X-3, 120	434.70	1.14
3X-4, 120	436.20	1.10
3X-5, 90	437.40	1.13
3X-6, 90	438.90	1.28
4X-1, 120	441.30	1.03
4X-2, 120	442.80	1.16
4X-3, 120	444.30	1.10
4X-4, 120	445.80	1.22
4X-5, 80	446.90	1.18
4X-6, 30	447.90	1.15
5X-1, 120	451.00	1.07
5X-2, 90	452.20	1.15
5X-3, 120	454.00	1.17
5X-4, 120	455.50	1.20
5X-5, 120	457.00	1.10
5X-6, 120	458.50	1.16
6X-1, 120	460.60	1.28
6X-2, 120	462.10	1.20
6X-3, 120	463.60	1.11
6X-4, 30	464.20	1.26
7X-1, 120	470.20	1.27
7X-2, 120	471.70	1.05
7X-3, 120	473.20	1.12
7X-4, 120	474.70	1.17
7X-5, 120	476.20	1.10
7X-6, 90	477.40	1.02
7X-7, 30	478.30	1.27
8X-1, 120	479.90	1.12
8X-2, 120	481.40	1.12
8X-3, 80	482.50	1.11
8X-4, 120	484.40	1.13
8X-5, 120	485.90	1.18
8X-6, 90	487.10	1.10
9X-1, 130	489.70	1.16
9X-2, 120	491.10	1.08
9X-3, 130	492.70	1.16
9X-4, 30	493.20	1.09
9X-5, 120	495.60	1.04
9X-6, 35	496.30	1.20
10X-1, 120	499.30	1.04
10X-2, 120	500.80	1.12
10X-3, 80	501.90	1.13
10X-4, 120	503.80	1.22
10X-5, 63	504.70	1.30
11X-1, 120	508.90	1.11
11X-2, 120	510.40	1.02
11X-3, 30	511.00	1.04
11X-4, 80	513.00	1.20
11X-5, 90	514.60	1.30
12X-1, 120	518.60	1.31
12X-2, 120	520.10	1.08
12X-3, 61	521.00	1.62
12X-4, 54	522.40	1.32
12X-5, 88	524.30	1.17
12X-6, 60	525.50	1.32
13X-1, 120	528.00	1.17
13X-2, 120	529.50	1.26
13X-3, 120	531.00	1.13
13X-4, 85	532.20	1.18
13X-5, 120	534.00	1.08
13X-6, 120	535.50	1.09
13X-7, 30	536.10	1.37
14X-1, 120	537.30	1.30
14X-2, 120	538.80	1.14
14X-3, 80	539.90	1.13
14X-4, 120	541.80	1.38
14X-5, 30	542.40	1.12
14X-6, 120	544.80	1.12
15X-1, 120	546.60	1.18
15X-2, 120	548.10	1.10
15X-3, 120	549.60	1.14
15X-4, 120	551.10	1.22
15X-5, 120	552.60	1.01
15X-6, 80	553.70	1.18
15X-7, 30	554.70	1.23
16X-1, 120	556.00	1.25
16X-2, 80	557.10	1.30
16X-3, 120	559.00	1.16
16X-4, 120	560.50	1.15
16X-5, 120	562.00	1.38
16X-6, 70	563.00	1.46
16X-7, 30	563.60	1.11
17X-1, 120	565.30	1.30
17X-2, 90	566.50	1.34
17X-3, 120	568.30	1.14
17X-4, 120	569.80	1.10
17X-5, 80	570.90	1.21
17X-6, 120	572.80	1.10
17X-7, 23	573.30	1.23
18X-1, 120	574.50	1.04
18X-2, 120	576.00	1.10
18X-3, 120	577.50	1.13
18X-4, 60	578.40	1.15
18X-5, 120	580.50	1.15
18X-6, 57	581.40	1.16
19X-1, 120	584.00	1.06
19X-2, 120	585.50	1.19
19X-3, 120	587.00	1.02
19X-4, 30	587.60	1.10
19X-5, 120	590.00	1.08
19X-6, 120	591.50	1.17
19X-7, 30	592.10	1.16

Both *P*- and *S*-wave velocities show a downhole increase in anisotropy below the décollement, reflecting an inherited basinal trend in the absence of large convergence-related compressional stress in the underthrust sequence. It is not clear if the absence of an apparent downhole trend in *P*-wave anisotropy in the upper part of the section is controlled by deformation-induced microfractures or other mechanisms modifying the acoustic properties of the accreted sediment.

DOWNHOLE LOGGING

Operations

Three sets of logs were run at Site 948: logging-while-drilling (LWD), open-hole, and cased-hole wireline logs. The LWD tool string was run from the seafloor to 583.7 mbsf, where hole conditions

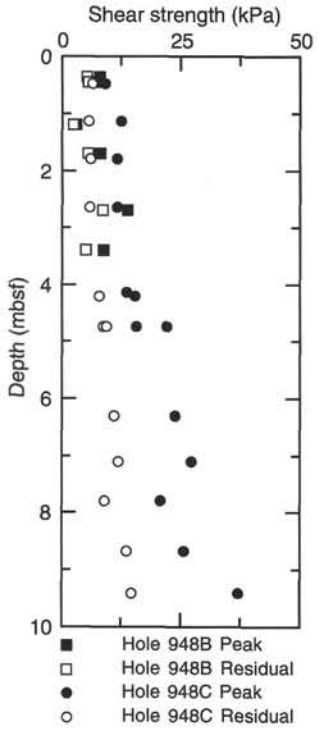

Figure 60. Undrained peak and residual shear strengths plotted as a function of depth for Site 948.

precluded further logging. The compensated dual resistivity with natural gamma-ray spectroscopy and compensated density-neutron LWD tools (see "Explanatory Notes" chapter, this volume) were used in Hole 948A at the beginning of Leg 156 operations. Wireline logs were primarily run to complement the LWD data with acoustic velocity, spectral gamma-ray, and lithodensity logs. Cased-hole cement bond tool (CBT) and array seismic imager (ASI) logs were run to determine the quality of cementation of the casing to the formation for the subsequent VSP experiment.

LWD Operations (Hole 948A)

At 0230 EST on 31 May, Hole 948A was spudded at 4929.3 mbsf (4940 mbrf). High torque on the drill string was encountered at 94 and 133 mbsf. At 2100 EST, the deepest LWD reading was taken. Because of high torque, the drillers switched to picking up single lengths of drill pipe and ran a short pipe trip. Torque and pump pressure continued increasing. At 0030 EST on 1 June, the previous total depth of 586 mbsf could not be reached, the drill pipe was sticking, and we were losing hole. Operations to back-ream at 65 m/hr to repeat a section began. At 0415 EST, back-reaming operations ended at 451 mbsf, as did LWD logging and depth tracking.

LWD Data Quality

The LWD tool allowed us to log the uppermost section of the borehole. This is not possible while running wireline logging tools, because the drill string must remain in the top section of the borehole. Effective rates of penetration (ROP) for the upper section (0–250 mbsf) of the hole varied from 25 to 50 m/hr. A constant ROP between 15 and 20 m/hr is necessary to ensure accurate spectral gamma-ray data. Such an ideal ROP cannot be maintained in the upper section, however, because the heave-compensation system is not capable of keeping weight on bit in soft formations. The effective ROP from 250 to 586 mbsf was more constant, between 30 and 40 m/hr. The high ROP resulted in reliable total gamma-ray data, but less reliable spectral data. Intermittent problems with one of the four neutron detectors were corrected during playback.

Table 27. Vane shear strength data for Holes 948B and 948C.

Core, section, interval (cm)	Depth (mbsf)	Peak (kPa)	Residual (kPa)
156-948B-			
1H-1, 37	0.37	8.0	5.3
1H-1, 45	0.45	7.9	5.7
1H-1, 120	1.20	3.1	2.4
1H-2, 20	1.70	8.2	5.7
1H-2, 120	2.70	13.9	8.7
1H-3, 40	3.40	8.8	5.1
156-948C-			
1H-1, 48	0.48	9.1	6.5
1H-1, 114	1.14	12.4	5.7
1H-2, 29	1.79	11.6	6.1
1H-2, 114	2.64	11.6	5.9
1H-3, 120	4.20	15.3	7.9
1H-3, 114	4.14	13.6	
1H-4, 24	4.74	15.6	8.7
1H-4, 24	4.74	22.1	9.4
1H-5, 30	6.30	23.8	10.9
1H-5, 111	7.11	27.2	11.9
1H-6, 30	7.80	20.7	9.0
1H-6, 118	8.68	25.7	13.6
1H-7, 42	9.41	37.1	14.7

A comparison of LWD to wireline logs illustrates some of the advantages of LWD technology. Overall noise level on LWD logs for Hole 948A (Fig. 62) is low compared to that on wireline logs for Hole 948C (Fig. 63). Excellent correlation of LWD bulk density to physical property measurements from Site 671 (Fig. 64) shows the consistency of these logging and shipboard laboratory measurements.

Wireline Operations (Hole 948C)

Based on past experience with logging operations at accretionary prisms, the need for acoustic velocity data, and the acquisition of LWD logs, a unique wireline tool string was used in Hole 948C. It consisted of the long-spaced sonic tool, natural gamma-ray spectroscopy tool, and the high-temperature lithodensity tool. The natural gamma-ray tool was run, in part, to enable us to correlate between LWD and wireline logs.

After drilling and coring were completed in Hole 948C, the borehole was conditioned with sepiolite drilling mud mixed with seawater. To run the wireline tool string to total depth below the décollement zone, the conical side-entry sub (CSES) was used. Operations started at 1530 EST on 7 June. Initial attempts to run the logging tool string downhole were unsuccessful because of bridges encountered at 132 and 185 mbsf. The tool string was pulled into the drill pipe, and the drill pipe and tool string were lowered to a total depth of 575 mbsf. The drill pipe was pulled up two stands (~60 m), and logging started from 575 mbsf while the drill pipe was pulled out of the hole ahead of the logging tool string. Hole instability below 490 mbsf, from within to just above the structurally defined décollement, made logging conditions particularly difficult. Because of poor hole conditions, sections were repeated from 437 to 386 mbsf and from 130 to 116 mbsf. The tool string was run in high-resolution mode (300 m/hr) to record spectral gamma-ray data, high-resolution bulk density, and high-resolution photoelectric effect data. Logging and a complete rigging down of the CSES was finished at 1630 EST on 8 June. Total wireline logging operations required 35 hr.

Wireline Data Quality

The wireline logs are greatly affected by the borehole conditions. As illustrated on the caliper log, the high-temperature lithodensity tool backup arm, which measures borehole diameter, was restricted from 525 to 330 mbsf (Fig. 63). From 525 to 465 mbsf the borehole was collapsing, resulting in constrictions. This is reflected in the low borehole-diameter measurements from the caliper and high wireline tensions measured uphole. Unstable borehole conditions caused both caving and constrictions from 267 to 127 mbsf. These borehole irregu-

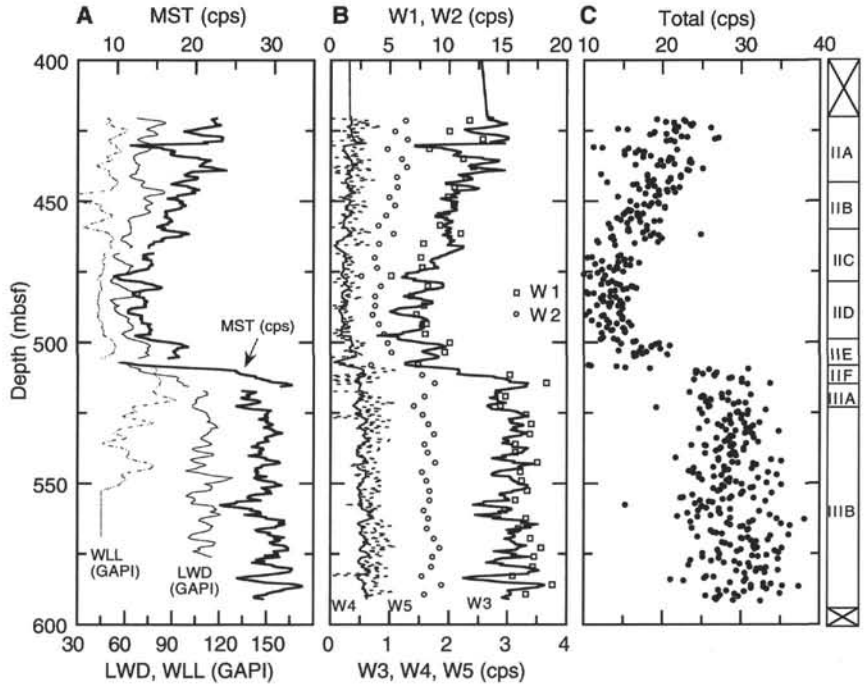

Figure 61. NGR records from XCB-cored section (421–592 mbsf). **A.** Comparison of MST, LWD, and WLL total count rates. **B.** Count rates of five NGR spectral windows (see "Explanatory Notes" chapter, this volume, for explanation and definition of windows). **C.** MST total count rate distribution.

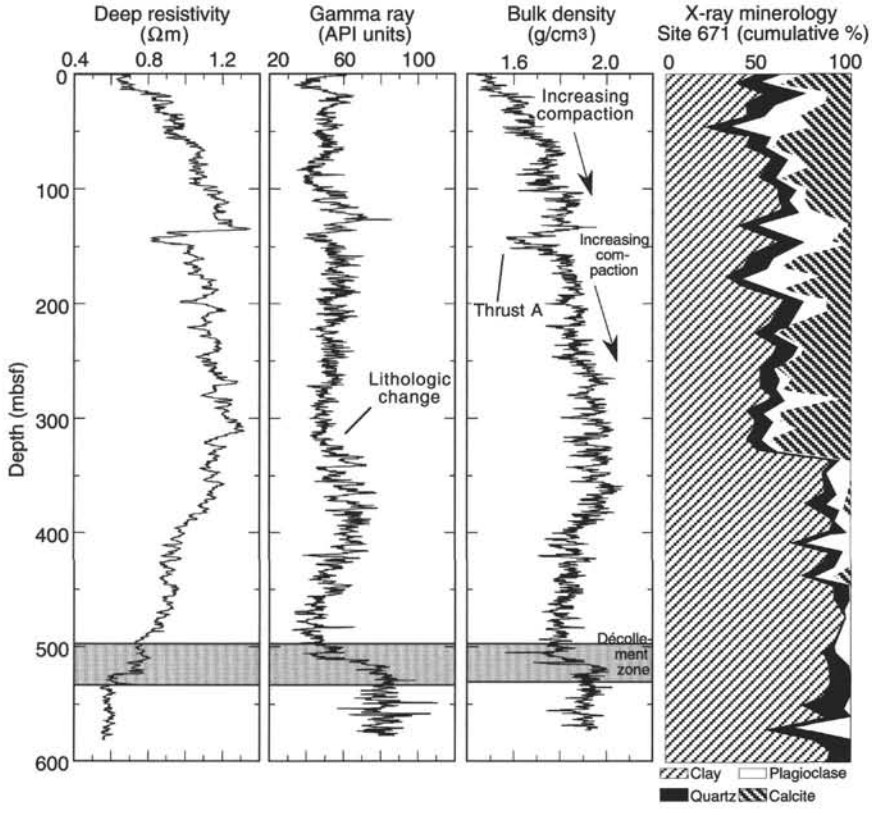

Figure 62. LWD deep-resistivity, natural gamma-ray, and bulk-density logs for Hole 948A and X-ray minerology from Site 671.

larities affected the density, gamma-ray, and the long-spaced sonic measurements. They also complicated depth correlation between LWD and wireline logs resulting from the stretch/shrink response of the wireline as it was pulled through constrictions in the borehole.

Cased-hole Operations (Hole 948D)

To check the quality of the bonding between the 13⅜-in. casing and the formation, the CBT was used. About 20 hr after the cement had been pumped down the casing, the cement in the bottom of the hole was drilled out with a rotary drill bit. When open hole was reached, the drill string was pulled out of the hole. The drill bit was dropped on the seafloor (using a mechanical bit release) to allow logging tools to pass through the BHA. The hole was reentered and logged from 481 to 60 mbsf. A repeat section was run from 134 to 58 mbsf.

After CBT logging, the ASI, a five-level, three-component VSP tool, was run in the hole to 171 mbsf. A gamma-ray depth tie-in log

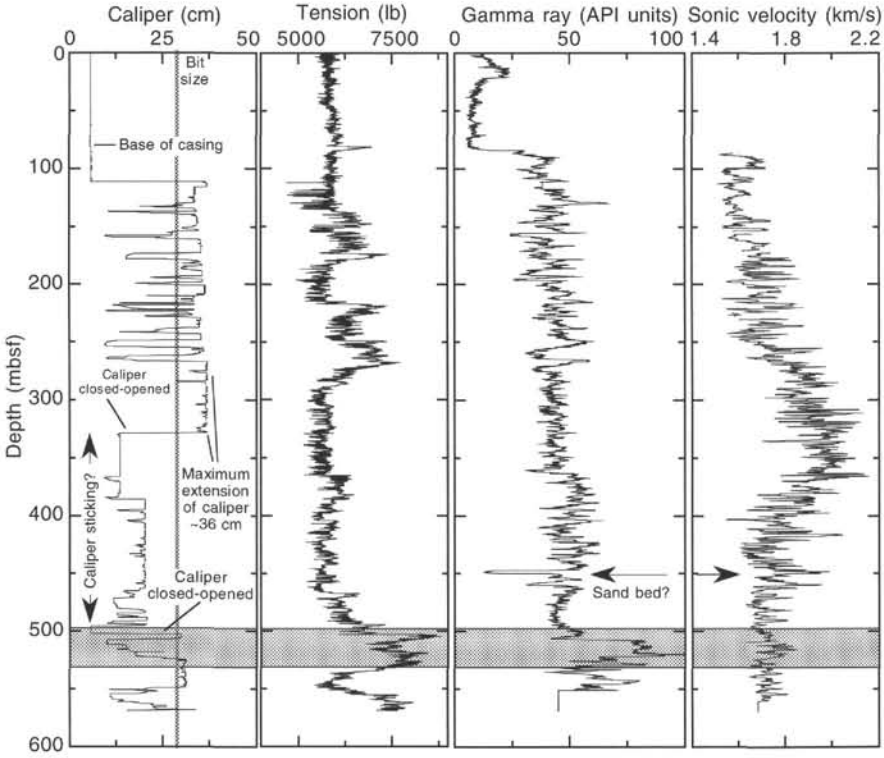

Figure 63. Wireline caliper, tension, natural gamma-ray, and sonic-velocity logs for Hole 948C.

was run to 51 mbsf to correlate the CBT and ASI depths. A difference of 0.6 m was measured. The ASI was set at 14 different levels, and data were recorded from 470 to 97 mbsf. A second VSP was attempted in the lower section of Hole 948D; however, unstable hole conditions prevented these last VSP measurements.

Cased-hole Data Quality

The CBT log indicated good cement filling (>80%) from 481 to 443 mbsf, partial cement from 443 to 325 mbsf, and no cementation from 35 mbsf to the bottom of drill collars at 71 mbsf. The VSP records responded to partially cemented and free pipe conditions with reduced signal quality as the VSP moved uphole (see "Vertical Seismic Profiling" section, this chapter).

Correlation with Lithostratigraphy

LWD resistivity, gamma-ray, and bulk-density logs at Site 948 show responses to several geologic features evident at Site 671. Bulk-density and resistivity logs are particularly sensitive to changes in porosity and thus compaction state, while gamma-ray and photoelectric-effect logs tend to be more responsive to changes in lithology. Good correlation of biostratigraphically defined tectonic units observed at Site 671 with logging data can be identified by compaction trends, as indicated by the LWD bulk-density and resistivity logs (Fig. 62). Abrupt changes in log response provide indications of location of faults and major lithologic contacts. A thrust fault at 132 mbsf, a lithologic change at about 325 mbsf, undercompaction between 395 and 500 mbsf, and the décollement zone are most distinctly reflected in the log responses.

Changes in response of the LWD resistivity, bulk-density, and gamma-ray logs at about 125–135 mbsf correlate with Thrust A (Mascle, Moore, et al., 1988), identified during Leg 110 at Site 671 (Fig. 65). At Site 671, this thrust, which emplaces upper Miocene calcareous muds over lower Pleistocene calcareous muds, is located at 128 mbsf. Abrupt decreases in the LWD bulk density and resistivity at 132 mbsf correlate with the boundary between biostratigraphically defined tectonic Packages A and B (Mascle, Moore, et al., 1988). At

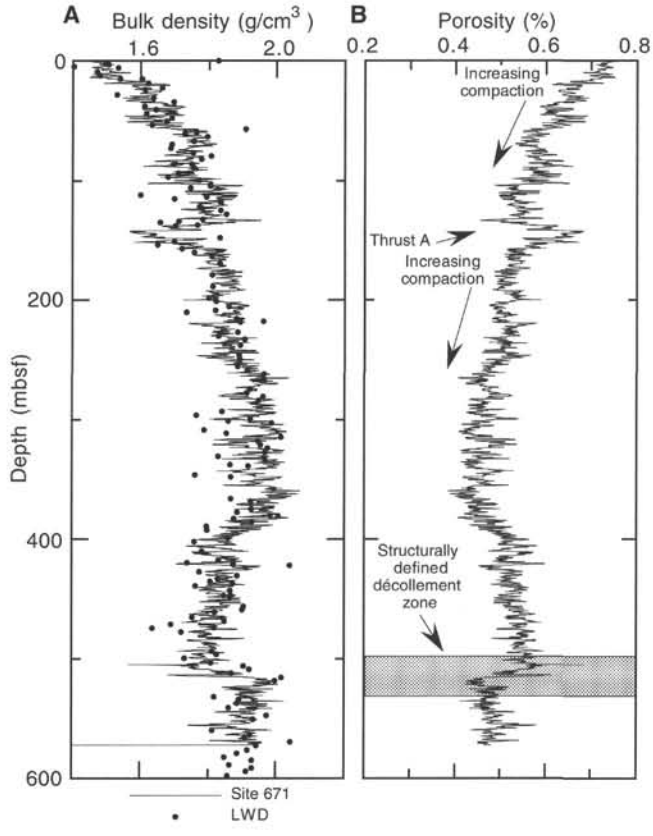

Figure 64. **A.** Comparison of LWD bulk-density log in Hole 948A with Site 671 shipboard bulk-density measurements. **B.** Porosity calculated from LWD bulk-density log in Hole 948A using grain density of 2.73 g/cm^3.

Site 948, porosity, as calculated from the LWD bulk-density log (ρ_m = 2.73 g/cm^3), reflects rapid compaction of the clays of Package A from a porosity of approximately 76% at mud line to 52% at the thrust fault at 132 mbsf (Fig. 64). The repetition of a similar compaction trend in the underlying lower Pleistocene–upper Miocene tectonic unit (Package B) is marked by an abrupt increase in porosity to 68%. The duplicated compaction trends of Packages A and B are seen in the resistivity log as well (Figs. 62 and 65). This repetition of increasing resistivity in the upper few hundred meters appears to be related to decreases in porosity. Unusually high total gamma-ray counts are observed at 125 mbsf in both the LWD and wireline logs. It seems likely that these high values are related to the fault at 132 mbsf. The localized nature of the high natural gamma-ray values could indicate lithologic changes within a discrete zone as a result of effects of fluid-matrix interactions or some other local effect.

At 315 mbsf, the LWD resistivity and gamma-ray logs show another abrupt change. Resistivity decreases steadily below this depth, while total gamma-ray counts increase for 65 m and then decrease. This may be explained by X-ray-mineralogy data from Leg 110 that show a distinct break in relative abundances of carbonate and clay minerals at approximately 325 mbsf (Fig. 62). Calcite content drops off to negligible amounts, while clay content increases from ~50 to ~80 wt%. Considering that clay minerals contain a larger proportion of radioactive elements, in particular potassium, and are generally more conductive than calcite, it seems likely that the observed gamma-ray and resistivity logs reflect changes in mineralogy. The steady decline in resistivity from 325 to 520 mbsf cannot be explained by a single discrete change in porosity or lithology, but may instead reflect a progressive undercompaction or other effects of matrix or pore-fluid properties.

The wireline far-receiver sonic-velocity log closely follows the trends of the LWD bulk-density log by increasing to a maximum of roughly 2000 m/s at ~350 mbsf. Velocity and density then continue a downward decrease toward the décollement (Figs. 62 and 63). This decrease occurs within the structurally defined Packages C and D, identified at Site 671 (Mascle, Moore, et al., 1988). Anomalously low density, velocity, and resistivity values on LWD and wireline logs between 400 and 500 mbsf suggest that this zone may be overpressured.

The wireline logs between 447 and 450 mbsf exhibit unusual log responses (Fig. 63), which may indicate a lithology that is distinctly different from the ubiquitous clay/claystones at Site 948. The shape of this feature and the absence of unusual tension or caliper responses suggest that the logs are responding to a different lithology. Low natural gamma-ray counts and high sonic velocities might identify a sand bed not evident in the cores, or not recovered. The corresponding cored interval is absent in Core 156-948C-4X.

The LWD logs exhibit pronounced changes within and across the décollement at Site 948. Resistivity drops, gamma ray counts increase, and bulk density increases. The changes in gamma ray and resistivity occur over the same 10-m interval that corresponds to the middle of the structurally defined décollement zone (Fig. 66). The resistivity decreases through the décollement zone and exhibits a sharp decrease at 523 mbsf. Resistivity, gamma ray, and bulk density show relatively constant average values in the underthrust sequence, with superimposed higher frequency (1–2 m) fluctuations in log values.

The increase in natural gamma-ray values within the underthrust sequence must be the result, at least in part, of the changes in clay mineralogy. The bulk shift to higher potassium radiation observed in the spectral gamma-ray logs within the underthrust sequence is likely to reflect the observed increase in the relative amount of illite at Site 671 (Tribble, 1990). An increase in the relative abundance of illite would also result in higher average grain density. Such an increase could explain only part of the observed increase in LWD bulk density. Even if a portion of the LWD bulk density response results from a decrease in porosity, we would expect a corresponding increase in resistivity. The observed resistivity decrease may be the result of increases in porosity or decreases in resistivity caused by variations in composition of either the fluid or matrix material of the underthrust sequence. Because illite is less conductive and the bulk density log suggests a decrease in porosity, pore-fluid composition seems the most likely cause of the observed behavior of the resistivity log in the underthrust section. However, the observed ~12% increase in salinity (see "Inorganic Geochemistry" section, this chapter) alone is insufficient to explain the ~25% decrease in resistivity. Additional factors, such as elevated temperatures and/or increases in matrix conductivity in the underthrust section, could contribute to the reduced resistivity values.

Within the structurally defined décollement zone are two spikes in the LWD bulk-density log at 505 and 514 mbsf. Minimum bulk densities of 1.57 and 1.67 g/cm^3 may have been caused by a local reduction in average grain density. Alternatively, assuming a constant grain density of 2.73 g/cm^3, these spikes would reflect 68% and 61% porosity, respectively, above background values of ~53% above the décollement zone and ~47% below the décollement zone (Fig. 64). The second spike is coincident with the lithologic boundary between Units II and III and spans a 2-m interval. This second spike also coincides with a local decrease in resistivity, suggesting that the bulk density is reflecting local abrupt increases in porosity. Such changes could reflect fault zone dilation, which would be beyond the resolution of the three-dimensional seismic data. A slight increase in the wireline sonic-velocity log at the décollement coincides with the overall increase in bulk density that marks the transition from prism to underthrust sequence.

Synthetic Seismogram

A synthetic seismogram (Fig. 67) was created using the LWD density log and a linearly increasing velocity profile. The resulting acoustic impedance log was convolved with the source wavelet extracted from the three-dimensional seismic data set, as described by Shipley et al. (1994). Three remarkable reflections are seen on the synthetic seismogram: the seafloor, the fault at approximately 128 mbsf, and the décollement. To compare these reflections to the three-dimensional seismic reflection data, we shifted the synthetic seismogram by 4.869 m to align the décollement reflection with the same reflection on three-dimensional Line 688 at CMP 1100. The synthetic trace was duplicated and inserted into the seismic section for display (Fig. 67).

The décollement reflection in the synthetic seismogram matches well the décollement reflection on Line 688. Both are asymmetric positive reflections, with the lower negative lobe having higher amplitude than the upper negative lobe. The wavelength of the reflection on both synthetic and recorded traces is the same.

Aligning the décollement reflections causes a mismatch in the seafloor reflections. The seafloor reflection of the synthetic seismogram is approximately 20 m shallower than the MCS seafloor reflection. This suggests that the velocity used to convert the three-dimensional seismic data from time to depth (1740 m/s) was in error by 20 m in 515 m, or less than 4%.

The thrust fault identified at 128 mbsf in cores at Site 671 and in the LWD logs at Site 948 is a high-amplitude, reversed-polarity reflection in the synthetic seismogram. This reflection correlates with the westward-dipping fault on Line 688. No other continuous reflections are seen on Line 688 between the fault and the décollement; thus, no other correlations can be made.

HEAT FLOW

WSTP Operations and Estimated Temperatures

The water sampler temperature probe (WSTP) was deployed in temperature-only configuration six times in Hole 948C, yielding six equilibrium temperature values (Table 28). All deployments took place in calm seas, during breaks in drilling while Hole 948C was washed from 9.5 to 420.8 mbsf. Although no cores were collected in this interval, deployment of the WSTP first required pulling a wash barrel from the bit. WSTP deployments are identified according to the wash barrel number following each measurement. These wash barrel

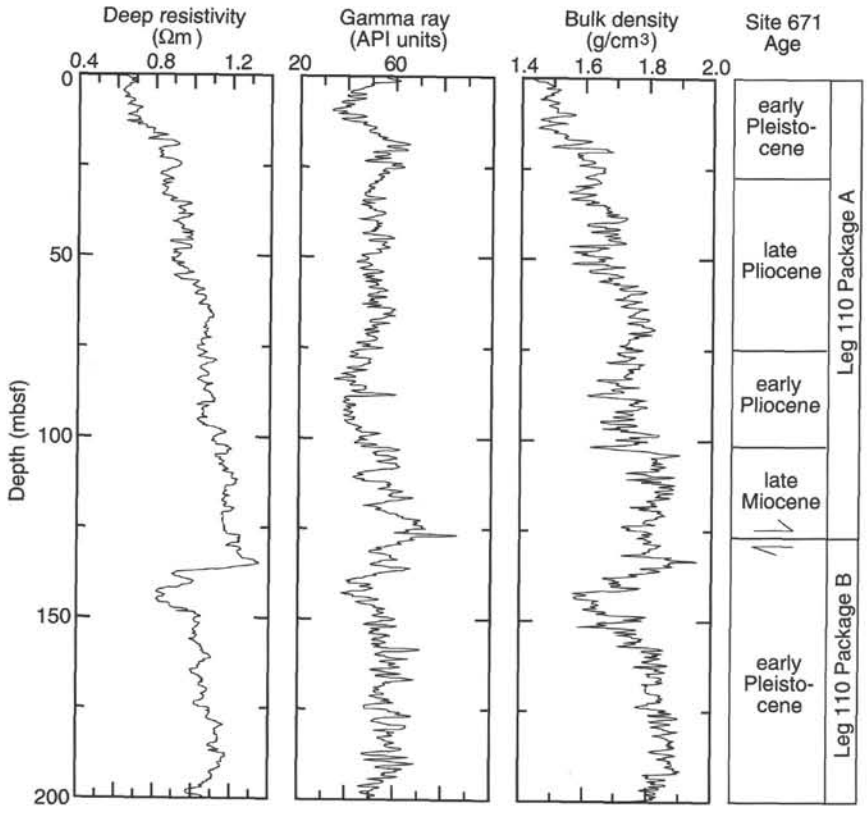

Figure 65. LWD deep-resistivity, natural gamma-ray, and bulk-density logs for Hole 948A across Leg 110 Thrust A.

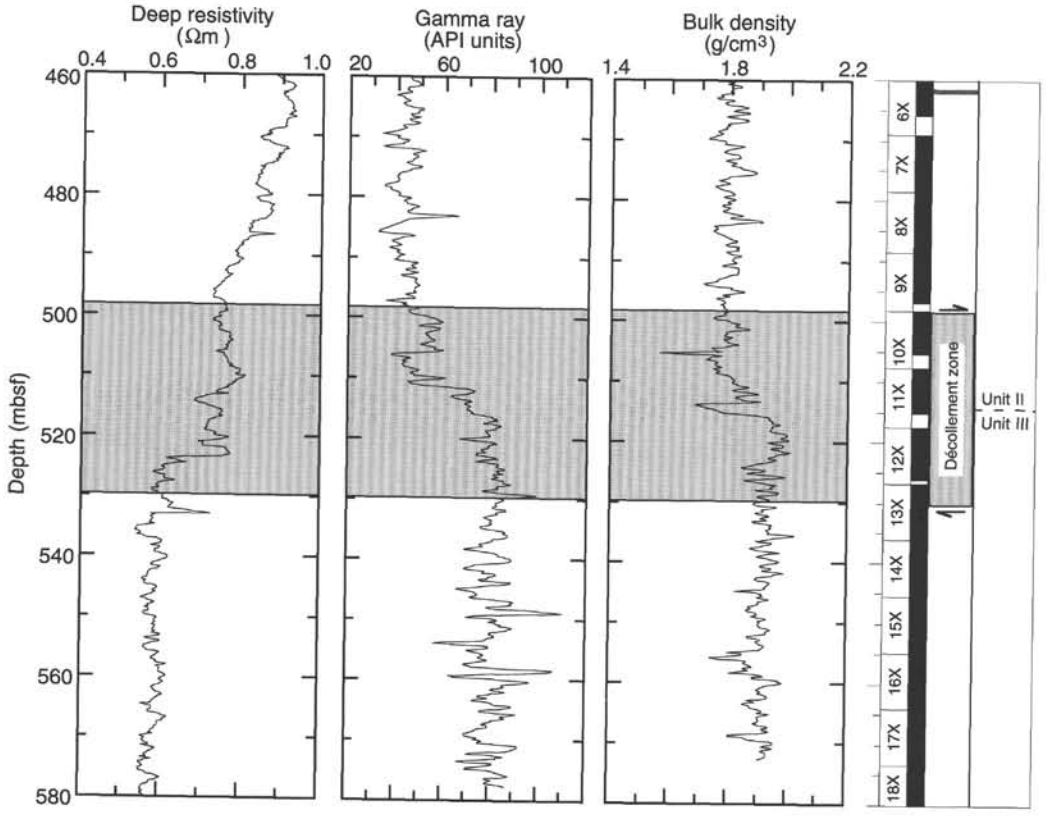

Figure 66. LWD deep resistivity, natural gamma-ray, and bulk density logs through the décollement at Site 948.

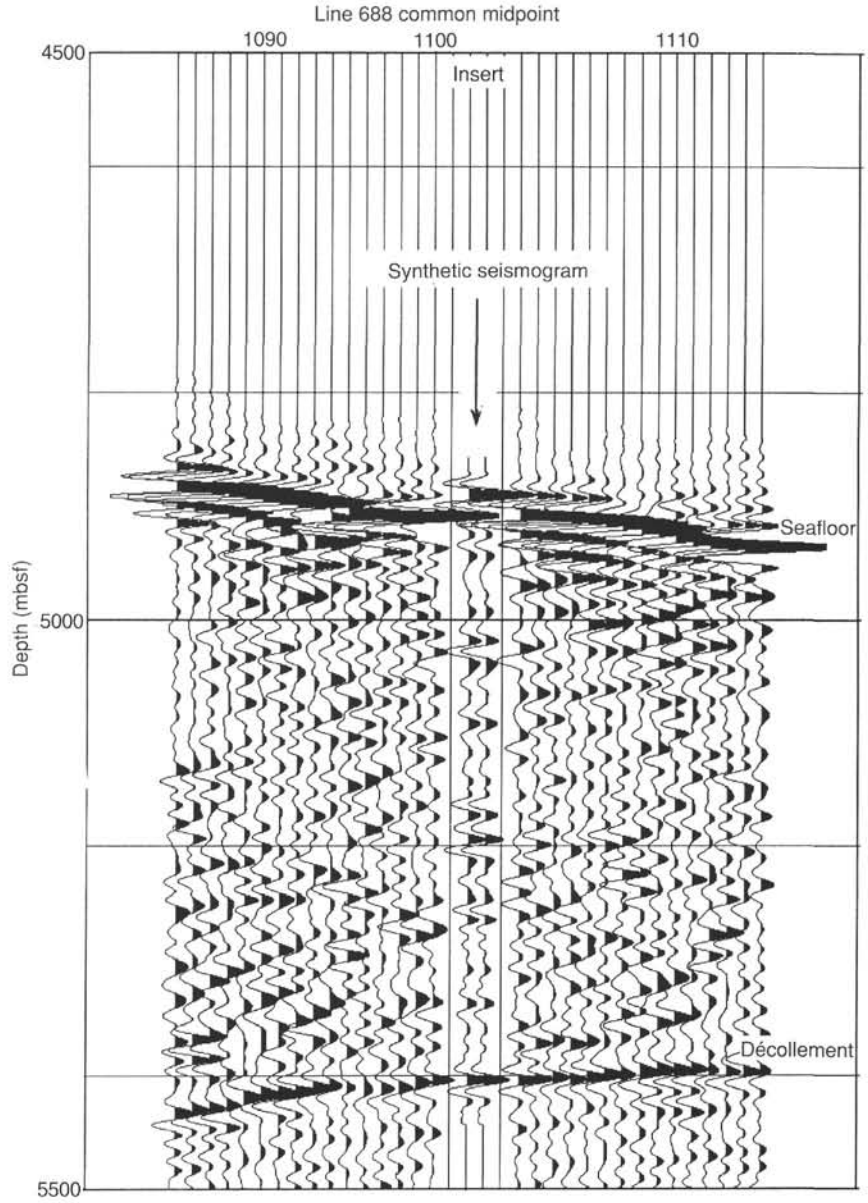

Figure 67. Synthetic seismogram inserted in seismic Line 688, generated using LWD bulk density and constant velocity.

numbers are used in this section for convenience only and do not appear elsewhere in this volume.

The temperature of bottom water at this site was determined to be 2.35° ± 0.05°C by holding the tools 20 m above the mud line for 5 to 10 min at the start of each deployment. Consistent results between successive deployments using the same sensor and data logger assured that measurements could be compared with confidence.

WSTP deployments 948C-3W and 948C-4W at 63.8 and 102.4 mbsf, respectively, provided excellent records (Fig. 68A, -B) and equilibrium temperatures of 8.3° ± 0.1° and 12.1° ± 0.1°C (Figs. 69A, 69B, and 70). Deployment 948C-5W was not ideal, as the probe moved while it was in the sediments about 3 min after insertion (Fig. 68C). Movement in the sediment caused reheating of the probe superimposed on the residual cooling curve following the initial insertion. As a result, only about 2 min of early data could be used to estimate the equilibrium temperature of 17.3° ± 0.5°C (Figs. 69C and 70). Using the remaining data from the insertion period would result in a much higher, probably incorrect, equilibrium temperature. Deployments 948C-6W and 948C-7W at 247.1 and 326.3 mbsf, respectively, were excellent (Fig. 68D, -E), yielding equilibrium temperatures of 21.8° ± 0.1° and 27.1° ± 0.1°C (Figs. 69D, 69E, and 70). The final deployment at 420.5 mbsf was flawed because of repeated movement of the probe while it was in the sediment (Fig. 68F), probably because the bit was set down on the bottom of the hole due to ship's heave. About 1 min of data was used to estimate an equilibrium temperature for this depth of 33.2° ± 0.5°C (Figs. 69F and 70).

Thermal Gradient and Heat Flow

Temperature values determined at Site 948 have been combined with earlier determinations at Site 671 during Leg 110 (Fisher and Hounslow, 1990) in Figure 71A. The shallowest two sediment temperatures from Site 671 were made with an APC tool. The deeper Leg 110 measurement was made with an earlier version of the WSTP and was probably taken in sediment which infilled the previously drilled hole, based on the shape of the deployment record and a comparison with shallower and deeper estimated in situ temperatures (Fig. 71A). When combined with the bottom-water temperature of 2.35°C, the shallowest four sediment temperatures yield a thermal gradient of 92° to 97°C/km over the upper 102.4 mbsf. The deepest three Hole 948C measurements yield a gradient of 66°C/km over 247.1–420.5 mbsf. The measurement at 199.0 mbsf appears to be slightly low, perhaps

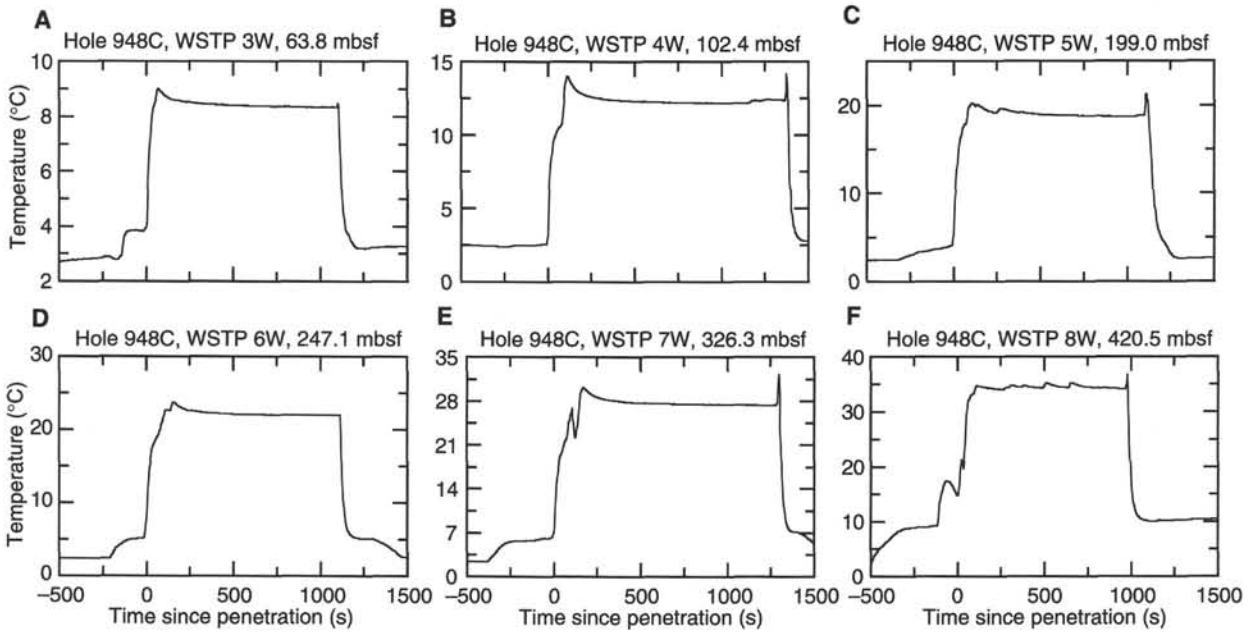

Figure 68. **A–F.** Temperature vs. time records for WSTP deployments in Hole 948C.

because the formation cracked or the probe did not penetrate deeply enough into the formation. Thermal conductivities from Sites 671 and 674 (Fisher and Hounslow, 1990) were used to calculate the cumulative thermal resistance at each WSTP deployment depth. These calculations may be revised following examination of corrected Leg 156 thermal conductivity data. The resulting plot of estimated temperature vs. cumulative thermal resistance reveals an average heat flow over the upper 420 mbsf of 92 mW/m^2. The uppermost four sediment temperatures and bottom water indicate seafloor heat flow of 110 mW/m^2, while the lowermost three sediment temperatures indicate heat flow of 89 mW/m^2.

Table 28. Summary of WSTP deployments in Hole 948C.

Measurement	Depth (mbsf)	Quality	Temperature (°C)	Comments
156-948C-				
3W	63.8	Excellent	8.3 ± 0.1	
4W	102.4	Excellent	12.1 ± 0.1	
5W	199.0	Fair	17.3 ± 0.5	Probe shifted
6W	247.1	Excellent	21.8 ± 0.1	
7W	326.3	Excellent	27.1 ± 0.1	
8W	420.5	Fair	33.2 ± 0.5	Probe shifted

VERTICAL SEISMIC PROFILES

Introduction

A zero-offset vertical seismic profile (VSP) was acquired in Hole 948D. The objective of the VSP was to tie the drilled section to the regional three-dimensional seismic reflection data set and to provide accurate interval velocity and time-depth functions for this part of the accretionary prism.

Acquisition

The acoustic source consisted of 2.0-L (120-in.^{3}) and 4.9-L (300-in.^{3}) air guns. Seismic arrivals were received by the five-element Schlumberger array seismic imager (ASI). A description of the ASI, as well as gun and receiver geometries, can be found in the "Explanatory Notes" chapter (this volume). We occupied 12 shot-firing stations from 470.3 to 97 mbsf. We recorded data from 50 geophone clamping positions; several geophone positions were occupied twice to overcome high noise levels near the top of the hole. A total of 8 to 15 shots were fired at each location to allow stacking of shots to increase signal-to-noise ratios. The ASI was moved uphole to yield geophone clamping levels at 7.62-m intervals.

During the 4 hr of the VSP experiment, the air guns, ASI, and MAXIS recording system all performed flawlessly. A combination of low sea state and good coupling of the casing to the prism sediments near the bottom of the hole yielded high signal-to-noise ratios during the first part of the experiment. Increasing sea state later in the experiment and decreasing bond quality in the upper part of the hole contributed to lower signal-to-noise levels in the shallow levels of Hole 948D during the VSP experiment.

An attempt to acquire VSP data in the lower cased section was unsuccessful because the casing had filled with mud. While lowering the ASI into the upper cased section of the hole, the ASI impacted the mud, causing the ASI cable to become tangled. Due to lack of time, a second attempt at acquiring VSP data in the lower part of the hole was not possible.

Shipboard Processing

Preliminary processing of the VSP data was performed on board the *JOIDES Resolution*. The following processing steps were performed (steps 1 through 6 applied to both vertical and horizontal components):

1. Edit bad shots,
2. Separate vertical and horizontal component data,
3. Edit bad traces from each geophone level for each component,
4. Subtract firing delay from each shot,
5. Apply bandpass filter (6-12-50-72 Hz), and
6. Stack all shots at each level.

Steps applied to vertical component only:

7. Apply $t^{1.25}$ gain to correct for amplitude decay with depth,
8. Pick first-break times,
9. Subtract first-break times to flatten first arrivals to zero time,

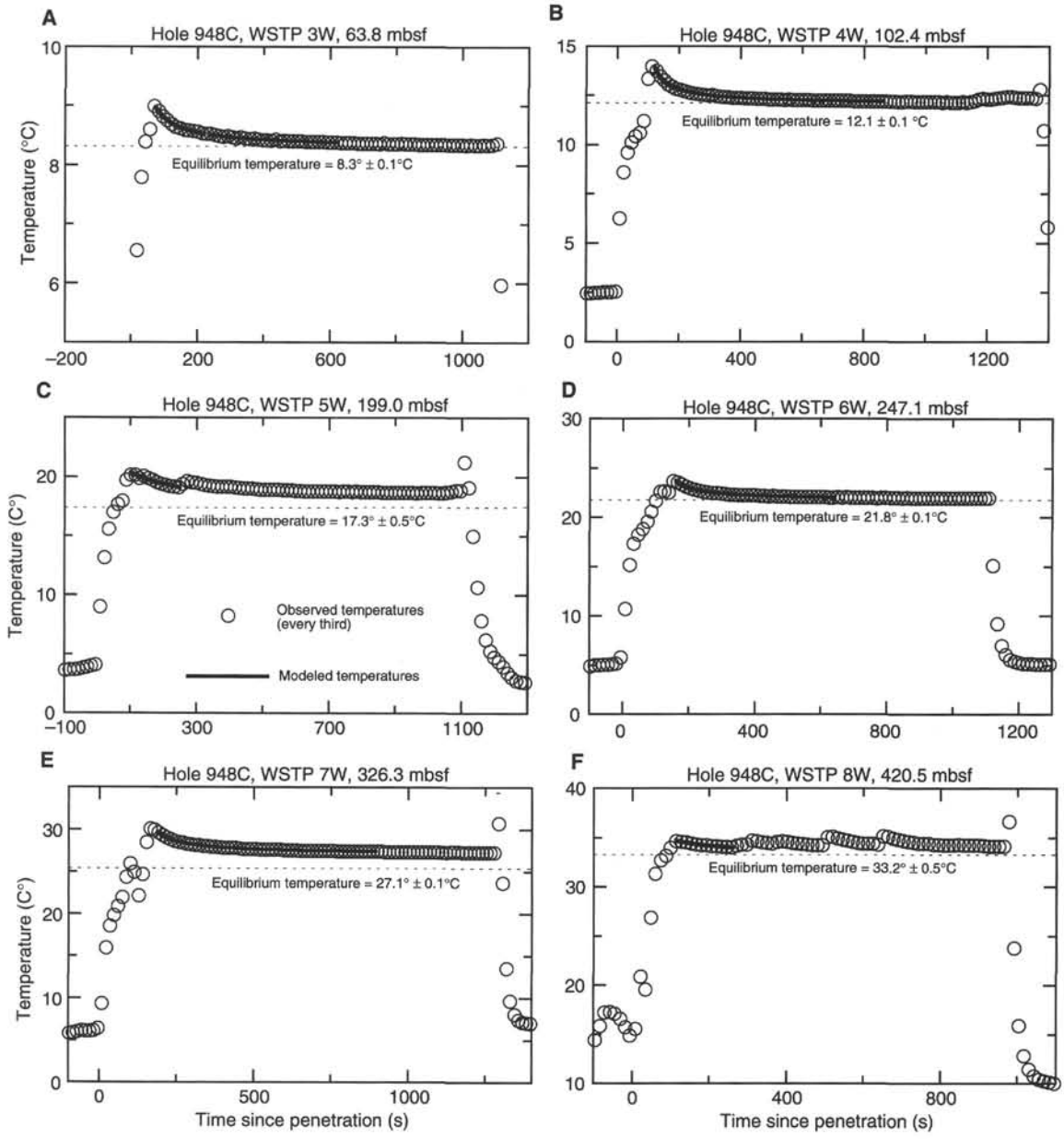

Figure 69. **A–F.** Comparison of measured and modeled temperatures from WSTP deployments in Hole 948C. Only one out of three measured temperature values is shown in each figure so that the comparison with the modeled values is clearer.

10. Apply filter in frequency-wavenumber (F-K) domain to alternate downgoing wavefield and enhance upgoing wavefield,
11. Shift to two-way traveltime by adding twice first-break time to each seismogram,
12. Select and apply corridor mute to eliminate noise approximately 0.5 s below first breaks, and
13. Stack all levels into a single trace (corridor stack).

Preliminary Results

Plots of the filtered and stacked vertical and horizontal components of VSP data are shown in Figure 72. The most prominent arrivals on all records are the direct arrivals (first breaks) and reflections from the oceanic crust. All events dipping parallel to the first arrival are downgoing waves; those dipping parallel to the basement reflection are upgoing (reflected) waves. Some reflections are visible between the first breaks and the basement reflection on the vertical component; however, the bubble pulse is strong and obscures any reflections within 250 ms of the first breaks.

The first-break times on the vertical component at each receiver depth provide a time-depth profile for the sampled interval (Fig. 73). The traveltime to the seafloor was determined by subtracting the height of the rig floor above sea level (11.0 m) and the depth of the air guns (7.0 m) from the depth from rig floor to seafloor (4949.0 m) and dividing by the velocity of sound in seawater for this area (1510 m/s). This yields a traveltime of (4949.0 – 11.0 – 7.0)/1510 = 3.2656 s. The upper nine first breaks are considered unreliable because of high noise levels resulting from the poor coupling. We have connected the calculated seafloor traveltime with the first reliable first-break time by a dashed line. The velocity implied by this line is 1604 m/s, which is our "best guess" for the velocity of the shallowest part of the prism. Velocities deeper in the section were computed by fitting line segments to the data points through least-squares linear regression. Data points in the three intervals fit the linear regression lines with little

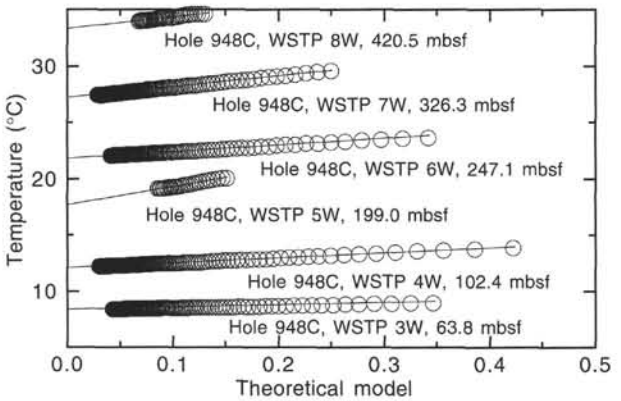

Figure 70. Temperatures vs. the theoretical model for all six WSTP deployments in Hole 948C.

scatter. The VSP velocity for the interval from 158 to 310 mbsf (1858 ± 16 m/s) is approximately 100 m/s higher than the corresponding velocities measured by the open-hole sonic log (see "Downhole Logging" section, this chapter). The break between velocities at 310–318 mbsf corresponds to the lithologic change recognized in the cores and LWD logs. The VSP velocity for the interval from 328 to 394 mbsf (2068 ± 18 m/s) is comparable to the sonic velocity from approximately 320 to 350 mbsf, but is higher than the sonic velocity between 350 and 394 mbsf. The break at 394–402 mbsf corresponds to a change in trend of bulk density in LWD logs and in sonic velocity in open-hole logs. VSP velocities below 400 mbsf (1825 ± 22 m/s) are generally about 75 to 90 m/s higher than sonic velocities in this interval. Core-sample velocities in this interval are generally more than 100 m/s slower than the VSP velocities (see "Core Physical Properties" section, this chapter). This large mismatch probably results from core-sample rebound and disturbance during drilling and sampling.

The horizontal (*X* and *Y*) components have lower signal-to-noise ratios than the vertical (*Z*) component, but still show the first break and presumed oceanic crust reflection (Fig. 72). The strong signal between 3.6 and 3.9 s traveltime over a depth range of 250 mbsf to the bottom of the survey is probably either a shear wave produced by mode conversion at the seafloor or a tube wave generated at the top of the borehole. It has the following properties:

1. It converges to the *P*-wave first arrival time at about 0 mbsf and has a lower apparent velocity.
2. Its amplitude on the horizontal components is greater than or equal to that on the vertical component.
3. Its traveltime-vs.-depth graph (Fig. 74) shows a uniform gradient above the lowermost 50 m.

Velocities (from least-squares line fits as shown) are 957 m/s for the upper part, decreasing to 682 m/s between 290 and 320 mbsf, increasing to 712 m/s down to approximately 430 mbsf, and decreasing to 641 m/s for the lowest five points (Fig. 74). The velocities are higher than the laboratory-measured shear-wave values of 300 to 500 m/s for 490 to 510 mbsf. A formation having a shear-wave velocity of 712 m/s and a *P*-wave velocity of 1700 to 1800 m/s gives mode-converted shear waves of less than a hundredth of the amplitude of the refracted *P*-wave at incidence angles of 1° or less (based on Zoeppritz's equations; Telford et al., 1976). A tube wave in this formation travels at 712 m/s if the shear-wave velocity is 678 m/s (with *P*-wave velocity of 1800 m/s and density of 1.5 g/cm^3; water velocity of 1490 m/s and density of 1.01 g/cm^3). Tube waves cause mostly vertical motion in the borehole fluid, but the motion in the sidewall is elliptical, with horizontal motion greater than or equal to vertical (Balch and Lee, 1984; Cheng and Toksöz, 1985). Further analysis is required to determine the origin of this wave.

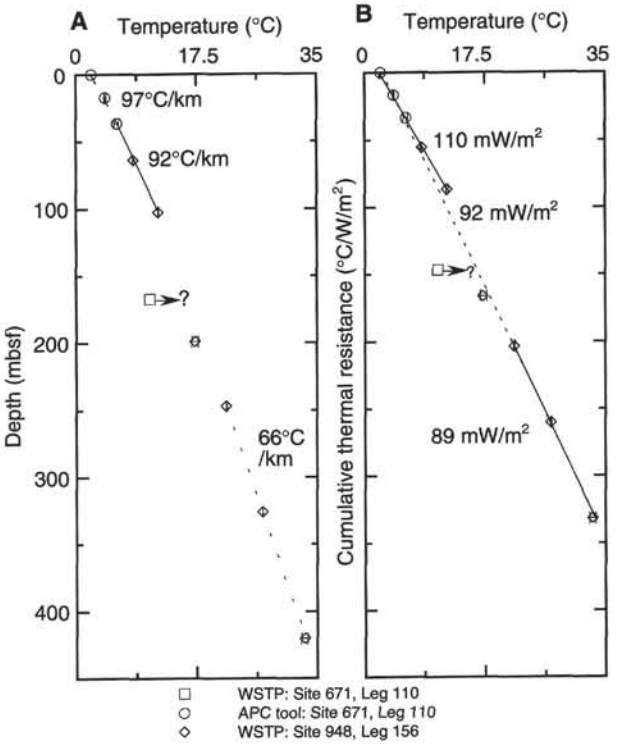

Figure 71. **A.** Temperatures vs. depth at Sites 948 (Leg 156) and 671 (Leg 110). Thermal gradients over several depth intervals are shown. **B.** Temperatures vs. cumulative thermal resistance (depth corrected for differences in thermal conductivity). Mean heat flow over several intervals is shown.

Figure 75 shows the upgoing wavefield converted to two-way traveltime. In this display, all reflections should be horizontal. A stack of this section is shown in Figure 76. The most prominent reflection in both the stacked and unstacked versions is from the oceanic crust at approximately 7.6 s. The décollement reflector should be just below the first arrival of the deepest geophone (470 mbsf, 7.06 s). This region has been distorted by the air-gun bubble pulse, however, and the décollement reflection is obscured. Additional processing, including wave-shaping deconvolution, will be necessary to image the décollement.

PACKER EXPERIMENTS

The TAM straddle-packer was set twice in Hole 948D. The final configuration of casing, screen, and open hole and the approximate location of packer seats are shown in Figure 77. Pressure records obtained from electronic gauges hung below the go-devil during each experiment are shown in Figure 78. These gauges measure and record absolute pressure including that of the overlying water column. In contrast, pressures added at the rig floor are relative to atmospheric. Following is a description of operations associated with these packer experiments and preliminary interpretations. Considerable additional analysis will be required before more complete, and more quantitative, interpretations can be made.

One day before the packer experiments, a short piece of pipe was attached below the top drive and plugged off to allow pressure testing of the rig plumbing. The system was pressurized to 13.8 MPa and shut in. Minor leakage was reduced through greasing and tightening of several valves, and the system was found to be tight.

The attempted VSP experiment immediately prior to packer work revealed that an obstruction was in the casing about 120 m above the screened zone. After recovery of the VSP tool, circulation was started and the pipe was lowered carefully to the bottom with the packer in the BHA. The pipe took some weight at the obstruction depth, then con-

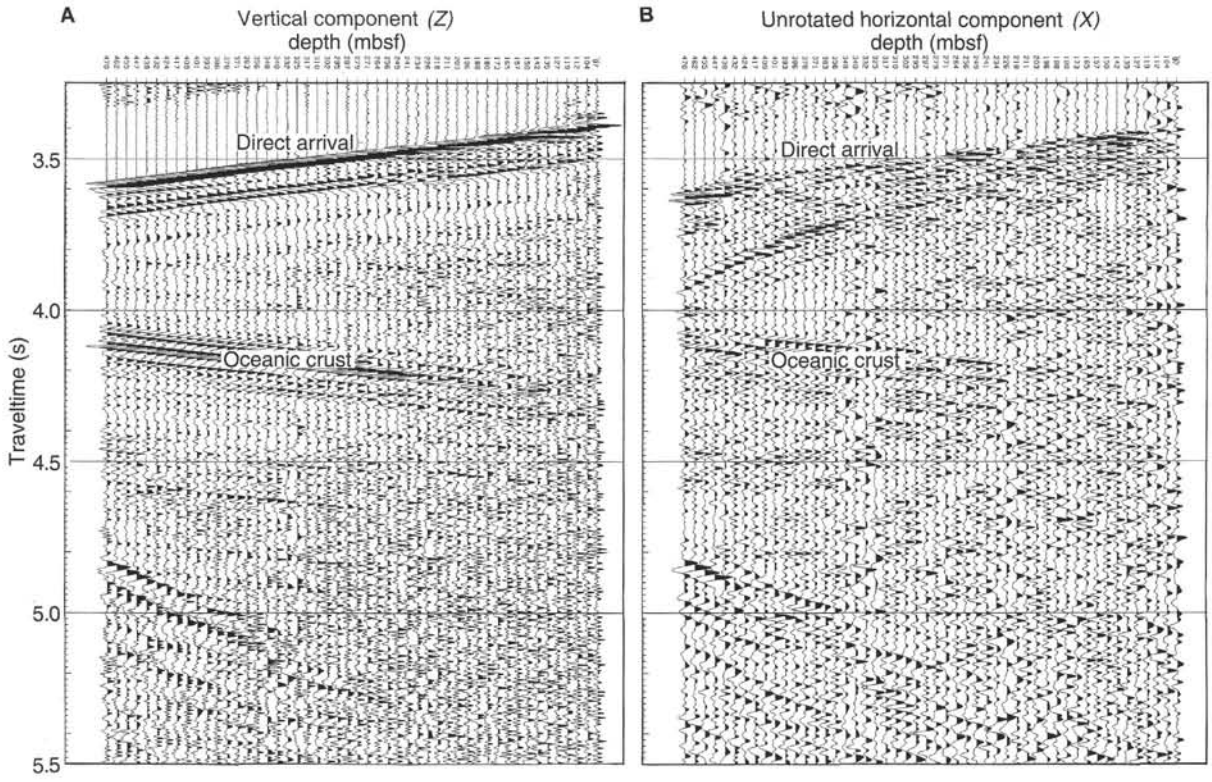

Figure 72. Stacked and bandpass-filtered (12–50 Hz) seismograms vs. receiver depth below seafloor for VSP in Hole 948D. **A.** Vertical (*Z*) component. **B.** Unrotated horizontal (*X*) component. **C.** Unrotated horizontal component (*Y*).

tinued to the bottom with only minor drag (see "Operations" section, this chapter). Circulation continued with the bit at total depth (TD) of 538 mbsf for another hour to be sure that the hole was clear. A plume of muddy water flowed freely from the reentry cone throughout cleanup of the hole. This flow was clearly visible on the VIT picture, as the VIT remained deployed throughout packer operations and proved to be useful for evaluating the effectiveness of the packer seal.

After circulating on bottom, the pipe was pulled back to 5423 mbrf, placing the packer at 5421 mbrf (472 mbsf). This placed the packer in the middle of the first joint of casing above the screened zone (Fig. 77). One electronic and one mechanical gauge were dressed and attached to the bottom of the go-devil, which was pumped down the pipe. The electronic gauge sampled with a 10.8-s data interval, while the mechanical gauge produced a 9-hr analog record.

The go-devil landed 30 min later, and we monitored hydrostatic pressure for 30 min. We inflated the packer element with 9.6 MPa and shut in this pressure at the rig floor. The pressure held for 10 min with no additional pumping. During this time, it appeared that the plume of effluent from the cone was reduced. The driller set down 9000 kg on the packer, by releasing air from the heave compensator, to shift the control sleeve and to lock the element into position while it was inflated. Normally, the control sleeve shifts quickly, opening a passage past the go-devil and into the isolated zone and releasing the inflation pressure remaining in the pipe. The packer behaved differently during this first set. Pressure in the pipe, rather than decreasing quickly, decreased slowly over the next 8 min, finally decreasing from 3.4 to 0.7 MPa over about 10 s. At this time, we noticed that the plume from the cone had started again and that the packer was slipping slightly. At first, we assumed that the element had failed to retain the inflation pressure.

Pressure in the pipe then began to climb slowly toward 1.4 MPa, and the packer held additional weight. The plume from the cone stopped flowing. We suspect that this short-lived plume may have been caused by the venting of fluid through relief ports above the element when it was set and that the slow inflation sequence may have resulted from mud that partially fouled the element, either from above or from inside (as described later). The presence of slick mud on the casing wall also may have reduced the element's holding ability.

We waited 30 min to record pressure in the isolated zone, then began a series of "negative" pulse and flow tests, exposing the isolated formation to hydrostatic pressure and monitoring recovery. We conducted two negative pulse tests by rapidly opening and closing the valve at the cement pump, which exposed the isolated zone to hydrostatic pressure. Following each pulse, we allowed 20 to 30 min for recovery. We then opened the valve at the cement pump and allowed the formation to flow back while we measured the rate. We intended to conduct this flow-back test for 20 to 30 min, then conduct an additional flow-back test at a higher flow rate. After 10 min of flow at 0.45 L/s, we found the packer was slipping down the hole. This may have occurred, in part, because the reduction of pressure in the isolated zone resulted in a loss of piston force below the packer.

After allowing for an additional 30-min recovery, we attempted our first positive slug test by quickly pumping 20 gal of seawater into the formation, then shutting it in. Pressure rose immediately in response to the pumping, but after a small initial decay, it remained elevated and constant for the next 55 min (Fig. 78A). At this point, we thought that the go-devil probably had clogged with rust or mud, and we elected to retrieve it and the gauges. Deflation took more than 1 hr, perhaps because of mud packed in above or in the packer element. When the go-devil was retrieved, the gauges included complete records of all testing, indicating that the go-devil had not been clogged after all. One explanation for the solid retention of pressure during the slug test is that the formation was sucked up inside the casing during the withdrawal flow test, clogging the screen and the bottom of the casing.

We redressed the gauges and sent down a second go-devil for another round of testing. While we were dressing the gauges, the pipe was lowered back to TD and seawater was circulated to clean the hole.

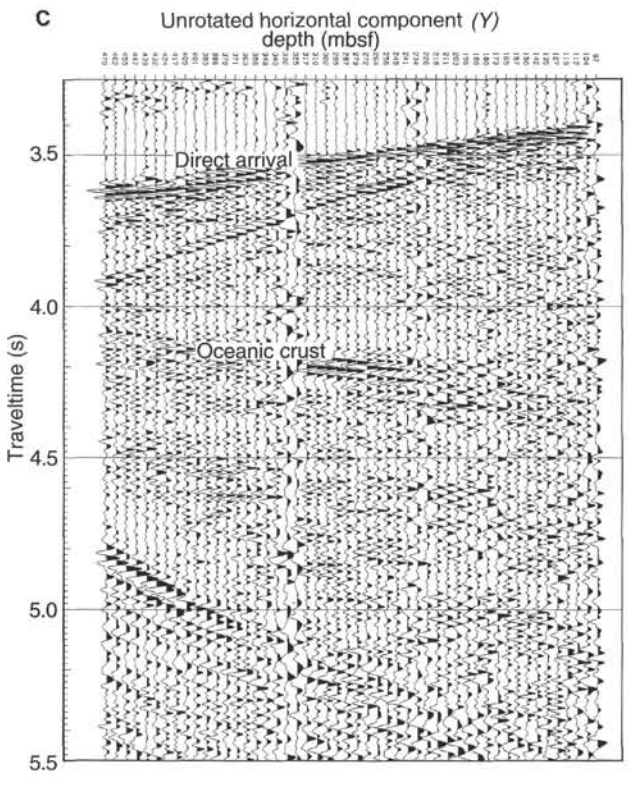

Figure 72 (continued).

After moving the pipe to place the packer near 471 mbsf, we pumped down the second go-devil and measured hydrostatic pressure for 30 min. Then, we inflated the element to 13.8 MPa and shut in at the rig floor. The packer held full pressure for 10 min, so we pressured up to 15.2 MPa, put weight down on the packer, and set the element inflated. This time, pressure bled off immediately, a more typical response, and the packer took full weight without slippage. After another 30-min equilibration period, we conducted three positive pulse tests at successively greater pressures, allowing for 15 to 20 min of recovery after each test. We then conducted three injection tests at three different rates (1.9, 3.8, and 6.2 L/s, respectively), pumping steadily for 20 min and shutting in to monitor recovery response for 20 min.

At the end of these tests, we deflated the packer to recover the second go-devil. Once again, packer deflation took more than 1 hr. Recovery of the go-devil was complicated because mud from the formation had extruded up the hole and through the packer, lifting the go-devil out of its seat and making it difficult to engage with the overshot. After several attempts, we recovered the go-devil and found that the records from both gauges were of high quality and showed excellent pressure response and recovery within the isolated zone (Fig. 78B). When the packer was recovered after pulling the pipe, the element and seals were found to be packed with sandy, silty clay. For mud to have gotten into the element and seal areas, it must have been in the drill pipe above the go-devil and then was pumped into the packer through ¼-in. inflation ports. It is not clear from the operational and pressure records at what time mud fouled the packer, but it may have been during the first set, as this could explain the unusual setting behavior. If this was the case, however, it would seem unlikely that we could achieve a second set. How mud got above the go-devils before either the first or second sets also is mysterious, as seawater was pumped continuously down the pipe except when we stopped pumping after the go-devils were landed.

The record from the second series of tests shows apparently typical pressurization and recovery behavior superimposed on an overall increase in fluid pressure, from about 2.1 MPa above hydrostatic (55.3 MPa) at the start of the tests to about 3.5 MPa above hydrostatic at the end of the tests. This final fluid pressure is close to the average lithostatic pressure within the isolated zone, estimated from LWD bulk-density data (see "Downhole Logging" section, this chapter) as being about 4 MPa above hydrostatic. It is unclear at present how much of this increase reflects charging of the formation during earlier drilling and casing operations (particularly during landing of the 10¾-in. casing string; see "Operations" section, this chapter) and how much is due to a true formation "overpressure," but it seems likely that the latter is an important part of the transient response to any plugging of the hole with the packer.

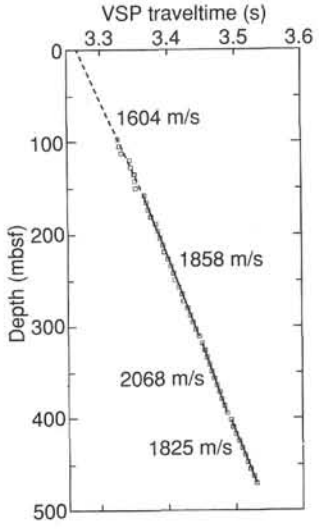

Figure 73. Traveltime vs. depth of first breaks selected from the vertical-component record. Lines show least-squares fit used to determine velocities.

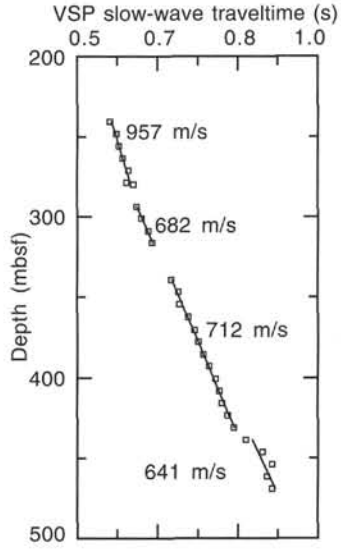

Figure 74. Traveltime of the slow wave vs. depth, selected from the *Y*-component record. Lines show least-squares fit used to determine velocities.

SUMMARY AND CONCLUSIONS

Site 948 was one part of the Leg 156 strategy to compare fault properties in at least two different locations in the accretionary prism and to investigate the relationship between fluids and tectonic features. Site 948 is in a location where the "seismic" fault has a normal-

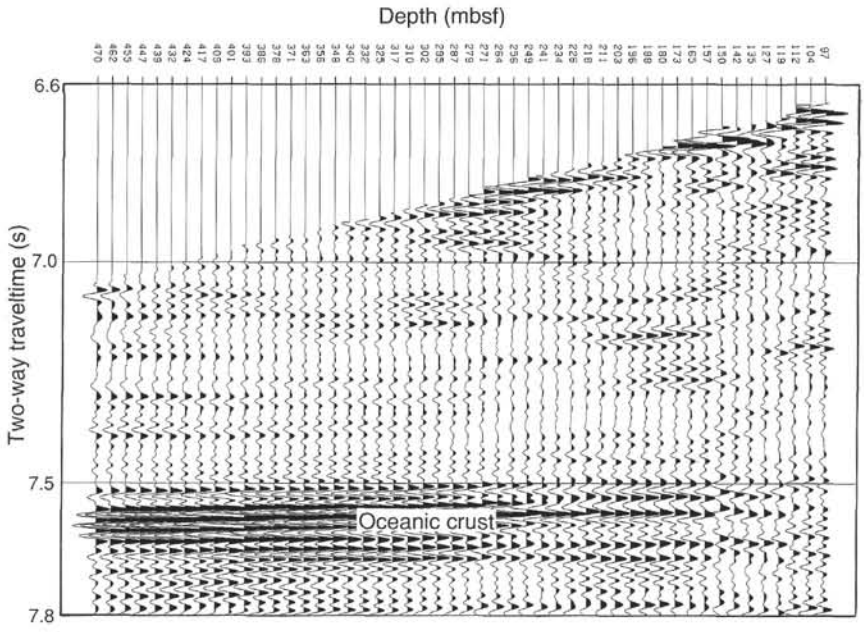

Figure 75. Upgoing wavefield of vertical component of VSP converted to two-way traveltime.

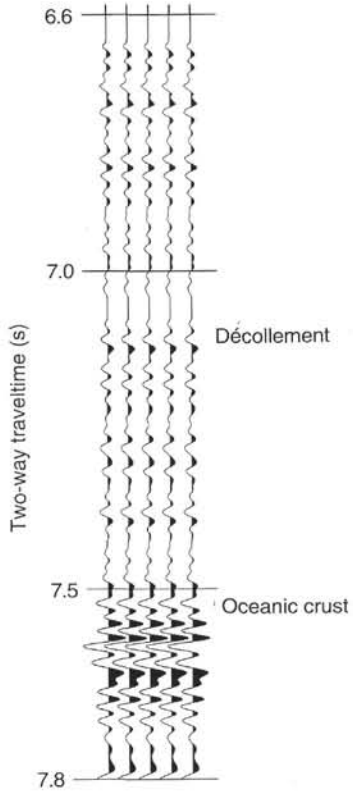

Figure 76. Stack of upgoing waves of vertical component.

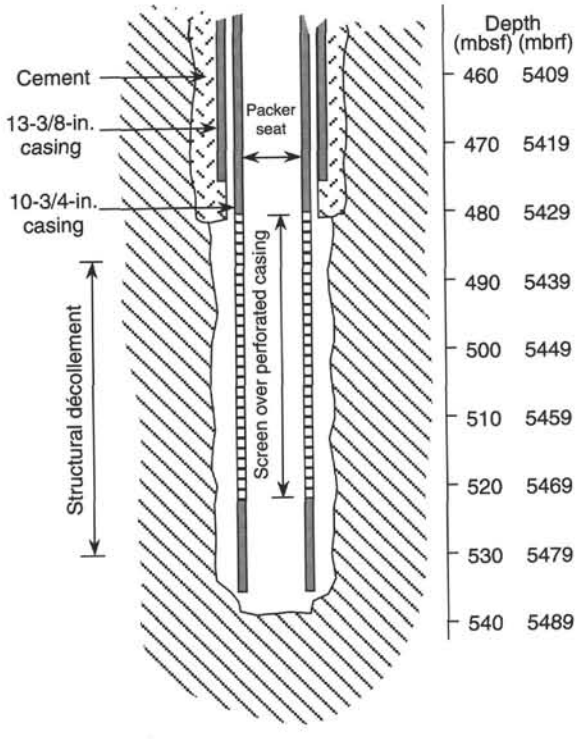

Figure 77. Configuration of the casing and open hole (approximate) during packer testing in Hole 948D. See the "Operations" section (this chapter) for a description of drilling and casing steps. The annulus between the 13⅜- and 10¾-in. casing strings may have been open up to the 10¾-in. casing hanger, where a rubber seal prevented communication with the overlying ocean, although it is also possible that the formation collapsed sufficiently tightly around the smaller casing to prevent communication with the casing annulus. Both possibilities will be examined during post-cruise data analysis.

polarity waveform. Modeling of the fault zone character indicates increasing impedance with depth, and it has been speculated that this means no dilation (Shipley et al., 1994). This site is less than 200 m from Hole 671B, which penetrated the 40-m-thick décollement and 151 m into the underthrust section. In contrast, at Sites 947 and 949, we examined the compound reversed-polarity waveform that is generally modeled as a low-velocity and density zone 10 to 14 m thick. Coring through the décollement again was to provide further descrip-

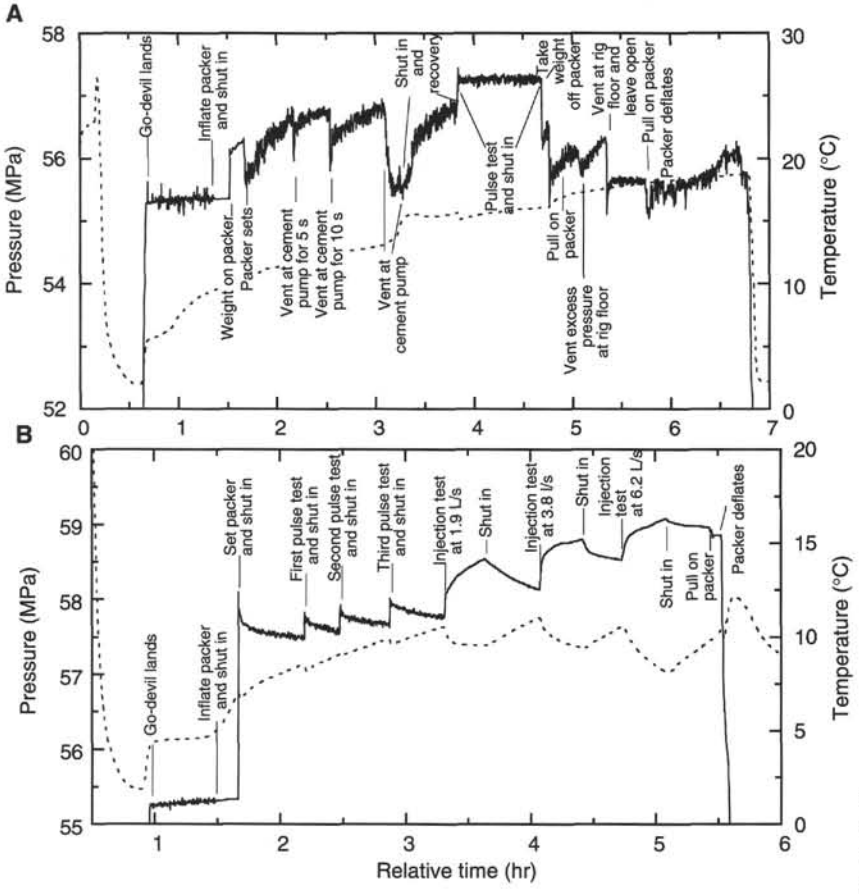

Figure 78. Annotated pressure vs. time records from electronic gauges hung below the go-devils during packer testing. Solid lines are pressures. Dotted lines are internal gauge temperatures. **A.** First go-devil. **B.** Second go-devil.

tion, physical property, and geochemical work, as well as more and larger samples for shore-based analysis.

The décollement zone, as we defined it, extends from 498 to 529 mbsf. The fault zone boundary is gradational over several meters at the bottom, but is sharp at the top. It contains limited zones of semipenetrative scaly fabric, interleaved with zones of fracture networks or stratal disruption, and structurally intact sediments. A major lithologic change near the middle of the fault zone at 513.9 mbsf marks a boundary between more brittle deformation above and more ductile deformation below. Veins are seen in the upper half, but not in the lower half. Discrete zones of shear fabric are well developed in both the upper and lower lithologies. Anisotropies of magnetic susceptibility (AMS) of mineral fabric orientations are consistent with other structural data that indicate abrupt changes in fabric geometry. In the prism, shortening is east-west, but the AMS orientation gradually changes to a geometry consistent with a vertical compaction fabric in the décollement.

The localization of the fault may be the result of the lithologic boundary at 513.9 mbsf. The lower unit (Unit III) is early Miocene and late Oligocene in age and consists of greenish-gray claystone as a background lithology, with rhythmic graded interbeds of gray turbidite claystone and nannofossil chalk. The upper part of this unit, from 513.9 to 523.8 mbsf, comprises gray to brown banded variegated claystones. The base of the overlying unit (Unit II) is a grayish-brown claystone. It is overlain by a distinctive pinkish-gray/brownish-gray radiolarian claystone of early to middle Miocene age from 498.1 to 507.7 mbsf. Above the décollement, the relative weight percentage of clay minerals is consistently about 60%, with a significant increase in the upper part of the décollement. The lithologic boundary at 513.9 mbsf and the overlying radiolarian-bearing, clay-mineral-rich sediments define the fault's location throughout the existing DSDP and ODP network of cores in the region.

Most laboratory and well-log physical property measurements are offset across the décollement zone, a result of the major lithologic change. One of the most spectacular successes of Leg 156 was the collection of logs through the entire accretionary prism and through the décollement using LWD technology. The nature of the LWD technique is such that it measures the formation within 1 to 3 min after drilling. Across the décollement, resistivity decreases and bulk density increases, and gamma-ray and resistivity changes also occur. These differences primarily reflect the changes in lithology and clay mineralogy at about 514 mbsf. The increase in gamma-ray count in the underthrust section must in part result from an increase in illite (potassium-rich) that was observed at Sites 671 and 948. Within the structurally defined décollement are two low-density spikes at 505 and 514 mbsf. These most likely reflect porosities of 68% and 61%, in contrast to surrounding sections having porosity values of 47% to 53%. The second spike is coincident with the lithologic boundary and spans a 2-m interval. A low density of about 1.8 Mg/m^3 in the 100 m above the décollement is similar to the density at only 100 to 200 mbsf. This low density indicates undercompaction and, thus, high fluid pressure, which also coincides with the lowest pore-water chlorinity.

Other downhole experiments used cased Hole 948D. A good cement bond in the lower 40 m interval of the second casing string isolates the hole hydrologically from the upper part. Open, screened casing was set below this through the fault zone. A series of packer shut-in and flow tests recorded pressure increases to near lithostatic values. However, these data will require substantial analysis and evaluation, given the significant formation disturbance during casing.

Temperature and pressure sensors were deployed for long-term measurement in the borehole, open at the screened section and sealed at the top with a borehole seal (CORK). Sediment flowing into the casing from below and muddy water flowing out the reentry cone at the seafloor foiled initial deployment of the sensors. The sediment

inflow was stopped by filling the hole with a column of 1.66 Mg/m^3 of barite, mixed bentonite mud from 538 to about 65 mbsf. The CORK was seated but did not latch, leaving the weight of the CORK to hold the seal in place. The radical use of heavy mud to prevent the formation from flowing into the casing will undoubtedly modify the hydrologic system further. The failure of the CORK to latch will be a potential problem, but may, at least in part, be accommodated by the heavy mud and multiple pressure sensors.

Some Shipboard Conclusions

Scaly fabric and stratal disruptions between 498 and 529 mbsf define the décollement with a sharp top boundary and gradational bottom. Its location is explained by a distinct change in porosity and strength in the pinkish-gray/brownish-gray radiolarian claystone and grayish-brown claystone of late early Miocene age overlying more ductile claystone.

The fluid flowing out the reentry cone probably reflects natural overpressuring, because the duration of flow was longer than when we initially pumped into the formation. The observed pressure increase during the packer experiment also indicates high pore pressures, as do the 0.5- and 2-m-thick layers at 505 and 514 mbsf that have densities similar to sediment at less than 50 mbsf. Maintaining such densities requires near-lithostatic pore pressure and dilation. At least the zone extending 100 m just above the décollement must also have high fluid pressures, given densities equivalent to 100 to 200 mbsf in the same hole.

Methane concentrations were low and shore-based isotopic analyses will be necessary to confirm any thermogenic origins. The chemical concentration depth profiles exhibit both diffusive and advective characteristics. Focused chloride dilution (about 18% seawater dilution) at the top of the décollement, along with other major and minor elements, is consistent with active, mostly lateral fluid flow. The CORK system sets the stage for long-term monitoring of the temperature and pressure at the main detachment. This 2-yr experiment will evaluate potential temporal variation in fluid flow and pressure.

Synthetic seismograms generated using the LWD density log confirm that the normal-polarity fault results from the increase in density at the décollement, which in turn is the result of changes in lithology. The thin, low-density dilatant(?) layers are below the resolution of the seismic data. Thus, the waveform represents a gradient (or essentially an interface) reflection to higher impedance, in contrast to the compound-negative reflection that is the more common waveform in the region.

REFERENCES*

Agar, S.M., Prior, D.J., and Behrmann, J.H., 1989. Back-scattered electron imagery of the tectonic fabrics of some fine-grained sediments: implications for fabric nomenclature and deformation processes. *Geology,* 17:901–904.

Balch, A.H., and Lee, M.W. (Eds.), 1984. *Vertical Seismic Profiling: Techniques, Applications, and Case Histories:* Boston (Int. Human Resour. Develop. Corp.).

Biju-Duval, B., Moore, J.C., et al., 1984. *Init. Repts. DSDP,* 78A: Washington (U.S. Govt. Printing Office).

Borradaile, G.J., 1991. Correlation of strain with anisotropy of magnetic susceptibility (AMS). *Pure Appl. Geophys.,* 135:15–29.

Cande, S.C., and Kent, D.V., 1992. A new geomagnetic polarity time scale for the Late Cretaceous and Cenozoic. *J. Geophys. Res.,* 97:13917–13951.

Cheng, C.H., and Toksöz, M.N., 1985. Generation, propagation and analysis of tube waves in a borehole. *In* Toksöz, M.N., and Stewart, R.R. (Eds.), *Vertical Seismic Profiling (Part B): Advanced Concepts:* London (Geophysical Press), 276–287.

Dolan, J.F., Beck, C., Ogawa, Y., and Klaus, A., 1990. Eocene-Oligocene sedimentation in the Tiburon Rise/ODP Leg 110 area: an example of significant upslope flow of distal turbidity currents. *In* Moore, J.C., Mascle, A., et al., *Proc. ODP, Sci. Results,* 110: College Station, TX (Ocean Drilling Program), 47–83.

Ekdale, A.A., Bromley, R.G., and Pemberton, S.G. (Eds.), 1984. *Ichnology: The Use of Trace Fossils in Sedimentology and Stratigraphy.* SEPM Short Course, 15.

Fisher, A.T., and Hounslow, M.W., 1990. Heat flow through the toe of the Barbados accretionary complex. *In* Moore, J.C., Mascle, A., et al., *Proc. ODP, Sci. Results,* 110: College Station, TX (Ocean Drilling Program), 345–363.

Gieskes, J.M., Blanc, G., Vrolijk, P., Elderfield, H., and Barnes, R., 1990. Interstitial-water chemistry—major constituents. *In* Moore, J.C., Mascle, A., et al., *Proc. ODP, Sci. Results,* 110: College Station, TX (Ocean Drilling Program), 155–178.

Gieskes, J.M., Gamo, T., and Brumsack, H.J., 1991. Chemical methods for interstitial water analysis aboard *JOIDES Resolution. ODP Tech. Note,* 15.

Hounslow, M.W., 1990. A magnetic susceptibility stratigraphy for Pleistocene and Pliocene sediments in the vicinity of the Barbados Ridge. *In* Moore, J.C., Mascle, A., et al., *Proc. ODP, Sci. Results,* 110: College Station, TX (Ocean Drilling Program), 365–377.

Jackson, M., Gruber, W., Marvin J., and Banerjee, S.K., 1988. Partial anhysteretic remanence and its anisotropy: applications and grainsize-dependence. *Geophys. Res. Lett.,* 15:440–443.

Jackson, M.J., Banerjee, S.K., Marvin, J.A., Lu, R., and Gruber, W., 1991. Detrital remanence, inclination errors, and anhysteretic remanence anisotropy: quantitative model and experimental results. *Geophys. J. Int.,* 104:95–103.

Kodama, K.P., 1988. Remanence rotation due to rock strain during folding and the stepwise application of the fold test. *J. Geophys. Res.,* 93:3357–3371.

Lowrie, W., 1990. Identification of ferromagnetic minerals in a rock by coercivity and unblocking temperature properties. *Geophys. Res. Lett.,* 17:159–162.

Mascle, A., Moore, J.C., et al., 1988. *Proc. ODP, Init. Repts.,* 110: College Station, TX (Ocean Drilling Program).

McDuff, R.E., 1981. Major cation gradients in DSDP interstitial waters: the role of diffusive exchange between seawater and upper oceanic crust. *Geochim. Cosmochim. Acta,* 45:1705–1713.

Moore, J.C., Mascle, A., et al., 1990. *Proc. ODP, Sci. Results,* 110: College Station, TX (Ocean Drilling Program).

Moore, J.C., Roeske, S.M., Lundberg, N., Schoonmaker, J., Cowan, D.S., Gonzales, E., and Lucas, S.E., 1986. Scaly fabrics from Deep Sea Drilling Project cores from forearcs. *In* Moore, J.C. (Ed.), *Structural Fabric in Deep Sea Drilling Project Cores From Forearcs.* Mem.—Geol. Soc. Am., 166:55–73.

Musgrave, R.J., Delaney, M.L., Stax, R., and Tarduno, J.A., 1993. Magnetic diagenesis, organic input, interstitial water chemistry, and paleomagnetic record of the carbonate sequence on the Ontong Java Plateau. *In* Berger, W.H., Kroenke, L.W., Mayer, L.A., et al., *Proc. ODP, Sci. Results,* 130: College Station, TX (Ocean Drilling Program), 527–546.

Ogawa, Y., Ashi, J., and Fujioka, K., 1992. Vein structures and their tectonic implications for the development of the Izu-Bonin forearc, Leg 126. *In* Taylor, B., Fujioka, K., et al., *Proc. ODP, Sci. Results,* 126: College Station, TX (Ocean Drilling Program), 195–207.

Peters, K.E., 1986. Guidelines for evaluating petroleum source rock using programmed pyrolysis. *AAPG Bull.,* 70:318–329.

Riedel, W.R., and Sanfilippo, A., 1978. Stratigraphy and evolution of tropical Cenozoic radiolarians. *Micropaleontology,* 24:61–96.

Shipboard Scientific Party, 1988. Site 671. *In* Mascle, A., Moore, J.C., et al., *Proc. ODP, Init. Repts.,* 110: College Station, TX (Ocean Drilling Program), 67–204.

Shipley, T.H., Moore, G.F., Bangs, N.L., Moore, J.C., and Stoffa, P.L., 1994. Seismically inferred dilatancy distribution, northern Barbados Ridge décollement: implications for fluid migration and fault strength. *Geology,* 22:411–414.

Taira, A., Hill, I., Firth, J.V., et al., 1991. *Proc. ODP, Init. Repts.,* 131: College Station, TX (Ocean Drilling Program).

* Abbreviations for names of organizations and publication titles in ODP reference lists follow the style given in *Chemical Abstracts Service Source Index* (published by American Chemical Society).

Ms 156IR-106

NOTE: Core-description forms ("barrel sheets") and core photographs can be found in Section 3, beginning on page 261. Forms containing smear-slide data can be found in Section 4, beginning on page 299. LWD, high-resolution, conventional, and cementation logs; sonic waveforms; and GRAPE, index properties, magnetic susceptibility, natural gamma-ray, *P*-wave, and reflectance data for Site 948 are presented on CD-ROM (back pocket).

SHORE-BASED LOG PROCESSING

Hole 948A

Bottom felt: 4940 mbrf
Total penetration: 583.7 mbsf

Logging Runs

Logging string 1: CDR/CDN

These logs were recorded using the LWD (logging-while-drilling) tools. The LWD employs tools that differ from the standard wireline logging tools (see "Downhole Logging" section, "Explanatory Notes" chapter, this volume). The following tracks are presented:

CDR = compensated dual resistivity
CDN = compensated density-neutron
R_{ad} = deep resistivity (Ωm)
P_{ps} = shallow resistivity (Ωm)
ROP = rate of penetration (ft/hr)

Processing

Depth shift: The LWD data have been shifted to reference the seafloor datum.

Note: Details on LWD can be found in the "Explanatory Notes" chapter, this volume. For further information about the logs, please contact:

Cristina Broglia
Phone: 914-365-8343
Fax: 914-365-3182
E-mail: chris@ldeo.columbia.edu

Elizabeth Pratson
Phone: 914-365-8313
Fax: 914-365-3182
E-mail: beth@ldeo.columbia.edu

Hole 948A: Natural Gamma Ray-Resistivity-Rate of Penetration Logging Data

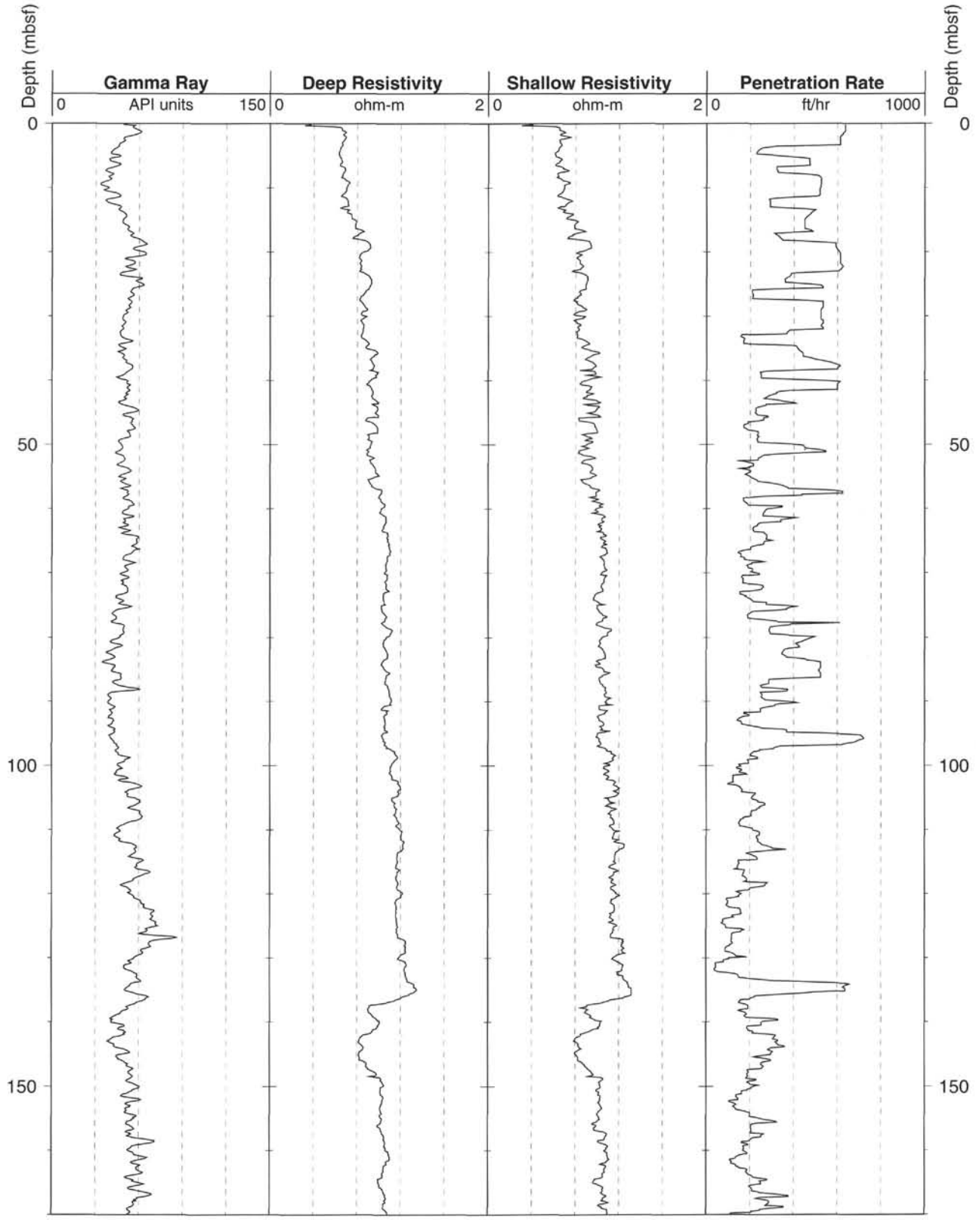

Hole 948A: Natural Gamma Ray-Resistivity-Rate of Penetration Logging Data (cont.)

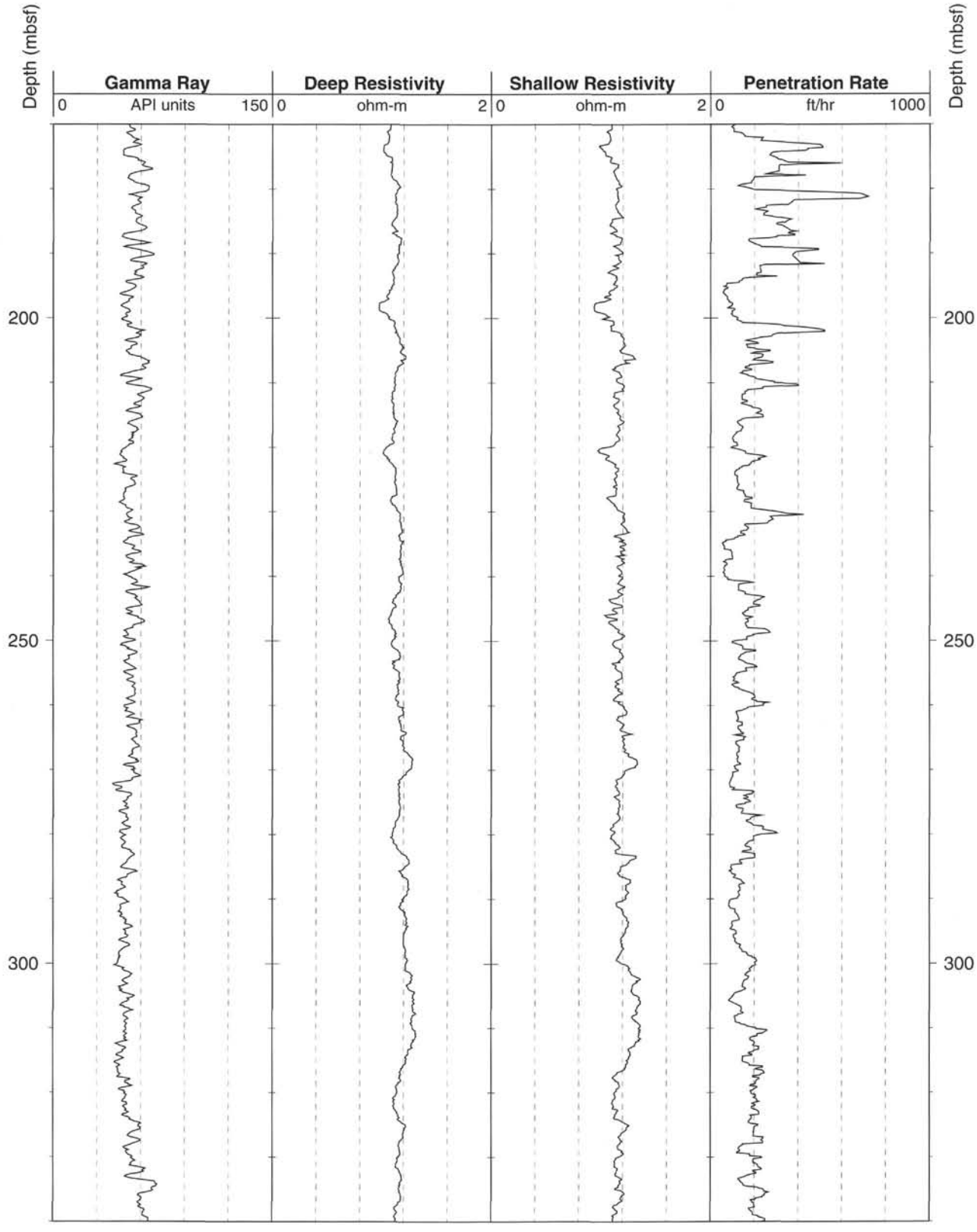

Hole 948A: Natural Gamma Ray-Resistivity-Rate of Penetration Logging Data (cont.)

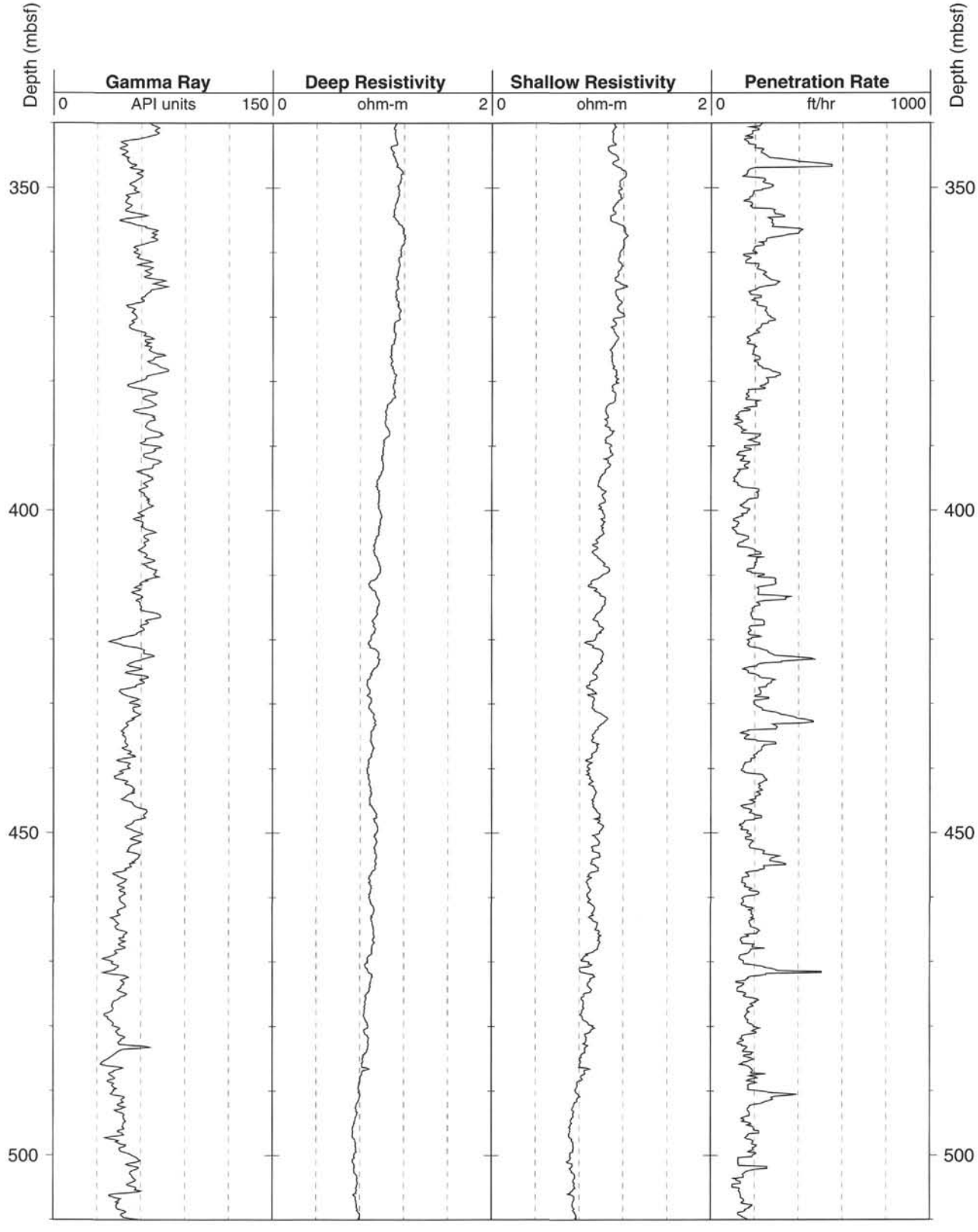

Hole 948A: Natural Gamma Ray-Resistivity-Rate of Penetration Logging Data (cont.)

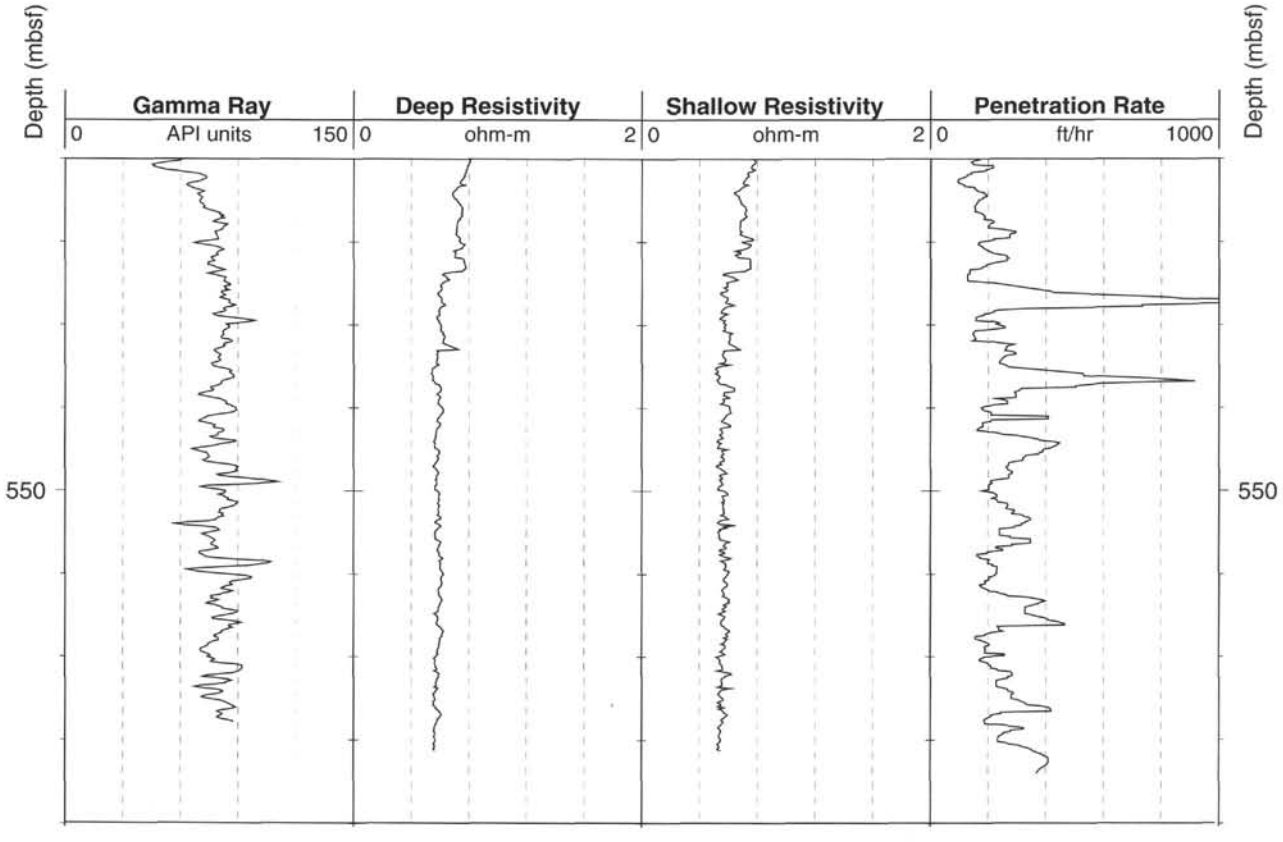

Hole 948A: Natural Gamma Ray-Density-Porosity Logging Data

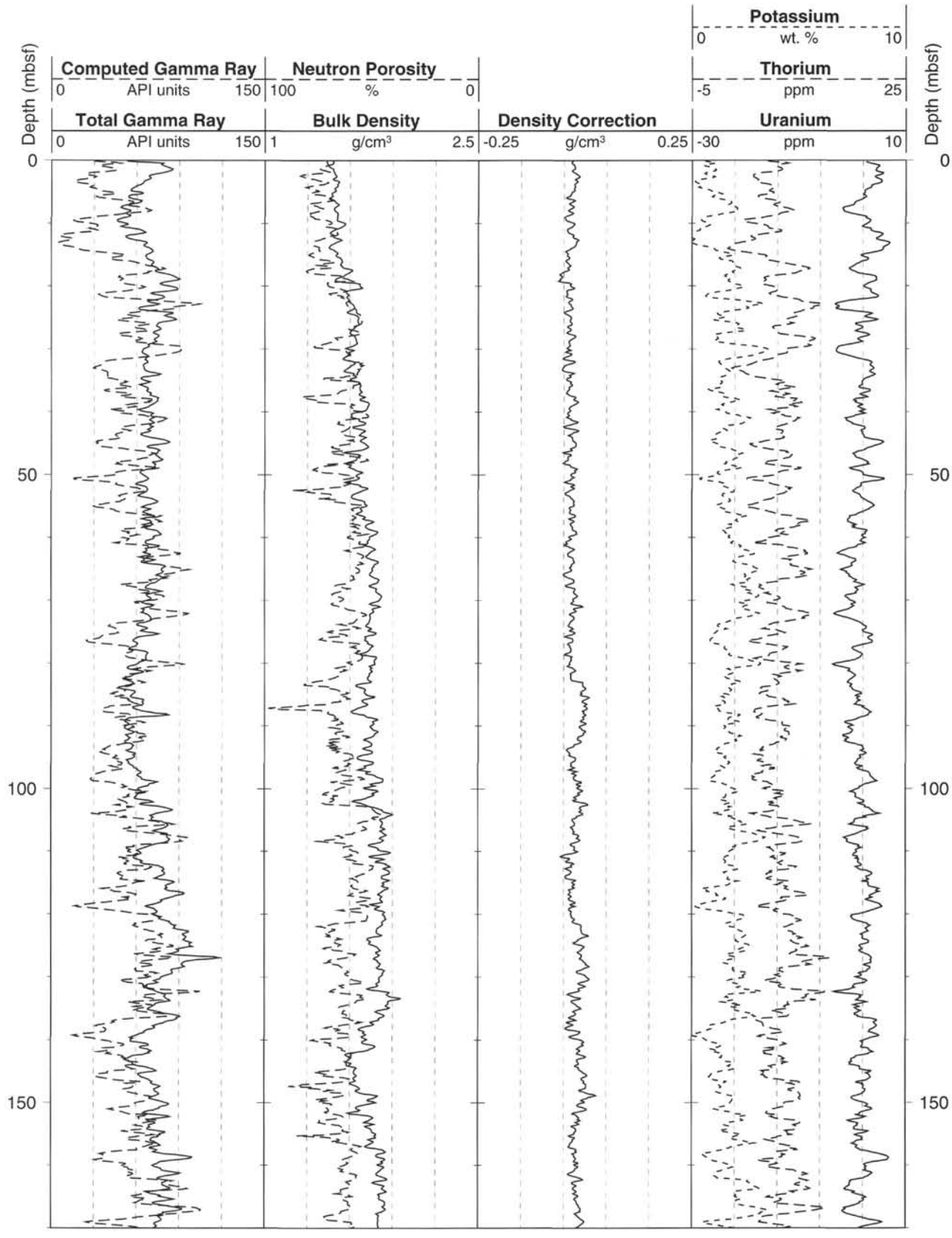

Hole 948A: Natural Gamma Ray-Density-Porosity Logging Data (cont.)

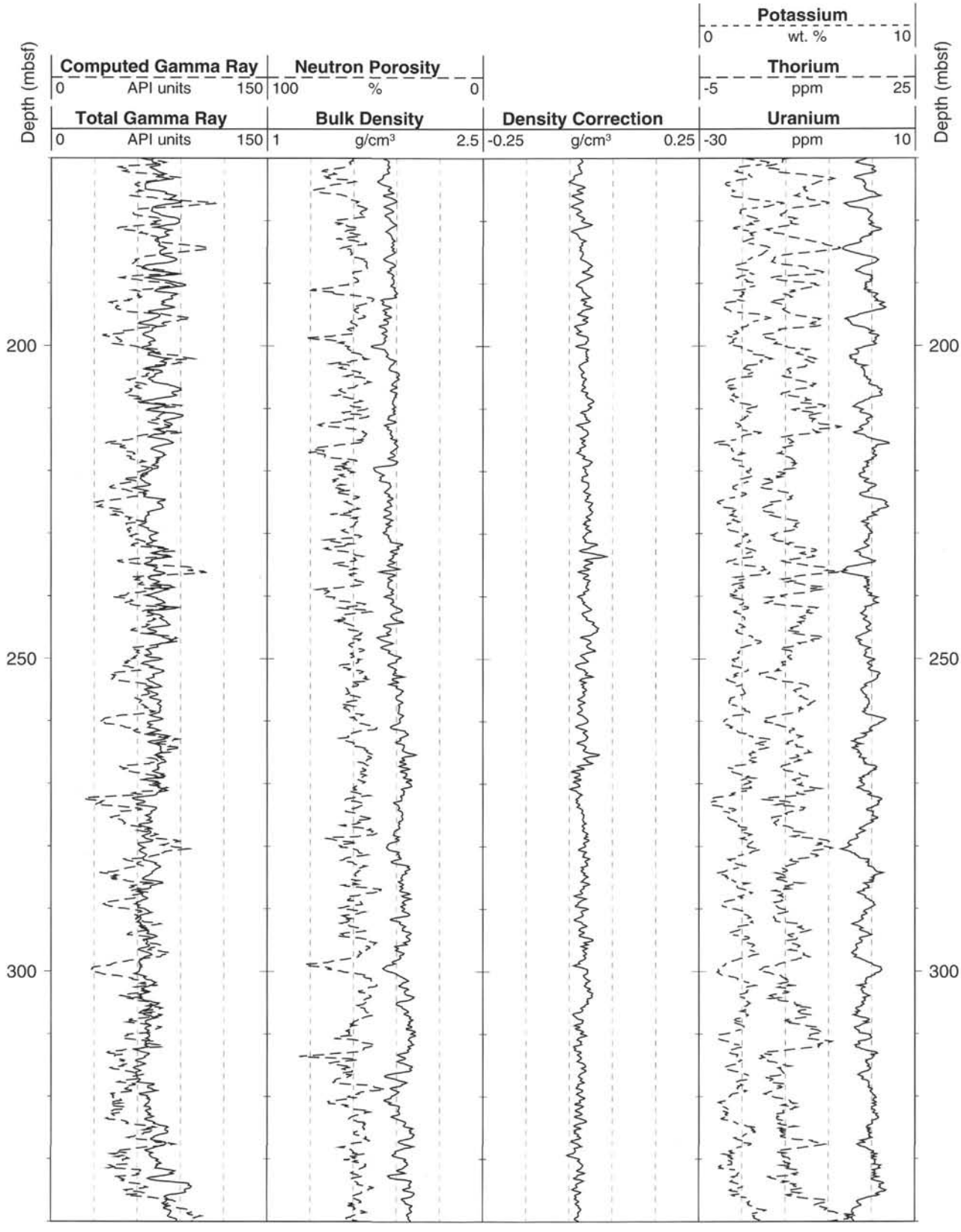

Hole 948A: Natural Gamma Ray-Density-Porosity Logging Data (cont.)

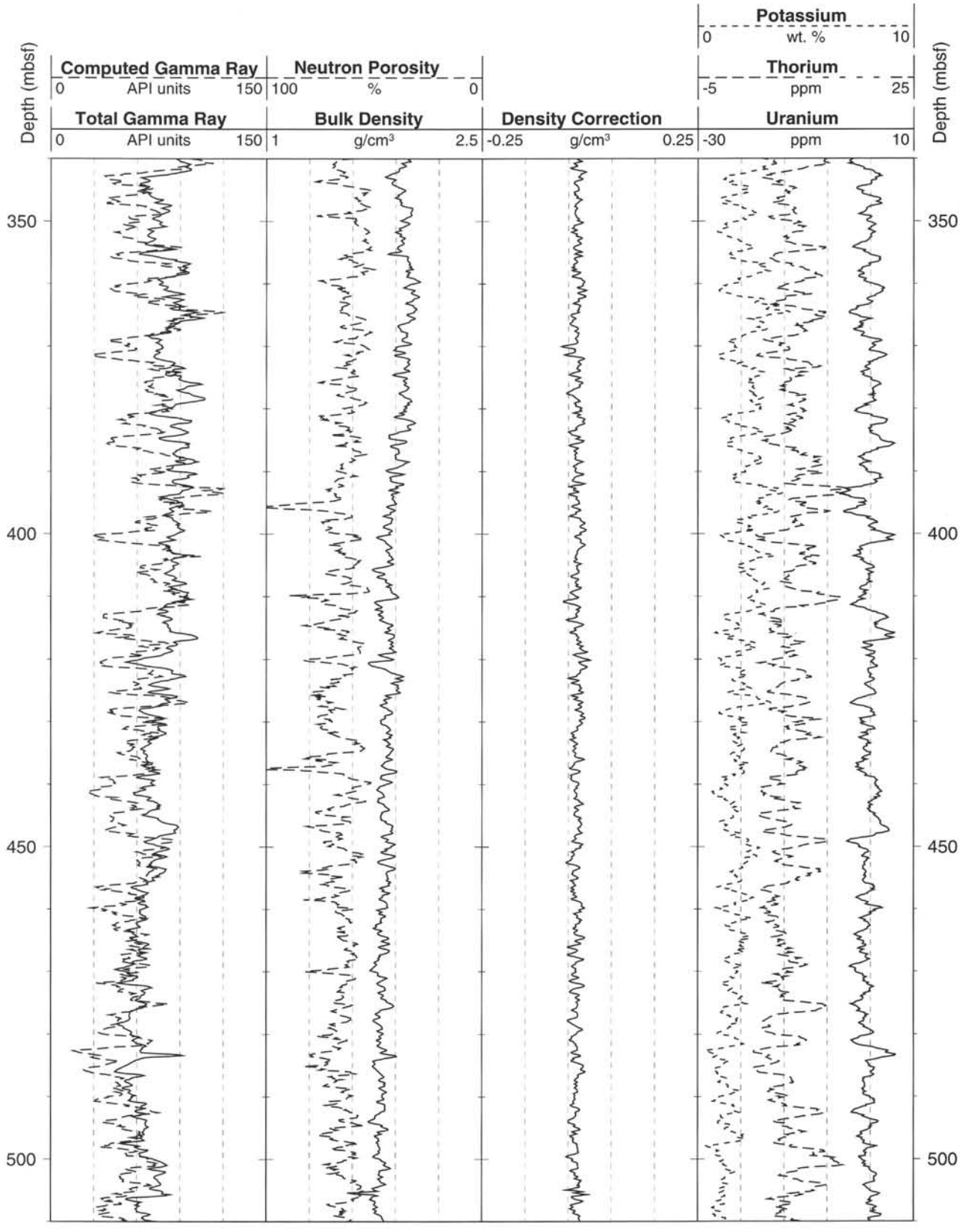

Hole 948A: Natural Gamma Ray-Density-Porosity Logging Data (cont.)

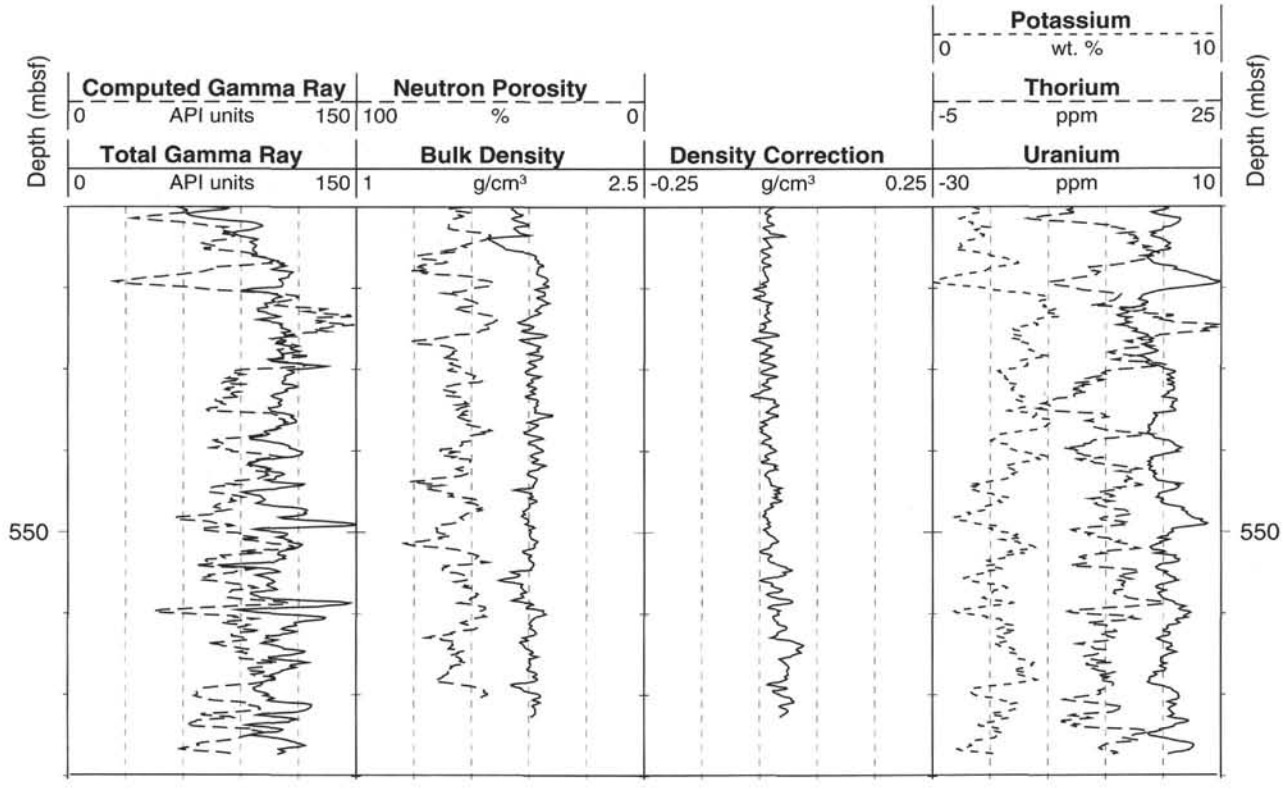

SHORE-BASED LOG PROCESSING

Hole 948C

Bottom felt: 4942.5 mbrf
Total penetration: 592 mbsf

Logging Runs

Logging String 1: LSS/HLDT/NGT
Wireline heave compensator was used.

Bottom-hole Assembly

The following bottom-hole assembly and drill-pipe depths are as they appear on the logs after differential depth shift (see "Depth Shift" section) and depth shift to the seafloor. As such, there might be a discrepancy with the original depths given by the drillers on board. Possible reasons for depth discrepancies are ship heave, use of wireline heave compensator, and drill string and/or wireline stretch.

LSS/HLDT/NGT: Bottom-hole assembly at ~84.5 mbsf; drill pipe at ~22.5 mbsf.

Processing

Depth shift: The LWD data have been shifted to reference the seafloor datum.
Gamma-ray processing: NGT data have been processed to correct for borehole size and type of drilling fluid.
Acoustic data processing: The sonic logs have been processed to eliminate some of the noise and cycle skipping experienced during the recording. Using two sets of the four transit-time measurements and proper depth justification, four independent measurements over a 2-ft interval centered on the depth of interest are determined, each based on the difference between a pair of transmitters and receivers. The program discarded any transit time that was negative or fell outside a range of realistic values selected by the processor.

Quality Control

During the processing, quality control of the data was performed by cross-correlation of all logging data. Large (>12 in.) and/or irregular borehole affects most recordings, particularly those that require 30-cm eccentralization (HLDT, for instance) and a good contact with the borehole wall. Invalid density spikes were recorded 394, 416, 437.5, 462–467, and 520–525 mbsf.

Hole diameter was recorded by the hydraulic caliper on the HLDT tool (CALI); the caliper was restricted from about 525 to 330 mbsf due to collapse of the hole. The caliper was closed at 102.5 mbsf before entering the bottom-hole assembly; consequently, the density logs could not be corrected in real time from 102.5 to 89 mbsf. Hole irregularities greatly affect the response of the logging tools; while the sonic log seems to yield a reliable response, the density log should be used with extreme caution. Its use for the calculation of an impedance curve for synthetic seismogram is not recommended.

Data recorded through pipe and bottom-hole assembly, such as the gamma ray recorded above 84 mbsf, should be used qualitatively only because the incoming signal is attenuated.

Note: Details of wireline logging procedures can be found in the "Explanatory Notes" chapter, this volume. For further information about the logs, please contact:

Cristina Broglia
Phone: 914-365-8343
Fax: 914-365-3182
E-mail: chris@ldeo.columbia.edu

Elizabeth Pratson
Phone: 914-365-8313
Fax: 914-365-3182
E-mail: beth@ldeo.columbia.edu

Hole 948C: Natural Gamma Ray-Density Logging Data

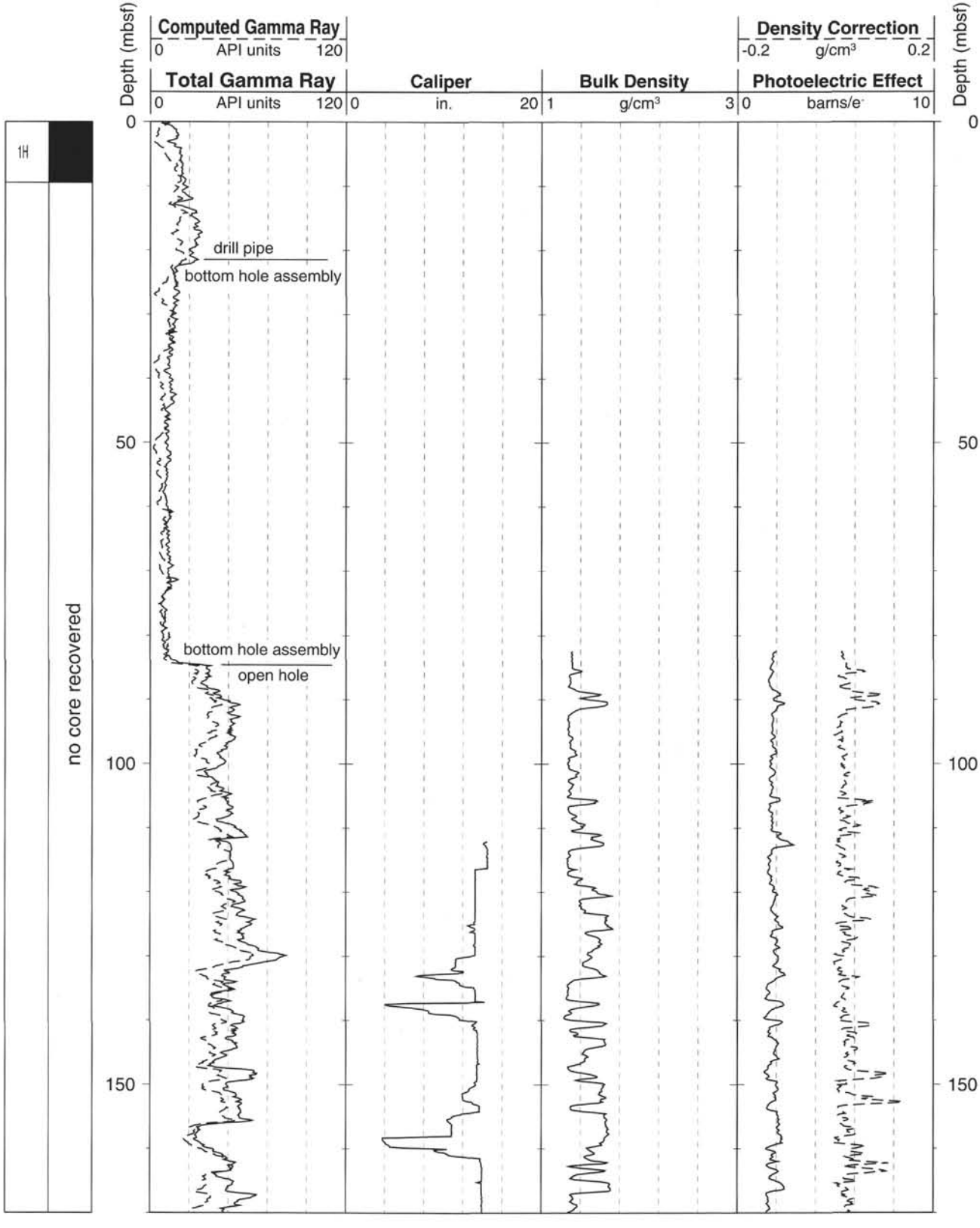

Hole 948C: Natural Gamma Ray-Density Logging Data (cont.)

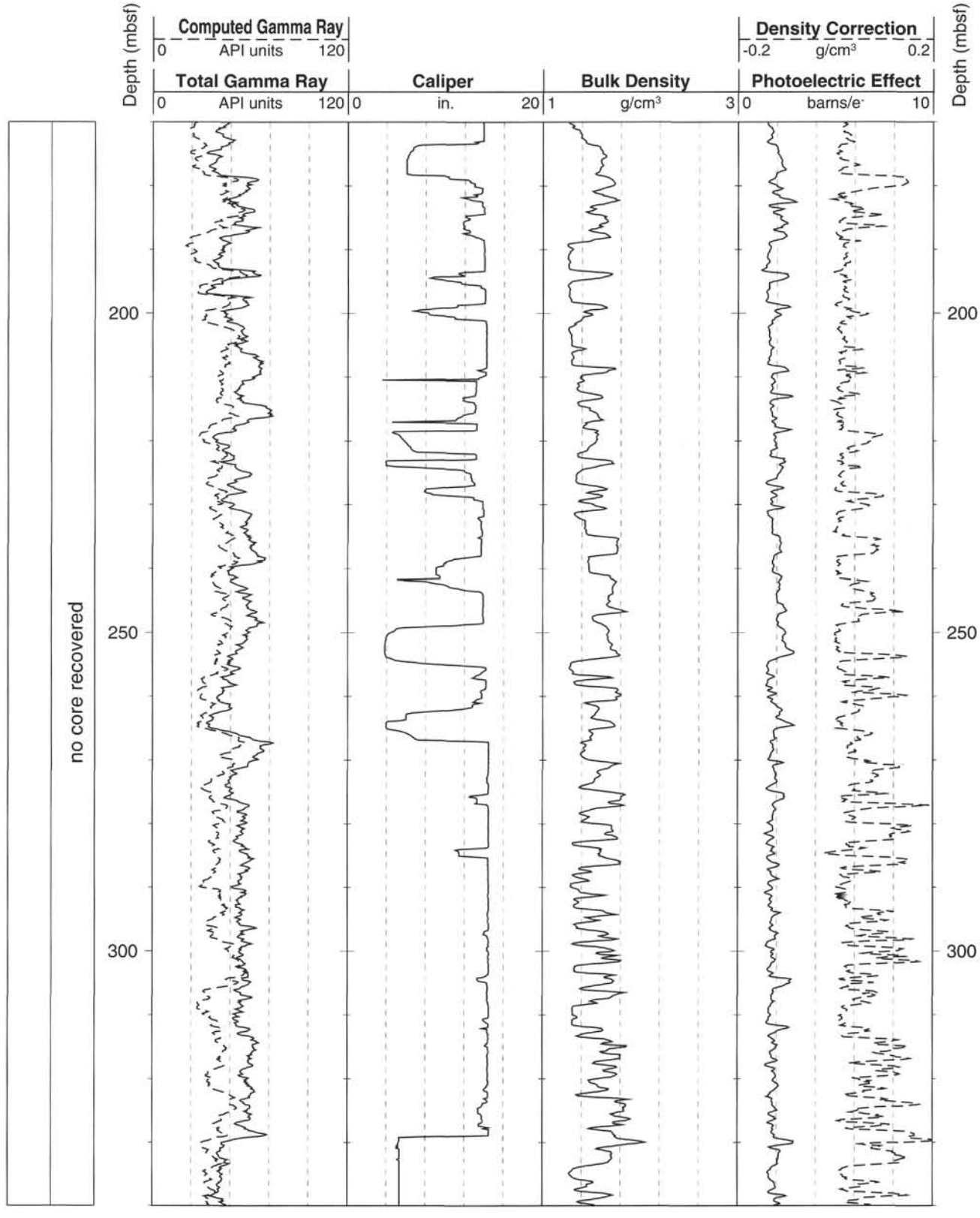

Hole 948C: Natural Gamma Ray-Density Logging Data (cont.)

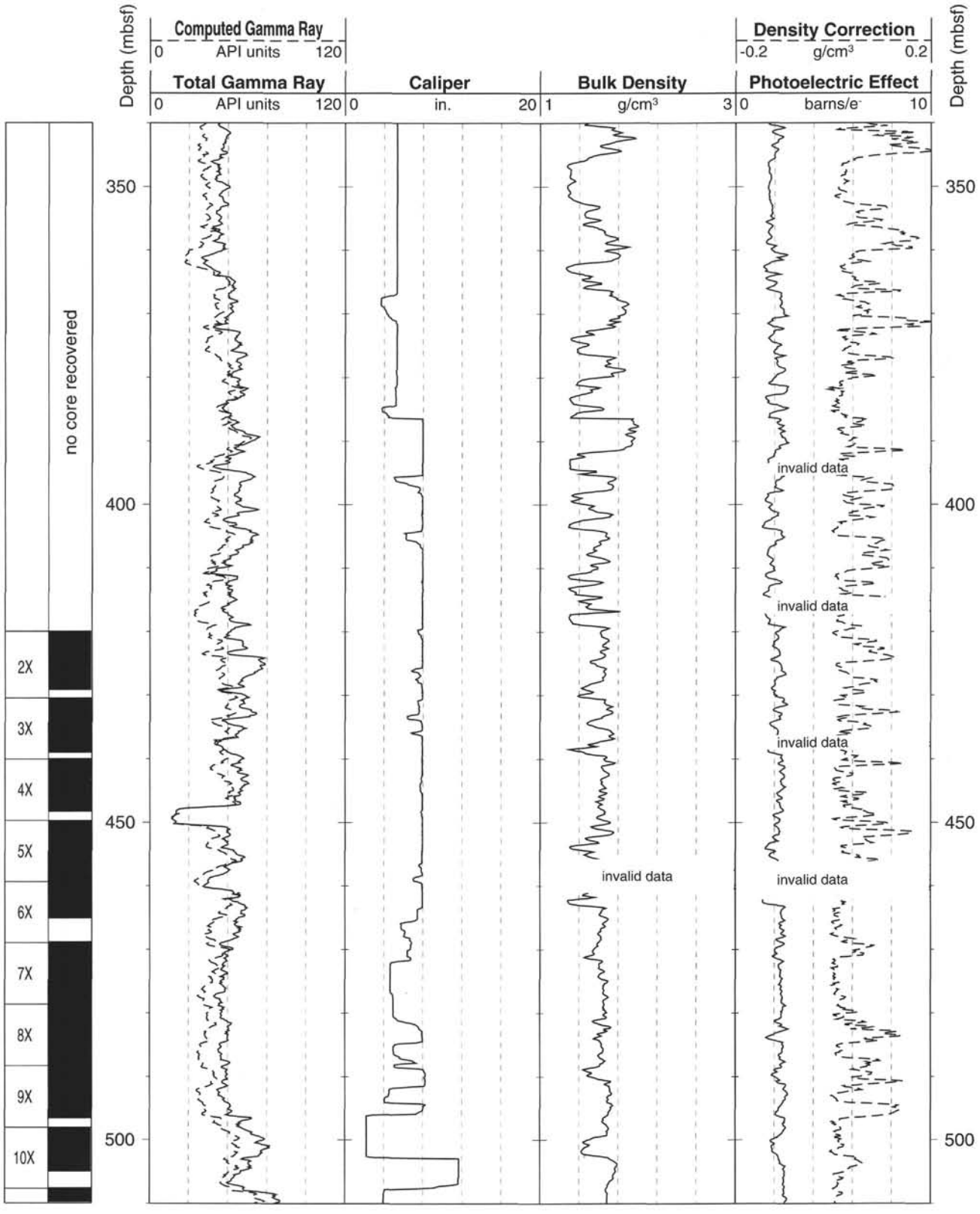

Hole 948C: Natural Gamma Ray-Density Logging Data (cont.)

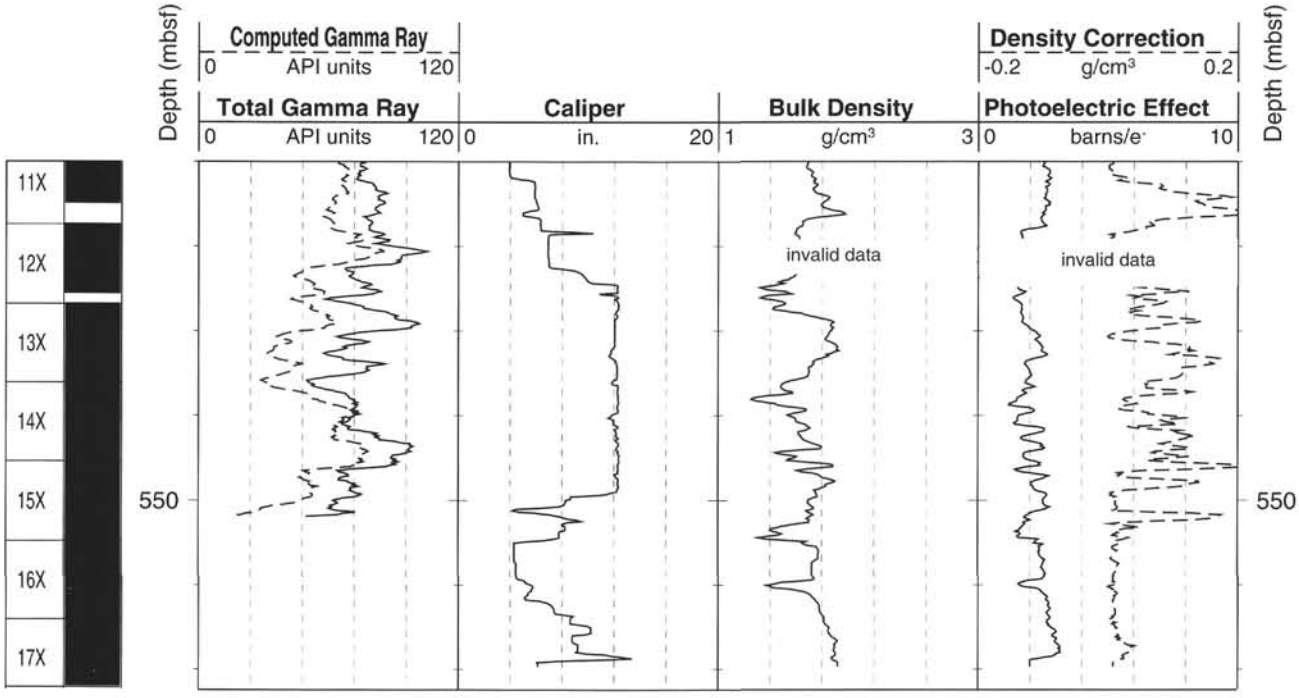

Hole 948C: Natural Gamma Ray-Tension-Velocity Logging Data

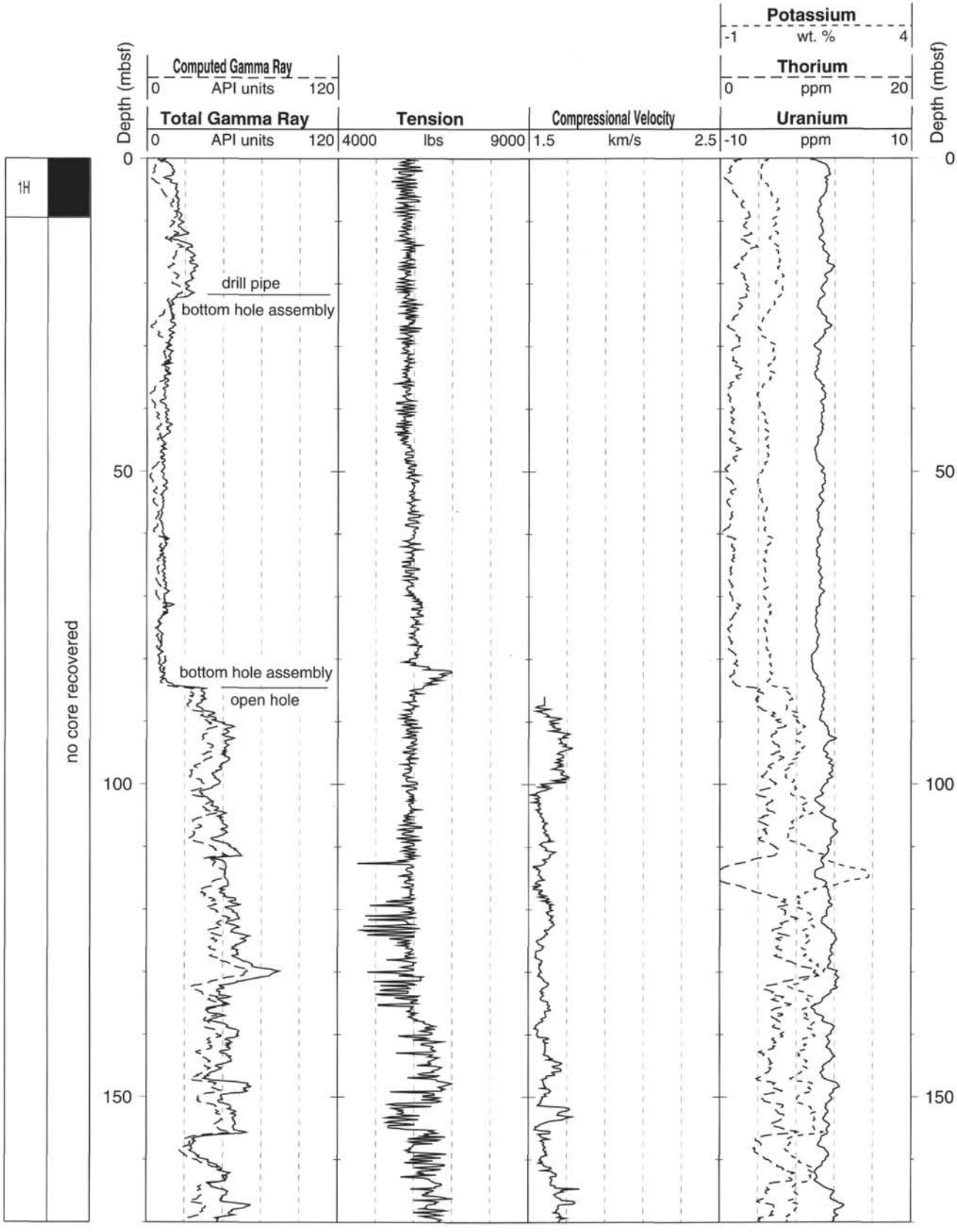

Hole 948C: Natural Gamma Ray-Tension-Velocity Logging Data (cont.)

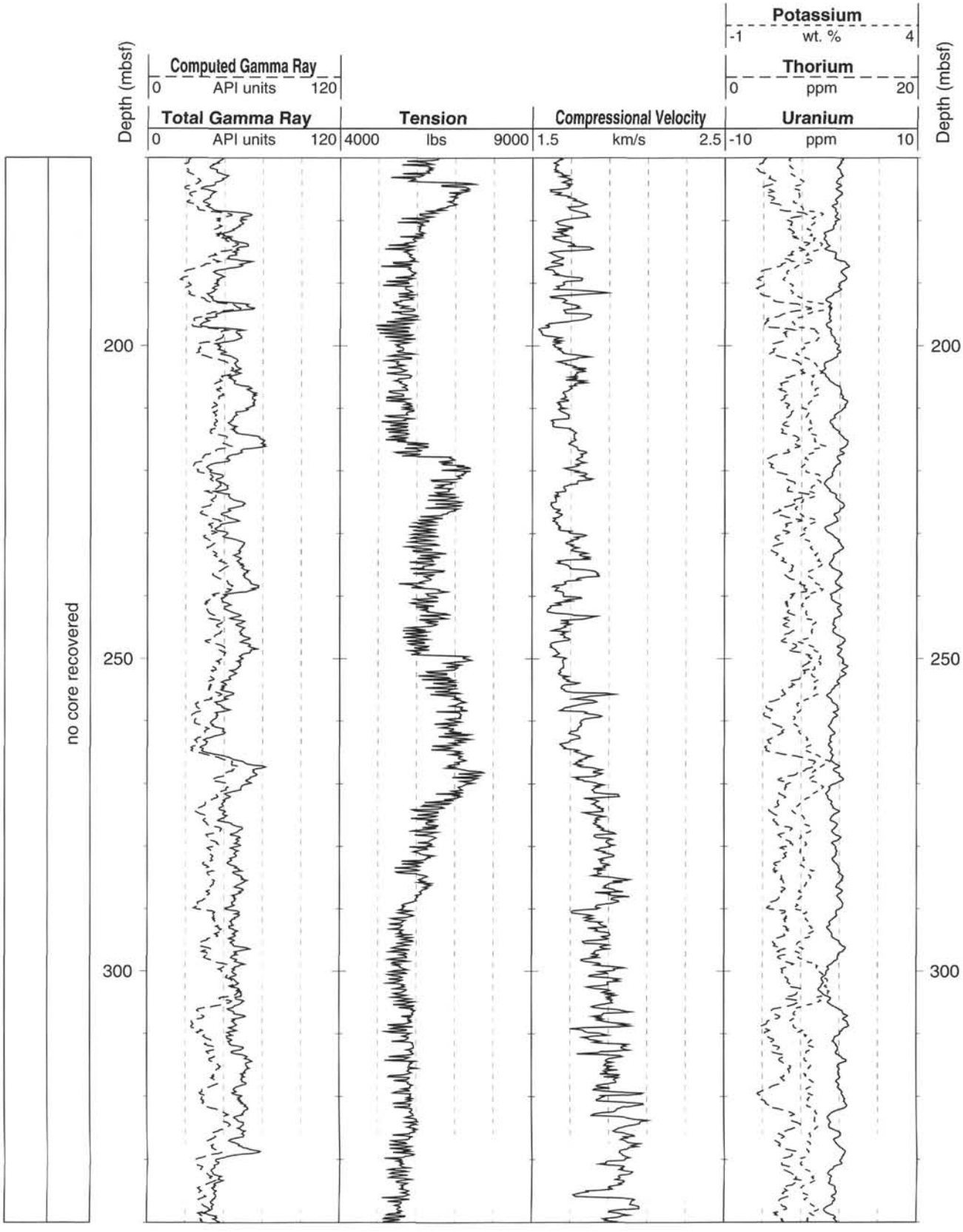

Hole 948C: Natural Gamma Ray-Tension-Velocity Logging Data (cont.)

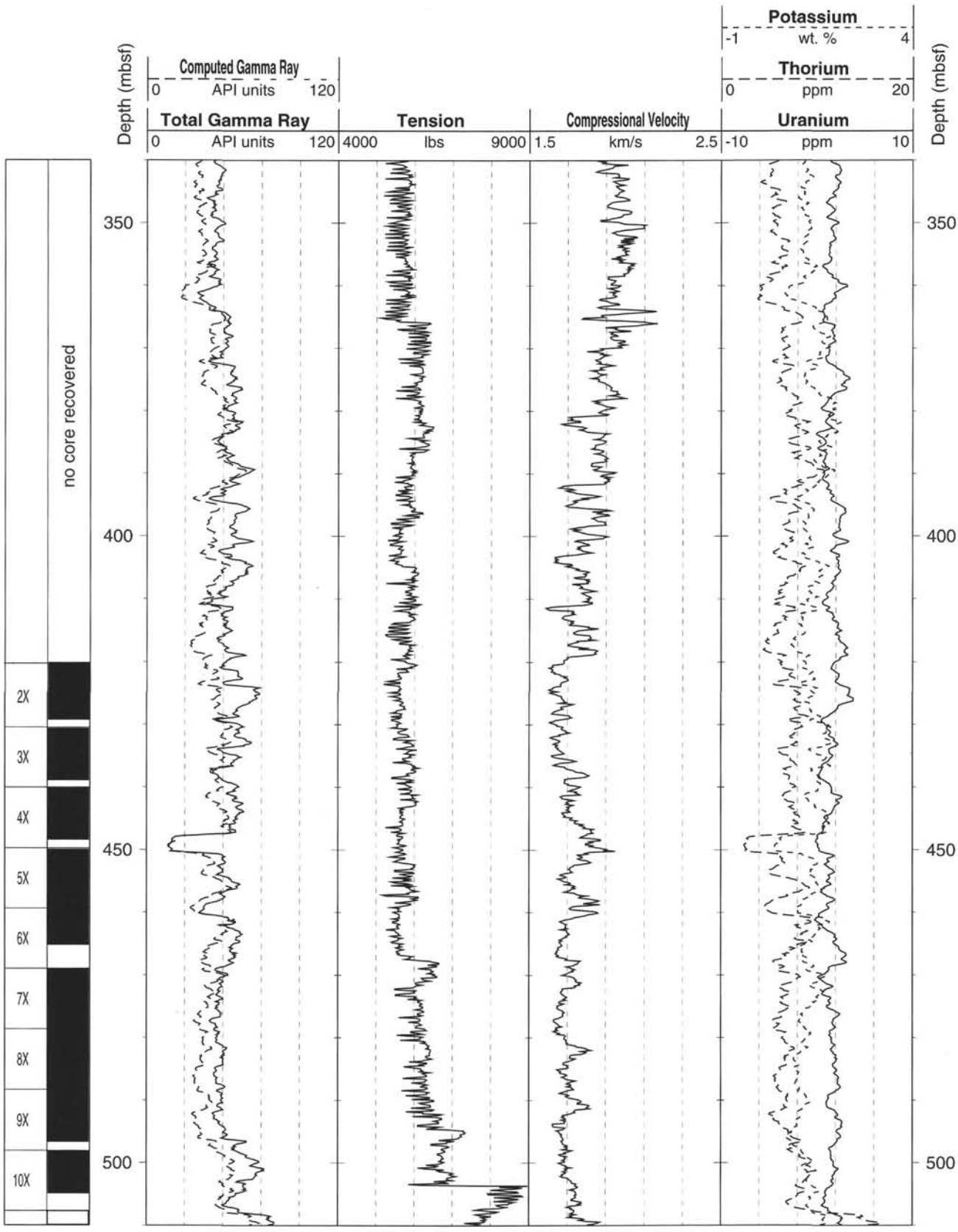

Hole 948C: Natural Gamma Ray-Tension-Velocity Logging Data (cont.)